Synthesis of ZnO Based Metal Oxide Nanomaterials for Multifunctional Application Studies

Buzuayehu Abebe

A Dissertation Submitted to
The Department of Applied Chemistry
School of Applied Natural Science

Presented in Fulfillment of the Requirement for the Degree of Doctor of Philosophy in Materials Chemistry

Office of Graduate Studies
Adama Science and Technology University

June, 2021
Adama, Ethiopia

Synthesis of ZnO Based Metal Oxide Nanomaterials for Multifunctional Application Studies

Buzuayehu Abebe

Supervisors

Main supervisor: H C Ananda Murthy (Assoc. prof., Ph.D.)

Co-supervisor: Enyew Amare Zereffa (Assoc. prof., Ph.D.)

A Dissertation Submitted to

The Department of Applied Chemistry

School of Applied Natural Science

Presented in Fulfillment of the Requirement for the Degree of Doctor of Philosophy in Materials Chemistry

Office of Graduate Studies

Adama Science and Technology University

June, 2021

Adama, Ethiopia

Approval Page of Ph.D. Dissertation

We hereby certify that the recommendations and suggestions made by the board of examiners are appropriately incorporated into the final version of the dissertation entitled "**Synthesis of ZnO Based Metal Oxide Nanomaterials for Multifunctional Application Studies**" by **Buzuayehu Abebe**.

Major Supervisor	Signature	Date
Co-supervisor	Signature	Date

We, the undersigned, members of the Board of Examiners of the dissertation open defense by **Buzuayehu Abebe** have read and evaluated the dissertation entitled "**Synthesis of ZnO Based Metal Oxide Nanomaterials for Multifunctional Application Studies**" and examined the candidate during open defense. This is, therefore, to certify that the dissertation is accepted for partial fulfillment of the requirement of the degree of Doctor of Philosophy in Materials Chemistry.

Chairperson	Signature	Date
Internal Examiner	Signature	Date
External Examiner 1	Signature	Date
External Examiner 2	Signature	Date

Finally, approval and acceptance of the dissertation is contingent upon submission of its final copy to the Office of Postgraduate Studies (OPGS) through the candidate's Department Graduate Council (DGC) and School Graduate Committee (SGC).

Department Head	Signature	Date
School Dean	Signature	Date
Postgraduate Dean	Signature	Date

DECLARATION

I hereby declare that this Dissertation entitled "**Synthesis of ZnO Based Metal Oxide Nanomaterials for Multifunctional Application Studies**" is my original work. That is, it has not been submitted for the award of any academic degree, diploma or certificate in any other university. All sources of materials used for this dissertation have been duly acknowledged through appropriate citations.

_____	_____	_____
Name of student	Signature	Date

RECOMMENDATION

We, the supervisors of this dissertation, hereby certify that we have read and revised the dissertation entitled "**Synthesis of ZnO Based Metal Oxide Nanomaterials for Multifunctional Application Studies**" prepared under our guidance by **Buzuayehu Abebe** submitted in partial fulfillment of the requirements for the degree of Doctor of Philosophy in **Materials Chemistry**. Therefore, we recommend the submission of the dissertation to the department for further review and defense.

_____	_____	_____
Main supervisor	Signature	Date
_____	_____	_____
Co-supervisor	Signature	Date

ACKNOWLEDGEMENTS

First of all, I would like to express my deepest gratitude to my supervisors Dr. H C Ananda Murthy and Dr. Enyew Amare Zereffa for their unreserved cooperation, constructive suggestions, supervision, appreciable encouragement, and fatherly consultancy throughout the work. I thank Guta Amanu and Eticha Abdisa for their help as technicians during laboratory work. Similarly, I thank Mr. Yeshaneh Adimasu and Mr. Demeke Tesfaye for their assistance during my work and sample characterization. Moreover, I acknowledge the ministry of science and higher education for sponsoring my Ph.D. study, Adama Science and Technology University for financial support, Department of Applied Chemistry, Department of Applied Biology, and Department of Materials Engineering for providing laboratory space and facility to accomplish this work. I would also like to extend my gratitude to my family for their unreserved moral support. Thanks to C. R. Ravikumar (Research Centre, Department of Science, East-West Institute of Technology, Bangalore 560091, India) for conducting different tests. Thanks to Dr. Bedasa Abdisa for providing valuable comments on my Ph. D work. Last but not least, my heartfelt gratitude goes to my colleagues and friends for their generous support and contributions.

TABLE OF CONTENTS

Contents

LIST OF TABLES

LIST OF FIGURES

LIST OF ABBREVIATIONS

Abbreviation	Full name	Abbreviation	Full name
BET	Brunauer–Emmett–Teller	NRs	Nanorods
BG	Bandgap (eV)	P_d	Pore diameter (nm)
BMONCs	Binary metal oxide nanocomposites	p_V	Pore volume
BMONCs	Binary metal oxide NCs	PVA	Poly(vinyl alcohol)
CB	Conduction band	PVA-BMONCs	PVA assisted Binary metal oxide nanocomposites
CLSM	confocal laser scanning microscopy	PVA-TMONCs	PVA assisted ternary metal oxide nanocomposites
CV	Cyclic voltammetry	Rh6G	Rhodamine 6G
DTA	Differential thermal analysis	RhB	Rhodamine B
EIS	Electrochemical impedance spectroscopy	ROS	reactive oxygen species
EPR	Electron paramagnetic resonance	SAED	Selected area electron diffraction
FEGEM	Field emission gun scanning electron microscope	SEM-EDS	scanning electron microscopy-Energy-dispersive X-ray spectroscopy
FESEM	Field emission scanning electron microscopy	SAV	Surface area to volume ratio
FETEM	Field-emission transmission electron microscopy	SSA	Specific surface area
FM	Fluorescence microscopy	TGA	Thermogravimetric analysis
FT-IR	Fourier transform-infrared	TMONCs	Ternary metal oxide nanocomposites
HRTEM	High-resolution transmission electron microscopy	UV-vis-DRS	UV–vis diffuse reflectance
MB	Methylene blue	XPS	X-ray photoelectron spectroscopy
MO	Methyl orange	VB	Valence band
NCs	Nanocomposites	XRD	X-ray diffraction
NHE	Normal hydrogen electrode	ZOI	Zone of inhibition
NPs	Nanoparticles	NCs	Nanocomposites

ABSTRACT

The application of metal oxides is one of the most promising practices in a diverse field. Zinc oxide (ZnO) is one of the novel metal oxides utilized for various applications such as sorption, photocatalysis, sensing, and antimicrobial. The electron-hole recombination that occurs due to the aggregation/agglomeration is the major limitation in employing ZnO for photocatalysis. Among several efforts made to enhance the charge transfer capability of ZnO, forming a heterojunction is a simple and economical way. The sol-gel followed by the auto-combustion method was utilized for synthesizing a high surface area to volume ratio and porous ZnO-based metal oxide nanocomposites. The effects of the synthesis techniques, type of precursors, amount of poly (vinyl alcohol) loading, and precursor percentage were studied and optimized. The synthesized nanoparticles and nanocomposites were characterized by DTG/DSC, UV-vis-DRS, XRD, FT-IR, BET, SEM/EDX, XPS, TEM/HRTEM/SAED, and CV/EIS/amperometric analytical techniques. The characterization results revealed the surface area to volume ratio, porosity, and charge transfer property improvement on the ternary nanocomposite (Zn/Fe/Mn oxide), compared to single ZnO and binary (Zn/Fe and Zn/Mn) oxide counterparts. From the DTG/DSC result, the calcination temperature of 500 ^{o}C was found to be ideal for degrading impurities and poly (vinyl alcohol) polymer after its role as a capping agent. Using the XRD pattern and TEM image analysis, the crystallite size of the nanoparticles and nanocomposites was confirmed to be in the nanometer range (7nm - 70 nm). The porous nature of the optimized nanocomposites was understood from the SEM image and BET analysis; consistent results were also noted from the HRTEM (IFFT) and SAED pattern analysis. The EDX, XPS, HRTEM analysis confirmed the presence of a predictable composition of the nanocomposites. As calculated from the BET analysis, the specific surface area (SSA) of the porous ternary nanocomposite was found to be 15 times greater than that of ZnO. The presence of greater charge transfer property for ternary nanocomposites, compared to ZnO and binary nanocomposites were evidenced from CV/EIS analysis. The electron transfer resistance values, as determined using Nyquist plot for $ZnO/Fe_2O_3/Mn_2O_3$, ZnO/Fe_2O_3, ZnO/Mn_2O_3, and ZnO were found to be 7, 25, 61, and 65 Ω, respectively. The adsorption test on methylene blue dye showed the domination of a chemisorption type of adsorption. The Langmuir, Freundlich, Dubinin-Radushkevich, Temkin, Flory-Huggins, and Fowler-Guggenheim isotherm models were applied to understand the adsorption process. Among them, the Langmuir and Flory-Huggins models showed better fitting. From the Langmuir model, the adsorption efficiency of ternary nanocomposites was determined to be 7.75 mg g^{-1}. Compared to the other nanoparticles and nanocomposites, ZnO/Mn_2O_3 nanocomposite showed better photocatalytic activity only on the acid orange-8 dye. However, the $ZnO/Fe_2O_3/Mn_2O_3$ nanocomposite is effective on both Congo red and Acid orange 8 dyes degradation. The $ZnO/Fe_2O_3/Mn_2O_3$ and ZnO/Fe_2O_3 nanocomposites showed superior ascorbic acid detection capacity. Compared to ZnO, the synthesized binary and ternary nanocomposites exhibited an enhanced antibacterial activity on both Gram-positive and Gram-negative bacteria. The highest zone of inhibition for ternary nanocomposite is 28 and 29 mm on E. coli and S. aureus bacteria, respectively. From these results, it is possible to conclude that the synthesized nanocomposites have good potential for multifunctional applications including photocatalysis, sensor, and antibacterial activities.

Keywords: *Porous ZnO based nanocomposites, Photocatalysis, Sensor, Adsorption, Antibacterial activity*

CHAPTER ONE

1. INTRODUCTION

Metal oxides are the most explored class of inorganic materials owing to their unique physical and chemical properties such as controllable particle size, low synthesis cost, and high stability (Nagvenkar et al., 2019). The nanosized inorganic particles, whose structure exhibits unique physical, chemical, and biological properties, have gained extreme interest over the past decades (Applerot et al., 2009). Besides, they have distinctive properties towards antimicrobial activity, intensive ultraviolet light absorption, and high catalytic activity. Recently, zinc oxide (ZnO) nanostructures have received much attention within the scientific community owing to their low cost, easy availability, biocompatibility, and the possibility of performing surface modifications with different functional groups (Díez-Pascual & Díez-Vicente, 2014).

With the rapid development of industrial society, increasing environmental safety threats pose the current global concern. Nowadays, water pollution is one of the most significant problems in the environmental field. As an example, the textile industry is one of the water-consuming and heavily polluting industries. It is estimated that over 500 tons of various dyes are being discharged into the water bodies, and approximately 80% of them are from the textile industry. Since these dyes are poorly biodegradable and have many functional groups, they are potentially harmful to humans life and cause chronic effects (Areerob et al., 2018). The methylene blue (MB), Congo red (CR), and Acid orange 8 (AO8) dyes are among the most commonly used substance for different applications. MB dye is not strongly poisonous, although, it has harmful effects on human beings (Hofmann et al., 1966; Liu et al., 2012; Tan et al., 2008). The CR (Madan et al., 2019; Nayak et al., 2020) and AO8 (Elizalde-González & García-Díaz, 2010; Guaratini & Zanoni, 2000) dyes have mutagenic and carcinogenic properties.

Previously, several physicochemical techniques such as sedimentation–flocculation, coagulation, molecular sieving, ion exchange, reverse osmosis, membrane filtration, ozonation, chlorination, chemical precipitation, adsorption, and photocatalysis were applied to remove toxic organic and inorganic pollutants (Adeleye et al., 2016; Charles et al., 2016; Dickhout et al., 2017; Miranda et al., 2016; Pype et al., 2016; Rizzo et al., 2014;

Subramani & Jacangelo, 2015; Xiaofei Zhang et al., 2017). However, some of those techniques are not efficient and adequate on cost, energy, and also lack the complete degradation properties of the contaminants (Ramos-Delgado et al., 2016). Among the advanced oxidation processes, heterogeneous photocatalysis for highly toxic organic pollutants was suggested to be simple, work under ambient conditions, cost-effective, environmentally safe, and does not give secondary pollution. Moreover, for less toxic pollutants the adsorption technique was also suggested to be simple, cost-effective, energy-efficient, and environmentally safe (Chen et al., 2017; Gómez-Pastora et al., 2017; Yagub et al., 2014).

The metal oxides-based heterogeneous photocatalysis and adsorption techniques are the most promising practices as environmental remediation (Vinu & Madras, 2010; Yagub et al., 2014). Nowadays, metal oxides such as TiO_2, ZnO, Fe_2O_3, Mn_2O_3, ZrO_2, V_2O_5, Nb_2O_5, and WO_3 are applied vigorously for environmental waste management, medicine, food preservation (Ahmed, Rasul, Martens, et al., 2011; Espitia et al., 2012; Yemmireddy & Hung, 2017), and pollutant sensing (Ibupoto et al., 2012) applications. Among these oxides, ZnO is ideal with low-cost and less toxic properties (Akkari et al., 2018). Compared to TiO_2, the production cost of ZnO is approximately 75% lower and also has higher absorption efficacy across a large fraction of the solar spectrum (Janotti & Van de Walle, 2009; Ong et al., 2018; Sakthivel et al., 2003). However, applying bare ZnO as a photocatalyst faces an e^-/h^+ recombination problem, and produces photo corrosion in alkaline solution under UV irradiation (Qamar et al., 2016). Recently, efforts such as doping (Yingming Wang et al., 2020), forming a heterojunction with equivalent or/and different bandgap materials (Desong Wang et al., 2008), dye sensitization (Macák et al., 2005), noble and non-noble metal deposition (An et al., 2009), simultaneous doping-sensitization, doping-deposition, and deposition-coupling are practiced to overcome these drawbacks and improve its structural stability (Kumar & Rao, 2017).

Among these efforts, forming ZnO-based heterojunction was found to be one of the novel preferences. Several ZnO based binary related bandgap heterojunctions such as TiO_2/ZnO (Bozkurt Çırak et al., 2019; Moradi et al., 2016) and SnO_2/ZnO (Chiang & Lin, 2013) and different bandgap heterojunctions such as ZnO/γ-Mn_2O_3 (Saravanan et al., 2014), and ZnO/Fe_2O_3 (Davari et al., 2017; Lachheb et al., 2017; Sin et al., 2018) have been investigated. In addition, the ZnO/Fe_2O_3/MnO_2 (Tedla et al., 2015), SnO_2/ZnO/TiO_2

(Guidong Yang et al., 2012), $ZnO/Ag_2O/Fe_3O_4$ (Cai et al., 2015), $Fe_3O_4/ZnO/CoWO_4$ (Shekofteh-Gohari & Habibi-Yangjeh, 2017), and $Fe_3O_4/ZnO/NiWO_4$ (Habibi-Yangjeh & Shekofteh-Gohari, 2017) ternary heterojunctions have also been studied. The enhanced surface area to volume ratio (SAV), photocatalytic, and antibacterial improvement was confirmed for both binary and ternary heterojunctions, compared to the bare ZnO (Lei et al., 2018; Mayank et al., 2019). Due to the synergistic effect (Maya-Treviño et al., 2015), the ternary heterojunctions further improve the separation of photogenerated electron/hole pairs compared to the binary heterojunctions (Lei et al., 2018; Xiaojuan Li et al., 2018; Pirhashemi et al., 2018). There is enough information regarding the fabrication of zinc/iron heterojunction and few studies on the construction of zinc/manganese hybrids. However, to the best of our knowledge, no reports focused on the ternary hybrids based on zinc/iron/manganese nanocomposite, which enhance the SAV, porosity, and charge transfer property concurrently.

The properties such as stability, visible light absorption, high SAV, and low toxicity offered by iron and manganese oxide make them promising materials (Behtaj Lejbini & Sangpour, 2019; Bigiani et al., 2019; Dehghani-Dashtabi et al., 2019; Rosa et al., 2019; Yu et al., 2019). Among different crystalline polymorphs of the n-type iron oxide semiconductor, the hematite (α-Fe_2O_3) is recommended as the most stable phase (Mishra & Chun, 2015). Forming a composite with Fe_2O_3 and protecting ZnO from dissolution during light irradiation were also reported (Qamar et al., 2016). Among different crystalline polymorphs of manganese oxide, the Mn_2O_3 crystalline polymorphs show a unique property towards SAV and stability for adsorption, photocatalysis, and antibacterial activity applications both in the amorphous and crystalline state (Moharreri et al., 2018; Selim et al., 2020; Guorui Yang et al., 2014). Because of its low charge transfer resistance and multitudinous defects, manganese oxide can also form heterojunctions with ZnO and enhances the electron-hole separation route (Yu et al., 2016). Coupling of the p-type Mn_2O_3 and n-type Fe_2O_3 with n-type ZnO has been practiced broadly (Ali et al., 2019; Davari et al., 2017; Hashim et al., 2019; Lachheb et al., 2017; Maya-Treviño et al., 2015; Saravanan et al., 2014). Mn_2O_3 possesses poor electronic conductivity, although, it's has a pronounced electrochemical redox activity through Mn^{3+} to Mn^{4+} transition giving rise to one-electron transfer (Nathan et al., 2008).

A small variation in the standard level of ascorbic acid (AA) creates diseases in human beings. AA has a significant role in the normal functioning of organisms and is also used as a treatment for a different illness (Rice, 2000). Therefore, it is necessary to develop novel methods to measure the concentration of ascorbic acid. Nowadays, metal oxide nanomaterials were frequently applied for sensor applications. Bare ZnO showed lower sensitivity towards ascorbic acid sensitivity (Ibupoto et al., 2012). Among several techniques used to improve the sensing properties of ZnO, forming a composite with other metal oxides and modifying the synthesized materials to have a mesoporous property that allows a rapid charge transfer process has been reported (Khan et al., 2016; Yuanying Liu et al., 2014). Fe_2O_3 is vital in mediating the final heterogeneous electrochemical reaction of the target agent; this is due to its high surface area and its environmentally biocompatible properties (Cao & Wang, 2011). The coupling of Mn_2O_3 with ZnO also has its own electrochemical and sensor improvement for ascorbic acid detection (Saravanan et al., 2015).

Hospital-acquired infections caused by microorganisms are becoming the most prevalent problems. In Europe, four million people get a hospital-acquired infection per year, of whom approximately 37, 000 people died (Ozkan et al., 2015). Metal oxides NMs have the potential to enter through the cell membrane and distract cellular parts of the bacteria. ZnO-based metal oxide nanocomposites (NCs) have drawn more attention as antibacterial materials with new properties. By the U.S. FDA (21CFR182.8991), it is categorized in the list of antimicrobial agents and safe materials for food preservation of foodborne diseases (Espitia et al., 2012; Yemmireddy & Hung, 2017). The reactive oxygen species (ROS) generation and antibacterial activities of iron oxide and manganese oxide were also confirmed (Pradip Basnet et al., 2013; Selim et al., 2020). Furthermore, forming a binary (Mayank et al., 2019; Panchal et al., 2019; Precious Ayanwale & Reyes-López, 2019; Rajith Kumar et al., 2020; Shimada et al., 2020) and ternary (Anaya-Esparza et al., 2019; Kaur et al., 2019; Munawar, Yasmeen, Hasan, et al., 2020; Owonubi et al., 2020; Paul et al., 2020) heterojunction between metal oxides has been reported for the improvement of surface active sites, SAV, polarity, and porous nature of the materials (Nagvenkar et al., 2016). The heterojunction can be made using the same or different bandgap metal oxides by developing either n–n or p–n heterojunction for binary and either p–n–n or n–n–n heterojunction for ternary metal oxides (Lei et al., 2018).

From methods used for the synthesis of inorganic NCs, the top-down and bottom-up approaches are common. Compared to the former, the latter is more popular and is considered a promising route to control the growth, morphology, and properties of NMs (Amin et al., 2018; Xin Li et al., 2016). Among many chemical methods, the impregnation (Larina et al., 2019), hydrothermal (Liao et al., 2010), sol-gel (Lachheb et al., 2017), self-propagation (Lutukurthi et al., 2020), sono-coprecipitation (Wang et al., 2018), solvothermal (Yu et al., 2019), and ultrasonic-microwave (Yang et al., 2018) are practiced broadly. Nowadays, it is recommended to use effective and economically feasible methods such as sol-gel, co-precipitation, self-propagation, and impregnation (Köse et al., 2015; Wang et al., 2018). As suggested by Osman and Akbulut (Köse et al., 2015), the sol-gel method was proved to be the most attractive method towards cost, easiness, and reliability. Besides, the co-precipitation and self-propagation methods also have positive attributes towards simplicity and inexpensiveness (Lutukurthi et al., 2020; Wang et al., 2018). The condensed/solid phase and solution phase synthesis approaches are the two classifications of the self-propagation technique. Compared to the condensed/solid phase, the solution phase synthesis approach is a novel procedure if a poly (vinyl alcohol) (PVA)-assisted nitrate salt precursor is used (Thakur et al., 2019; Wu et al., 2014).

Nowadays, numerous studies are being conducted without considering the risk assessments of toxic solvents. Solvents, especially, which are certified under the severe human health risk phrases category of Global Harmonized System (GHS) and Hazard and Precautionary (H & P) agency are carcinogenic, toxic to the reproduction, and mutagenic. The other important issue is the assessment of the safety score related to the flammability and explosion score as well as reactivity and stability scores (Alder et al., 2016; Bumajdad et al., 2018). Therefore, the synthesis procedure that reduces the stated solvent risk, economically visible, and avoids complex preparation procedures should be developed. Recent research is also adjusting the present sol-gel procedure using environmentally benign water as a solvent and fewer cost tactics (Ciciliati et al., 2015), suggesting that the improved organic solvent-free and lower production cost method gives superior nanostructured materials (Ong et al., 2018). As an example, compared to different solvents used to synthesize nanomaterials (NMs), it is evidenced that using water as a solvent can give equivalent photo-catalytically active morphology and crystallite size (Kumar Jangir et al., 2017).

Metal oxide nanoparticles (NPs) have large SAV and high surface energy; consequently, they aggregate/agglomerate easily to one another (Moeinian & Akhbari, 2015). The aggregation/agglomeration of metal oxide NPs reduces the generation of the reactive oxygen species and hydroxyl radicals. This is due to the quenching of holes and electrons with neighboring aggregate electrons and holes, respectively (Jassby et al., 2012). Aggregation occurs due to flow motion and net interparticle attractive forces. The aggregation process is dependent on the concentration of the NPs, reaction temperature, and agitation speed. High concentration, high temperature, and slow agitation speed facilitate the aggregation quickly. Agglomeration occurs because of the accumulation of extra molecules on the aggregated NPs surface. The classical nucleation, growth, collision, and attachment are the steps resulting in aggregation. Whereas cluster aggregation, nucleation, and growth are the steps that result in agglomeration (Jassby et al., 2012). For this aggregation/agglomeration problem, nowadays, a polymer matrix has been effectively applied as a capping and structure-directing agent (Wu & Wu, 2015). By using a polymer, synthesizing novel mesoporous materials with well-defined morphology has been strongly encouraged for several applications (ALOthman, 2012).

Among numerous polymers, PVA is an eco-friendly, biocompatible, nontoxic, lubricant, biodegradable, water-soluble, and better film-forming agent (Hong et al., 2009; Madkour et al., 2019; Zhang et al., 2017). Due to its novel mechanical strength, PVA is used as a matrix for the formation of the NCs (Zhang et al., 2016). Besides, its hydroxyl groups on the backbone carbon chain act as a source for the formation of hydrogen bonding and enhance the development of the NCs (Mallakpour & Adnany Sadaty, 2016). As indicated in numerous works concerning PVA polymer or PVA-metal oxide composite, an optimum temperature of 500 °C is suitable to degrade the PVA polymer and to remove unwanted impurities (Abd-Elrahman, 2013; Ghafari et al., 2017; Radhamani et al., 2016). In the thermal analysis study of PVA, at about 100-250 °C the slow intramolecular decomposition occurs; within the PVA melting point ranges of 220 °C - 400 °C the degradation of its amorphous part at 300 °C and the intermolecular decomposition at 385 °C occurred (Abd-Elrahman, 2013; Kumar et al., 2019). The crystalline part of PVA decays at 398 °C (Radhamani et al., 2016; Rahmanian et al., 2015), and complete decomposition to yield carbon and hydrocarbons that results in the liberation of CO_2 gas and ash/residue happens in the temperature range of 400 - 500 °C (Ghafari et al., 2017; Mallakpour et al., 2015; Radhamani et al., 2016). Moreover, increasing the annealing

temperature can also enhance the aggregation/agglomeration of NCs. Therefore, optimizing the calcination temperature of PVA that assists the oxidation of the oxides and removing volatile impurities such as the polymer matrix is also essential.

Considering all the above-indicated ideas the present work aims to synthesize ZnO-based poly (vinyl alcohol) (PVA) assisted binary and ternary metal oxides NCs using a simple and green sol-gel followed by auto-combustion technique. The optical, chemical bonding, crystallinity, morphological, compositional, textural, and electrochemical properties of the synthesized materials were characterized by UV-vis-DRS/UV-vis, FT-IR, XRD, SEM and HRTEM, XPS/EDX, BET, and CV/EIS techniques, respectively. The adsorption effectiveness of the optimized ternary nanocomposite (NC) was evaluated on the less toxic MB dye. The Langmuir, Freundlich, Dubinin-Radushkevich (D-RK), Temkin, Flory-Huggins (FH), and Fowler-Guggenheim (FG) isotherm models are used to understand the adsorption process. Besides, the pseudo-first-order (PFO), pseudo-second-order (PSO), Elovich, Bangham, and intraparticle diffusion (IPD) kinetic models were applied to study the adsorption reaction and adsorption-diffusion process. The degradation efficiency of NPs and NCs was tested on CR and AO8 dyes. The potential of the synthesized NPs and NCs towards the sensor and antimicrobial activities was also studied.

1.1. Statement of the Problems

Environmental pollution, hospital-acquired pathogens infection, and particular toxic gas detection are countable worldwide problems. Paper, textile, cosmetics, plastics, printing, food processing, pharmaceutical, leather, and dye manufacturing sectors use common dyes such as MB, AO8, and CR and discharge their waste directly into the soils and water bodies without treatments. About 1-20% of the total world dyes are lost during the dyeing process, which leads to contaminate the water and causes health problems. Among numerous pollutant sources, the textile industries are one of the most water-consuming and polluting sectors.

Due to the inconsistency between water pollution and worldwide industrial water requirements, familiarizing novel water treatment and recycling technologies is essential. In the past decade, several physicochemical techniques such as sedimentation–flocculation, coagulation, molecular sieving, ion exchange, reverse osmosis, membrane

filtration, chlorination, chemical precipitation, adsorption, and photocatalysis were applied to remove toxic organic and inorganic pollutants. However, some of the techniques are not efficient and also lack the complete degradation of the contaminants. Among these, the heterogeneous advanced oxidation processes (AOP) using metal oxides were suggested to be simple, work under ambient conditions, cost-effective, energy-efficient, environmentally safe, and is also not give secondary pollution. From several metal oxides used as a heterogeneous photocatalyst, nowadays, ZnO NPs are showing a decent property in different fields. However, it has a noticeable drawback including the low SAV and electron-hole recombination. Among several efforts used to reduce these drawbacks, forming ZnO-based binary and ternary heterojunction was found to be one of the novel preferences. Compared to the binary, the ternary heterojunctions improve the separation of photogenerated electron/hole pairs, due to the presence of a greater synergistic effect. The present study also uses a PVA polymer as a capping and structural directing agent and Mn_2O_3 and Fe_2O_3 NPs as a SAV and charge transfer enhancing agent through forming ZnO-based heterojunctions.

Ascorbic acid has a significant role in the normal functioning of organisms. A slight deviation from the normal level of AA is generally considered a symptom of sickness. It is also crucial for the treatment of different illnesses. Thus, emerging efforts should be developed for sensing ascorbic acid. Nowadays, conventional methods such as UV–vis spectroscopy, chromatography, fluorescence spectroscopy, fluorimetry, and electrochemical methods have been used for the determination of the level of AA. Among them, the electrochemical technique received interest in accuracy, stability, sensitivity, and cost. However, AA detection by bare conventional electrodes also contaminates the electrodes due to the irreversible oxidation process of AA to 2, 3-diketogluconic acid. Thus, researchers are modifying the normal electrodes by metal oxide NMs as a redox-active electrochemical sensor site to improve the sensitivity and to avoid multi-selectivity activities. Herein, we also use metal oxide NMs as a redox-active electrochemical sensor site for the detection of ascorbic acid.

Infections related to multidrug-resistant microorganisms also need urgent treatment. By 2050, it is expected that about 10 million annual deaths happen due to these multidrug-resistant microorganisms' pathogens, which is higher than the death that occurred due to cancer. Therefore, unless immediate intervention is developed, this had a profound impact

on public health. Up to date, antibiotics that are applied for an antibacterial curing agent for several years have different limitations including the development of antibiotic-resistant bacteria. Currently, the nanotechnology-based curing agent is being practiced broadly. ZnO is categorized in the list of antimicrobial agents and safe materials for food preservation of foodborne diseases. Furthermore, forming a hybrid between metal oxides improves the active sites, particle size to volume ratio, polarity, and porous nature of the materials. Among several metal oxides, iron and manganese oxides are also received attention as antibacterial active materials.

1.2. Objectives

1.2.1. General objective

- The general objective of this study was to synthesize and characterize the single, binary, and ternary ZnO-based nanomaterials for adsorption, photocatalysis, sensor, and antibacterial activity studies.

1.2.2. Specific objectives

The specific objectives were:

- To synthesize single ZnO, Fe_2O_3, Mn_2O_3 nanoparticles,
- To synthesize binary Zn-Mn and Zn-Fe oxides nanocomposites,
- To synthesize ternary Zn-Fe-Mn oxides nanocomposites.
- To characterize the as-synthesized NPs and NCs for their thermal stability analysis by DSC and DTG techniques, chemical bonding by FTIR, crystallinity and phase purity by XRD, optical properties by DRS-UV-vis, SSA/pore size distribution by the BET method, morphological analysis by SEM and TEM, surface compositional analysis by EDX, XPS, and HRTEM-SAED, and electrochemical properties by CV and EIS analytical techniques.
- To study the synthesized nanomaterials efficiency on:
    - Methylene blue dye adsorption,
    - Congo red and Acid orange 8 dyes degradation,
    - Ascorbic acid sensor, and
    - Antibacterial activities.

1.3. Significance of the Study

Problems related to hazardous waste remediation and drug-resistant infections disease-causing microorganisms have emerged as a national and international priority. Different research activities are underway using different advanced analytical, biochemical, and physicochemical methods for the elimination of hazardous chemicals and to fight the drug resistance disease-causing microorganisms. According to works of literature, the advanced oxidation process (AOP) is an alternative way of treating undesirable pollutants including dyes. Heterogeneous catalysis has been successfully employed for the degradation of various families of hazardous materials using semiconductor nanoparticles as a catalyst, in which ZnO has been extensively investigated as a heterogeneous photo-catalyst. ZnO-NPs also exhibit attractive antibacterial properties due to increased specific surface area as the reduced particle size leading to enhanced particle surface reactivity. ZnO is a bio-safe material that possesses photo-oxidizing and photocatalysis impacts on chemical and biological species. Furthermore, due to their stability, high SAV, and low toxic properties; iron and manganese oxides are also reported to be promising materials.

Herein, we are also going to modify the multifunction material zinc oxide with Iron (III) and Manganese (III) oxides to enhance its adsorption, photocatalytic, antibacterial, and sensor properties. The bottom-up approach is considered a promising route to control the growth, morphology, and properties of the material. This study also uses the bottom-up sol-gel, co-precipitation, and auto-combustion techniques using environmentally benign water as a solvent. The aggregation/agglomeration of metal oxide NPs can be avoided by using polymers as a capping agent. Among the polymers, PVA is an eco-friendly, biocompatible, nontoxic, lubricant, biodegradable, water-soluble, and better film-forming agent. The work also proved the capping agent and structural-directing agent properties of the PVA polymer.

CHAPTER TWO

2. LITERATURE REVIEW

2.1. Metal Oxides

Oxide materials in bulk and thin-film form and metal oxide nanostructures exhibit a great variety of functional properties which make them ideal for applications in gas sensors, optoelectronic devices, catalysis, corrosion protection, and environmental protection. Metal oxide's functional properties are strongly dependent on oxide's crystal structure, composition, and native defects, which govern their optical, electrical, chemical, and mechanical characteristics (Grilli, 2020). In recent years, ZnO NPs have drawn the attention of many researchers for their unique optical and chemical behaviors which can be easily tuned by changing the morphology. ZnO NPs have been used in various cutting-edge applications like photocatalysis, electronics, adsorption, communication, sensors, cosmetics, environmental protection, biology, and the pharmaceutical industry (Bala et al., 2015). It has a similar bandgap with TiO_2 (3.2 eV) but possesses greater quantum efficiency. Compared to TiO_2, ZnO has better photoresponse capabilities (Daneshvar et al., 2004). However, the two most dominant drawbacks that have to be considered related to the potential application of ZnO are (i) photo corrosion under UV light at a higher pH range and (ii) aggregation/agglomeration.

Among several narrow-band semiconductors, iron oxides (Fe_xO_y) with abundance (6.3 wt. % as earth's crust), environment-friendly, thermodynamically stable, low cost, high surface area, and magnetic properties have received greater significance. Fe_xO_y utilizes efficient absorption of visible light during the formation of heterojunction with ZnO photocatalyst. Furthermore, it can absorb approximately 20% of the solar spectrum (Jiamprasertboon et al., 2019; Sivula et al., 2011; Wang et al., 2019). Depending on the applied temperature, among different crystalline polymorphs of Fe_2O_3 namely, hematite (α-Fe_2O_3), β-Fe_2O_3, maghemite (γ-Fe_2O_3), ε-Fe_2O_3, and ζ-Fe_2O_3; the α-Fe_2O_3 phase is more stable and easy to be formed. The pathway for the formation of α-Fe_2O_3 follows γ-$Fe_2O_3 \rightarrow \varepsilon$-$Fe_2O_3 \rightarrow \alpha$-$Fe_2O_3$ (Lee & Xu, 2016).

Similarly, manganese oxide (Mn_xO_y) is also confirmed to be a promising material with its superior properties. Among different crystalline polymorphs of manganese oxide

including MnO, Mn_3O_4, Mn_2O_3, Mn_5O_8, and MnO_2; Mn_2O_3 is cheap and environmentally safe (Guorui Yang et al., 2014). Both in the amorphous and crystalline state, α-Mn_2O_3 is used in a wide range of photocatalytic applications (Moharreri et al., 2018). Furthermore, because of its low charge transfer resistance and multitudinous defects, it can form a heterojunction with ZnO and enhances the electron/hole separation route. Besides, due to the presence of unpaired electrons in the outer electronic orbitals of both α-Fe_2O_3 and α-Mn_2O_3, once doped in the ZnO matrix, the atoms can form magnetic materials such as manganese zinc ferrite (Zhiwen et al., 1997). Hence, the composite acts as a diluted magnetic semiconductor material (Ghosh et al., 2019). Furthermore, in the nanosize range, α-Fe_2O_3 and α-Mn_2O_3 can also enhance the adsorption capacity of pollutants during heterojunction and are also sensitive to ultraviolet and visible light (Zhao et al., 2017). The structures of stable ZnO, α-Mn_2O_3, and α-Fe_2O_3 that were developed using VESTA 3D visualization program software depending on the American mineralogist crystal structure database (AMCSD) search result are given in Figure 1(a)-(c), respectively (Kolm, 2009).

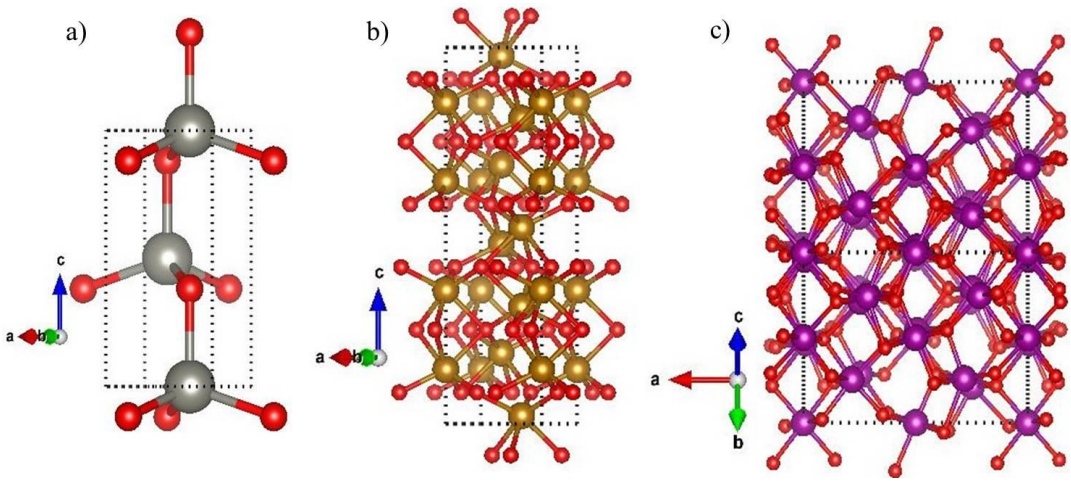

Figure 1. The ball-and-stick style crystal structures of (a) ZnO, (b) Fe_2O_3, and (c) Mn_2O_3 (red is for O atoms).

2.2. Adsorption

Adsorption is a surface interaction process in which adsorbate molecules bind to the adsorbent either through physical (physisorption) or chemical (chemisorption) interactions. The three common mechanisms that are involved in the adsorption process are (1) pore diffusion, (2) film diffusion, and (3) surface reaction (Zhang et al., 2018). As a standard, if the magnitude of the heat of adsorption is between 5 - 40 kJ mol^{-1}, it indicates

physisorption as the leading adsorption progress. While, if it is between 40 - 125 kJ mol^{-1}, it indicates the domination of the chemisorption process (Zhou et al., 2014). The adsorption and degradation efficiency was evaluated using equations 1 and 2, respectively. Further, understanding this adsorption process by applying the adsorption isotherm and adsorption kinetics is important. This interpretation leads to an appropriate justification of the adsorption mechanism and designing an effective adsorption system. For a proper understanding of the adsorption process, the adsorption isotherm models (equations 3-8) and adsorption kinetics models (equations 9-13) ought to be used. To study the reaction dynamics during photocatalysis pseudo-first-order kinetic equation (equation 14) is used.

$$q_e = \frac{V}{m}\, x\, (C_o - C_e) \tag{1}$$

$$\%\,\eta = \frac{C_o - C_e}{C_o}\, x\, 100 \tag{2}$$

$$\text{Langmuir: } \frac{C_e}{q_e} = \frac{C_e}{q_m} + \frac{1}{q_m K_L}, \quad R_L = \frac{1}{1 + K_L C_o} \tag{3}$$

$$\text{Freundlich: } \log q_e = \frac{1}{n}\log c_e + \log K_F \tag{4}$$

$$\text{Dubinin} - \text{Radushkevich: } \ln q_e = -\beta\varepsilon^2 + \ln q_s, \varepsilon = RT\ln\left(1 + \frac{1}{C_e}\right), E = \frac{1}{\sqrt{2\beta}} \tag{5}$$

$$\text{Temkin: } q_e = \frac{RT}{b}\ln c_e + \frac{RT}{b} ln K_T \tag{6}$$

$$\text{Flory} - \text{Huggins: } \ln\frac{\theta}{C_o} = n\ln(1-\theta) + \ln K_{FH},\ \Delta G^o = -RT\ln(k_{FH}) \tag{7}$$

$$\text{Fowler} - \text{Guggenheim: } \ln\frac{C_e(1-\theta)}{\theta} = \frac{2w}{RT}\theta - \ln k_{FG} \tag{8}$$

$$\text{Pseudo} - \text{first} - \text{order: } \log(q_e - q_t) = -\frac{K_1}{2.303}t + \log q_e \tag{9}$$

$$\text{Pseudo} - \text{second} - \text{order: } \frac{t}{q_t} = \frac{t}{q_e} + 1/k_2 q_e^2 \tag{10}$$

$$\text{Elovich: } q_t = \frac{1}{\beta}\ln t + \frac{1}{\beta}\ln(\alpha\beta) \tag{11}$$

$$\text{Intra} - \text{particle adsorption} - \text{diffusion: } \mathrm{q_t} = \mathrm{K_{id}}\sqrt{\mathrm{t}} + \mathrm{C} \tag{12}$$

$$\text{Bangham model: } \ln q_t = \frac{1}{m}\ln t + \ln k_b \tag{13}$$

$$\text{Pseudo} - \text{first} - \text{order kinetics: } \log\frac{\mathrm{C}}{\mathrm{C_o}} = -kt \tag{14}$$

Where, C_o & C_e are the initial and equilibrium concentrations of MB dye ($mg\,L^{-1}$), respectively; η is the photo decolorization efficiency; q_e & q_m are the amounts of adsorbate accumulated per gram of adsorbent and its maximum uptake ($mg\,g^{-1}$), respectively; V is the volume of adsorbate taken in liter (L), m is the mass of adsorbent (g); K_L in Langmuir model is the ratio of adsorption and desorption rate constant ($L\,mg^{-1}$); K_F in Freundlich is the distribution coefficient; 1/n is empirical constant related to the heterogeneity of the surface; β is the constant related to free energy; ε is Dubinin-Radushkevich constant; and q_s is saturation capacity; k_T is the Temkin equilibrium constant related to maximum binding-energy; $\frac{RT}{b}$ is constant related to the heat of adsorption and b Temkin isotherm constant, n is the number of ions on adsorption sites, T is the temperature (K), and R is the universal gas constant ($8.314\ J\,mol^{-1}\,K^{-1}$); θ ($1-(C_e/C_o)$) is fractional surface coverage; k_{FH} is constant for Flory-Huggins model; k_{FG} is Fowler-Guggenheim constant; w is the energy of interaction; k_1 is pseudo-first-order rate constant; k_2 is pseudo-second-order rate constant; k_i is the intraparticle diffusion constant; C (equation 12) is intercept that gives an idea about boundary layer thickness; m and k_b are Bangham constants; C_o and C (equation 14) are the initial concentration of the dye solution and its residual concentration after irradiation at a time t, respectively; k is pseudo-first-order kinetic constant (Ayawei et al., 2017).

2.3. Photocatalysis

In recent years, the remediation of hazardous organic contaminants using semiconductor metal oxide photocatalyst has attracted extensive attention. Next to TiO_2, ZnO has been well-known as a significant photocatalyst material (Akkari et al., 2018; Janotti & Van de Walle, 2009). Even though photocatalysis using bare ZnO is useful in pollutant remediation owing to the presence of different defects, several drawbacks make it less effective. To reduce these drawbacks, forming a heterojunction between different bandgap metal oxides was suggested to be one of the preferences (Lei et al., 2018; Xiaojuan Li et al., 2018). Among different metal oxide semiconductors that form a suitable heterojunction with ZnO, depending on the ideas of regeneration, surface area, and stability; this work focuses on iron oxide (Fe_2O_3) and manganese oxide (Mn_2O_3) materials (Qamar et al., 2016; Yu et al., 2016). Different analytical techniques that confirm the

improvement of bare ZnO towards electron-hole recombination, surface area, photo corrosion, and regeneration are revised.

2.3.1. Presumed mechanism

The band edges position of metal oxides is dependent on the surface charge. To propose the mechanism of the formation of heterojunction between metal oxides, conducting photoelectrochemical, spectroelectrochemical, and an electrochemical investigation is a requirement (Beranek, 2011). Using the reported information from previously reported works, the general electron-hole separation mechanism of a photocatalyst that supports the acceleration of the light-induced photocatalytic reaction is given in Figure 2 (Lachheb et al., 2017; Lin et al., 2015; Pirhashemi et al., 2018).

As seen from Figure 2(a)**,** the first step in photocatalysis is the adsorption of pollutants on the active sites of the photocatalyst. After adsorption, the interaction of the photocatalyst with light can generate electron-hole pairs on the CB and VB band of the photocatalyst, respectively. Due to the reaction of electron and hole with oxygen and water, respectively, a strong oxidizing agent was produced. Consequently, the created oxidizing agents led to the mineralization of pollutants to the non-toxic CO_2, H_2O, and mineral acids. The curved arrows in Figure 2(a) seem to indicate an escaping of the excited species from the surface to the bulk solution. Therefore, to remove this misperception, it is advised to modify as depicted in Figure 2(b)-(d) (Herrmann, 2010).

The electron/hole recombination is the main drawback of bare ZnO without heterojunction. To have an efficient photocatalyst, forming a precise junction between metal oxides should be the requirement. As shown in Figure 2(b), among the three main electronic arrangements of semiconductor metal oxide heterojunctions, the staggering gap type is recommended as a precise junction for electron/hole recombination hindrance. It is reported that during the formation of a junction between those oxides, the straddling energy band structure was expected to be formed. During irradiation; a mismatch between the metal oxides results and the combination of the two acts as the same bandgap (Pirhashemi et al., 2018). This can activate the electron/hole recombination process. Therefore, proper matching of the bandgap between metal oxides is a crucial issue.

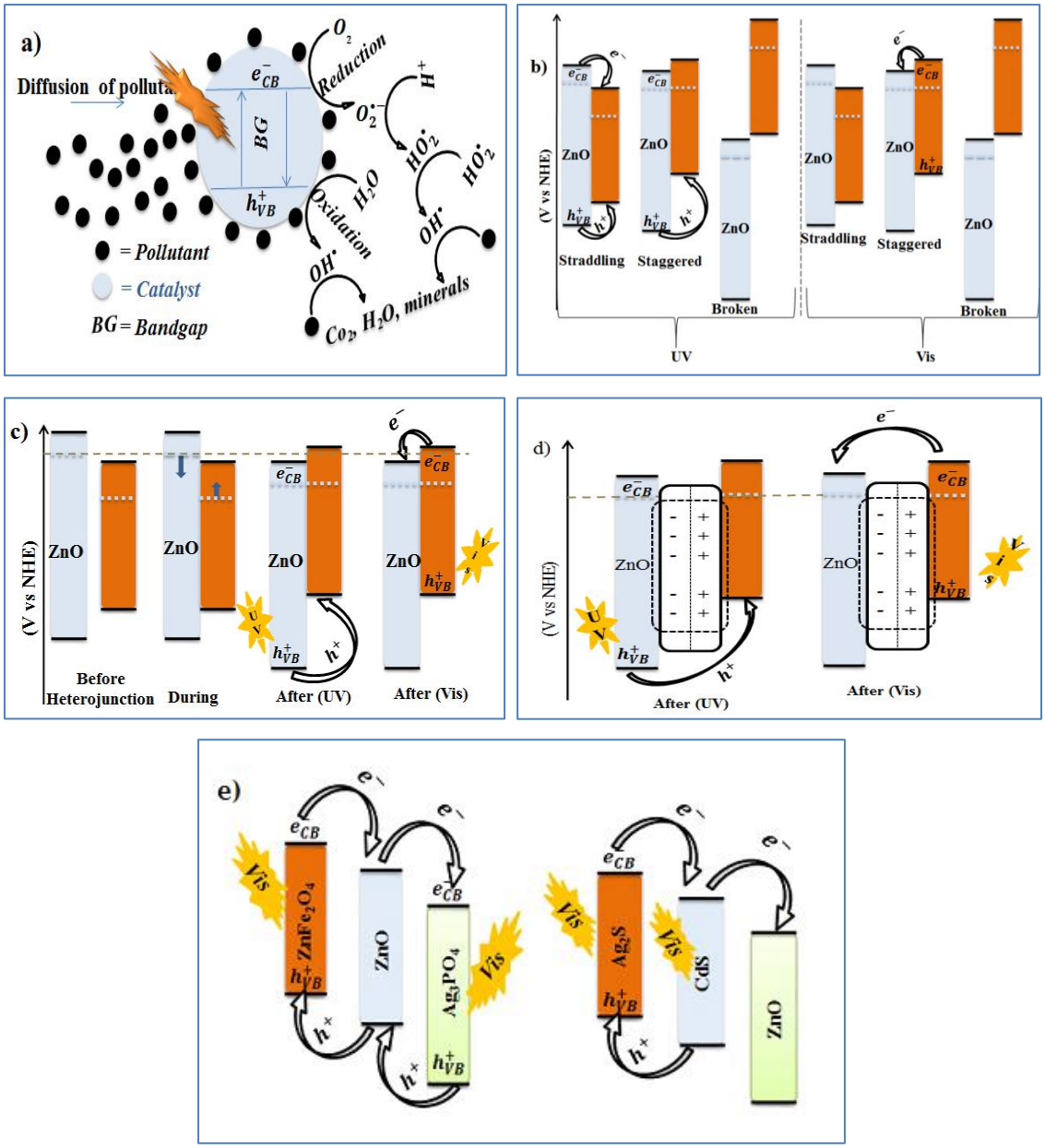

Figure 2. (a) The general photocatalysis mechanism, (b) the three main electronic arrangements of semiconductor, (c) up and down movement of the Fermi level (FL) after contact, (d) the depletion layer formed produces an electric field, (e) electron/hole separation through bandgap engineering of ternary semiconductors (Lachheb et al., 2017; Lin et al., 2015; Pirhashemi et al., 2018).

As reported, this matching can be clarified in terms of ionic bond strength between metal ions and oxygen (Abdullah Mirzaie et al., 2012). As an example, the electronegativity value of Zn, Fe, and O is 1.65, 1.83, and 3.4, respectively. Therefore, the order of ionic nature becomes the inverse of electronegativity; consequently, the difference in energy levels between main components of CB s state and VB of O 2P is in the order of Zn > Fe

> O. As shown in Figure 2(d), during the formation of the heterojunction when the Fermi level (FL) of one n-type semiconductor core is in contact with the FL of the other n-type semiconductor, by up and down movement [Figure 2(c)], the depletion layer created (Roy, 1995). The activated electric field drives the drift of the photogenerated electron and hole out of the depletion layer and results in the activation of the photocatalytic reaction (Pirhashemi et al., 2018).

Apart from the binary NCs, recently forming a junction between ternary or multi-component hetero-structure resulted in a great improvement in photocatalytic reaction. As explained in both (Anandan et al., 2010) and (Irie et al., 2008) studies, creating a junction with low bandgap materials has the probability of forming shallow 4s levels. To prevent these types of hitches, expectantly forming a ternary metal oxide heterojunction or doping of metal ions becomes the best option. According to bandgap engineering, increasing the number of metal oxides and forming a precise heterojunction led to fastening the electron transfer process from one metal oxide to the other. This is due to the adjustment in the energy levels of the metal oxides. The detailed mechanism towards enhancement of the photocatalytic ability by combining three components was confirmed by (Chen et al., 2016) (ZnO/CdS/Ag_2S) and (Li et al., 2015) (Ag_3PO_4/$ZnFe_2O_4$/ZnO). The diagram that represents the electron/hole pair separation in ZnO/CdS/Ag_2S and Ag_3PO_4/$ZnFe_2O_4$/ZnO heterojunction is shown in Figure 2(e). Hence, compared to the binary n–n or p–n heterojunctions, forming ternary heterojunction in either p–n–n or n–n–n approach showed great photocatalytic improvement due to the synergistic effect (internal electric field) (Pirhashemi et al., 2018).

2.3.2. Photocatalytic activity of bare ZnO

During synthesis, optimizing important parameters that are valuable to control the size, morphology, shape, and efficiency of the photocatalyst is critical. The effects of solution pH and concentration of nitrate ion on the physical properties of ZnO nanorods (NRs) were studied by (Singh & Dutta, 2019). The NRs were synthesized using a simple wet chemical method following the steps listed from equations 15-17. The UV-vis absorption spectra of ZnO synthesized with a higher concentration of nitrates is showing greater absorption efficiency. In the FESEM morphological analysis result, as the concentration of nitrates increases, a shape change from irregular to rod form was observed. At the

optimized nitrate concentration, the pH optimization test is showing the formation of smaller particle sizes at a higher pH region. Furthermore, compared to uncalcined ZnO the redshift on absorption spectra for calcined ZnO indicated to be the complete removal of unstable $Zn(OH)_2$ phase.

$$Zn(NO_3)_2.6H_2O + 2NaOH \rightarrow Zn(OH)_2 + 2NaNO_3 + 6H_2O \quad (15)$$

$$Zn(OH)_2 + 2H_2O \rightarrow Zn^{2+} + 2OH^- + 2H_2O \rightarrow [Zn(0H)_2]^{-4} + 2H^+ \quad (16)$$

$$[Zn(0H)_2]^{-4} \rightarrow ZnO + H_2O + 2OH^- \quad (17)$$

The possibilities of enhancing the photocatalytic activities of ZnO by controlling its aspect ratio, areal density, and specific surface area using ethylene glycol (EG) and water as a solvent and cadmium ions as additive was confirmed (Tian et al., 2019). The obtained optimum concentration of cadmium ions, volume ratio of EG to water, and the aspect ratio of mesoporous ZnO NRs that have the highest photocatalytic activity were 2 mM, 1:5, and 53.85, respectively. Besides, ZnO with 2 mM Cd^{+2} was confirmed to be a more porous material. This porosity has more surface defects and enhances visible light absorption efficiency. Furthermore, the study conducted by (Vahdat Vasei et al., 2019) also showing the great effect of fuel to oxidant ratio on photocatalytic activity. As the concentration of fuels increased, due to the rapid cooling of the product, increasing the gaseous products and decreasing the particle size were stated.

By using oleylamine as a surfactant and capping agent, (Hu et al., 2018) also confirmed the complete dependency of the photocatalytic activities of ZnO on the oleylamine ratio. (Wang et al., 2018) also tested the effects of precursor's concentration on the photocatalytic activity of phenol. The selected precursors for their study were sulfate ($ZnSO_4.7H_2O$), nitrate ($Zn(NO_3)_2.6H_2O$), acetate ($Zn(Ac)_2.2H_2O$), and chloride ($ZnCl_2$). The obtained FESEM images were indicating the dependency of the morphologies and diameters of each microsphere on the anions of the salt from which it was formed. This indirectly has great effects on the generation, separation, and transfer properties of photogenerated electrons and holes. The BET analysis, which shows the textural properties of the synthesized materials, namely specific surface areas and pore volumes, is confirming a type IV with H_3 hysteresis loops for all microspheres. This indicates the formation of slit-like mesopores between the nanosheets. Compared to the other metal oxides, ZnO synthesized using sulfates as a precursor showed the strongest visible light

absorption on UV-vis-DRS spectra and the presence of superior oxygen deficiency region on XPS measurement.

Furthermore, the highest photocurrent density and smaller arc radius on Nyquist plots are showing the greater electron-hole separation and smaller charge transfer resistance, respectively. With the help of electron paramagnetic resonance spectroscopy and 5, 5-dimethyl-1-pyrroline-N-oxide as a spin trapping agent, the formation of $O_2^{\bullet -}$ and $OH^{\bullet}$ radicals was also verified. Using a different stabilizing agent, base, and precursor to base ratio, (Xie et al., 2011) also synthesized the rod-, needle-, rugby-, and flower-like morphology of ZnO. The result is also showing a pronounced effect of cation that comes from the alkali metal hydroxide on the nucleation and growth steps. The effect of the cation is dependent on the charge density and ionic surfactant.

In addition to the optimization of the above-discussed precursors, conditions, and capping agent, (Bazazi et al., 2018) studied the effect of milling on the hydrothermal method. The result indicates that the milling of the precursor before applying the solution method helps to enhance the surface area. However, (Chen et al., 2014) confirmed the negative effects of increasing milling time and speed on size and photocatalytic activity. This indicates that, the necessity of optimizing a suitable milling time and speed.

Furthermore, the effects of increasing calcination temperature of ZnO on morphology, surface composition, optical property, and photocatalytic efficiency were also studied by (He et al., 2018). The SEM morphology result shows that as the temperature increases the rod-like structure becomes thick and shorter. Since increasing temperature led to the enhancement in the number of available oxygen atoms, but the defective surface oxygen concentration was found to be lesser. The same result was also obtained on (Junpeng Wang et al., 2012) work. Likewise, in (Byzynski et al., 2018) study, the combined temperature, reaction time, and solvent effects on the morphology of ZnO were confirmed by FEG-SEM image analysis. It is also showing that the presence of great impacts on the optical and photoelectrochemical properties. With the help of the photocurrent response experiment, (Bai et al., 2013) tested the performance of ZnO calcined at different temperatures. The obtained result indicates that under visible light irradiation, ZnO calcined at a lower temperature (400 ^{o}C) shows a greater photocurrent value. With the help of photoluminescence and XPS analytical technique, (Bora et al., 2017) also confirmed

temperature-dependent surface oxygen vacancy enhancement and visible light-activated ZnO towards methylene blue dye degradation (Figure 3).

By introducing the presence of inherent defects that reduces the electron/hole recombination and possibilities of establishing different morphologies (including 0D, 1D, 2D, 3D), (Achouri et al., 2018) synthesized ZnO NRs for the degradation of orange II dye and antibacterial activity against *Escherichia coli* bacteria. The presence of continuous lattice fringes with 186 nm in lengths and 20 nm in diameters was characterized by SEM, TEM, and XRD techniques. The damaged *E. coli* bacterial strains were confirmed by SEM, AFM, epifluorescence microscopy, and fluorescence spectroscopy. To the contrary, (Chen et al., 2014) confirmed the created defects on the surface acting as electron/hole recombination's center, thus decreasing the photocatalytic activity. However, through increasing the calcination temperature, the possibilities of repairing the created defects and enhancement of the degradation activity were also verified. This may indicate that, the presence of opposite behavior of forming a defect on bulk and nanoscale ZnO photocatalyst.

The creation of more oxygen vacancies on the surface of ZnO that acts as an electron capturing and electron/hole recombination's hindrance agent was also indicated in (Zhang et al., 2018) study (equation 18), which was proved on EPR and XPS analysis. ZnO is synthesized by dry vacuum treatment after loading the pristine ZnO powder into a quartz tube and placing it in a vacuum drying oven. Unlike that of the commercial ZnO powder, the appearance of an EPR signal with a g factor value of 2.0035 on synthesized ZnO powder shows the presence of an unpaired electron trapped in the oxygen vacancies. The related result was also obtained in (Liu et al., 2014) study.

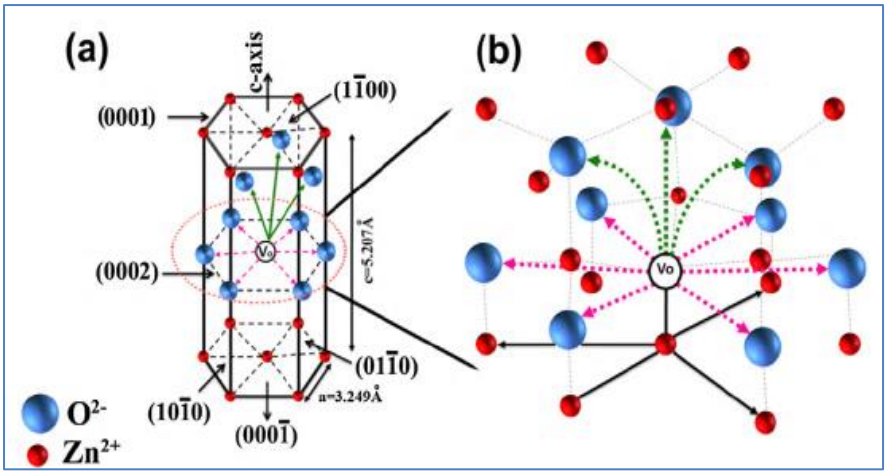

Figure 3. (a) normal, (b) expanded in-plane and out-of-plane diffusion of oxygen vacancies in the ZnO wurtzite crystal view of the ZnO wurtzite unit cell structure (Bora et al., 2017).

$$[ZnO4]^{x} + [ZnO_3.V_o^{x}] \rightarrow [ZnO4]' + [ZnO_3 \cdot V_o^{\bullet}] \quad (18)$$

Furthermore, enhancing the oxygen-vacancy and photocatalytic performance under visible light through increasing the BET surface area from 6.7 to 34.5 m^2/g was also developed. Due to the small percentage of the Ag_3PO_4 loaded on ZnO, the ZnO_{NPs}/Ag_3PO_4 composite with a small defect on ZnO showed lower activity under visible light irradiation. However, increasing the defect through forming $ZnO_{nanosheets}/Ag_3PO_4$ composite, the photocatalytic activity was enhanced due to the synergistic effect. As seen in the mechanism of charge transfer synergy in Figure 4, both the VB and CB values of Ag_3PO_4 are lower than the VB of ZnO and ZnO oxygen vacancies. Under visible light irradiation, the electrons are excited from VB of ZnO and Ag_3PO_4 to the ZnO vacancies and CB of Ag_3PO_4, respectively. Through the synergetic effect, the excited electrons move from ZnO vacancies to the CB of Ag_3PO_4 and the hole from VB of Ag_3PO_4 to the VB of ZnO. This can reduce the electron-hole recombination and activate the photocatalytic activity under visible light irradiation (Jing Wang et al., 2016).

(Miao et al., 2016) synthesized a flower-like 3D ZnO photocatalyst using a simple hydrothermal method. During synthesis, sodium dodecyl sulfate (SDS) was used as a capping agent and urea and hexamine as a hydrolyzing agent. The XRD characterization result shows the presence of $Zn_4(CO_3)(OH)_6 \cdot H_2O$ (equation 22) intermediate during the formation of hydrangea-like ZnO and $Zn_5(CO_3)_2(OH)_6$ intermediate (equation 26) during

the formation of rose-like ZnO. The SEM-EDS optimization result indicates the great effects of SDS amount and different solvents on the structure of the final product. The mechanism of transformation of the precursor to hydrangea- and rose-like ZnO was given in equations 19-23 and equations 24-27, respectively. Using $Zn_5(OH)_6(CO_3)_2$ that helps as releasing gas and generating holes, (D. Liu et al., 2014) also synthesized porous ZnO nanosheet using the solvothermal-annealing method.

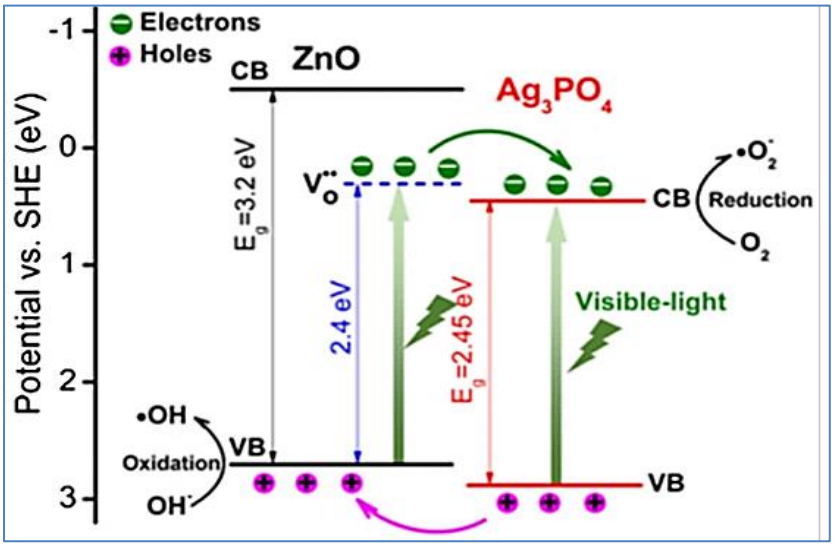

Figure 4. A schematic illustration of the band structure and charge-transfer process of oxygen defect-rich ZnO coupled with Ag_3PO_4 under visible-light illumination (Jing Wang et al., 2016).

Hydrangea-like ZnO

$$CO(NH_2)_2 + 3H_2O \rightarrow 2NH_3.H_2O + CO_2 \quad (19)$$

$$NH_3.\ H_2O \rightarrow NH_4^+ + OH^- \quad (20)$$

$$CO_2 + 2OH^- \rightarrow CO_3^{2-} + H_2O \quad (21)$$

$$4Zn^{2+} + 6OH + CO_3^{2-} + H_2O \rightarrow Zn_4(CO_3)(OH)_6.H_2O \quad (22)$$

$$Zn_4(CO_3)(OH)_6.H_2O \rightarrow 4ZnO + CO_2 + 4H_2O \quad (23)$$

Rose-like ZnO

$$(CH_2)_6N_4 + 6H_2O \rightarrow 6HCHO + 4NH_3 \quad (24)$$

$$NH_3.H_2O \rightarrow NH_4^+ + OH^- \quad (25)$$

$$5Zn^{2+} + 10OH^- + 2CO_2 + 2H_2O \rightarrow Zn_5(CO_3)_2(OH)_6 + 4H_2O \quad (26)$$

$$Zn_5(CO_3)_2(OH)_6 \rightarrow 5ZnO + 2CO_2 + 3H_2O \quad (27)$$

The detailed characterization analysis conducted by the EPR spectroscopy shows a strong EPR signal [Figure 5(a)], UV-vis spectroscopic techniques showing a large absorption tail in the visible region, and the PL spectra that show strong band defect-related emission from 450 to 600 nm [Figure 5(b)]. A sharp emission at 388 nm and wide yellow-green emission at 494 nm represents the intrinsic emission from zinc oxide and a singly ionized surface oxygen vacancy, respectively. (Guo et al., 2015) work confirms the presence of oxygen-deficient ZnO (ZnO_{1-x}) nanosheets compared to ZnO [Figure 5(c)]. Hence, extending to visible-light absorption and enhancing the photocatalytic degradation of methyl orange. This deficient ZnO_{1-x} was synthesized by using the simple hydrothermal method in the presence of NH_4HCO_3 as a CO_2 creation source. The created CO_2 oxidizes metal Zn into ZnO. During synthesis, due to the creation of crystal lattice distortion, the electron/hole recombination reduced greatly. Furthermore, the intermittent on-off visible light cycle test, which is used to test the light sensitivity of the photocatalytic activity, also shows a noble response [Figure 5(d)].

The hydrothermally synthesized high surface area ZnO (25.74 m^2/g) microarchitectures showed great photocatalytic activities towards the degradation of methyl orange dye. The synthesized different citrate ion to Zn^{2+} ratio (0 - 0.1) was characterized by SEM-EDX, XRD, TEM, HRTEM, and PL analytical techniques. Compared to the other, the 3D hierarchical ZnO microarchitecture obtained with 0.02 molar ratios of citrate ion shows enhanced photocatalytic activities. Using PL spectroscopic techniques, the analysis conducted on 5 x 10^{-2} M terephthalic acid in place of methyl orange is confirming the generation of $OH^{\bullet}$, this can confirm photocatalytic degradation activity to be due to the generation of $OH^{\bullet}$ (Lu et al., 2011).

The summarized details of the methods and precursors used, pollutant applied, characterization results, parameter optimization, and time-taken for the degradation of the pollutant are presented in Table 1. However, even though the photocatalytic activities a single ZnO has nice towards the degradation of pollutants, the concept of charge transfer synergy, regeneration of the catalyst that helps to prevent the secondary contamination of the photocatalyst itself, photo corrosion of ZnO under UV light irradiation, and sufficient surface area improvement may not be achieved. Therefore, to improve these key ideas, forming a heterojunction with low bandgap metal oxides is discussed in the subsequent sub-sections (2.3.3 to 2.3.6 sub-sections).

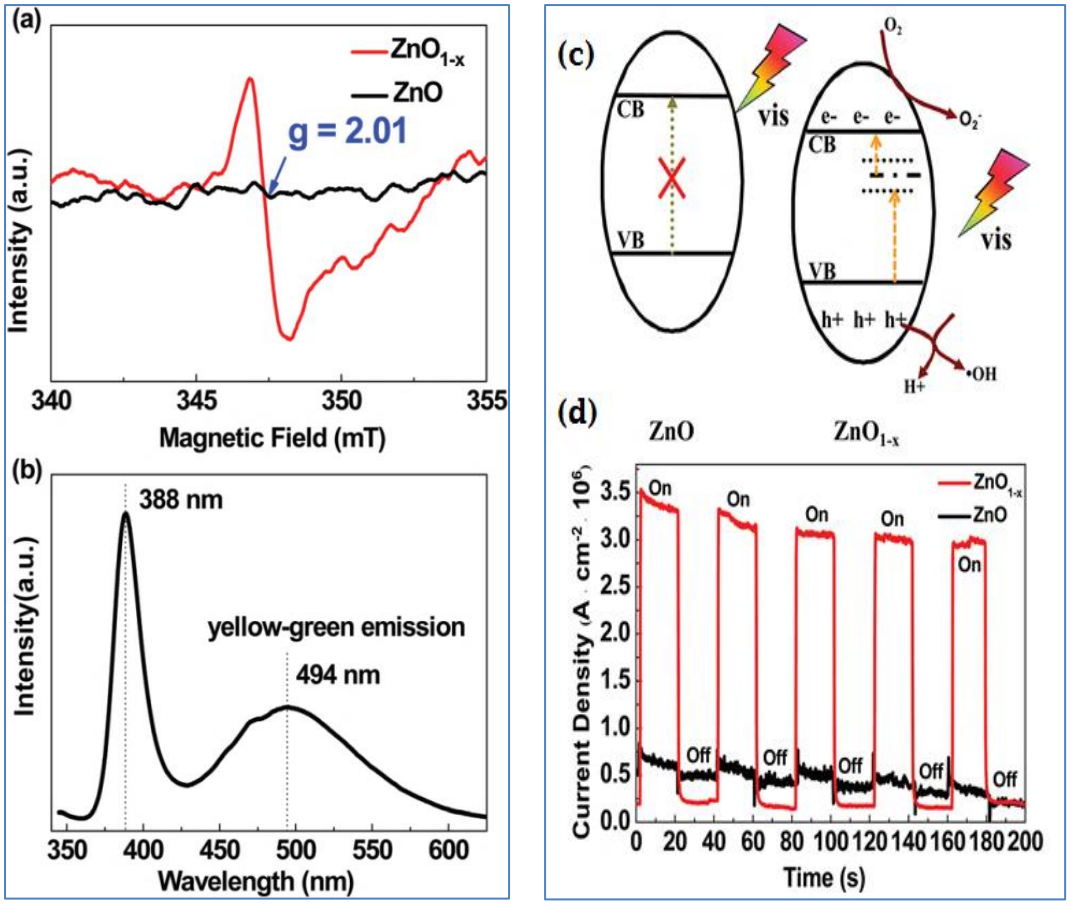

Figure 5. (a) The X-band EPR spectra of the ZnO_{1-x} and ZnO, (b) PL spectrum of the ZnO_{1-x}, (c) charge transfer of the ZnO_{1-x} and ZnO photocatalyst, (d) intermittent irradiation at a bias potential of 0.5 V vs. Ag/AgCl ($\lambda \geq 400$ nm) (Guo et al., 2015).

Table 1. The summarized details of the photocatalytic activities of ZnO.

Method	Pollutant	Precursor	Properties		Optimization			Kinetics	Ref.
		Zn	S_{BET}, p_v, P_d	D, SEM/TEM, BG	T(°C)	[ ]	m (g)	t(min.),	
Wet chemical	MB & Rh6G	$Zn(NO_3)_2.6H_2O$		-, NRs, 2.7–3.6	500	50	0.5	300	(Singh & Dutta, 2019)
Facile solution process	MB	$Zn(Ac)_2.2H_2O$	8.670, -, -	~16, NRs,-	350	~16	0.008	350	(Tian et al., 2019)
Solution combustion	MB, MO & RhB	$Zn(NO_3)_2$	141, -, -	8, Honey-comb, 3.18	250	15	0.1	180	(Vahdat Vasei et al., 2019)
Grinding	MB	ZnO powder	-	59 x 300, -, -	-	~8	0.05	60	(Sahoo et al., 2019)
Grinding	RhB & MB	$Zn(Ac)_2.2H_2O$		-, NRs, 3.18	100		0.05	80 & 45	(Parita Basnet et al., 2019)
Antisolvent precipitation	Crystal violet	$Zn(Ac)_2.2H_2O$	12, -, -	65, Tetrapods, 3.10	500	10	0.15	180	(Franco et al., 2019)
Microalgae chlorella extract	Dibenzo-thiophene	$Zn(Ac)_2.2H_2O$	-	~20, Spherical, 3.46	50	10	0.01	190	(Khalafi et al., 2019)
Hydrothermal	MO	$Zn(Ac)_2.2H_2O$	-	-, Astray, 2.1	500	10	0.05	75	(Farooq et al., 2019)
Ball mill & hydrothermal	Phenazo-pyridine	$ZnCl_2$	13.54, 0.2017, 59.59	-, quasi-prismatic, 3.27	80	30	0.1	150	(Bazazi et al., 2018)
Pyrolysis	MO &4-nitrophenol	$Zn(Ac)_2.2H_2O$	-	NRs, 3.2		10	0.05	30	(He et al., 2018)
Facile approach	MO	$Zn(Ac)_2.2H_2O$	-	-, Conical-column, 3.19	-	~7	0.02	100	(Hu et al., 2018)
Hydrothermal	RhB	ZnSO4.7H2O	91, 0.41, 17.7	8.9, nanosheets, -	300	10	0.02	60	(Wang et al., 2019)
Microwave-hydrothermal	RhB	$Zn(Ac)_2.2H_2O$	8.46, -, -	-, Flower, 3.22	80	2.5	0.002	120	(Byzynski et al., 2018)
Hydrothermal & microwave	MO & phenol	$Zn(Ac)_2.2H_2O$	35.0, 0.2790, - 25.8, 0.2147, -	~25, -, 3.2 ~30, - , 3.1	400	20 50	1	120	(Jaramillo-Páez et al., 2018)
Vacuum treatment	MB	Pristine ZnO	6.34, -, -	60, NRs,-	250	4	0.05	50	(Zhang et al., 2018)
Solvothermal	Orange II & Escherichia coli	$Zn(Ac)_2.2H_2O$	-	-, NRs, 3.25	50	10	0.04	210 & 180	(Achouri et al., 2018)
Combustion	MO	$Zn(NO_3).6H_2O$	-	20–45, -, -	700	20	0.085	160	(Bhatia & Verma, 2017)
Hydrothermal	MB & phenol	$Zn(Ac)_2.2H_2O$	-	100 x 1800, NRs, -	250	~ 3.2 & 10	-	240	(Bora et al., 2017)
Spin coating	RhB	$Zn(Ac)_2.2H_2O$	-	30, NRs, 3.56	200	10	0.08	275	(Kaviyarasu et al., 2017)
Sol-Gel	MO	$Zn(Ac)_2.2H_2O$	-	~23, NRs, -	400	30	0.01	30	(X. Chen et al., 2017)
Deposition	MB	$Zn(Ac)_2.2H_2O$	-	160, NRs, -	500	~4.8	-	240	(Di Mauro et al., 2017)
Ultra-rapid solution	RhB	Commercial ZnO	34.5, -, 30	10–15, nanosheets, -	55	10	0.01	90	(Jing Wang et al., 2016)
Hydrothermal	RhB	$Zn(Ac)_2.2H_2O$	37.3, -, 3-100	-, flower, -	500	10	0.02	45	(Miao et al., 2016)
High temp. quenching	RhB	$Zn(Ac)_2.2H_2O$	3, 0.013, 20.6	-, NRs, 3.21	600	~9.6	0.03	42	(Fang et al., 2015)
Soluble-starch-assisted	RhB	$Zn(NO_3)_2.6H_2O$	24, -, 50	21, -, 3.02	500	5	0.5	240	(Saikia et al., 2015)
Hydrothermal	MO	$ZnCl_2$	-	-, nanosheets, 3.15	500	10	0.05	50	(Guo et al., 2015)
Ball-milling	MB	ZnO	13, -, -	-	350	~9.6	0.025	40	(Chen et al., 2014)
solvothermal-annealing	phenol	$Zn(NO_3)_2.6H2O$	39.18, -, 5–30	10–30, nanosheets, -	500	20	0.025	70	(Liu et al., 2014)
Thermal decomposition	MB MO	$Zn(Ac)_2.2H_2O$	8.6, -, -	24, NRs, 3.44	350	~9.6 ~9.8	0.5	120	(Saravanan et al., 2013)
Solution phase approach	RhB	$Zn(Ac)_2.2H_2O$	-	20–30, spherical, 3.29	60	10	0.15	80(0.0343)	(Rahman et al., 2013)
Direct calcination	MB	$Zn(Ac)_2.2H_2O$	6.05, -, -	-, Rod, -	600	-	-	120(0.022)	(Tian et al., 2012)
Hydrothermal	MO	$Zn(NO_3)_2.6H_2O$	25.74, -, -	-, flower, -	90	20	0.025	40	(Lu et al., 2011)

S_{BET}: Specific surface area (m^2/g), $p_{V:}$ pore volume (cm^3/g), P_d: pore diameter (nm); D: crystallite size (nm), []: Concentration (mg/L), BG: bandgap.

2.3.3. Photocatalytic activity of binary ZnO–Fe_2O_3

Iron oxides have unique magnetic, catalytic, and biochemical properties that make them suitable for different applications. The common forms of iron oxide that occur as a mineral compound present in nature are hematite (α-Fe_2O3), magnetite (Fe_3O_4), and maghemite (γ-Fe_2O_3). Others synthesized in the laboratory are the beta (β-Fe_2O_3) and epsilon (ε-Fe_2O_3) forms. The hematite is the final product of all other thermally decomposed iron oxide forms. α-Fe_2O3 is n-type semiconducting material that is easily synthesized and has valuable properties including magnetic, semi-conductive, high thermal stability, high corrosion resistance, low cost, and good heterogeneous photocatalyst (Machala et al., 2011).

The solar degradation capacity of ZnO/Fe^o and ZnO/Fe_2O_3 were compared on (Maya-Treviño et al., 2015) work. The obtained 2, 4-D degradation result shows the efficiency of ZnO/Fe^o to be much higher compared to ZnO/Fe_2O_3. On ZnO–Fe^o photocatalyst, a continuous transporting of electrons produced on the CB of ZnO to the Fe^o CB and holes produced on Fe^o towards the VB of ZnO were proposed. Due to this Schottky barrier effect, a superior electron/hole recombination hindrance was achieved. Iron has two stable valances, the Fe^{2+} and Fe^{3+}. Compared to Zn^{+2} (0.74 Å), Fe^{2+} has bigger ionic radii (0.78 Å). During synthesis, incorporation of Fe^{2+} in ZnO lattice reported the shifting of the XRD pattern peaks towards a lower 2θ value. Or else, if it is appeared as Fe^{+3} (0.68 Å) state, shifting towards the higher 2θ value happened.

By taking the cost and harmful environmental effect of organic solvent into consideration, (Shooshtari & Ghazi, 2017) applied the surfactant-free room temperature synthesis route for the synthesis of ZnO/α-Fe_2O_3 nanosheets. The synthesized material has bandgap energy of 2.31 eV. The photocatalytic degradation efficiency test conducted within 140 minutes on efixime trihydrate verifies the nobility of the synthesized materials. This greater degradation capability is explained to be due to continuous charge transport properties. Similar transport properties due to the formation of heterojunction between ZnO and Fe_2O_3 were also reported on the salicylic acid degradation experiment (Achouri et al., 2014). This is interpreted to be the more negative values of both CB and VB of iron oxide compared to ZnO. Therefore, it acts as a sensitizer during visible light irradiation.

Using disodium terephthalate and nitroblue tetrazolium scavenging assay techniques they also confirmed the higher $OH^{\bullet}$ and $O_2^{\bullet -}$ production capability of ZnO/Fe_2O_3 than ZnO.

The non-structural distortion of ZnO due to the formation of heterojunction with Fe_2O_3 was verified in (Lachheb et al., 2017) work. This indicates that the composite is free from Fe^{3+} incorporation. This means Fe_2O_3 is present as a separate phase by forming only a local heterojunction. During the photocatalytic investigation, the presence of an interfacial electron transfer from the dye present on its excited state to the CB of the photocatalyst was also verified. This can activate the visible light absorption probabilities of the material through indirect photocatalysis processes. Due to this behavior, the weaknesses of the dyes to be used as a standard for photocatalyst nobility tests were indicated. Using DRS along with their correspondent Tauc plots, the bandgap energy value of the composite was obtained to be 2.9 eV. Compared to bare ZnO (3.2 eV), the higher photocatalytic behavior of the composite has also been verified through the electrochemical characterization techniques.

By spraying different volumes of 0.2 M ZnO solution on the pre-synthesized thin-film of Fe_2O_3, (Suryavanshi & Rajpure, 2018) prepared a distinctive Fe_2O_3/ZnO anode photoelectrode composite for photocatalytic degradation of benzoic acid. It was synthesized. The increased behavior of current-voltage with the negative polarity to the deposited film confirms Fe_2O_3/ZnO is an n-type semiconductor. The relative hydrophilic nature of the material was also proved by contact angle (41^o) measurement. From the result, it was clarified that the usefulness of the hydrophobic nature of the photocatalyst towards enhancement of photocatalytic reaction. Furthermore, the flat band potential of the materials was also determined from the intercept of the Mott-Schottky plot. The more negative values of Fe_2O_3/ZnO than Fe_2O_3 indicate the greater electron/hole recombination hindrance capacity of the material.

Via addressing the less usage of renewable natural sunlight as an energy source, the photocatalytic activities of ZnO coated γ-Fe_2O_3 under daylight illumination were tested by (Qamar et al., 2016). With the help of the CV voltammogram, the effect of γ-Fe_2O_3 on cathodic and anodic dissolution of ZnO during irradiation (equations 28 and 29) was also studied. From the voltammogram study under illumination, the presence of a $Zn(OH)_4^{2-}$

peak on ZnO indicates the formation of photo corrosion. While the absence of a $Zn(OH)_4^{2-}$ peak on ZnO coated γ-Fe_2O_3 composite confirms the prevention of photo corrosion [see Figure 6(a) and (b)]. This is due to the enhancement of quantum efficiency and photo-stability of the photocatalyst.

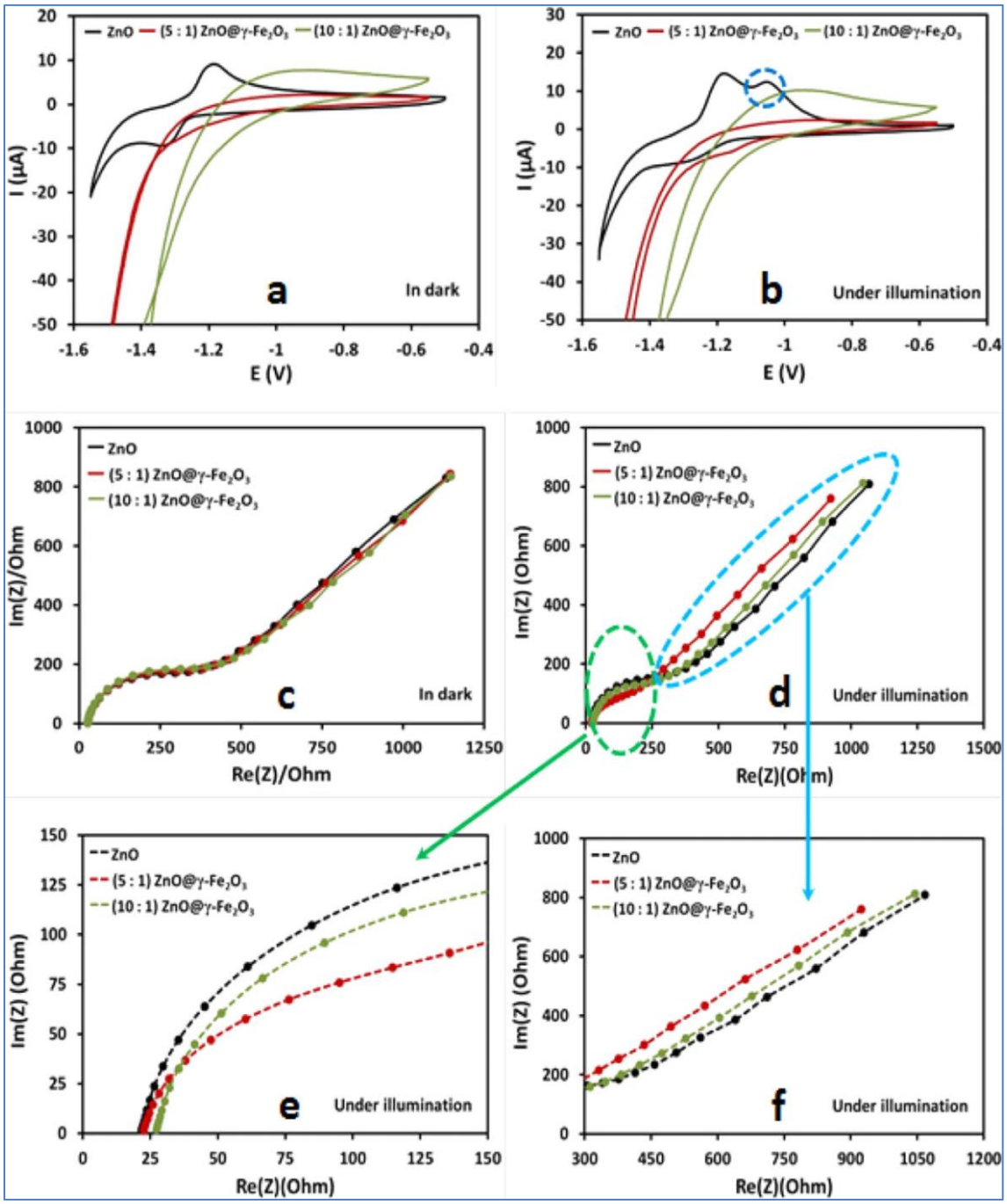

Figure 6. The comparison of the CV behavior (a and b), EIS spectra (c and d) of ZnO, ZnO/$\boldsymbol{\gamma}$-Fe_2O_3 in the dark and under illumination (Qamar et al., 2016).

Anode: $ZnO + 2h^{+}_{VB} + H_2O \rightarrow Zn^{2+}(solution) + 1/2O_2\,(solution)$ (28)

Cathode: $ZnO + 2e^{-} \rightarrow Zn^{2+}(solution) + 2O^{-}\,(surface)$ (29)

This photo corrosion protection is reported to be due to the continuous transfer of holes created on ZnO that causes oxidation to the VB of Fe_2O_3. Through the help of the EIS study [Figure 6(c) - (f)], they also confirmed the presence of greater charge transfer synergy for ZnO coated γ-Fe_2O_3 than single ZnO. Conducting the magnetically recovering study, due to the presence of γ-Fe_2O_3, the possibility of recovering almost 99 % of the photocatalyst was obtained. After the IVth and Vth cycle regeneration test only a 2% reduction was observed.

As generalized by (Xie et al., 2015), the improved photocatalytic activity of ZnO/α-Fe_2O_3 compared to bare ZnO is due to (i) the formation of narrow bandgap, (ii) improved optical absorption range, (iii) enhanced surface area to volume ratio, (iv) greater adsorption of reactant and diffusion of product, and (v) fewer electron-hole recombination due to the transfer of electron and hole from one to the other. The summarized forms of the above discussed and some other additional ZnO-Fe_2O_3 works are presented in Table 2.

Table 2. A review in the photocatalytic activity of binary ZnO–Fe_2O_3.

Method	Pollutant	Precursor		Properties		Optimization			Kinetics	Ref.
		Zn	Fe	S_{BET},p_v,P_d	D, SEM/TEM, BG	T(^{o}C)	[ ]	m(g)	t(min.)	
Sol–Gel	2,4-Dichloro-Phenoxyacetic	$Zn(Ac)_2.2H_2O$	$Fe(C_5H_7O_2)_3$	20.9,-,-	22.6, -, 2.8	450	10	0.5	-	(Maya-Treviño et al., 2015)
Hydrothermal	Cefixime Trihydrate	$Zn(NO_3)_2.6H_2O$	$Fe(NO_3)_3.9H_2O$	-	35, -, 2.31	25	10.11	0.41	127	(Shooshtari & Ghazi, 2017)
Facile Synthesis	Salicylic Acid	ZnO	$FeCl_3.6H_2O$		-	100	10	0.03	120	(Achouri et al., 2014)
Solid-State Reaction	Congo Red	$Zn(Ac)_2.2H_2O$	α-Fe_2O_3	23, -, -	16, Nanoflower, Redshift	25	50	0.83	-	(Abdullah Mirzaie et al., 2012)
Sol–Gel	MB & Benzoic Acid	$Zn(Ac)_2.2H_2O$	$Fe(NO_3)_3{\cdot}9H_2O$	20, -, -	10–60, Hexagonal, 2.9	550	30 & 10	1	120	(Lachheb et al., 2017)
Hydrothermal-Sintering	Ciprofloxacin	ZnO	$FeSO_4.7H_2O$	133, -, -	60–78, Core-Shell, -	450	10	0.5	-	(Li, Zhang, et al., 2017)
Photochemical Deposition	MB	$ZnCl_2$	$FeCl_3{\cdot}6H_2O$	-	-, Tubular, -	400	3.2	-	60	(Yanjun Liu et al., 2015)
Spray Pyrolysis	Benzoic Acid	$Zn(Ac)_2.2H_2O$	$FeCl_3$	-	44, Petal, 2.65	500	122.1	-	325	(Suryavanshi & Rajpure, 2018)
Hydrothermal	MB	$Zn(Ac)_2.2H_2O$	Fe_2O_3	-	56, Core/Shell, 3.2	500	-	-	60	(Karunakaran & Vinayagamoorthy, 2017)
	Chlorophenol Derivatives		Fe_2SO_4	-	33, Irregular, -	400	50	0.75	300	(Qamar et al., 2016)
Precipitation	RhB	$Zn(NO_3)_2.H_2O$	$FeCl_3.6H_2O$	-	-, -, 3.0	400	5	1	150	(Yang et al., 2018)
Hydrothermal	MO	$Zn(Ac)_2.2H_2O$	$Fe(NO_3)_3{\cdot}9H_2O$	-	-, Spindle, -	25	10	0.03	140	(Yan et al., 2011)
Impregnation Deposition	RhB	$Zn(Ac)_2.2H_2O$	$Fe(NO_3)_3$	-	-, NRs, -	400	5	0.02	150	(Yin et al., 2014)
-	Pentachloro-phenol	$Zn(NO_3)_2.H_2O$	$Fe(NO_3)_3.H_2O$	37.6,-, 9.6	30 x 1370, Flower, -	-	10	0.15	-	(Xie et al., 2015)

S_{BET}: Specific surface area (m^2/g), $p_{V:}$ pore volume ($cm^3/g_{)}$, P_d: pore diameter (nm); D: crystallite size (nm), []: Concentration (mg/L), BG: bandgap.

2.3.4. Photocatalytic activity of binary ZnO–Fe_3O_4

Nowadays, reducing nanotoxicity through recycling of the photocatalyst was getting attention. Mostly this is working by overturning metal oxides to have magnetic properties. Magnetite (Fe_3O_4) that has an inverse spinel structure has unique magnetic and electric properties (Yan et al., 2009). The significant influences of microwave reaction time and magnetite percentage on the 4-nitrophenol pollutant degradation ability of Fe_3O_4/ZnO NPs were studied by (Liu et al., 2019). The material was synthesized by solvent-thermal techniques. The result indicates that, increasing the percentage of Fe_3O_4 increases the magnetic properties and size of the materials.

As suggested by (Atla et al., 2018), instead of only forming heterojunction between Fe_3O_4 and ZnO, coating of Fe_3O_4 with SiO_2 and functionalizing it by (3-aminopropyl) triethoxysilane confirmed the enhancement of crystallinity, diminishing of the aggregation, and better degradation efficiency of methylene blue. The absorption study indicates that the presence of silica has greater absorption efficiency compared to both Fe_3O_4/ZnO and Fe_3O_4/ZnO with (3-aminopropyl) triethoxysilane.

Fernández and his co-workers also synthesized ZnO/Fe_3O_4 NC photocatalyst for the degradation of antibiotics (Fernández et al., 2019). As seen in equation 30, they verified the creation of extra $OH^{\bullet}$ as an additional organic contaminant oxidizing agent. With the help of orange II model dye, the creation of $OH^{\bullet}_{ads}$, $OH^{\bullet-}_{2ads}$, and hole species by Fe_3O_4/ZnO NC were confirmed during UVA-assisted photodegradation studies. The genotoxic property of the photocatalyst was also tested by incubating DNA with Fe_3O_4/ZnO composite. The result indicates that only 1.6% of DNA degradation was obtained. Therefore, it was concluded that no significant genotoxicity is present. Since most of the semiconductors have amphoteric properties, the significance of optimization of the pH of the solution that affects the particle interaction and stability of the surface was also embodied. When the pH is below the point of zero charges (PZC) of the material (Fatehah et al., 2014), the surface becomes positively charged and when it is above the point of zero charges it becomes negatively charged, as seen in equations 31 and 32.

$$H_2O_2 + Fe^{2+} + H^+ \rightarrow Fe^{3+} + OH^{\cdot} + H_2O \quad (30)$$

$$\equiv Zn-OH + H^+ \leftrightarrow \equiv ZnOH_2^+ \quad (31)$$

$$\equiv Zn-OH + OH^- \leftrightarrow ZnO^- + H_2O \quad (32)$$

However, (Fernández et al., 2019) found the PZC value of synthesized composite to be at pH 3, the specified reason for this is due to the presence of acetate groups as ligands on the surface of the composite. Therefore, this indicates that the PZC value becomes dependent on groups attached to the oxide materials. The hybrid Fe_3O_4-ZnO NPs synthesized by (Patel et al., 2017) also showed the great dependency of Fe_3O_4, ZnO, and NC on the pH of the solution. On the ICP-OES analysis, at a lower pH value, the dissolution of both Fe_3O_4 and ZnO was observed. Consequently, this led to the suppression of photocatalytic activity. However, as the pH increases, reducing the dissolution rate were observed. The same justification was also observed in (Xia et al., 2011) work. Moreover, the dependency of the effects of pH on PZC values of the semiconductor and types of pollutants was also studied (Safari et al., 2014).

As explained by (Xia et al., 2011), the degradation ability of the pollutant has a great dependency on the dosage of the photocatalyst. As the amount of dosage increases, since the number of active sites also increases, it is expected that the degradation efficiency to be enhanced. Further increasing the dosage above the optimum point, diminishing the photocatalytic activity was observed. This is explained to be due to the formation of turbidity that prevents light penetration ability. After discussing the interpretation of several researchers on the effects of concentration of the pollutant, (Safari et al., 2014) obtained the absorption of a large number of water molecules that led to producing hydroxide radicals at low pollutant concentrations. However, as the concentration of the pollutant increases, the absorption of water molecules is reduced. Furthermore, by indicating the scavenging negative effects at higher concentrations, the optimization study on H_2O_2 by (Fernández et al., 2019) confirmed the electron/hole recombination hindrance abilities and acting as a strong oxidizing agent at optimized value.

The concept of controlling and modifying the specific morphology of the catalyst through regulating the amount of iron precursor, hexamethylenetetramine, and urea was explained in (Xu et al., 2014) work. The synthesized Fe_3O_4/ZnO via a one-step synthesis route for

degradation of Rhodamine B dye indicates, applying a higher percentage of iron precursors above the optima can create a complete lattice distortion of the regular monodispersed micro-rods structure of ZnO. Adding hexamethylenetetramine (HMTA) shows size improvement on both in diameter and length of the pencil-like NRs. The presence of HMTA is also used to cut off the contact between Zn^{+2} ions and ZnO crystal that distort the polar (001) face for epitaxial growth. The addition of urea also shows improvement from irregularly agglomerated shapes of hexagonal rods to the regular less agglomerated shape. Therefore, it acts as a surfactant and is used to tune the growth of the material in a different direction. However, increasing above the optima led to further facilitating agglomeration. From the result obtained, they concluded that the presence of Fe_3O_4 can assist for further improvement of active sites that help for the adsorption of both inorganic and organic pollutants.

The hydrothermally synthesized Fe_3O_4/ZnO nanosheets by (Karunakaran et al., 2014) show the perfect implementation of Fe_3O_4 in the ZnO shell. As seen in Figure 7(a), unlike that of ZnO, the magnetic hysteresis curves of Fe_3O_4/ZnO show the superparamagnetic nature of the photocatalyst. Therefore, this enhances the chances to recover all of the photocatalysts from the dispersed medium. As seen in Figure 7(b), the less charge carrier resistance properties of Fe_3O_4/ZnO were verified by solid-state impedance spectroscopic techniques via the Nyquist plot, compared to ZnO. Furthermore, the deep level emission that occurs due to extrinsic and intrinsic structural defects and near bandgap emission which arises due to electron/hole recombination was observed on the photoluminescence spectra. The spectra show the violet, blue, green, and yellow emission. Blue emission occurs due to electron transmission from shallow donor levels of Zn interstitials and oxygen vacancies to the VB. The green and yellow vacancies arise due to the vacancies and defects of oxygen.

The morphological effect of forming tetramethylammonium hydroxide (TMAH) and citric acid (CA) surfactants bond on the surface of the NPs were examined by (Feng & Lou, 2015). The SEM images of Fe_3O_4/ZnO linked with TMAH shows dense and smaller particle size compared to the link formed with CA. This is explained to be due to the more positive zeta potential values of Fe_3O_4 with TMAH than Fe_3O_4 with CA. This means the more positively charged Fe_3O_4 (TMAH) NPs attracted more towards the negatively charged $[Zn(OH)_4]^{2-}$, compared to Fe_3O_4 (CA). Furthermore, the repulsive force between

the same charge of CA and acetate from the precursor prevents the attraction between the two. The summarized forms of the above discussed and some other additional ZnO-Fe_3O_4 works are presented in Table 3.

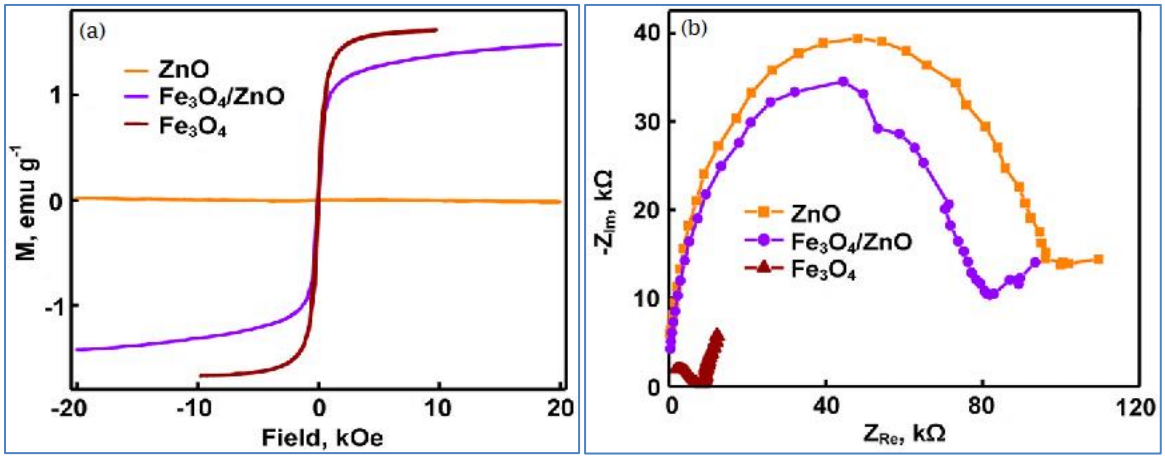

Figure 7. (a) Magnetic hysteresis curves, (b) solid-state impedance spectra of Fe_3O_4/ZnO and ZnO nanosheets and precursor Fe_3O_4NPs (Karunakaran et al., 2014).

Table 3. A review in the photocatalytic activity of binary ZnO–Fe_3O_4.

Method	Pollutant	Precursor		Properties		Optimization			Kinetics	Ref.
		Zn	Fe	S_{BET}, p_v, P_d	D, SEM/TEM, BG	T(^{o}C)	[ ]	m(g)	t(min.)	
Solvent-Thermal	4-Nitrophenol	$Zn(Ac)_2.2H_2O$	$FeCl_3.6H_2O$	27.52, 0.07, 14	200-800, Spherical, 3.22	160	30	-	120	(Liu et al., 2019)
-	MB	$Zn(NO_3)_2.6H_2O$	$FeCl_3$-$6H_2O$	-	-, sugar apple, -	50	5	0.5	60	(Atla et al., 2018)
Facile Surfactant-Free	Escherichia Coli&Phenol	$Zn(Ac)_2.2H_2O$	$FeCl_3$-$6H_2O$	43, -, -	200–600, spherical, -	30	10	0.024	180	(Singh et al., 2013)
Co-Pre- Cipitation	RhB	$Zn(NO_3)_2$. $6H_2O$	$FeCl_3$.$6H_2O$ $FeSO_4.7H_2O$	-	-, NRs, -	60	47.9	0.015	35	(Wang et al., 2015)
-	Antibiotics	$Zn(Ac)_2.2H_2O$	$FeCl_3·6H_2O$ $FeSO_4·7H_2O$	-	200–300, spherical, -	25	50	0.1	240	(Fernández et al., 2019)
One-Step Synthesis Route	RhB	$Zn(NO_3)_2$. $6H_2O$	$FeCl_3.6H_2O$ $FeCl_3·6H_2O$	-	100–200, micro-rods, -	500	10	0.03	40	(Xu et al., 2014)
Hydrothermal	MB	$Zn(Ac)_2.2H_2O$	$FeCl_2·4H_2O$	-	-, rod shaped, -	140	10		180	(Goyal et al., 2018)
Hydrothermal	MB	$Zn(Ac)_2.2H_2O$	Fe_3O_4	-	-, nanosheets, -	500			60	(Karunakaran et al., 2014)
Precipitation	MB	$Zn(Ac)_2.2H_2O$	Fe_3O_4	-	21.4, cubic, 2.9	25	50	0.51	90	(Patel et al., 2017)
Solvothermal	MO	$Zn(Ac)_2.2H_2O$	$FeCl_3·6H_2O$	-	-, -, red shift	10	19.64	0.03	60	(Xia et al., 2011)
Precipitation	Methyl Tert-Butyl Ether	$Zn(Ac)_2.2H_2O$	$FeCl_3.6H_2O$ $FeSO_4.7H_2O$	-	-	-	89.14	1.78	-	(Safari et al., 2014)
-	Phenol	$Zn(Ac)_2.2H_2O$	$FeCl_2.4H_2O$ $FeCl_3.6H_2O$	95.6,0.19, 5.8	34, -, 3.3	25	20	0.325	150	(Feng & Lou, 2015)
Precipitation	Phenol	$Zn(Ac)_2.2H_2O$	$FeCl_3.6H_2O$ $FeSO_4.7H_2O$	-	48, core/shell, -	550	100	1	300	(Nikazar et al., 2014)

S_{BET}: Specific surface area (m^2/g), $p_{V:}$ pore volume ($cm^3/g_)$, P_d: pore diameter (nm); D: crystallite size (nm); BG: bandgap, []: Concentration (mg/L), BG: bandgap

2.3.5. Photocatalytic activity of binary ZnO–Mn_xO_y

A manganese oxide semiconductor also has several favorable properties. It has different crystalline polymorphs including MnO, Mn_3O_4, Mn_2O_3, Mn_5O_8, and MnO_2 (Guorui Yang et al., 2014). Among them, α-Mn_2O_3 finds a wide range of photocatalytic applications both in the amorphous and crystalline states (Moharreri et al., 2018). Furthermore, because of its low charge transfer resistance and multitudinous defects, manganese oxides can form a heterojunction with ZnO and enhances the e^- and h^+ separation route. In the nanosized range, α-Mn_2O_3 can enhance the adsorption capacity of the pollutants during heterojunction (Zhao et al., 2017). There are obvious ionic radius differences between Zn^{2+} (0.074nm) and Mn^{+4} (0.053 nm). Therefore, instead of doping, forming a heterojunction between MnO_2 and ZnO was suggested (Yu et al., 2016). The formed heterojunction was synthesized using the co-precipitation method. As seen in equations 33-38, due to the high concentration of Zn^{+2}, the addition of base can form the $Zn(OH)_2$ and $[Zn(OH)_4]^{2-}$ species. Further reaction of these products in the presence of H_2O_2 can form a ZnO nucleus. Due to the formation of ZnO, a large number of OH^- released and react with a smaller concentration of Mn^{+2} to form $Mn(OH)_2$, $MnO(OH)_2$, and then MnO_2 by applying heat. The performance of the synthesized MnO_2/ZnO photocatalyst was tested on the degradation of Rhodamine B dye.

$$Zn^{2+} + OH^- \rightarrow Zn(OH)_2 \quad (33)$$

$$Zn(OH)_2 + OH^- \rightarrow [Zn(OH)_4]^{2-} \quad (34)$$

$$[Zn(OH)_4]^{2-} + Zn(OH)_2 + H_2O_2 \rightarrow ZnO\ nuclei + H_2O + OH^- \quad (35)$$

$$Mn^{+2} + OH^- \rightarrow Mn(OH)_2 \quad (36)$$

$$Mn(OH)_2 + Mn(OH)_2 \rightarrow MnO(OH)_2 + H_2O \quad (37)$$

$$MnO(OH)_2 + heat \rightarrow MnO_2 + H_2O \quad (38)$$

Using the facile synthesis method, (Wang et al., 2019) synthesized ZnO-MnO_2 NC for the photocatalytic degradation of tetracycline. Compared to ZnO, the greater absorption intensity on UV-vis-DRS, greater surface area, and a smaller radius of the EIS arc of ZnO-MnO_2 composite indicates its superior catalytic abilities. The smaller the arc radius of the EIS spectra indicates the faster the interface charge transfer rate, so the improved photoelectron-hole pair's separation efficiency. This charge transfer efficiency was also further confirmed by comparing the spectral intensity of PL. The smaller intensity for

$ZnO\text{-}MnO_2$ relative to ZnO indicates the presence of reasonable electron/hole recombination prevention performance. The involvement of radical species in photocatalytic activity was also tested by ESR measurement. The obtained strong signal for both $OH^{\bullet}$ and $O_2^{\bullet -}$ indicates the involvement of those species. Moreover, compared to ZnO, due to the luminous energy absorption ability of MnO_2, the simulated photothermal conversion (1 hr) result shows a better absorption capacity of the $ZnO\text{-}MnO_2$ composite. The summarized forms of the above discussed and some other additional $ZnO\text{-}Mn_xO_y$ works are presented in Table 4.

Table 4. A review in the photocatalytic activity of binary $ZnO–Mn_xO_y$.

Method	Pollutant	Precursor		Properties		Optimization			Kinetics	Ref.
		Zn	Mn	S_{BET}, $p_{v,}$ P_d	D, SEM/TEM, BG	T(^{o}C)	[ ]	m(g)	t(min.)	
Coprecipitation	RhB	$Zn(Ac)_2.2H_2O$	$Mn(CH_3CO_2)_2·2H_2O$	-	-, NRs, 3.06	600	-	-	20	(Yu et al., 2016)
Facile	Tetracycline	$Zn(Ac)_2.2H_2O$	$KMnO_4$	17.33, -, -	-, NRs, 3.21	500	10	0.125	80	(Wang et al., 2019)
Impregnation & Coprecipitation	4-Bromo And 4Chlorophenol	ZnO	$Mn(NO_3)_2·4H_2O$	-	-, -, 3	-	50	0.004	240	(Qamar et al., 2017)
Thermal Decomposition	MB & MO	$Zn(Ac)_2.2H_2O$	$Mn(C2H_3O_2)_2.4H_2O$	2.8, -, -	-, NRs, 32 x 38, core-shell	350	9.59	0.5	210	(Saravanan et al., 2014)
Hydrothermal	Cr(VI)	ZnO	$MnCl_2·4H_2O$	198, -, -	-	-	10	0.15	120	(Li, Tian, et al., 2017)

S_{BET}: Specific surface area (m^2/g), $p_{V:}$ pore volume ($cm^3/g_)$, P_d: pore diameter (nm); D: crystallite size (nm), []: Concentration (mg/L), BG: bandgap

2.3.6. Photocatalytic activity of ZnO based ternary metal oxides

It is reported that combining the equivalent or different bandgap metal oxides materials can improve the surface area and the continuous charge transfer capacity of the materials. (Lei et al., 2018) confirmed the ability to prevent electron/hole recombination, wide visible light absorption, thermal stability enhancement, and so the photocatalytic improvement through forming a ternary heterojunction between CeO_2, Fe_2O_3, and ZnO. The heterojunction was performed on the polyimide substrate using the direct ion exchange method. Compared to binary heterojunction, the observed superior redshift with an approximate bandgap energy value of 1.6 eV approves the improvement of visible light absorption efficiency.

(Xiaojuan Li et al., 2018) also verified the extended visible light activity of Fe_2O_3/ZnO/$ZnFe_2O_4$ heterojunction. It was confirmed that, due to the reaction of Fe_2O_3 and ZnO, the formation of $ZnFe_2O_4$ which has high visible light absorption ability is highly dependent on the calcination temperature. As the calcination temperature increases, the formation of $ZnFe_2O_4$ also increases. The growth of $ZnFe_2O_4$, which has approximate bandgap energy of 1.9 eV is highly important for the absorption of abundant visible light and total separation of the generated electron/hole pairs. The proposed mechanism indicates that during degradation electrons are transported from $ZnFe_2O_4$ to Fe_2O_3 and then to the ZnO, whereas, the holes move from Fe_2O_3 to $ZnFe_2O_4$. The direct relationship between temperature and formation of Zn-based impurity ($ZnTiO_3$) was also observed on the ternary SnO_2/ZnO/TiO_2 composite study (Guidong Yang et al., 2012). However, increasing the temperature for the formation of these impurities may lead to increasing the particle size. This may lead to decreasing absorption and photocatalytic activity. The summarized forms of the above discussed ZnO-based ternary oxides heterojunctions are presented in Table 5.

Table 5. A review in the photocatalytic activity of ZnO-based ternary metal oxides.

Method	Pollutant	Precursor			Properties		Optimization			Kinetics	Ref.
		Zn	P2	P3	S_{BET}, $p_{v,}$ P_d	D, SEM/TEM,BG	T(^{o}C)	[ ]	m(g)	t(min.)	
Facial	RhB	$ZnCl_2$	$Mn(CH_3COO)_2$	$CuSO_4.5H_2O$	-	-, Cubic, -	80	30	-	45	(Hoseinpour & Ghaemi, 2018)
Solvothermal	RhB, Cr(VI)	-	-	-	155, 0.3, 6.1	-, nanosheet, - 2.91	400	-	-	150	(Yu et al., 2019)
Sol-Gel	MB	$ZnSO_4.7H_2O$	$FeSO_4.7H_2O$	$CuSO_4.5H_2O$	-	-, spherical, 2.9	100	20	0.03	120	(Taufik et al., 2015)
Ion Exchange	MO	$Zn(NO_3)_2{\cdot}6H_2O$	$Fe(NO_3)_2{\cdot}6H_2O$	$Ce(NO_3)_3{\cdot}6H_2O$	-	- ,spherical, 1.6	550	16.35	0.3	12	(Lei et al., 2018)
Hydrothermal	RhB	$Zn(NO_3)_2.6H_2O$	$Fe(NO_3)_3.9H_2O$	-	53, -, 5-20	600, Shuttle, 2.33	500	20	0.03	60	(Xiaojuan Li et al., 2018)
Multistep Precipitation	RhB	$Zn(Ac)_2.2H_2O$	$FeSO_4.7H_2O$ $FeCl_3.6H_2O$	$Si(OC_2H_5)_4$	160, -, -	300, chestnut, -	25	6.17	0.015	80	(Bian et al., 2015)
Precipitation	MO	$Mn(NO_3)_2$	$FeCl_3{\cdot}6H_2O$	$Si(OC_2H_5)_4$	44.8, 0.12, 10	-, Core–shell, -	300	20	0.1	60	(Yang et al., 2015)
One-Step Impregnation	MB & Sewage	$Zn(NO_3)_2{\cdot}6H_2O$	$Fe(NO_3)_2{\cdot}6H_2O$	MnO_2	-	-, -, 2.75	400	10	0.125	120	(Tedla et al., 2015)
N719	CO_2 to Methanol	$Zn(NO_3)_2{\cdot}6H_2O$	$Fe(NO_3)_3{\cdot}9H_2O$	TiC_{l4}	178	-, Flower, 2.62	800	-	-	180	(Xia et al., 2016)
-	Oxidation of phenol	$ZnCl_2$	$FeCl_3$	$KMnO_4/MnO_2$	166, 0.161, -	-, Flower, -	60	20	0.1		(Yuxian Wang et al., 2014)
Sol–Gel	MO	$Zn(Ac)_2.2H_2O$	$SnCl_4{\cdot}5H_2O$	$C_{16}H_{40}O_4Ti$	-	-, solid particle, 2.95	400	10	0.15	300	(Guidong Yang et al., 2012)
Co-Precipitation	MB	$Zn(Ac)_2.2H_2O$	$FeCl_3$	Rectorite	16.0, -, -	6–35,		5	0.9	150	(Wang et al., 2018)

S_{BET}: Specific surface area (m^2/g), $p_{V:}$ pore volume (cm^3/g), P_d: pore diameter (nm); D: crystallite size (nm), []: Concentration (mg/L), BG: bandgap.

2.4. Dyes

Dyes find numerous applications in our daily life in clothing, food, paper, leather, cosmetics, plastics, drugs, electronics, and printing. Nearly 80% of the synthetic dyes produced in the world are consumed by the textile industry. One of the major bottlenecks in the textile industry is dye fixation, i.e., spent dye baths, residual dye liquors, and water from washing operations contain dye in the hydrolyzed and unfixed form. Nearly 10% of the dyes are discharged into the effluent as a result of this process. Conventional treatment of wastewater results in 70–80% of pollutant degradation. However, maintaining the organic carbon load in the effluent needs attention. Biodegradation methods are effective in reducing the biological oxygen demand of the effluent, but reducing the chemical oxygen demand and toxicity to permissible levels is also a challenging task. Hence, the role of heterogeneous advanced oxidation processes in the degradation of dye wastewaters is very critical (Vinu & Madras, 2010).

There are many ways to classify dyes in terms of method of application, color, and structure. But the application classification is often favorable due to the extent and complexity of the nomenclature of color from the system of chemical structure. Dyes are usually categorized according to the charge of the particle upon dissolution in an aqueous solution such as anionic (acid, reactive, and direct dyes), cationic (all basic dyes), and non-ionic (dispersed dyes). Based on the functional group that constitutes the dyes, dyes are classified as azoic, anthraquinone, heteropolyaromatic, aryl methane, xanthene, indigo, acridine, nitro, nitroso, cyanine, and stilbene (Ahmed, 2016; Yagub et al., 2014).

The degradation of a dye can be characterized in two ways: percent decolorization and percent mineralization. Decolorization refers to the reduction in the concentration of the parent dye molecule under consideration at its characteristic wavelength but does not refer to the complete removal of the organic carbon content. This is due to the formation of colored dye intermediates, which absorb at different wavelengths. Hence, complete degradation or mineralization occurs when all the organic carbon is converted to CO_2 (Houas, 2001; Modirshahla et al., 2007).

2.4.1. Methylene blue dye

Methylene blue ($C_{16}H_{18}ClN_3S$, MB) is a commonly used substance for dying garments such as cotton, wool, and silk (Tan et al., 2008). The IUPAC name of MB is [7-(dimethylamino) phenothiazin-3-ylidene]-dimethylammonium chloride. The molecular structure of methylene blue is given in Figure 8(a). It can cause eye burns which may be responsible for permanent injury to the eyes of humans and animals. Due to its known strong adsorption onto solids, MB often serves as a model compound for removing dyes and organic contaminants from aqueous solutions (Hameed et al., 2007). Although not strongly poisonous, MB can have some harmful effects on human beings (Sheng et al., 2009). Inhalation of MB dye can give rise to short periods of rapid or difficult breathing while ingestion through the mouth produces a burning sensation and may cause nausea, vomiting, profuse sweating, mental confusion, and methemoglobinemia (Hofmann et al., 1966; Tan et al., 2008). Therefore, the treatment of effluent containing such dye is of interest due to its harmful impacts on receiving waters.

2.4.2. Congo red dye

The congo red ($C_{32}H_{22}N_6Na_2S_2O_6$, CR) is an anionic secondary organic diazo dye with complex aromatic structures, which make the dye more stable and non-biodegradable, and hence the removal process is quite difficult. The IUPAC name of CR is 1-naphthalene sulfonic acid, 3, 3-(4, 4- biphenylene bis (azo)) bis (4-amino disodium) (Nayak et al., 2020). The molecular structure of CR is given in Figure 8(b). It is highly soluble in water and exists as a brownish-red crystal. It is stable in air with a solubility of 1 g/30 mL in water and even a small concentration of it is carcinogenic to aquatic life. It creates problems in the skin, respiratory system, eyes, and reproductive system as well (Mittal et al., 2009). Therefore, to control the hazardous effects of CR dyes on human health, the environment, and aquatic life, it is essential to minimize or remove the traces of CR dye concentration from dye contaminated water before their discharge.

2.4.3. Acid orange-8 dye

Acid orange 8 ($C_{17}H_{13}N_2NaO_4S$, AO8) also belongs to the azo dye family, which is a highly soluble pollutant found in textile wastewater and has a high resistance to photo-

oxidation. The IUPAC name of AO8 is sodium; 4-[(2-hydroxy naphthalene-1-yl) diazenyl]-3-methyl benzenesulfonate. The molecular structure of acid orange 8 is given in Figure 8(c). It accounts for over 50% of the world's annual production of one million tons of dye. It exists in their hydrazone tautomeric forms, which exhibit good stability. AO8 is resistant to photo-oxidation and chemical oxidation. The aromatic amines are the principal products of cleavage of the azo group, and these are potentially mutagenic and carcinogenic (Elizalde-González & García-Díaz, 2010; Guaratini & Zanoni, 2000). As a strong electrolyte, AO8 dissociates completely and is used in the dyeing process. AO8 was one of the ten detected dyes in water samples from municipal and industrial wastewater treatment plants in Northern Italy in 2002, together with phenols, carboxylic acids, aromatic sulfonates, aromatic amines, pharmaceuticals, and surfactants (Elizalde-González & García-Díaz, 2010; Loos et al., 2003).

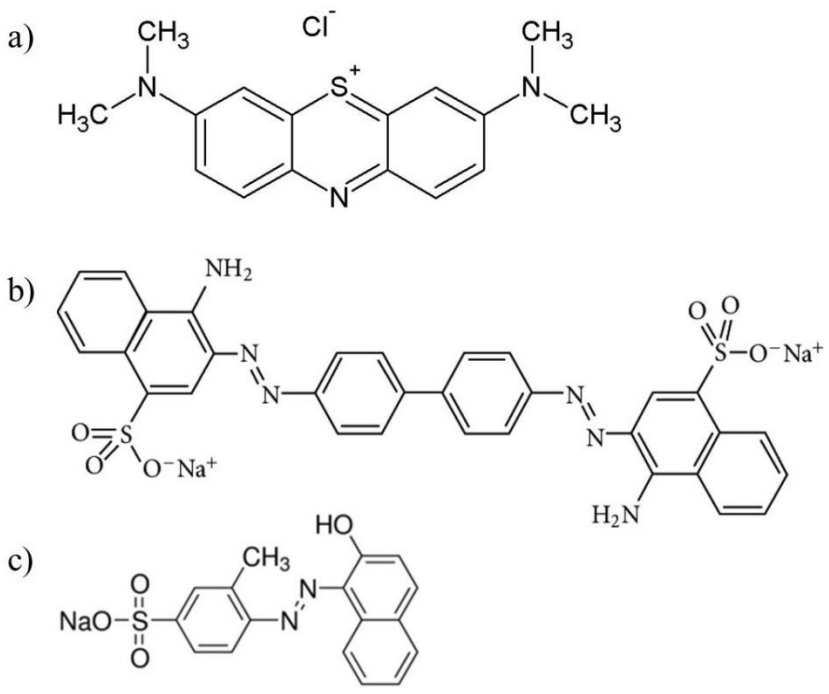

Figure 8. The molecular structure of (a) methylene blue, (b) congo red, and (c) acid orange 8 dyes.

2.5. Parameter Optimization

2.5.1. Effect of pollutant concentration

It is important both from a mechanistic and an application point of view to study the dependence of substrate concentration on the photocatalytic reaction rate. Catalyst dosage and concentration of pollutant optimization have similar plot flow properties. As the initial concentration of the dye increases, the efficacy of dye adsorption decreases according to the saturation of adsorption sites on the surface of the adsorbent. At a low concentration of dye, there will be unoccupied binding sites on the surface of the adsorbent and when the initial concentration of dye increases, there will be insufficient sites for the dye molecules to adsorb, so decreases the removal efficiency (Robati et al., 2016). Besides, an increase in substrate concentration can lead to the generation of intermediates, which may adsorb on the surface of the catalyst. Slow diffusion of the generated intermediates from the catalyst surface can result in the deactivation of active sites on the photocatalyst and result in a reduction in the degradation rate. At low concentrations, the number of catalytic sites will not be the limiting factor and the rate of degradation will be proportional to the substrate concentration, under apparent first-order kinetics (Ahmed, Rasul, Brown, et al., 2011; Herrmann, 1999)

2.5.2. Effect of catalyst dosage

During the photocatalytic degradation experiment, the amount of photocatalyst is dependent on the type and dimensions of the reactor as well as the type and concentration of pollutants. The initial rates of reaction were found to be directly proportional to the mass m of the catalyst, which is known as the true heterogeneous catalytic regime. Above a certain value of m, the point at which all the particles are illuminated, the reaction rate levels off and becomes independent of m. This limit depends on the geometry and the working conditions of the photoreactor (Haque et al., 2006). Loading of the catalyst above the optima also leads to the screening effect of excess particles or non-uniform light intensity distribution, which covers the photosensitive part. Also, loading above the optima results in the agglomeration/agglomeration between the NPs, which results in a reduction of surface active sites for light absorption and hence a drop in the photocatalytic degradation rate (Adesina, 2004; Herrmann, 1999).

During the optimization of catalyst mass m and initial concentration of pollutants, up to the formation of the plateau the reaction rate r has a linear relationship to both the mass of the catalyst and concentration of the pollutant (Herrmann, 2010). This is due to the availability of free active sites n_t on the surface, which is calculated by equation 39:

$$n_t = m \times S_{EBT} \times d_s \qquad (39)$$

where S_{BET} is the specific surface area of the catalyst and d_S is the areal density of the sites whose maximum value is estimated to be $\leq 5\times10^{18}$ m^2/g (Boehm, 1966). However, an excess of the catalyst will produce negative effects due to particle aggregation and an increase of solution opacity, which will reduce the effective path length of the radiation (Xia et al., 2011).

2.5.3. Effect of solution pH

An important parameter in the photocatalytic reactions taking place on the particulate surfaces is the pH of the solution since it dictates the surface charge properties of the photocatalyst and the size of aggregates it forms (Haque et al., 2006). The pH has been considered an important factor affecting the transformation of pollutants in the natural environment. Solution pH can not only change the speciation and chemical characteristics of pollutants but also affect the characteristics and existing forms of surface functional groups of reaction media, this is explained to be due to the change of pH has a significant effect on the absorbance of dissolved organic matters (Gao et al., 2015; Jin et al., 2017).

Characteristics of organic pollutants in wastewater differ greatly in several parameters, particularly in their speciation behavior, solubility in water, and hydrophobicity. At pH below its pKa value, an organic compound exists as a neutral state. Above this pKa value, the organic compound attains a negative charge. Some compounds can exist in positive, neutral, and negative forms in aqueous solutions. This variation can also significantly influence their photocatalytic degradation behavior. The surface charge of the photocatalyst and the ionization or speciation (pKa) of an organic pollutant can be profoundly affected by the solution pH (Ahmed, Rasul, Martens, et al., 2011).
The interpretation of the pH effect on the photocatalytic process is a difficult task because of its multiple roles, such as electrostatic interaction between a semiconductor surface,

solvent molecules, substrate, and charged radicals formed during photocatalytic oxidation. Besides, the protonation and deprotonation of the organic pollutants can take place depending on the solution's pH. Sometimes protonated products are more stable under UV radiation than their main structures (Ahmed, Rasul, Brown, et al., 2011). Therefore the pH of the solution can play a key role in the adsorption and photocatalytic oxidation of pollutants. The ionization state of the surface of the photocatalyst can be protonated ($\equiv M - OH_2^+$) under acidic conditions and deprotonated ($\equiv M - O^-$) under alkaline conditions (Haque et al., 2006). Furthermore, the adsorption of a water molecule on the surface of metal oxides results in the formation of hydroxide layers ($\equiv M - OH$). Depending on this theoretical assumption, optimizing the pH of the solution in which it forms the required interaction with targeted pollutants is important. Due to the large photo adsorption coefficient values of dye pollutants, it may not be possible to show a turnover of the photocatalyst, therefore standardization of the photocatalyst using dye may not work (Bendjabeur et al., 2017; Ohtani, 2010).

Besides, the presence of external oxidizing agents/electron acceptors like $KBrO_3$, $(NH_4)_2S_2O_8$, and H_2O_2 can improve the photocatalytic degradation of organic compounds attributed to the increasing of the $OH^{\bullet}$ concentration and other oxidizing species to accelerate the degradation efficiency of intermediate compounds (Nguyen et al., 2020; Rajeshwar et al., 2008; Vinu & Madras, 2010). This is because the formation of these radicals can inhibit the electron/hole recombination by adding other (irreversible) electron acceptors to the reaction and improve photodegradation efficiency through the following equations (Haque et al., 2006).

BrO_3^- can generate $BrO_2^{\bullet}$ and Br^- depending on the number of mole of e_{CB}^- and H^+ (equations 40 and 41).

$$BrO_3^- + e_{CB}^- + 2H^+ \rightarrow BrO_2^{\bullet} + H_2O \quad (40)$$

$$BrO_3^- + 6e_{CB}^- + 6H^+ \rightarrow [BrO_2^-, HOBr] \rightarrow Br^- + 3H_2O \quad (41)$$

$S_2O_8^-$ can generate sulfate radical anions $SO_4^{\bullet -}$ both thermally and photolytically in an aqueous solution. $SO_4^{\bullet -}$ then reacts with H_2O to produce $OH^{\bullet}$ radicals (equations 42 and 43).

$$S_2O_8^- + e_{CB}^- \rightarrow SO_4^{\bullet -} + SO_4^{2-} \quad (42)$$

$$SO_4^{\bullet -} + H_2O \rightarrow SO_4^{2-} + OH^{\bullet} + H^+ \quad (43)$$

H_2O_2 can also generate $OH^{\bullet}$ radicals by reacting with superoxide ions (equation 44).

$$H_2O_2 + O_2^{\bullet -} \rightarrow OH^{\bullet} + OH^- + O_2 \quad (44)$$

When the concentration of H_2O_2 is above the optimum, the quenching of the hydroxyl radicals results and decreases the degradation rate (equations 45 and 46). This indicates that careful optimization of oxidant concentrations is necessary for enhancing photocatalytic activity (Vinu & Madras, 2010).

$$H_2O_2 + OH^{\bullet} \rightarrow 3H_2O + HOO^{\bullet} \quad (45)$$

$$HOO^{\bullet} + OH^{\bullet} \rightarrow 3H_2O + O_2 \quad (46)$$

2.6. Ascorbic Acid Sensor using Metal oxides

Ascorbic acid plays a vital role in the metabolic process and helps in the treatment of different illnesses (Lu Yang et al., 2014). A small variation in the standard level of AA is generally a symptom of sickness (Yin et al., 2016). AA acts as an antioxidant, enzyme cofactor, and neuromodulator in the brain (Rice, 2000), and it also indicates the human immunodeficiency virus (Han et al., 2017). The UV–vis spectroscopy, chromatography, fluorescence spectroscopy, fluorimetry, and electrochemical methods are the conventional methods used for the determination of the level of AA. Among them, the electrochemical technique received interest in accuracy, stability, sensitivity, and cost (Zhou et al., 2013). However, AA detection by bare conventional electrodes fouls the electrodes due to the irreversible oxidation process of AA to 2,3-diketogluconic acid (Jiang & Du, 2014; Peik-See et al., 2014). Nowadays, researchers are modifying the normal electrodes by metal oxide NMs as a redox-active electrochemical sensor site to improve the sensitivity and to avoid the multi-selectivity activities (Alam et al., 2020; Khan et al., 2016).

Among the metal oxides, ZnO NPs has been broadly used as biosensor due to its diverse decent properties (Saravanan et al., 2015), although, it showed not satisfactory sensing capability (Bai et al., 2020; Ibupoto et al., 2012). Among several techniques used to improve the reliability and toxicant biomolecules detection properties of ZnO, creating NCs via n-n or n-p junctions were employed. This junction produces a depletion layer in the interface and assists electron and hole flow without recombination (Alam et al., 2020; Ghanbari & Bonyadi, 2018; Huang et al., 2013; Khan et al., 2016; Murugan et al., 2019). Also, modifying the synthesized materials to have a mesoporous property allows a rapid charge transfer process (Khan et al., 2015; Khan et al., 2016; Yuanying Liu et al., 2014). Fe_2O_3 is vital in mediating the final heterogeneous chemical redox reaction of the target agent due to its high SAV and environmentally biocompatible properties (Cao & Wang, 2011). The coupling of Mn_2O_3 with ZnO has its own electrochemical and sensor improvement towards ascorbic acid (Saravanan et al., 2015). The hydrothermal (Nadargi et al., 2020), sol-gel auto-combustion (Han, 2020; Tikare et al., 2020), self-propagation/combustion (Zou et al., 2017), co-precipitation-hydrothermal (Bai et al., 2020), and the ultrasonic-microwave (Nadargi et al., 2020) methods are also frequently applied for synthesizing NMs for sensor application. Among them, the sol-gel and sol-gel auto-combustion procedures are reported as efficient and economically feasible (Dey & Sarkar, 2020; Han, 2020).

2.7. Antibacterial Activity of Metal Oxides

Metal oxide NMs are one of the preferences as antibacterial active materials (Dadi et al., 2019). Due to its distinctive electronic configuration and suitable properties, ZnO is one of the novel antibacterial active materials (Pavithra et al., 2020). Nowadays, researchers are making a serious effort to improve the antibacterial activities of ZnO by forming a composite with the same/different bandgap semiconductor materials (Anaya-Esparza et al., 2019; Munawar, Yasmeen, Hussain, et al., 2020). Applying capping agents such as polymers and plant extract that control the morphology and size of the NMs and optimizing different conditions also enhance the antibacterial activity. Forming a NCs and doping reduces the electron/hole recombination, increases the surface area to volume ratio, and also improves the stability towards dissolution and corrosion. The release of antimicrobial ions, electrostatic interaction, reactive oxygen species (ROS) generations are the crucial antibacterial activity mechanism (Espitia et al., 2012). This review also

presents a detailed discussion of the antibacterial activity improvement of ZnO by forming a composite, doping, and optimizing different conditions. The morphological analysis using scanning electron microscopy, field emission-scanning electron microscopy, field-emission transmission electron microscopy, fluorescence microscopy, and confocal microscopy can confirm the antibacterial activity and also supports developing a satisfactory mechanism.

2.7.1. Mechanisms of antibacterial activities of NPs

Metal oxides readily undergo redox reactions catalyzed by light radiation. This is due to their distinctive electronic configuration (such as an occupied conduction band (CB) and a vacant valence band (VB)). Semiconductor metal oxides have a specific bandgap that absorbs the characteristic wavelength of light for the generation of electron and hole pairs on the CB and VB, respectively. The produced electrons and holes have the probability of recombining in picoseconds or react with other species such as O_2 and H_2O adsorbed on the surface of the metal oxides. Through different chain redox reactions, the generated ROS ((hydroxyl radical ($OH^{\bullet}$), hydrogen peroxide (H_2O_2), and superoxide ($O_2^{\bullet -}$)) believed to degrade the bacterial cell into CO_2, H_2O, and other nontoxic minerals (Yemmireddy & Hung, 2017) (see Figure 9).

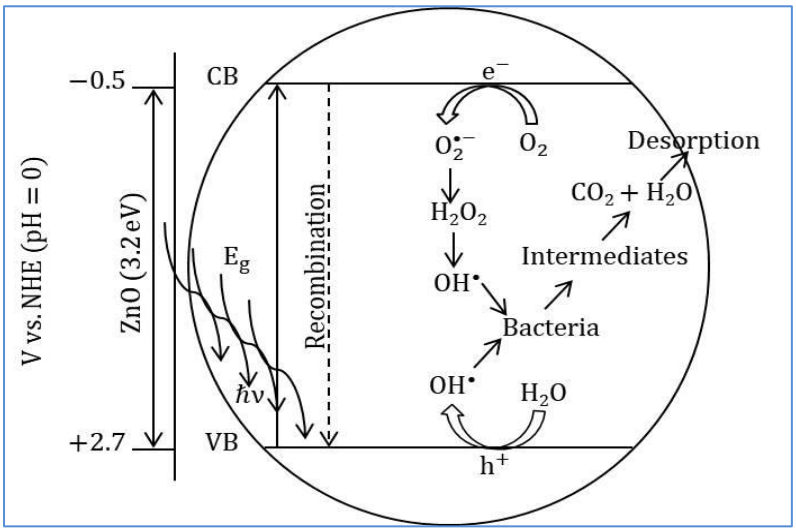

Figure 9. Schematic illustration of the ZnO photocatalytic bacterial degradation mechanism.

However, this redox reaction is dependent on the VB and CB positions of the metal oxides and redox potentials of the acceptor species. For efficient photocatalysis, the bottom of the CB must be more negative than the redox potential of H^+/H_2 (0 V compared with NHE),

and the top of the VB must be more positive than the redox potential of O_2/H_2O (1.23V compared with NHE) (Hoffmann et al., 1995; Mills & Le Hunte, 1997). From the thermodynamic requirement, the oxidation potential of $OH^{\bullet}$, ($E^0(H_2O/OH^{\bullet})$ = 2.8 V vs NHE) and the reduction potential of $O_2^{\bullet -}$ ($E^0(O_2/O_2^{\bullet -})$ = −0.28 V vs NHE) should lie with the bandgap of the catalyst. The VB and CB of some metal oxides such as TiO_2, ZnO, and ZrO_2 full fill the requirement and generate the $OH^{\bullet}$ and $O_2^{\bullet -}$ radicals on the surface of the catalyst (Vinu & Madras, 2010).

2.7.2. Antibacterial activity of single metal oxides

A. Antibacterial activities of ZnO

The in vitro antibacterial activity of NMs can be performed using different methods such as broth dilution followed by colony count, agar dilution method, disk diffusion assay, microtiter plate-based method, flow cytometry viability assays, and conductometric assay (Espitia et al., 2012). The antimicrobial activity of ZnO NPs has been tested against both Gram-positive bacteria such as *B. subtilis* and *S. aureus* and Gram-negative bacteria such as *P. aeruginosa, C. jejuni,* and *E. coli*. In addition to a thin peptidoglycan layer, Gram-negative bacteria have an outer membrane lipopolysaccharide. This layer acts as a barrier that prevents from entering negatively charged ROS (Russell, 2003). On the contrary, the cell membrane of Gram-positive has a less negative charge that allows penetration of negatively charged ROS (Gordon et al., 2011). ZnO shows good antibacterial properties on both Gram-positive and Gram-negative bacteria. Yet, the antibacterial activity of ZnO is highly dependent on crystallite size. It was reported that decreasing the particle size results in enhancing the antibacterial activity of ZnO (Premanathan et al., 2011). To indicate, Jones et al. compared the antibacterial activities of MgO, TiO_2, Al_2O_3, CuO, CeO_2, and ZnO against *S. aureus RN6390* bacteria. Among them, ZnO NPs showed significant growth inhibition. To check the effects of ZnO particle size on the antibacterial activities, differently sized ZnO materials, namely >1 μm, 8 nm, and 50-70 nm were studied. Compared to the other, the antibacterial activities of small-sized 8 nm ZnO were found to be superior (Jones et al., 2008).

For the antibacterial activities of ZnO, several mechanisms have been proposed. As seen in Figure 10, the antimicrobial activity mechanism of NPs may follow three mechanisms including the release of antimicrobial ions (Espitia et al., 2012; Kasemets et al., 2009), the interaction of NPs with microorganisms (Zhang et al., 2008), and the formation of ROS by the effect of light radiation (Jalal et al., 2010). As reported (Espitia et al., 2012), the release of antimicrobial ion/solubility of metal oxides is dependent on different factors such as the concentration of metal oxides, time of interaction, and the nature of microorganisms.

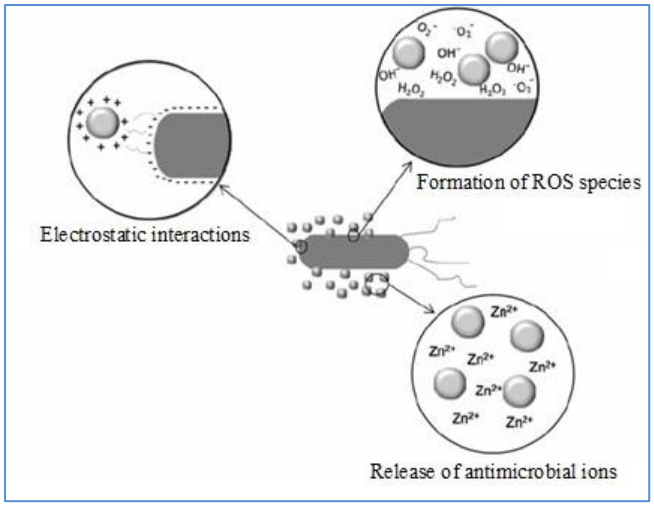

Figure 10. Different mechanisms of antimicrobial activity of ZnO NPs (represented by gray spheres) (Espitia et al., 2012).

i. The release of antimicrobial ions

(Joe et al., 2017) revealed the release of antimicrobial Zn^{2+} ions under dark conditions. The level of free Zn^{2+} ions was evaluated by Zn^{2+}-selective two-photon fluorescent turn-on probe (AZn2) microscopy. Compared to the control [Figure 11 (a and k)], the approximate mean two-photon excited fluorescence intensities of Zn^{+2} were obtained to be 12 and 6 times higher for *S. aureus* and *K. pneumoniae* bacteria, respectively. The result confirmed the source for Zn^{+2} to be from the dissolution of ZnO.

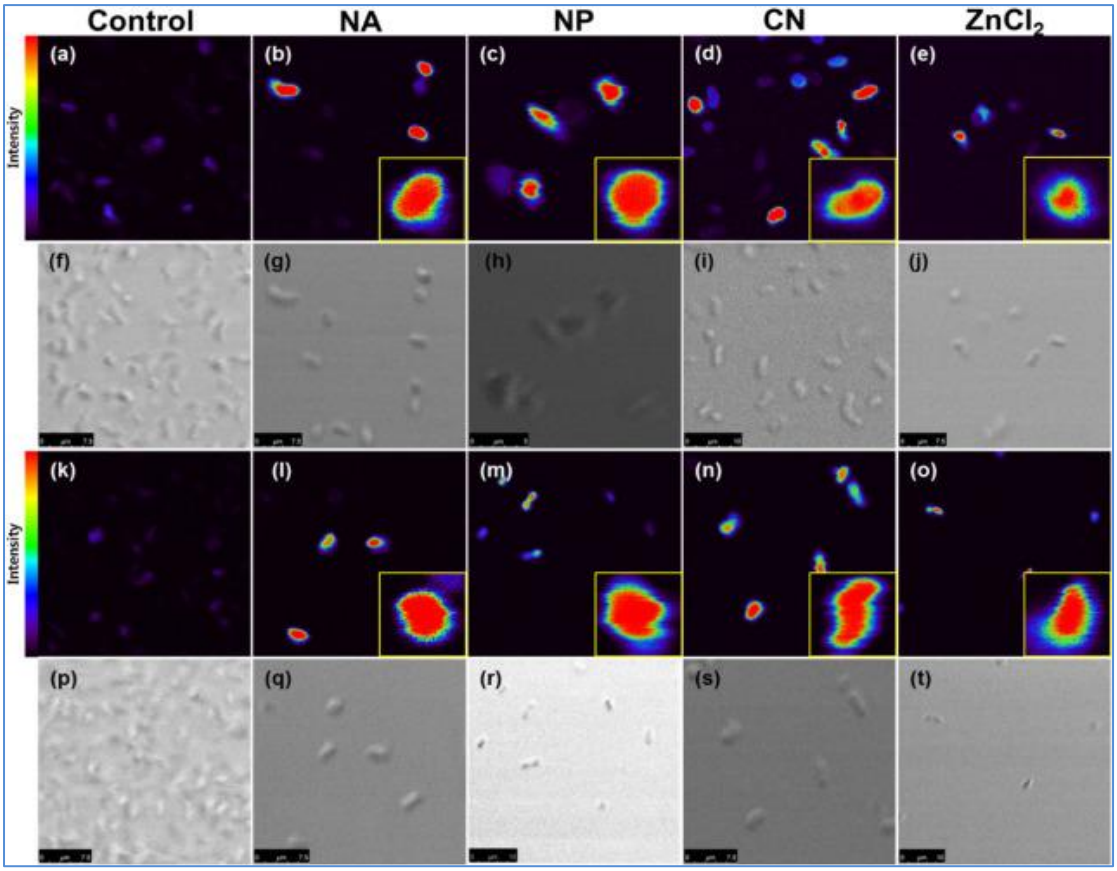

Figure 11. Two-photon fluorescence microscopy and bright-field images of AZn2-labeled (a–j) *S. aureus* and (k–f) *K. pneumoniae*. Both species were treated with ZnO NPs (NA, NP, and CN) and $ZnCl_2$ of 0.35 mM. Two-photon images were collected at 500–620 nm upon 780 nm excitation with femtosecond pulses (Joe et al., 2017).

Teichoic acid on the peptidoglycan layer of Gram-positive bacteria and lipoteichoic acid on the outer membrane of the bacteria are the source of negative charges for cell walls. This can also facilitate the attachments of the positively charged ZnO and further dissolution of it. The active and dead cells (calcein-AM (green fluorescence) and PI (red fluorescence), respectively) were confirmed by double immunofluorescence [Figure 12(a–e and k–o)]. The indirect relationship of the size of the ZnO NPs with antibacterial activity was confirmed. However, the number of oxygen defect sites on the surface of the ZnO NPs has not shown a relation with its anticlerical activities. Compared to nano-assemblies and nanoplates, the conventional ZnO NPs showed the highest antibacterial activity on both *S. aureus KCTC No. 3881* and *K. pneumonia KCTC No. 2246* bacteria. The transport of Zn^{+2} ions into the cytoplasmic inner membrane is believed to be through various membrane metalloproteins (Hood & Skaar, 2012; Lawrence et al., 1998; Da Wang et al.,

2012). The release of antimicrobial Zn^{2+} ions in the medium containing microorganisms was also suggested as a reasonable hypothesis about the toxicity of ZnO against *S. cerevisiae* (Kasemets et al., 2009).

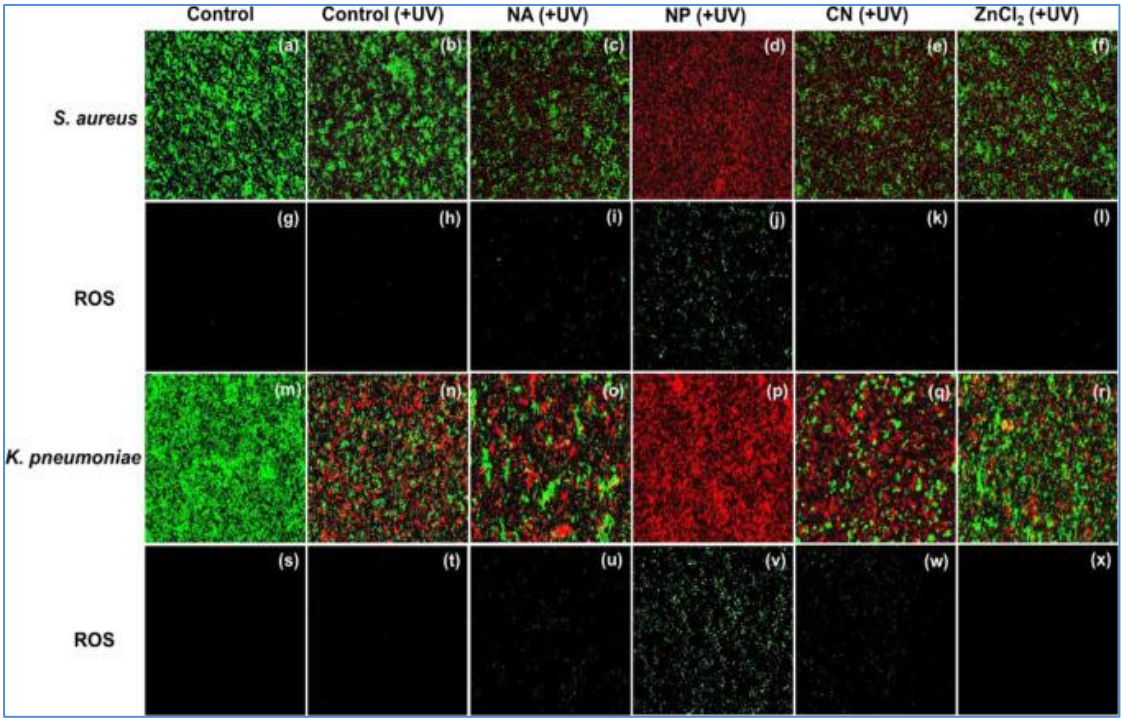

Figure 12. Dual immunofluorescence and ROS staining images for *S. aureus* (a–j) and *K. pneumoniae* (k–t) treated with nano-assemblies, NPs, conventional NPs, and $ZnCl_2$ (0.35 mM) under dark conditions (Joe et al., 2017).

ii. The direct interaction of NPs **with microorganisms**

The direct contact of ZnO NPs with the bacterial cell and production of ROS close to the bacterial membrane that causes damage to bacterial cells has also been suggested to be the other mechanism (Zhang et al., 2008). First the cell wall of the bacteria and then the oxidative damage proceeds to the inner cytoplasmic membrane and peptidoglycan layer. Affecting the respiratory activities, slow leakage of RNA and proteins, and rapid leakage of K^+ ions are believed to be the primary reason for bacterial death. The global negative charge of the bacterial cells at biological pH was occurred due to the dissociation of carboxylic groups (Stoimenov et al., 2002) and ZnO has positively charged properties at the zeta potential of +24 mV (Zhang et al., 2008). The interaction/electrostatic force that occurred between negatively charged bacterial cells and positively charged ZnO leads to disruption of the cell wall and damage occur by entering into the cell.

The ZnO nanofluid synthesized by (Zhang et al., 2007) was also reported for direct contact antibacterial activity on *E. coli DH5α* bacteria. It was synthesized by ultrasonication of the commercially obtained agglomerated ZnO powder. Increasing the concentration of ZnO NPs from 0.1 to 0.25 g/l and decreasing its particle size led to an increase in the death rate for the bacteria. The result shows considerable damage to the bacterial cell membrane after treatments. This bacterial damage due to the interaction of the bacterial cell and the NPs was further confirmed using electrochemical measurements by a model dioleoyl-phosphatidylcholine monolayer. Polyethylene glycol and polyvinylpyrrolidone were also used as effective stabilizing agents. As reported, the presence of these capping agents does not have much effect on the antibacterial activity of ZnO nanofluids.

(Thakur et al., 2019) proposed the direct and indirect mechanism for the interaction of cerium oxide NPs with the bacteria cell. As seen in Figure 13, the direct interaction of cerium oxide NPs led to damage to the cell wall and generates ROS inside. Whereas, the indirect mechanism shows the interaction of cerium oxide NPs with the bacterial environment outside the cell and generates ROS that further enters into the cell by damaging the cell wall. Both mechanisms finally led to cell death by affecting the DNA, ribosomes, and proteins of the bacteria.

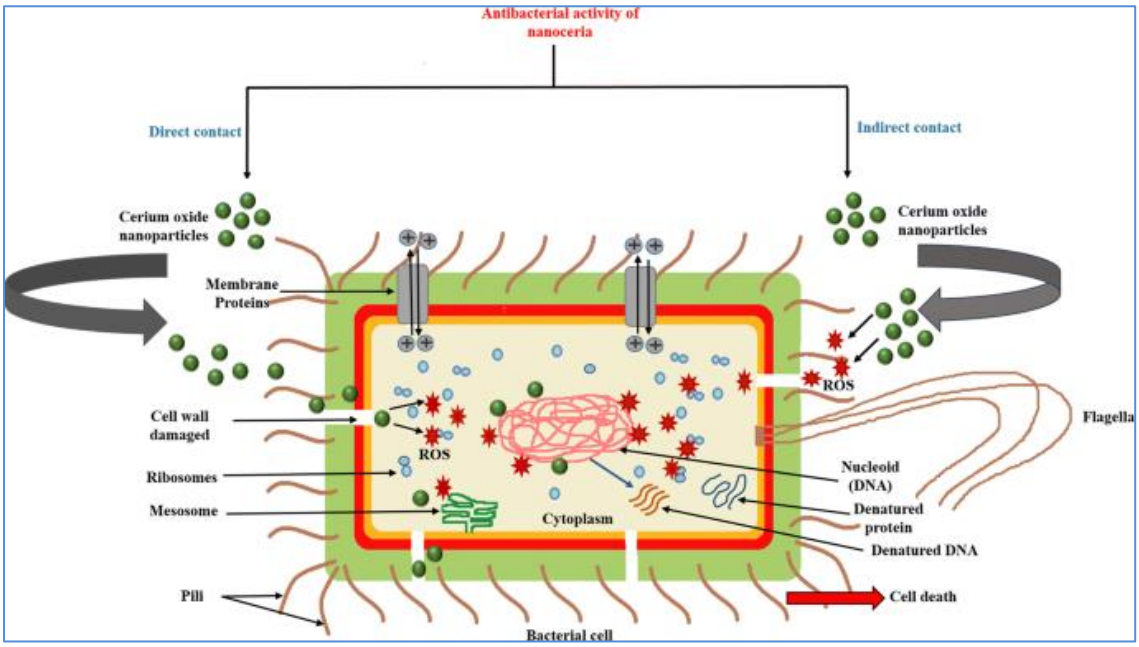

Figure 13. Antibacterial activity mechanism of cerium oxide NPs a. Direct contact, b Indirect contact (Thakur et al., 2019).

iii. The formation of ROS by the effect of light radiation

The generation of ROS by the effect of visible/UV light radiation was reported in several studies as bacteriostatic and bactericidal properties. Among the other ROS ($OH^{\bullet}$ and $O_2^{\bullet -}$), due to the negatively charged properties of the surface of the bacterial cell, only the H_2O_2 reported entering through the cell (Gordon et al., 2011; Jalal et al., 2010). The earlier work (Nagvenkar et al., 2016), confirmed the creation of ROS using ESR techniques and their effective antibacterial activity. The novel one-step sonochemical process was used to synthesize the ZnO-PVA composite. The antibacterial activity against *E. coli* and *S. aureus* was conducted using colony-forming units per milliliter method. Compared to ZnO without PVA (~80-100 nm), the ZnO NPs synthesized using PVA as a capping agent (~4-6 nm) showed enhanced antibacterial activity on both E. *coli* and *S. aureus* bacteria. This confirms the dependency of antibacterial activity on the size of the particles. Using propidium iodide fluorescent dye, the dead cells (red fluorescence) and live cells (green fluorescence) were identified by confocal laser scanning microscopic images, as seen in Figure 14. To confirm the ROS generation, the ESR measurements were also carried out using 5,5-Dimethyl-1-pyrroline N-oxide (DMPO) that give DMPO–OH the final product after trapping both $OH^{\bullet}$and $O_2^{\bullet -}$ radicals. As seen in Figure 15b, the ESR spectra show the less amount of DMPO–OH signal (*) produced from the breakdown of the DMPO–OOH adducts which comes from $O_2^{\bullet -}$ radical. Therefore, $OH^{\bullet}$ is reported to be the major contributor to ROS generation.

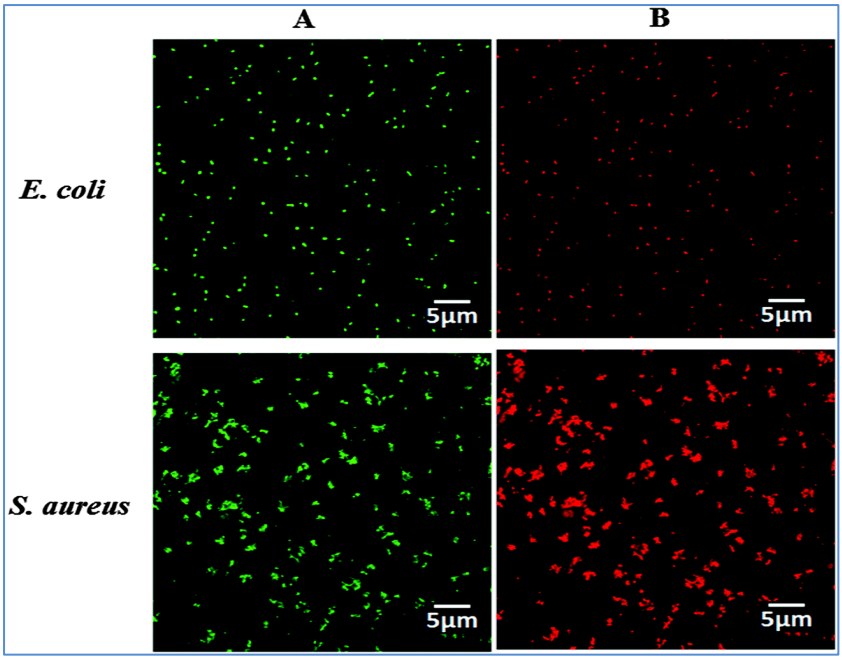

Figure 14. Fluorescence microscopy images of *E. coli* and *S. aureus* treated (A) without and (B) with ZnO–PVA NPs. Green fluorescence is characteristic of live cells, whereas red fluorescence is due to dead cells (Nagvenkar et al., 2016).

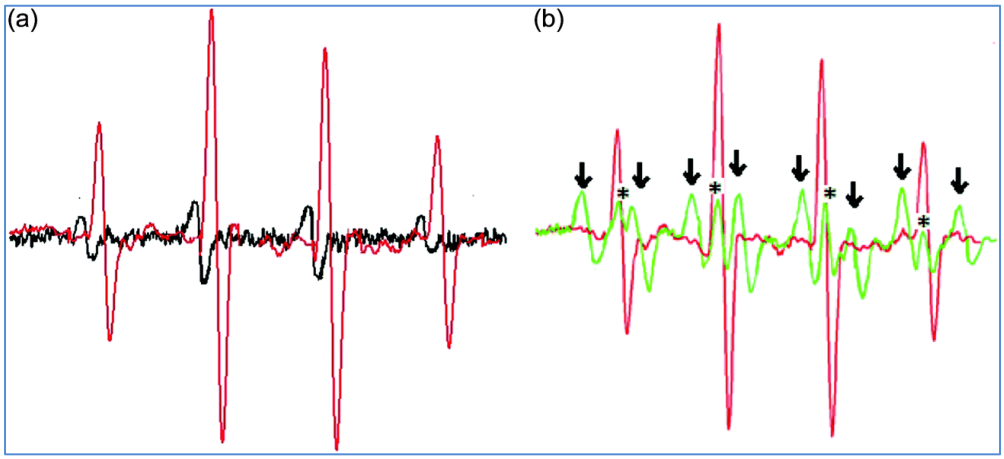

Figure 15. ESR spectra demonstrating (a) relative concentration of ROS production by pure ZnO (black line) and ZnO–PVA nanofluid (red line), (b) ROS formation by ZnO–PVA suspension (red line) upon treatment with DMSO (green line) (Nagvenkar et al., 2016).

Using di-dodecyl dimethylammonium bromide (DDAB) as a surface modifying agent, (Viswanathan et al., 2020) synthesized greatly dispersed and less aggregated ZnO NPs compared to ZnO NPs synthesized without DDAB. DDAB also improves the affinity of ZnO towards the negatively charged bacteria causing the surface more positive. Compared

to pure ZnO, surface-modified ZnO showed better antibacterial activity against both *S. aureus KCCM-11335* and *E. coli DH5α* bacteria. Due to surface charge and dispersion improvement, increasing the amount of DDAB and time of contact, the antibacterial activity also increased. The antibacterial mechanism was proposed to be due to ROS generation. The greater the surface charge, the higher the $OH^{\bullet}$ generation capacity (Arakha et al., 2015). Compared to single ZnO and cellulose, the enhanced antibacterial activity of ZnO/cellulose NC was also reported and explained to be due to the smaller crystal size of ZnO in the composite (Lefatshe et al., 2017). The agglomerated irregular disc, sheet, and dispersed ZnO on cellulose matrix SEM micrographs were observed for ZnO, cellulose, and ZnO/nano cellulose composite materials, respectively.

B. Antibacterial activities of Fe_2O_3 and Mn_2O_3

The novel antibacterial activity of Fe_2O_3 was also recently verified in different works (Haseena et al., 2020; Naz et al., 2019; Pallela et al., 2019). (Pallela et al., 2019) synthesized Fe_2O_3 with an average particle size of 16 nm. The morphological study using SEM images showed the presence of spherical nanoclusters. The d-spacing value of 0.27 nm obtained using HRTEM analysis matches with (104) crystal plane of Fe_2O_3. The antibacterial activity of Fe_2O_3 against *B. subtilis NCIM 2063, S. aureus NCIM 2079, E. coli 2065,* and *K. pneumonia NCIM 2327* bacteria was tested. Compared to the other, Fe_2O_3 shows enhanced antibacterial activity towards *B. subtilis.* However, Fe_2O_3 NPs synthesized by Naz et al. were confirmed to have less antibacterial activity against *S. aureus, P. aeruginosa, E. coli,* and *B. subitilis* bacteria (Naz et al., 2019).

In addition to ZnO and Fe_2O_3, the novel antibacterial activity of the hydrothermally synthesized α-Mn_2O_3 was also reported (Selim et al., 2020). Compared to γ-MnOOH and γ-AlOOH, α-Mn_2O_3 NRs showed greater antibacterial activity against *S. aureus ATCC23235, B. subtilis ATCC23857, E. coli ATCC25922, B. pertussis ATCC9797,* and *P. aeruginosa Pao1ATCC15692* bacteria. The approximate highest zone of inhibition (ZOI) was determined to be 18 mm on *P. aeruginosa* bacteria. The morphology of untreated and nanorod-treated microbial strains was determined using SEM analysis (Figure 16). Except for *C. Albicans*, α-Mn_2O_3 showed massive deterioration, lethal effect, and morphological changes for all other bacteria. Furthermore, the inhibition of bacterium growth was further

confirmed by fluorescence microscopy on *E. coli* (*E. coli*-GFP). The confocal microscopy confirms α-Mn_2O_3 to be the highest killing material compared to the other.

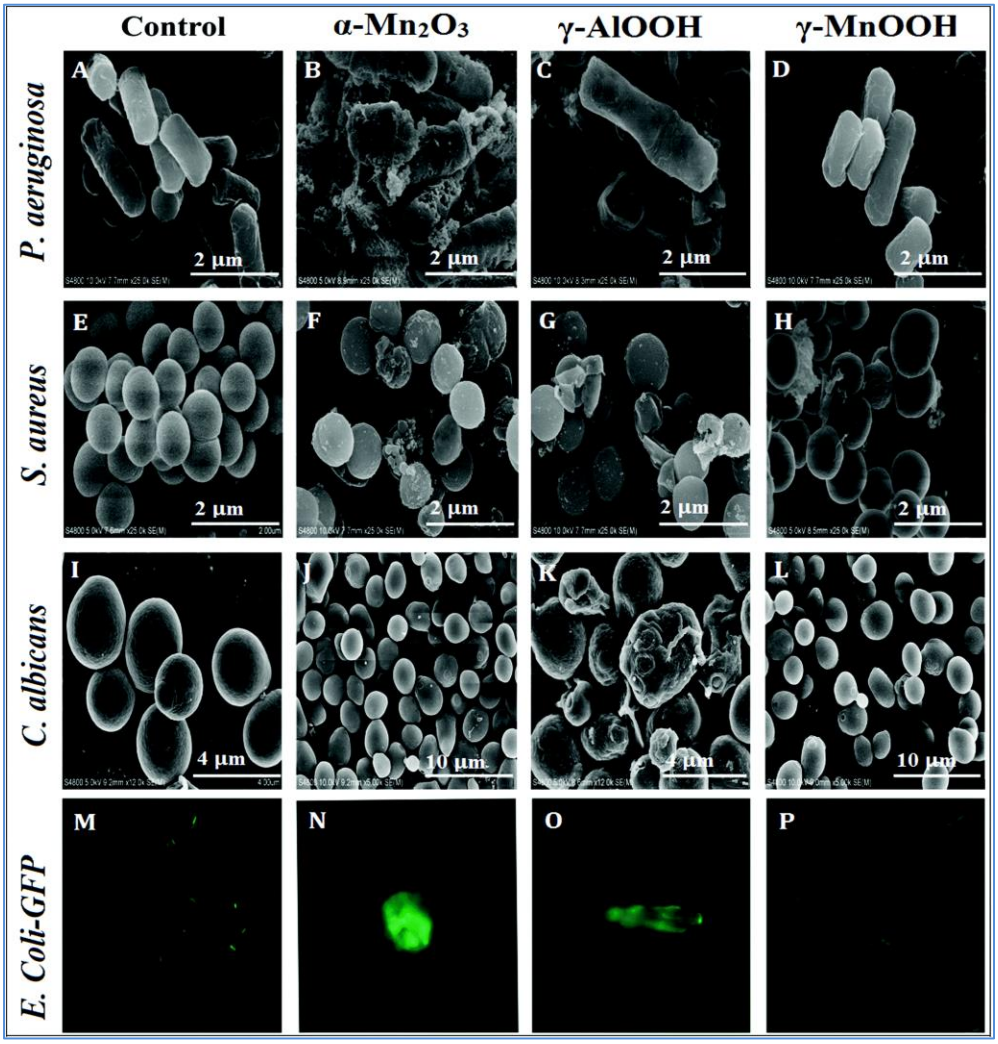

Figure 16. SEM images of untreated and treated bacterial strains using the prepared NRs; where (A−D) are for *P. aeruginosa*, (E−H) for *S. aureus*, (I−L) for *C. Albicans,* and (M−P) for *E. coli-GFP* as a control (untreated) and treated with α-Mn_2O_3, γ–AlOOH, and γ–MnOOH NRs, respectively (Selim et al., 2020).

The antibacterial activity of chemically- and green-synthesized Mn_2O_3 was also tested (Amsaveni et al., 2020). From SEM analysis, the morphology of chemically-synthesized and green-synthesized Mn_2O_3 was determined to be a crystalline cubic structure with 30–50 nm size and spherical with 20–50 nm size, respectively. The antibacterial activity test result showed good bacterial growth inhibition on *E. coli* bacteria compared to *S. aureus.* The size-dependent antibacterial mechanism was reported to be due to the release of

positively charged manganese ions and its electrostatic interaction with the negatively charged bacterial cell wall.

2.7.3. Antibacterial activity of binary and ternary ZnO based materials

Compared to single metal oxide NMs, optimizing synthesis procedure and forming a binary, ternary, or more heterojunctions can enhance the surface area to volume ratio and diminish the recombination of electron/hole pairs due to the synergistic effect. The heterojunction can be made either with the same or different bandgap metal oxides. It may either in the n–n or p–n procedure for binary metal oxides or p–n–n or n–n–n approach for ternary heterojunction (Lei et al., 2018).

(Mayank et al., 2019) synthesized α-Fe_2O_3/NiO composites using a co-precipitation method. Compared to pure α-Fe_2O_3 and NiO, the enhanced antibacterial activities of α-Fe_2O_3/NiO binary NCs were confirmed. Compared to NiO, α-Fe_2O_3 shows a greater inhibition zone. The antibacterial activity of the composite increases as the concentration of NiO increases. The results of the disc diffusion assay establish the susceptibility order of the exposed bacteria against Fe/Ni oxide composite NPs to be *E. coli* > *B. subtilis* > *S. aureus* > *S. typhi*. The ZnO-CuO composites materials synthesized by solution combustion techniques using *colotropis gigantea* leaf extract also showed good antibacterial activity against *E. coli* and *S. aureus* bacteria. The synthesized spherical and hexagonal-shaped NMs have a particle size of 10 - 40 nm (Rajith Kumar et al., 2020). Using *Ricinus communis L.* plant seedless fruit extract as a green synthesis procedure Panchal et al. also synthesized a granular nanoflakes morphology of MgO clusters, irregular morphology of ZnO, and granular nanoflakes shaped MgO/ZnO NC materials (Panchal et al., 2019). The antibacterial activity conducted on *E.coli* and *Klebsiella* photogenic bacteria show enhanced ZOI for the MgO/ZnO NC compared to single MgO and ZnO. The obtained highest ZOI on *E. coli* bacteria was 28 mm.

(Shimada et al., 2020) reported a new mechanical rupture-based antibacterial active ZnO/SiO_2 binary material that was safe regarding toxicity for normal cells. The ZnO/SiO_2 nanowire was synthesized by bottom-up approaches. Based on the silicon oxides (SiOx)-based surface, the antibacterial activity of SiO_2 film substrate and ZnO/SiO_2 nanowire was evaluated against bare glass substrate (equation 47). The result showed superior

antibacterial activity value for ZnO/SiO_2 nanowire substrate compared to SiO_2 film substrate against *E. coli* bacteria. From fluorescence images using propidium iodide test ZnO nanowire showed high cytotoxicity due to zinc ions, while ZnO/SiO_2 nanowire showed less cytotoxicity. This cell viability on ZnO/SiO_2 nanowire is reported to be due to zinc ions elution suppression by the SiO_2 shell layer.

$$R = \left\{\log\left(\frac{B}{A}\right) - \log\left(\frac{C}{A}\right)\right\} = \log\left(\frac{B}{C}\right) \quad 47$$

A, B and C are the average counts of colonies formed on the agar medium just after incubation, after culturing on a bare glass substrate for 24 h, and after culturing on SiO_2 film substrate or ZnO/SiO_2 nanowire substrate for 24 h, respectively.

The $nZnO/TiO_2$ coated on the Ti substrate was synthesized by hydrothermal followed by a low-temperature liquid phase method with different temperate (50, 70, and 90 °C) (Pang et al., 2019). From SEM analysis the shape of the composites was obtained to be rhombic prismatic and aligned in nanoarray. Increasing temperature from 50 – 90 °C results in increased particle size from 50 – 90 nm. Compared to *E. coli*, the size-dependent antibacterial activity of the composites is greater for *S. aureus*. Precious Ayanwale and Reyes-López synthesized 26 - 34 nm-sized ZrO_2–ZnO NPs for deactivation of *B. subtilis ATCC 19163, S. aureus ATCC 25923, S. mutans ATCC 25175, E. coli ATCC 25922, K. oxytoca 13182,* and *P. aeruginosa ATCC 27853* bacteria (Precious Ayanwale & Reyes-López, 2019). Among different percentages of the composites and single metal oxides, ZnO showed a greater ZOI. The effects of the weight ratio of the metal oxides were also indicated in (Gordon et al., 2011) study. Different [Zn]/[Fe] weight ratio of 1:9, 3:7, 1:1, 8:2, and 9:1 was prepared for the formation of a mixture of Fe^{2+} and Zn^{2+}. From TEM/HRTEM morphology, the FCC structure of Fe_3O_4 and $ZnFe_2O_4$ was confirmed to have the same d-spacing value of 0.298 nm. The result indicates the higher the weight ratio of zinc the higher the antibacterial activity. However, increasing the amount of Fe ratio shows decreasing the antibacterial activity; this is reported to be due to the formation of zinc ferrite ($ZnFe_2O_4$) that has no significant antibacterial activity.

In addition to binary metal oxide composites, due to continuous charge transfer synergy, the ternary heterojunction show enhanced antibacterial activity. Anaya-Esparza et al.

synthesized TiO_2-ZnO-MgO NMs by the sol-gel techniques (Anaya-Esparza et al., 2019). Using SEM analysis, the materials were confirmed to have less than or equal to 100 nm-sized semi-globular-ovoid shapes. The antibacterial activity of the composites against *E. coli ATCC 8739, S. paratyphi ATCC 9150, S. aureus ATCC 33862,* and *L. monocytogenes ATCC 15313* bacteria shows good results. Compared to the composite, TiO_2 showed poor antibacterial activity on all bacteria (only 5–9 mm inhibition zone). The highest ZOI obtained on *S. paratyphi* bacteria is 18 mm. The ROS generation and electrostatic force interaction were suggested to be the probable antibacterial mechanism that led to bacterial death.

Munawar et al. synthesized ZnO-Yb_2O_3–Pr_2O_3 ternary NC that showed a highly enhanced antibacterial activity (31 mm) on the *S. aureus* bacteria (Munawar, Yasmeen, Hasan, et al., 2020). The ternary ZnO-Pr_2O_2–Yb_2O_3 NC that was synthesized using a co-precipitation technique has porous morphology. The high surface area and porous nature of the material were reported to have good contact with the bacteria. Moreover, the dual-Z-scheme ZnO-Er_2O_3-Yb_2O_3 material synthesized using co-precipitation techniques was also reported to be highly effective on *S. aureus* bacteria (Munawar, Yasmeen, Hussain, et al., 2020). Kaur et al. synthesized ZnO plates/Fe_2O_3 rods/Ag NPs composites for the antibacterial activity of *E. coli* bacteria (Kaur et al., 2019). The antibacterial activity of the Ag/Fe_2O_3/ZnO heterostructures studied at different visible light exposure times (30, 60, and 120 min) presented good results. An increase in the concentrations of Ag/Fe_2O_3/ZnO NC from 0 to 2000 µg/mL, results in decreasing the concentration of *E. coli*. The generation of ROS was suggested to be the mechanism of bacterial deactivation. The TEM image analysis was used to realize antibacterial interactions with Ag/Fe_2O_3/ZnO NC.

Paul et al. synthesized a spherical ternary CuO-NiO-ZnO NC for antibacterial test against *S. aureus* and *E. coli* bacteria (Paul et al., 2020). The obtained result from growth curve analysis and colony-forming unit reduction study showed promising antibacterial activity, specifically an enhanced number of colony counts of bacterial strains reduction on *S. aureus* bacteria. FESEM analysis result also shows the effect of CuO-NiO-ZnO NC that causes rupturing, cracking, and release of intracellular components.

Owonubi et al. investigated the antibacterial activity of CuO, Fe_2O_3 (FeO), ZnO, ZnO/CuO-FeO_x and ZnO-CuOFeO_x materials (x = 0.1, 0.5 g). The antibacterial activity

test was conducted against three different bacterial strains. Among them, the synthesized material was more effective on *S.pneumoniae* bacteria. The order of antibacterial activity test were determined to be CuO > $ZnOFeO_{0.5}CuO_{0.5}$ > $CuOFeO_{0.5}$ > $ZnOFeO_{0.1}CuO_{0.1}$ > Fe_2O_3 > $ZnOFeO_{0.5}$ > ZnO (Owonubi et al., 2020). This indicates that the coupling of more metal oxides enhances the inhibition of the bacteria. A brief data on the antibacterial activities of ZnO-based composites have been presented in Table 7.

Table 6. A set of parameters obtained for antibacterial activities of ZnO-based composites and different optimization.

Methods	Bacteria's	Precursors used		Morphological analysis	highest ZI (mm)	Ref.
		Zn	Other	SEM/TEM/HRTEM/SAED		
Co-precipitation	E. coli, B. subtilis, S. aureus, S. typhi.	-	$FeSO_4.7H_2O$ and $(NiNO_3)_2.6H_2O$)	Crystalline 0.25 [110] α-Fe_2O_3 and 0.207 [200] NiO	25 on *E. coli*	(Mayank et al., 2019)
Green and combustion	E. coli NCIM-5022 and S. aureus NCIM-505	$Zn(NO_3)_2.6H_2O$	$Cu(NO_3)_2.3H_2O$ Calotropis gigantea	10–40 nm sized spherical and hexagonal irregular shapes	9 on *E. coli*	(Rajith Kumar et al., 2020)
Hydrothermal bottom-up approaches	E. coli DH5α	$Zn(AC)_2.2H_2O$	Tris(dimethylamino)silane	71.7 nm sized ZnO/SiO2 nanowires	-	(Shimada et al., 2020)
Hydrothermal and low temperature liquid phase	S. aureus (ATCC 25923) and E. coli (ATCC 25922)	$Zn(NO_3)_2.6H_2O$	Tetrabutyl titanate and Ti (TA_2, China)	50 – 90 nm sized nanoarray aligned rhombic prismatic shape	-	(Pang et al., 2019)
Sol−gel	B. subtilis, S. aureus S. mutans, E. coli, K. oxytoca, P. aeruginosa	$[Zn(NO_3)_2$	$Zr(C_4H_9O)_4$	Cluster of amorphous particles	~ 7 on B. subtilis	(Precious Ayanwale & Reyes-López, 2019)
Sol-gel	E. coli ATCC 8739 , S. paratyphi ATCC 9150, S. aureus ATCC 33862 , and L. monocytogenes ATCC 15313	$Zn(NO_3)_2.6H_2O$	Titanium-(IV) butoxide, and magnesium di-tert-butoxide	~100 nm sized semi globular-ovoid shape	18 on S. paratyphi	(Anaya-Esparza et al., 2019)
Green	E. coli, Klebsiella	$Zn(NO_3)_2.6H_2O$	$Mg(NO_3)_2.6H_2O$ and Ricinus communis L.	Granular nanoflakes	28 mm on E. coli	(Panchal et al., 2019)
Co-precipitation technique	E. coli and S. aureus	$Zn(NO_3)_2.6H_2O$	$Yb(NO_3)_3.6H_2O$ and $Pr(NO_3)_3.6H_2O$	Highly agglomerated porous materials	31 on S. aureus	(Munawar, Yasmeen, Hasan, et al., 2020)
Co-precipitation	S. aureus and E. coli	$Zn(NO_3)_2.6H_2O$	$Er(NO_3)_3.6H_2O$ and $Yb(NO_3)_3.6H_2O$	Loosely packed porous morphology	*21 on* E. coli	(Munawar, Yasmeen, Hussain, et al., 2020)
Precipitation	E. coli	$Zn(AC)_2.2H_2O$	$Fe(NO_3)_3.9H_2O$	ZnO nanoplates/α-Fe_2O_3 nanorods/Ag NPs heterostructure	-	(Kaur et al., 2019)
Co-precipitation	E. coli and S. aureus	$Zn(NO_3)_2{\cdot}6H_2O$	$Cu(NO_3)_2{\cdot}3H_2O$ and $Ni(NO_3)_2{\cdot}6H_2O$	Agglomerated spherical NPs	-	(Paul et al., 2020)
One-pot low-	E. coli (ATCC 25922), A.	$Zn(NO_3)_2.6H_2O$	$NiSO_4.6H_2O$	2.0 to 3.0 μm in length with	24 on E.	(Naskar et al.,

temperature solution	baumannii (ATCC 19606), S. aureus (ATCC 25923), S. epidermidis (ATCC 12228),			150 to 200 nm in diameters nanoroads	coli	2020)
Co-precipitation	E. coli, S. aureus, B. cereus, and K. pneumoniae	$Zn(NO_3)_2.6H_2O$	$Ni(NO_3)_2.6H_2O$	Nanorods are decorated by NPs	27 on B. cereus	(Thambidurai et al., 2020)
Two-step solution-based technique	*S. aureus*	$Zn(AC)_2.2H_2O$	Sodium selenite	ZnO cross bridged Se heterojunction composite	*5 cm on S. aureus*	(Ahmad et al., 2020)
Sonochemical	E. coli or P. aeruginosa, S. aureus, and B. subtilis	$Zn(NO_3)_2.6H_2O$	AgNO3 and CTMAB	2 μm sized ZnO Nanoflowers and Ag-NPs decorated ZnO		(Ray et al., 2019)
Electrospinning technique	S. aureus and E. coli	$Zn(NO_3)_2.6H_2O$	$FeCl_3$	Optimizing the homogenous loading of Fe-doped ZnO on PVA	19 on S. aureus	(Sekar et al., 2019)
Green	*E. coli* (ATCC 25922), *P. aeruginosa* (ATCC 27853), B. *subtilis* (ATCC 6633), and S. *aureus* (ATCC 25923).	$Zn(NO_3)_2.6H_2O$	$Mn(AC)_2{\cdot}4H_2O$ *Melastoma malabathricum* (*L.*)	Agglomerated spherical NPs	15 on *B. subtilis*	(Khan et al., 2020)
sol-gel	E. coli (CCTCC AB 204033) and S. aureus (ATCC 25923)	$Zn(NO_3)_2.6H_2O$	$Er(NO_3)_3{\cdot}5H_2O$ and sodium silicate	Porous with an irregular shape	-	(Yang et al., 2020)
Aqueous microwave	E. coli and S. aureus	$Zn(AC)_2.2H_2O$	Mg alloy	Crack filled morphology after UV-irradiation	-	(Sun et al., 2020)
Electro-deposition	S. aureus (MRSA252; ATCC)	$Zn(NO_3)_2.6H_2O$	TiO_2 nanotubes	~4 μm length and ~50 nm diameter TiO_2 nanotubes	-	(Yao et al., 2018)
self-assembly	*E. coli*	$Zn(AC)_2.2H_2O$	Oleylamine	3 μm sized spherical cluster	-	

AC: acetate; S_{BET}: Specific surface area (m^2/g), $p_{V:}$ pore volume (cm^3/g), P_d: pore diameter (nm); d: d-spacing (nm); p: crystal plane; ZI(mm): zone of inhibition in millimeter.

2.7.4. Effects of different conditions on the antibacterial activity

For enhanced antibacterial activities of metal oxide NMs, optimizing different parameters such as size of the NMs, concentration/dosage, temperature, capping agent, and reducing agent ought to be taken into consideration. To indicate, due to the large surface area and surface energy properties of metal oxides, aggregation/agglomeration occurs. These aggregation/agglomeration properties lead to the reduction of the generated radioactive oxygen species and hydroxyl radicals. This is due to the e^- and h^+ quenching with the neighboring aggregate. To avoid this problem, capping of the NPs with a polymer matrix that acts as a structure-directing agent through forming a non-covalent or/and a covalent bond was reported to be an effective way (Jassby et al., 2012; Wu & Wu, 2015).

(Yamamoto, 2001) studied the effect of ZnO particle size on the antibacterial activity of *S. aureus* (9779) and *E. coli* (745) bacteria cultured in the Brain Heat Infusion medium. The different particle sizes of ZnO namely 0.1, 0.2, 0.3, 0.5, and 0.8 μm were synthesized by heating the reagent grade ZnO powder at 1400 °C and the planetary ball milling process. The antibacterial test of the ZnO powder was conducted by changing the electrical conductivity with bacterial growth. It was found that as the particle size decreases, the antibacterial activity increases. The role of ZnO size on the antibacterial activity of *E. coli W3110* and *S. aureus ATCC 25923* bacteria was also studied (Nair et al., 2009). From the SEM morphological analysis, the uniform spherical morphology of ZnO was obtained using polyethylene glycol and the rod-shaped structure using starch as a capping agent. By varying the concentration of NaOH, different sizes of the ZnO NPs (40 nm to 1.2 μm) were synthesized. The result indicates the antibacterial activity of ZnO increases as the particle size decrease from micro to the nano range.

The effects of pH and annealing temperature on the particle size of ZnO during synthesis were effectively studied (Doan Thi et al., 2020). The ZnO NPs that are used to test the antibacterial activity against *S. aureus* and *E. coli* are synthesized using orange fruit peel extract. The clear spherical-like shape with 10-20 nm-sized ZnO NPs was synthesized at a pH value of 6. The XRD pattern and FTIR spectra of as-prepared and different temperature calcined materials are depicted in Figure 17.

The XRD pattern and TEM image (Figure 18) analysis result indicate that increasing the annealing temperature results in increasing the intensity of the diffraction peaks and increasing the crystalline size from 22 nm at 300 °C to 95 nm at 900 °C. This is reported (Tong et al., 2015) to be due to the reorienting and reducing the number of defects in grain boundaries. At higher annealing temperatures, the intensity of these peaks gradually decreased. Furthermore, with increasing annealing temperature, the intensity of the Zn–O absorption peak increased and the peak shifted to lower wavenumbers (higher energies). This can be explained by the improvement of the crystalline structure of the ZnO NPs with increasing annealing temperatures indicated by the XRD results. The dependency of the antibacterial activity on the pH value was also observed. An increase in pH from 4 to 10 results in enhancing the antibacterial activity of ZnO. This is reported to be due to the ability of a generation of more ROS as pH increases during the synthesis of ZnO NPs. Compared to *S. aureus*, the antibacterial activity against *E. coli* bacteria was obtained to be greater. The great effects of pH on the size and antibacterial activity of ZnO NPs were also reported (Padalia et al., 2017).

The effects of temperature on the size and morphology of ZnO synthesized by pineapple peel extract and its antibacterial activity were also reported (Hassan Basri et al., 2020). When the temperature increased from 28 to 60 °C, the size of the ZnO NPs also increased from 8–45 nm to 73–123 nm. FESEM analysis shows a mixture of spherical rod- or flower- rod-shaped structures of ZnO heated at 28 to 60 °C, respectively. Furthermore, increasing the temperature results in increasing the agglomeration of NPs. Compared to *Salmonella enterica serovar Choleraesuis* Gram-negative bacteria, ZnO-starch material showed enhanced antibacterial activity on *B. subtilis UPMC1175* Gram-positive bacteria. This is reported to be due to the greater thickness of the cell wall of Gram-negative bacteria that prevents penetration of ZnO into the cell. As the annealing temperature reduced, the size of the material reduced. This results in the improvement of the antibacterial activity of the material. (Mohammadi Arvanag et al., 2019) also synthesized ZnO/extract (particle size ~ 19 nm) using Silybum marianum L seed and ZnO (particle size ~ 22 nm) NPs using a chemical method for antibacterial activity of *E. coli ATCC 25922*. The experiment was conducted in Muller-Hinton broth media in a concentration range of 0.8 - 0.05 mg mL^{-1}. Both ZnO/extract and ZnO NPs have the potential on preventing the survival of the *E. coli* bacteria as well as completely killing them.

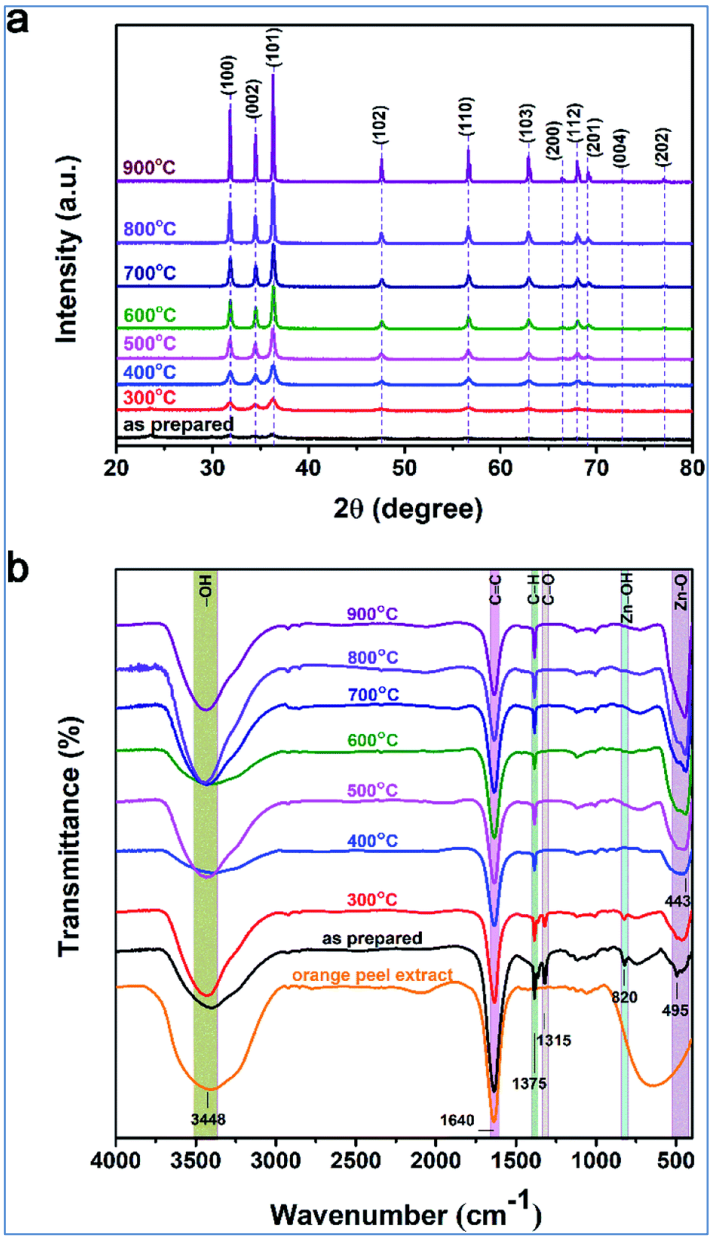

Figure 17. The X-ray diffraction pattern of synthesized ZnO NPs annealed at temperatures of 300–900 °C (Doan Thi et al., 2020).

Different concentrations of ZnO NPs incorporated in poly (3-hydroxybutyrate-co-3- hydroxy valerate) (PHBV)/polyethylene oxide (PEO) microfibers were synthesized through the electrospinning technique (Mahamuni-Badiger et al., 2020). From the toxicological and biocompatibility point of view of the polymers as active wound dressing materials, the antibacterial activities of PHBV-PEO-ZnO microfibers against *S. aureus NCIM 2654* and *P. aeruginosa NCIM 5032* bacteria were investigated. Compared to the control PHBV-PEO, the

antibacterial activities of PHBV-PEO-ZnO showed greater ZOI. The tensile strength of the microfiber increases with an increase in the ZnO amount.

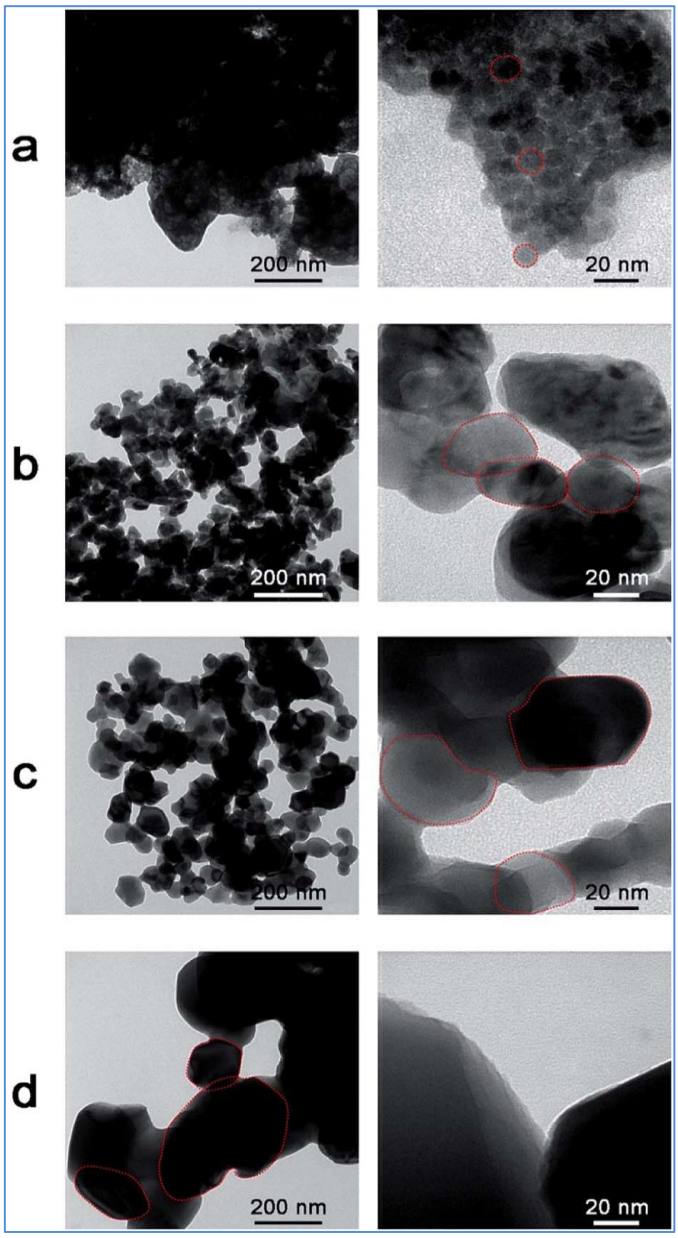

Figure 18. TEM images of ZnO NPs with different annealing temperatures. (a) as-prepared sample and (b - d) annealed at 400, 700, and 900 °C, respectively (Doan Thi et al., 2020).

The uniqueness of a capping agent towards surface area and antibacterial activity was further confirmed in (Gutha et al., 2017) study. Compared to single chitosan (CS) and poly(vinyl alcohol) (PVA), the enhanced antibacterial and wound healing properties of chitosan/poly(vinyl alcohol)/zinc oxide (CS/PVA/ZnO) beads was found. The 2θ values of separate CS and ZnO, as well as, CS/PVA and CS/PVA/ZnO composites, were precisely

confirmed on the XRD pattern. The smooth, nanoflake, and porous morphology for chitosan, ZnO, and CS/PVA/ZnO, respectively, were observed on SEM images. The uniformly distributed ZnO nanorods on the surface of chitosan/poly(vinyl alcohol) were also clearly observed on the TEM image. The highest antibacterial activity on *S. aureus ATCC 29523* bacteria was obtained to be 20 mm on CS/PVA/ZnO material. The effect of various capping agents such as ethylene glycol, gelatin, polyvinyl alcohol, and polyvinylpyrrolidone on the antibacterial activity of ZnO NPs was studied by (Akhil et al., 2016). The polydispersed states of ZnO NPs on the capping agent and its hexagonal shape were characterized by FESEM and FETEM. On the contrary, the antibacterial test conducted on *S. aureus MTCC 3160* and *P. aeruginosa MTCC 1688* bacteria show enhanced action for ZnO NPs without a capping agent.

Using citrus lemon extract in a green synthetic approach, (Prasad et al., 2020) synthesized 11 nm-sized spherical ZnO NPs. Agar well diffusion assay and broth microdilution assay-MIC and MBC were used for antibacterial activity of ZnO NPs against *K. pneumonia MTCC3384, S. aureus MTCC87, E.coli MTCC41,* and *P. mirabilis* bacteria. As the amount of ZnO NPs dosage/concentration increases, the ZOI also increases. Compared to the other, ZnO NPs showed enhanced antibacterial activity on *P. mirabilis* bacteria.

The direct contact to the surface of cell walls and entering of the ZnO into the bacterial cells (*E. coli, K. pneumoniae, S. Typhimurium,* and *S. aureus*) by breaking the membrane was shown on the Bio-TEM images analysis (Wahab et al., 2020). The peanut-shaped antibacterial active ZnO nanostructures material was synthesized via a chemical process from a zinc nitrate precursor. Based on their morphological interpretations, cellular cytoplasm leakage and H_2O_2 generation are proposed to be the sources for inhibition in the microbial cell membrane. However, bigger particles are not very uniform and have not shown any effective antibacterial action against the tested pathogens. The structure of the nanomaterial was confirmed from the lattice fringes result obtained using HRTEM analysis. The d-spacing value of ~0.526 nm was obtained to be consistent with the wurtzite phase ZnO that develops in the c-axis of [0001]. Further crystallinity and consistency with the HRTEM image and XRD pattern were confirmed by the selected area electron diffraction (SEAD) pattern. The NPs size and pH of the solution dependency on the antibacterial activity were also indicated. Compared to acidic pH, ZnO NPs synthesized at alkaline pH were obtained to have good antibacterial activity.

Using peels of pomegranate (*Punica granatum*) the hexagonal bottom-neck structured of ZnO nano pencils was synthesized for antibacterial study (Kaviya et al., 2017). During the synthesis, different concentrations of $Zn(NO_3)_2.6H_2O$ precursor (2, 3, and 4 g which is coded as ZnO-2, ZnO-3, and ZnO-4, respectively) and 1.5 mL of peel extract were used. The optimum morphology was obtained on a 3 g precursor to 1.5 mL peel extract ratio. Increasing the precursor amount to 4 g led to the aggregation of the ZnO NPs. The crystallinity of the material was confirmed by the selected area electron diffraction pattern (SAED). The obtained highest ZOI on *S. aureus* bacteria was 21 mm. The synthesized spherical ZnO nanocrystals immobilized onto silicon wafers by self-assembly techniques were informed as antibacterial deactivating materials under dual UV irradiation (Jin et al., 2019). Compared to dual UV irradiation without ZnO, the dual UV irradiation in the presence of ZnO NP's showed good *E. coli* bacterial deactivation within 30 seconds. Furthermore, the spherical ZnO nanocrystals immobilized onto silicon wafers showed enhanced bacterial deactivation within 10 seconds. The ROS generation was proposed to be the major disinfection mechanism against *E. coli.*

The size-dependent antibacterial activity of ZnO NPs synthesized by taking a different amount of *Mar Ivanios* leaf extract (10, 20, and 50 ml) was also studied (Rufus et al., 2017). As the amount of the leaf extract increases the particle size decreases. The smaller the particle size, the higher the antibacterial activity. The concentration-dependent antibacterial activity of ZnO NPs against *E. coli* and *S. aureus* bacteria shows a good ZOI. As the concentration of the ZnO NPs increase from 25 - 100 μg/μL the antibacterial activity also increases. The synthesized smaller particle-sized ZnO (29 nm) at 100 μg/μL showed 17 and 18 mm ZOI on *E. coli* and *S. aureus* bacteria, respectively. Using solution combustion techniques, (Saif et al., 2019) also synthesized ZnO NPs using different percentages of *Cordia myxa* leave extract. The disk diffusion antibacterial test of the synthesized ZnO NPs against *S. aureus* and *E. coli* bacteria showed enhanced activity. Brief information on the antibacterial activities of single zinc, iron, and manganese oxides was presented in Table 6.

Table 7. A set of parameters obtained for antibacterial activities of single zinc, iron, and manganese oxides.

Method	Bacteria's used	Precursors used		Morphological analysis	highest ZI (mm)	Ref.
		Zn	Other	SEM/TEM/HRTEM/SAED		
Hydrothermal and calcination	*S. aureus* ATCC23235, *B. subtilis* ATCC23857, *E. coli* ATCC25922, *B. pertussis* ATCC9797, *P.s aeruginosa* Pao1ATCC15692	-	$KMnO_4$, $AlCl_3.6H_2O$, and sodium dodecyl benzene sulfonates	20 nm mean diameter NRs	18 mm on *P. aeruginosa*	(Selim et al., 2020)
Green and precipitation	E. coli (ATCC 25922) and S. aureus	-	$Mn(AC)_2{\cdot}4H_2O$ CTMAB and tea extract	Crystalline spherical and cubes NPs with 20–50 nm size	-	(Amsaveni et al., 2020)
One-step sonochemical	S. aureus and E. coli	$Zn(AC)_2.2H_2O$	-	Dull appearance of PVA polymer with dispersed 4-6 nm ZnO NPs	-	(Nagvenkar et al., 2016)
Soft-solution	S. aureus(KCTC No. 3881) and K. pneumoniae(KCTC No. 2246)	$Zn(AC)_2.2H_2O$	-	ZnO NPs (0001): 60 nm x 10 nm spherical ZnO NAs: 10 nm conventional NPS: 30 nm	-	(Joe et al., 2017)
Ultrasonication and milling	E. coli (DH5α)	Commercial ZnO	-	ZnO nanofluid		(Zhang et al., 2008)
Nucleation-controlled growth	E. coli and S. aureus	$ZnCl_2$	$FeCl_2{\cdot}4H_2O$	Cubic FCC structure		(Gordon et al., 2011)
-	E. coli (DH5α)	Commercial ZnO	Polyethylene Glycol and Polyvinylpyrolidone	ZnO nanofluid		(Zhang et al., 2007)
-	S. aureus KCCM-11335 and E. coli – DH5α	ZnO NPs	Didodecyldimethyl-ammoniumbromide	Flake-like	E. coli > S. aureus and	(Viswanathan et al., 2020)
In-situ solution casting	E. coli and S. aureus	$Zn(NO_3)_2.6H_2O$	oil palm empty fruit bunches	ZnO dispersed on cellulose matrix		(Lefatshe et al., 2017)
Green method	*B subtilis (NCIM 2063), S. aureus (NCIM 2079), E. coli (2065), K. pneumonia (NCIM 2327)*	-	$Fe(NO_3)_3.9H_2O$	16 nm-sized spherical Fe_2O_3 with 0.27 nm d value with (104) planes	*16 on B. subtilis*	(Pallela et al., 2019)
Green	S. aureus, P. aeruginosa, E. coli and Bacillus subitilis	-	$FeCl_3$ and Rhus punjabensis	~48 nm sized spherical NPs	10 on P. aeruginosa	(Naz et al., 2019)
Green	S. aureus and E. coli	$Zn(NO_3)_2.6H_2O$	Orange fruit peel	Spherical particles that increases as increasing the annealing temperature	E. coli > S. aureus	(Doan Thi et al., 2020)

Casting	B. subtilis UPMC1175 and Salmonella enterica serovar Choleraesuis	$Zn(NO_3)_2.6H_2O$	Starch	Spherical and rod-shaped structure	15 on *B. subtilis*	(Hassan Basri et al., 2020)
Green and chemical method	*E. coli* ATCC (25922)	$Zn(NO_3)_2.6H_2O$	-	spherical crystalline NPs	-	(Mohammadi Arvanag et al., 2019)
Electrospinning	*S. aureus* (NCIM 2654) and P. *aeruginosa* (NCIM 5032)	$Zn(AC)_2.2H_2O$	Poly (3-hydroxybutyrate-co-3-hydroxyvalerate) and polyethylene oxide	2.04-2.2 μm diameter ZnO reinforced microfibers	2.2-3.1 μm rod	(Mahamuni-Badiger et al., 2020; Mahamuni et al., 2019)
Hydrothermal method	S. aureus (ATCC strain 29523) and E. coli (ATCC strain 29522)	$Zn(AC)_2.2H_2O$	Chitosan and PVA	uniformly distributed ZnO on the surface of the CS/PVA polymer	20 on S. aureus	(Gutha et al., 2017)
Co-precipitation	S. aureus and P. aeruginosa	ZnSO4	Ethylene glycol, gelatin, polyvinyl alcohol, and polyvinylpyrrolidone	ZnO NPs dispersed on capping agent and its hexagonal shape	-	(Akhil et al., 2016)
Green synthetic strategy	*K. pneumoniae (*MTCC3384), *S. aureus (*MTCC87), *E. coli (*MTCC41), *P. mirabilis*	$Zn(AC)_2.2H_2O$	-	11 nm sized semi-crystalline ZnO with 0.19 nm d-spacing value,	18 on *P. mirabilis*	(Prasad et al., 2020)
Chemical process	E. coli, K. pneumoniae, S.Typhimurium, S. aureus	$Zn(NO_3)_2.6H_2O$	-	~0.526 in the c-axis [0001] direction	-	(Wahab et al., 2020)
Pomegranate peels (punica granatum)	E. coli and S. aureus	$Zn(NO_3)_2.6H_2O$	-	50 nm hexagonal bottom-neck nano pencils	21 on S. aureus	(Kaviya et al., 2017)
Green synthesis (Anacardiumoccidentale)	E. coli and S. aureus	-	$FeCl_3$	26-60 nm sized irregular shape	-	(Rufus et al., 2017)

AC: acetate; S_{BET}: Specific surface area (m^2/g), $p_{V:}$ pore volume (cm^3/g), P_d: pore diameter (nm); d: d-spacing (nm); p: crystal plane; ZI(mm): zone of inhibition in millimeter; CTMAB: Cetyltrimethylammonium Bromide.

CHAPTER THREE

3. MATERIAL AND METHODS

3.1. Chemicals and Reagents

All the reagents were obtained commercially and were used without further purifications. zinc nitrate hexahydrate ($Zn(NO_3)_2.6H_2O$, ≥ 98%, Sigma-Aldrich); zinc acetate dihydrate ($Zn(CH_3CO_2)_2 \cdot 2H_2O$, ≥ 99.0%, Sigma-Aldrich), iron nitrate nonahydrate ($Fe(NO_3)_3.9H_2O$, 99.95%, Sigma-Aldrich); manganese sulfate monohydrate ($MnSO_4.H_2O$, 99%, Sigma-Aldrich); poly(vinyl alcohol) (PVA, Mn 25,000, 99% hydrolyzed, Thermo Fisher Scientific India Pvt. Ltd); congo red (CR, 35%, Sigma-Aldrich); acid orange-8 (AO8, 65%, Sigma-Aldrich); ascorbic acid (AA, 99%, Sigma-Aldrich); sodium hydroxide (NaOH, 98%, Oxford Lab Fine Chem LLP), and methylene blue dye (MB, 95%, Sigma-Aldrich).

3.2. Synthesis of Metal Oxide NPs and NCs

3.2.1. Synthesis of single NPs

The ZnO, Fe_2O_3, and Mn_2O_3 NPs were synthesized using a simple and environmentally-friendly sol-gel method. To synthesize single ZnO NPs, $Zn(NO_3)_2.6H_2O$ was added into 100 mL of distilled water while stirring on a magnetic stirrer to form a 0.01 mol L^{-1} solution (at room temperature, for ~15 minutes). The Sol (colloidal particles of metal hydroxides) formed was aged for two days to form a gel (-M-O-M-) and dried in an oven at about 110 °C for about 8 hrs. Then, the product was crushed using mortar and pestle. Finally, the powder was calcined at 500 °C for 3 hrs. The same aforementioned procedure was followed for synthesizing Fe_2O_3 and Mn_2O_3 NPs by using $Fe(NO_3)_3.9H_2O$ and $MnSO_4.H_2O$ salt precursors, respectively.

3.2.2. Synthesis of binary and ternary metal oxide NCs

The PVA-assisted NCs were also synthesized using a simple and environmentally-friendly sol-gel method followed by the auto-combustion process. To synthesize the binary NCs;

first, the PVA polymer was dissolved in distilled water while stirring on a magnetic stirrer for about 15 minutes (at ~115 °C) (Liu et al., 2016). Then, the $Zn(NO_3)_2.6H_2O$ and $Fe(NO_3)_3.9H_2O$ salt precursors were added for synthesizing the Zn-Fe oxide NC and the $Zn(NO_3)_2.6H_2O$ and $MnSO_4.H_2O$ precursors for synthesizing the Zn-Mn oxide NC to the above dissolved and cooled PVA polymer solution. The Sol (colloidal particles of metal hydroxides) formed was aged for two days to form a gel (-M-O-M-) and dried in an oven at about 110 °C. Then, the product was crushed using mortar and pestle to reduce the bulk of the combusted material. Finally, the powder was calcined at 500 °C for 3 hrs. A scheme showing the synthesis procedure is shown in Figure 19. The same protocol was also followed for synthesizing the PVA-assisted ternary Zn-Fe-Mn metal oxide NCs by mixing the $Zn(NO_3)_2.6H_2O$, $Fe(NO_3)_3.9H_2O$, and $MnSO_4.H_2O$ metal salt precursors.

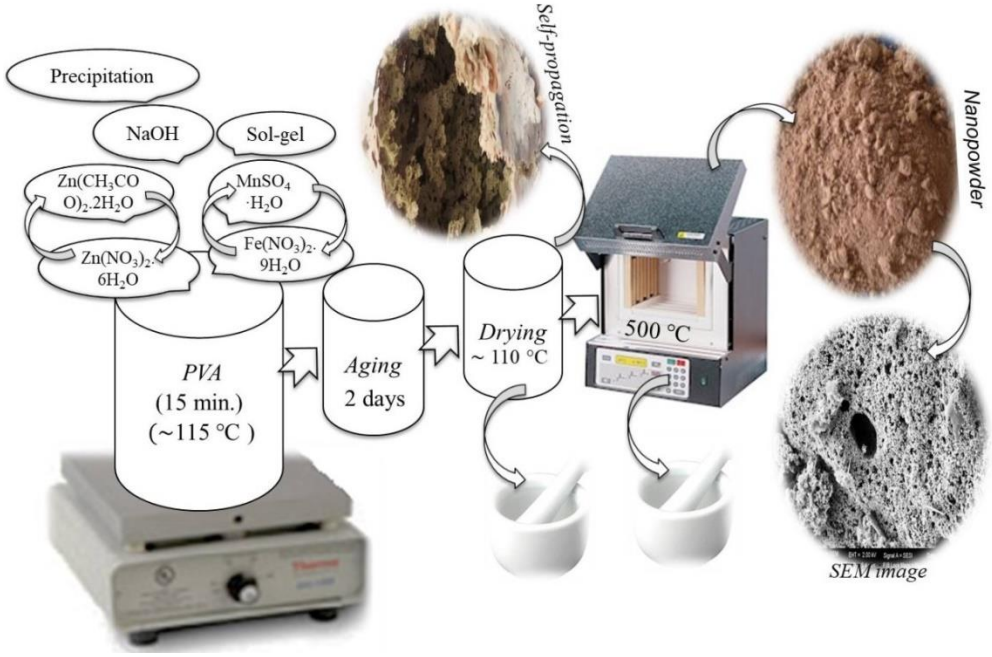

Figure 19. Scheme showing the co-precipitation and sol-gel-auto-combustion synthesis procedure of metal oxide nanocomposites.

To synthesize the binary and ternary metal oxides NCs without PVA; except, for the first procedure used to dissolve the PVA polymer, the same protocol was followed. Besides, the sol-gel and co-precipitation method was also used for the synthesis of ternary NC materials. The co-precipitation method was used by dropwise addition of dilute NaOH. The synthesized binary metal oxide nanocomposites (BMONCs) without PVA were coded as BMO1 and BMO2 for Zn-Fe and Zn-Mn oxides, respectively. The BMONCs synthesized using PVA (PVA-BMONCs) were coded as PVA-BMO1 and PVA-BMO2,

for Zn-Fe and Zn-Mn oxides, respectively. The synthesized ternary metal oxide nanocomposites (TMONCs) using the sol-gel (M1) and co-precipitation (M2) techniques were coded as TMOM1 and TMOM2, respectively.

Using M1, the PVA-assisted ternary NCs were further studied to optimize the SAV and SSA for zinc nitrate (P1) and zinc acetate (P2) precursors. The synthesized PVA-assisted TMONCs (PVA-TMONCs) using P1 and P2 precursors were coded as PVA-TMOP1 and PVA-TMOP2, respectively. Further PVA amount and precursor percentages optimization were conducted for PVA-TMOP1 NC. For percentage optimization, constant amount of PVA (0.7 g) and different precursors percentage [(30, 50, 70, 90, and 100), (35, 25, 15, 5, and 0), and (35, 25, 15, 5, and 0)] for zinc, iron, and manganese were used, respectively and the respective codes are given as 30(0.7), 50(0.7), 70(0.7), 90(0.7), and 100 (0.7). For PVA amount optimization, constant salt precursor's percentages [zinc (90%), iron (5%), manganese (5%)] and different amount of PVA (0, 0.2, 0.4, 0.7, 1.5, and 3 g) were used and coded as 90(0), 90(0.2), 90(0.4), 90(0.7), 90(1.5), and 90(3), respectively (see Table 12 and 13).

3.3. Batch Adsorption Studies

The adsorption studies are investigated in 100 mL Erlenmeyer flasks. The PVA-TMOP1 NC adsorbent to the MB dye adsorbate solution ratio is 2:2.5 (20 mg of PVA-TMOP1 to 25 mL of 20 mg L^{-1} MB dye solution). Dilute HCl and NaOH solutions were used to adjust the pH of the solution as required. The equilibration of adsorption experiments is conducted on a rotary shaker at a speed of 140 rpm. The influence of pH of the solutions (pH of 2, 4, 6, 8, 10, and 12) and amount of PVA-TMOP1 (dosage of 0.005, 0.01, 0.02, 0.04, 0.08, and 0.16 g) were optimized. The adsorption kinetics study was conducted using the adsorbate-adsorbent contact time of 10, 30, 50, 70, 90, 110, 130, and 150 minutes. The adsorption isotherm tests were conducted using MB dye concentrations of 1, 5, 10, 15, 20, 25, 30, and 35 mg L^{-1}.

3.4. Batch Degradation Studies

The photocatalytic experiments were conducted by taking 20 ppm of CR and AO8 dyes in 250 mL aqueous solution with 0.06 g of ZnO NPs and PVA-BMO1, PVA-BMO2, and

PVA-TMOP1 NCs photocatalysts. Earlier to illumination, the reaction suspension was stirred continuously in the dark for 30 min to create the adsorption/desorption equilibrium of AO8/CR on the NPs/NCs. The degradation experiment was carried out in the 176.6 cm^2 circular glass reactor. A medium-pressure mercury vapor lamp (Hg lamp) was used as light source (λ_{max} = 365 nm, 125 W). The samples were irradiated directly by focusing light into the reaction mixture at a distance of 20 cm. Magnetic stirring at a speed of 110 rpm was applied to continuously mix the solution. The temperature of the overall reactor was controlled by water circulation with purging of oxygen during the experiment. Taking 5 mL of the dye solution every 15 minutes, the concentrations at time *t* were measured by UV-vis spectrophotometer. The photocatalytic degradation efficiency in percent was calculated using equation 2. The pseudo-first-order kinetic equation (equation 14) was used to study reaction dynamics (Kumar et al., 2020; Surendra et al., 2018).

3.5. Fabrication of Working Electrode for Ascorbic Acid Sensor

For the preparation of carbon paste, the graphite powder (< 20 μm, 98% purity), silicone oil (as electrode mechanical strength-enhancing agent), and the synthesized ZnO NPs and PVA-BMO1, PVA-BMO2, and PVA-TMOP1 NCs with a mass ratio of 70:15:15, respectively, was blended with a mortar and pestle (~ 30 min.). Then, the synthesized paste was inserted in a Teflon tube from the bottom with high pressure to ensure better electrical contact. The electrical connection was made by inserting a copper wire into the Teflon tube. For a smooth and polished glassy surface generation, a small plug of the paste was rapidly extruded on a stainless steel rod, and the resulting surface smoothed on wax paper (Eliana & Bojorge, 2011; Rashmi et al., 2020). For the detection of ascorbic acid, the ZnO, PVA-BMO1, PVA-BMO2, and PVA-TMOP1 modified electrode, the Ag/AgCl saturated KCl electrode, and a platinum wire was applied as a working, reference, and counter electrode, respectively.

3.6. Antibacterial Activity Studies

The in vitro antibacterial activity of ZnO NPs, and PVA-BMO1, PVA-BMO2, and PVA-TMOP1 NCs were carried out by the disk diffusion method and compared to the commercial antibiotic Ampicillin. Firstly, as per the manufacturer procedure (13 g L^{-1}), the nutrient broth medium was prepared and autoclaved at 121 °C for 15 minutes. The

prepared medium nutrient broth was poured into a test tube (4-5 mL/test tube), and are allowed to cool for 24 hours at room temperature. Then, the pure bacteria strain was inoculated and incubated at 37 °C for 24 hours. The turbidity of the cultured bacteria strains was adjusted as 0.5 McFarland standards (a mixture of 0.5 mL of 0.048 mol/L $BaCl_2$ and 99.5 mL of 0.18 mol/L H_2SO_4). For the antibacterial susceptibility test, as per manufacturer procedure, the Muller Hinton agar was prepared (38 g L^{-1}) and autoclaved at 121 °C for 15 minutes. The prepared medium was poured into a petri-dish (25-30 mL/plate). After solidification under sterilized conditions, the grown culture was seeded on the petri-dish overnight after evenly swabbing with the help of a sterilized cotton swab (Gebreyohannes et al., 2013).

The antibacterial activities of ZnO and PVA-TMONCs were evaluated with three concentrations of 75, 100, and 125 μg mL^{-1}. Depending on the PVA-TMONCs catalyst amount optimization, the 125 μg mL^{-1} concentration was used for the antibacterial test of the PVA-BMONCs. The antimicrobial activity was evaluated in terms of zone of inhibition by measuring with a ruler in millimeters (mm). The bacteria used for the test are *Escherichia coli (E. coli) (ATCC* 25922), *Staphylococcus aureus (S. aureus) (ATCC* 25923), *Pseudomonas aeruginosa* (*P. aeruginosa) (*ATCC 27853), *and Bacillus subtilis (B. subtilis) (*ATCC 6633*)* (Gebreyohannes et al., 2013).

3.7. Characterization

3.7.1. Thermogravimetry/differential thermal analyzers and differential scanning calorimetry

The DTG (Shimadzu DTG-60H) and DSC (Perkin Elmer, DSC 4000, USA) techniques in a nitrogen atmosphere at 20.0 mL min^{-1} flow rate and 50 °C min^{-1} ramp time were used to study the thermal stability and degradation behavior of the polymer (PVA), the parent material of ZnO NPs and PVA-BMO1, PVA-BMO2, and PVA-TMOP1 NCs.

3.7.2. UV–vis diffuse reflectance spectroscopy

The ultraviolet-visible spectroscopic technique [Shimadzu UV-vis, SM-1600 (for solution analysis) and Shimadzu UV-vis-DRS, UV-2600 (for powder analysis)] in the range of

200–800 nm were used to study the optical properties of ZnO NPs and binary and ternary metal oxide NCs.

3.7.3. Fourier transform infrared spectroscopy

Fourier transform-infrared spectroscopy (Perkin Elmer FT-IR, Spectrum 65) using KBr pellets in the range of 400–4000 cm^{-1} was used to study the surface functional groups behavior of ZnO NPs and binary and ternary metal oxide NCs before and after calcination.

3.7.4. X-ray powder diffraction

The X-ray diffraction (XRD, Shimadzu, XRD-7000) was used to study the crystallographic structure of PVA, single ZnO, Fe_2O_3, Mn_2O_3 NPs, and the binary and ternary metal oxide NCs synthesized with and without PVA.

3.7.5. Scanning electron microscopy with energy dispersive X-ray

The scanning electron microscopy with energy-dispersive X-ray spectroscopy (SEM-EDX-EVO 18 with low vacuum facility and ALTO 1000 cryo attachment) was used to study the morphologies of ZnO NPs and binary and ternary metal oxide NCs.

3.7.6. High-resolution transmission electron microscopy

The morphological studies and composition of the binary and ternary metal oxide NCs were also further characterized by a high-resolution transmission electron microscopy (JEOL TEM 2100 HRTEM).

3.7.5. X-ray photoelectron spectroscopy

Further evidence for the composition of the product was inferred from X-ray photoelectron spectroscopy. XPS is a quantitative spectroscopic method that determines the elemental composition, empirical formula, chemical state, and electronic state of the elements present in the sample. XPS analysis was conducted using AXIS ULTRA from AXIS 165, integrated with Kratos patented magnetic immersion lens, charge neutralization

system, and spherical mirror analyzer. The peak energies were calibrated based on the energy of external carbon.

3.7.7. Brunauer-Emmett-Teller surface area analyzer

The Brunauer–Emmett–Teller (BET) method was utilized to calculate the SSA of the samples in the relative pressure (P/P_o) range of 0.05–0.35. The pore-size distributions of the samples were determined by the Barrett–Joyner–Halenda (BJH) method. The total pore volume of the NCs was accumulated at a relative pressure of $P/P_o = 0.99$. N_2 sorption measurements of all the NPs and NCs were carried out at 77 K using a Quanta chrome instrument.

3.7.8. Cyclic voltammetry and electrical impedance spectroscopy

For electrochemical properties investigation, the cyclic voltammetric studies were made using the CHI604E potentiostat (tri-electrode system: the ZnO NPs and binary and ternary metal oxide NCs modified electrode as a working electrode, platinum wire as a counter electrode, and Ag/AgCl as a reference electrode with 1M KOH as an electrolyte. The potential ranges utilized during these studies are ranging between −1.2 V and 1 V and adjusted as needed. The scanning rate was carried out from 10 mV/s to 50 mV/s. AC impedance measurements were carried out in the frequency range of 1 Hz - 1 MHz with an AC amplitude of 5 mV.

CHAPTER FOUR

4. RESULTS AND DISCUSSION

4.1. Characterization

4.1.1. Thermal stability analysis

The thermal stability of PVA, ZnO NPs, and PVA-BMO1, PVA-BMO2, and PVA-TMOP1 NCs before calcination (after drying at ~ 110 °C) was studied by DTG analytical technique in a nitrogen atmosphere at 20.0 mL min^{-1} flow rate and 50 °C min^{-1} hold time (Figure 20). The DTG and DSC thermal parameters of NPs and NCs were also given in Table 8. Thermogravimetric analysis (TGA) is a technique used to measure the change in mass as a function of temperature and used for selecting an optimum decomposition temperature of a material. For PVA, four mass loss steps including evaporation of adsorbed water molecules, slow intramolecular decomposition, dehydration of crystal water (metal hydroxides decompositions) or/and degradation of amorphous parts of PVA (side chains), and decomposition of the main chain/intermolecular decomposition of PVA are observed [Figure 20(a)], and finally, the crystalline part decomposition takes place to give carbon, hydrocarbons, and ash (> 600 °C) (Dai et al., 2018; Kumar et al., 2019; Radhamani et al., 2016; Rahmanian et al., 2015). As seen from Figure 20(a), PVA was not still stable after ~600 °C; this instability indicates the presence of further carbon and hydrocarbon decomposition into ash. The respective approximate decomposition temperature ranges of 50 - 160 °C, 160 - 250 °C, 250 - 370 °C, and 370 - 580 °C are for PVA. Whereas, temperature ranges 40 - 120 °C, 120 - 180 °C, 180 - 220 °C, 220 - 280 °C, and 280 - 430 °C, were found to be the approximate decomposition temperature ranges for PVA-TMOP1 NC [Figure 20(b)].

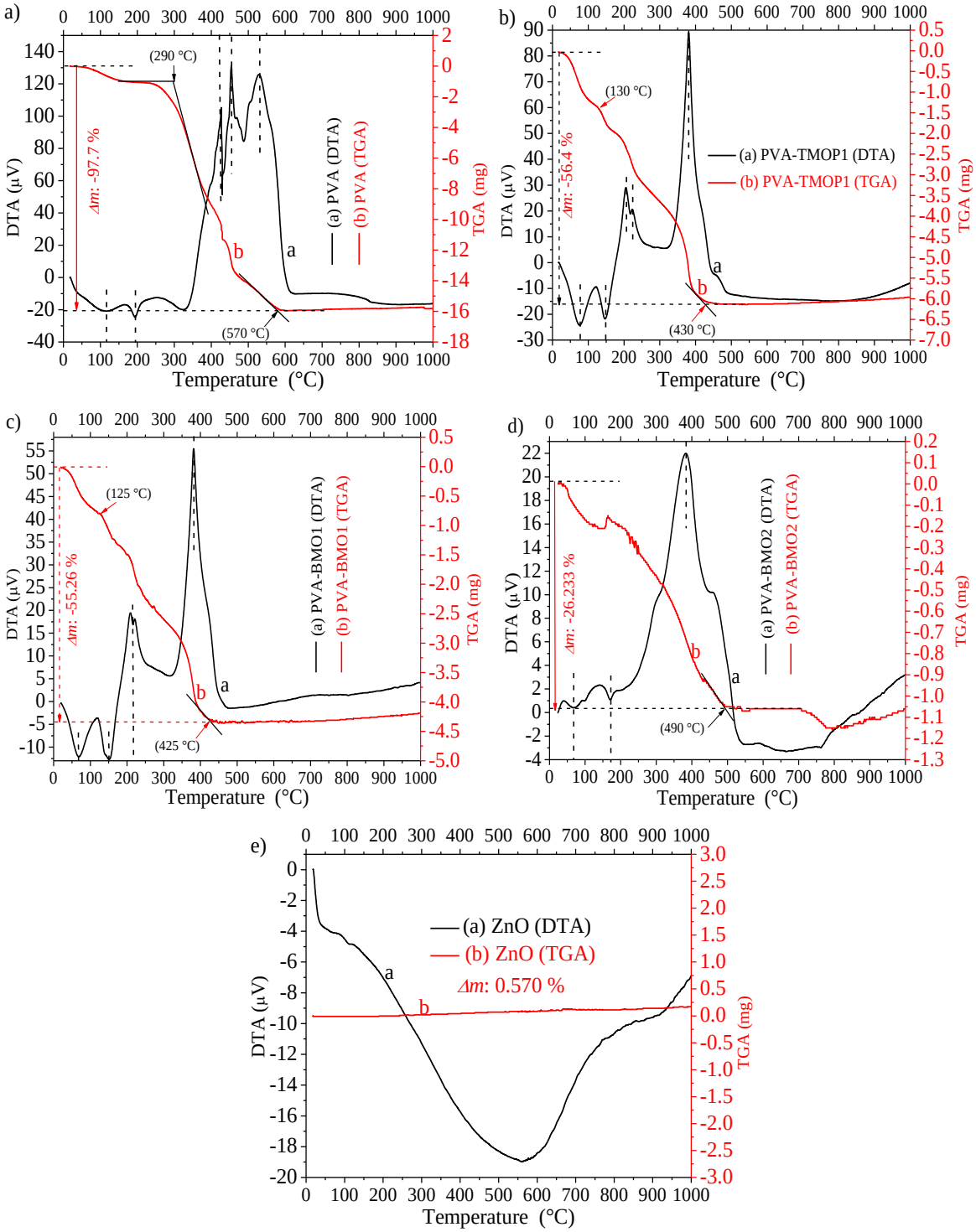

Figure 20. TGA/DTA plots of (a) PVA polymer, (b) PVA-TMOP1 NC, (c) PVA-BMO1 NC, (d) PVA-BMO2 NC, (e) ZnO NPs; the analysis were conducted after drying the sample at about 110 °C.

For PVA alone, almost 98% of decomposition took place and left with 2% carbon part. For PVA-TMOP1 NC about 56% decomposition took place and left with ~ 42% of PVA-TMOP1 metal oxide NC. The 56% is due to the decomposition of the PVA polymer and

byproducts of the salt left after the 110 °C dying process (Radhamani et al., 2016). In addition to the indicated steps for PVA, a unique decomposition stages of 180 - 220 °C and 220 - 280 °C observed on PVA-TMOP1 NC can be attributed to the metal hydroxide decompositions or loss of water due to constituents such as $Zn(OH)_2$, $Fe(OH)_2$, and $Mn(OH)_2$ [Figure 20(b)] (Singh & Dutta, 2019). For the ZnO NPs synthesized without PVA, only 0.6% weight loss attributed to the evaporation of adsorbed water molecules and dehydration of crystal water (metal hydroxides decompositions) has been detected [Figure 20(e)].

Figure 20(c) and (d) also show the DTG analysis for PVA-BMO1 and PVA-BMO2 NCs, respectively. Except for slight decomposition temperature (< 5 °C) and stability differences, the PVA-BMO1 NC has almost similar decomposition steps with PVA-TMOP1 NC. Between the temperature ranges of 500 – 900 °C, the PVA-TMOP1 NC show better stability compared to the PVA-BMO1 NC, indicating that the presence of manganese oxide is improving the stability of the ternary NC (Najafi et al., 2018). The PVA-BMO2 NC decomposition temperature steps has also similarities to the PVA-BMO1 and PVA-TMOP1 NCs, although, there is great stability loss between 500 °C - 900 °C. In conclusion, the thermal stability order of the materials is found to be as follows: ZnO > PVA-TMOP1 > PVA-BMO1 > PVA-BMO2 > PVA.

The total decomposition temperature of PVA, PVA-BMO1, PVA-BMO2, and PVA-TMOP1 NCs ends at about 570 °C, 430 °C, 425 °C, and 490 °C, respectively. Hence, the approximate average temperature of 500 °C was selected for the total decomposition temperature of PVA after serving as a capping agent and impurities that have a boiling point less than 500 °C. This calcination temperature (500 °C) was also applied for the subsequent analysis and application tests. PVA alone has a higher DTG decomposition temperature compared to the NCs. It indicates that metal oxides are acting as a catalyst for the degradation of PVA. In fact, metal oxides act as catalysts for the degradation of polymers is common (Shawaphun et al., 2010). The other probability for having a lower decomposition temperature of the NCs is due to the higher crystalline properties of metal oxides (crystal structure perfection), compared to the polymers (Ren et al., 2015).

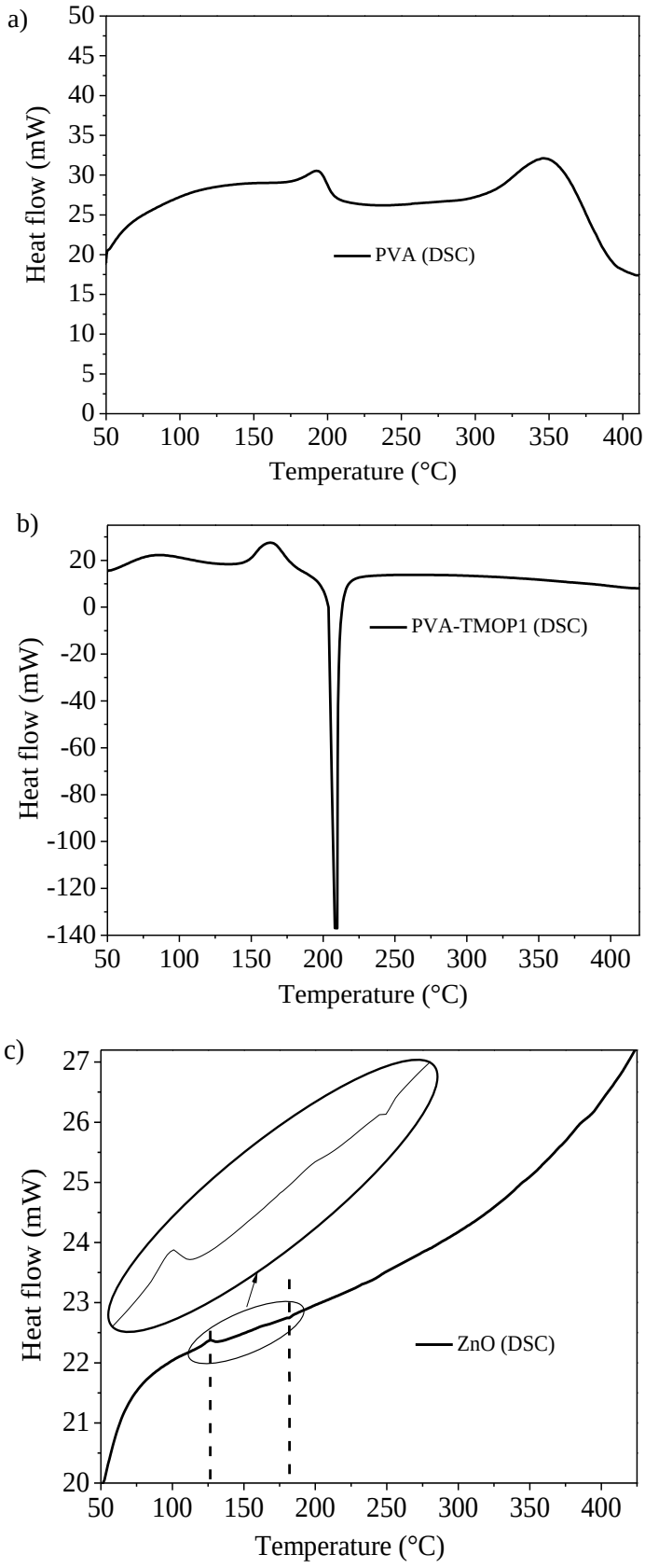

Figure 21. DSC plots of (a) PVA, (b) PVA-TMOP1 NCs before calcination, and (c) ZnO NPs before calcination. Inset (c): magnified ZnO DSC plot.

Table 8. The DTG/DSC thermal parameters of pure PVA polymer and binary and ternary NCs.

	DTG							DSC	
	T_{onset} (°C)	T_{max1} (°C)	T_{max2} (°C)	T_{max3} (°C)	T_{max4} (°C)	T_{max5} (°C)	Δm (%)	T_{g} (°C)	T_{m} (°C)
S1	290	115	195	424	453	530	97.7	170	290
S2	130	76	148	205	222	379	56.4	144	204
S3	125	65	145	200	219	375	55.26	-	-
S4	-	40	150	365	445	570	26.23	-	-

S1: PVA, S2: PVA-TMOP1, S3: PVA-BMO1, S4: PVA-BMO2

The phase behaviors of the selected PVA, ZnO NPs, and PVA-TMOP1 NC were also characterized by the DSC technique. The first broad peak that appeared at about 100 °C for PVA is attributed to the loss of absorbed water. The two exothermic DSC peaks that appeared at around 195 °C and 345 °C are attributed to the degradation of side-chain (the scission of C–O) and main chain (the scission of C–C), respectively [Figure 21(a)], a consistent result was also reported elsewhere in the literature (Sui et al., 2005). Unlike that of PVA polymer, the byproducts of zinc salt left after the 110 °C drying processes for ZnO and the PVA-TMOP1 NC have both exothermic and endothermic peaks. The PVA-TMOP1 NC exhibited two exothermic peaks due to the evaporation of adsorbed volatile components at 80 °C and the glass transition temperature (T_g) at 144 °C (Table 8). The third sharp endothermic peak at 210 °C was probably due to the phase transformation of other forms of iron or/and manganese oxides to the Fe_2O_3 and Mn_2O_3 (Radhamani et al., 2016). The melting temperature (T_m) of PVA-TMOP1 NC was found to be 204 °C [Figure 21(b)]. For the DSC plot of zinc oxide, the first decomposition noted at around 125 °C is due to the loss of water of crystallization. The second endothermic peaks at 185 °C correspond to the thermal decomposition of the byproducts of the zinc salt left after the 110 °C dying processes (zinc hydroxide/loss of water due to constituents) (Singh & Dutta, 2019) [Figure 21(c)].

4.1.2. XRD analysis

The XRD patterns that confirm the crystallinity and phases of single ZnO, Fe_2O_3, Mn_2O_3, BMONCs and TMONCs are shown in Figures 22-28. As seen in Figure 22 inset label (c), the diffraction angles with their respective crystal planes [~32^o(100), 34^o(002), 36^o(101), 47^o(102), 57^o(110), 63^o(103), 66^o(200), 68^o(112), 69^o(201), 73^o(004), and 77^o(202)]

corresponds to the hexagonal structure of ZnO NPs (ICSD: 00-036-1451, P63mc (#186-1) space group) (Gupta et al., 2012; Xinyu Zhang et al., 2015). The diffraction angles with their respective crystal planes of ~24°(012), 33°(104), 36°(110), 42°(113), 51°(024), 54°(116), 63°(214), and 65°(330) are indexed to hematite, α-Fe_2O_3 [ICSD: 00-033-0664, R-3c (#167-1) space group)] [Figure 22 inset label (a)] (Chen et al., 2016). The diffraction angles with their corresponding crystal planes of ~22°(211), 33°(222), 38(400)°, 49°(431), 56°(440), and 64°(622) are matched with α-Mn_2O_3 (ICSD: 24342, PBCA space group) [Figure 22 inset label (b)] (Hazarika et al., 2018). In fact, phases of iron oxide (Ketteler et al., 2001) and manganese oxide (Nathan et al., 2008) in air at a calcination temperature of 500 °C reported to give Fe_2O_3 and Mn_2O_3, respectively. Figure 22 inset labels (d) is the XRD pattern for PVA-TMOP1 NC drawn for comparison. The structure of stable ZnO, Mn_2O_3, and Fe_2O_3 crystals that was developed using VESTA 3D visualization program software depending on the AMCSD cif data search result is given in Figure 1(a)-(c), respectively (Kolm, 2009).

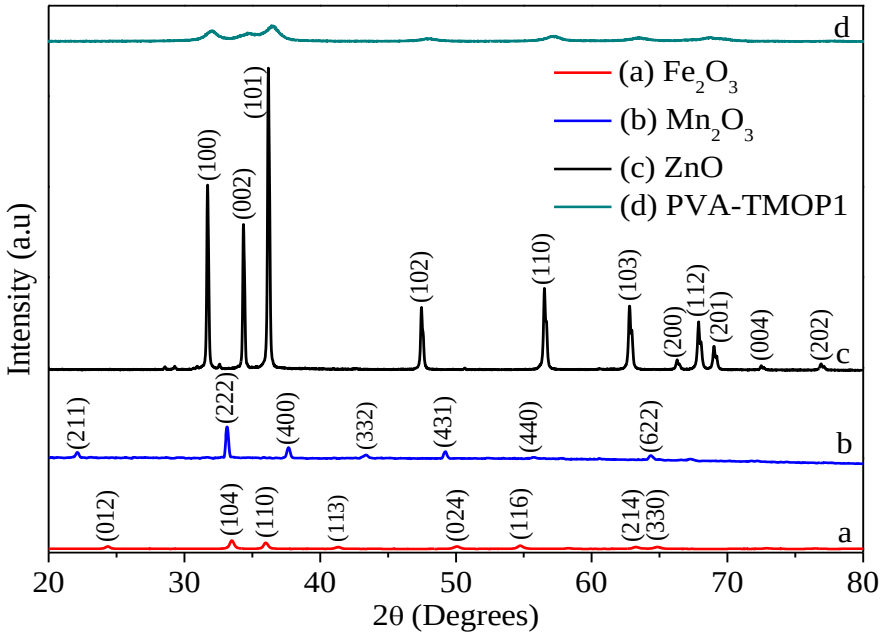

Figure 22. XRD patterns of ZnO, Fe_2O_3, Mn_2O_3 NPs, and PVA-TMOP1 NCs calcined at 500 °C.

The synthesized BMONCs with and without PVA are given in Figures 23 and 24 (Tables 9 and 10). Compared to the BMONCs synthesized without PVA, the PVA-assisted BMONCs showed greater SAV. The approximate average crystallite size values for BMO1 and PVA-BMO1 were determined to be 53 nm and 29 nm, respectively. Also, the

approximate average crystallite size values for BMO2 and PVA-BMO2 were found to be 48 nm and 23 nm, respectively. This substantiates the role of PVA polymer as a capping agent for shielding the NPs from aggregation/agglomeration (León-Silva et al., 2016; Sudha et al., 2012). In fact, PVA plays a critical role to delay the cations' mobility and minimizing unwanted aggregation/agglomeration of the metal oxides (Ciciliati et al., 2015). In this work, the single ZnO, Fe_2O_3, and Mn_2O_3 NPs and binary Zn-Mn oxide (Khan et al., 2018; Qamar et al., 2017; Saravanan et al., 2014; Wang et al., 2019; Yu et al., 2016) and binary Zn-Fe oxide NCs (Davari et al., 2017; Lachheb et al., 2017; Sin et al., 2018) materials were synthesized for comparison as they were also studied in previous studies.

Table 9. XRD crystallite size analysis results of ZnO and Fe_2O_3 NPs and Zn-Fe oxides NCs. For BMO1 and PVA-BMO1 NCs, 90% zinc and 10% iron oxides were used.

	Peak area	2θ (°)	FWHM (radians)	Height (a.u)	D (nm)	BET (m^2 g^{-1})
ZnO	2081	34.10	0.14723	11128	59	1.51
Fe_2O_3	121	31.01	0.32119	299	27	13.4
BMO1	2772	33.98	0.16273	10561	53	1.93
PVA-BMO1	1579	41.49	0.30647	4203	29	8.85

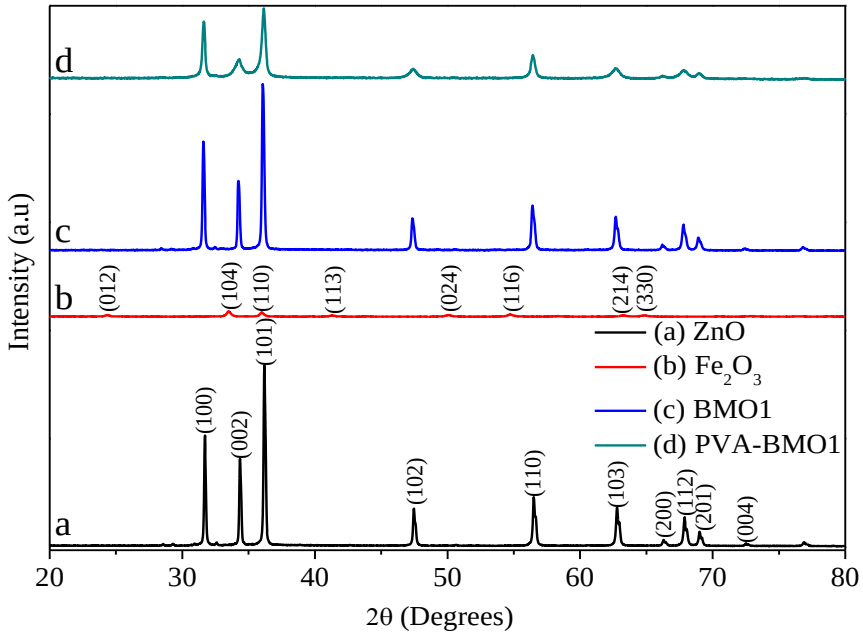

Figure 23. XRD patterns of ZnO and Fe_2O_3 NPs and BMO1 and PVA-BMO1 NCs calcined at 500 °C.

The XRD data and the respective crystallite size are calculated using Debye-Scherrer's formula (equation 48):

$$D = \frac{K\lambda}{\beta \cos(\theta)} \qquad (48)$$

Where λ is the wavelength of X-ray radiation (for Cu Kα 0.15418 nm), K is constant, β is the line width at half maximum height, and θ is the diffracting angle.

Table 10. XRD crystallite size analysis results of ZnO and Mn_2O_3 NPs and Zn-Mn oxides NCs. For BMO2 and PVA-BMO2 NCs, 90% zinc and 10% iron oxides were used.

	Peak area	2θ (°)	FWHM (radians)	Height (a.u)	D (nm)	BET (m^2 g^{-1})
ZnO	2081	34.10	0.14723	11128	59	1.51
Mn_2O_3	303	40.01	0.27986	958	32	2.92
BMO2	2772	33.35	0.18077	12109	48	3.00
PVA-BMO2	1428	33.90	0.37881	3008	23	8.43

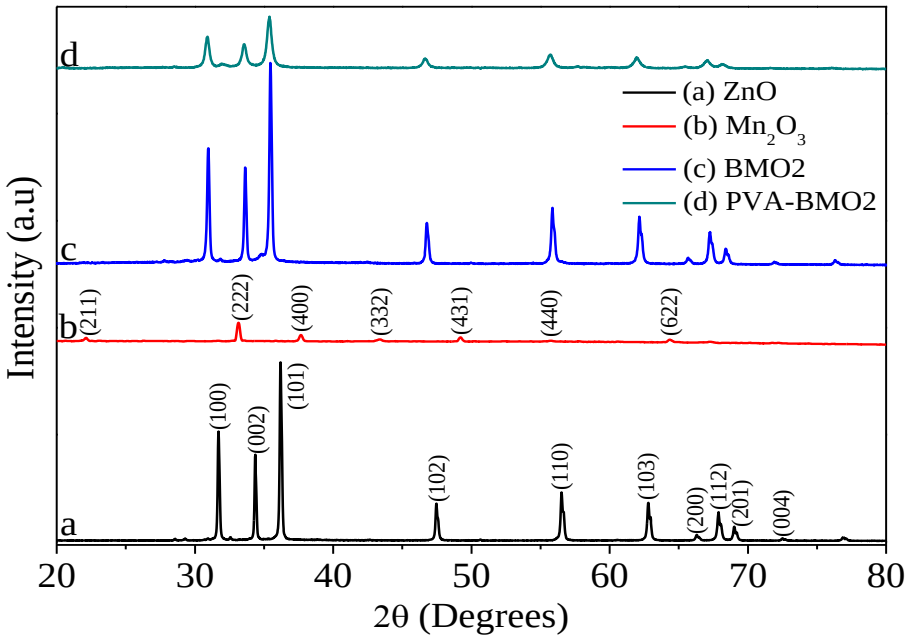

Figure 24. XRD patterns of ZnO and Mn_2O_3 NPs and BMO2 and PVA-BMO2 NCs calcined at 500 °C.

The methods (sol-gel and co-precipitation) and precursor type (Figure 25, Table 11), precursors' percentage (Figure 26, Table 12), and PVA amount (Figure 27, Table 13) were

also optimized for TMONCs. The approximate average crystallite size values for TMOM1 and TMOM2 were obtained to be 28 nm and 49 nm, respectively. Hence, by using the optimized sol-gel (M1) method, the effects of precursor type (i.e., zinc nitrate hexahydrate and zinc acetate dihydrate) were further studied. Compared to the acetate precursor that has an approximate average crystallite size value of 21 nm, the nitrate precursor yielded greater SAV with an approximate average crystallite size value of 10 nm (Table 11). As understood during the synthesis time, this improved SAV for NCs synthesized using a nitrate precursor is due to the creation of a higher auto-combustion process that assists greater porosity (Han et al., 2019). Thus, further PVA amount and precursors percentage optimization were conducted for the optimized PVA-TMOP1 NC. As seen from Figure 25 of the synthesized TMONCs, the sharpness of the peaks for the NCs synthesized without PVA show high crystallinity [see Figure 25 inset labels (b) and (c)]. The other TMONCs synthesized using PVA polymer has a broad and weak peak [Figure 25 inset labels (d) and (e)]. The broadness of the peaks shows the presence of greater SAV. The approximate height ratio in the arbitrary unit between ZnO NPs and PVA-TMOP1 NC is approximately 7:1.

Table 11. XRD crystallite size analysis results of ZnO, Fe_2O_3, and Mn_2O_3 NPs and TMONCs**.** For all TMOM1, TMOM2, PVA-TMOM1, and PVA-TMOM1 NCs, 90% zinc, 5% iron, and 5% manganese oxides were used.

Code	Peak area	2θ (^{o})	FWHM (radians)	Height (a.u)	D (nm)	BET (m^2 g^{-1})
ZnO	2081	34.10	0.14723	11128	59	1.51
Fe_2O_3	121	31.01	0.32119	299	27	13.4
Mn_2O_3	303	40.01	0.27986	958	32	2.92
TMOM1	2694	33.64	0.31557	6812	28	4.47
TMOM2	1981	33.54	0.17759	8787	49	4.44
PVA-TMOP1	1968	49.75	0.90002	1696	10	23.9
PVA-TMOP2	1526	34.01	0.41356	2985	21	11.2

TMOM1 and TMOM2 = sol-gel & co-precipitation, PVA-TMOP1 and PVA-TMOP2 = nitrate and acetate zinc precursor, respectively.

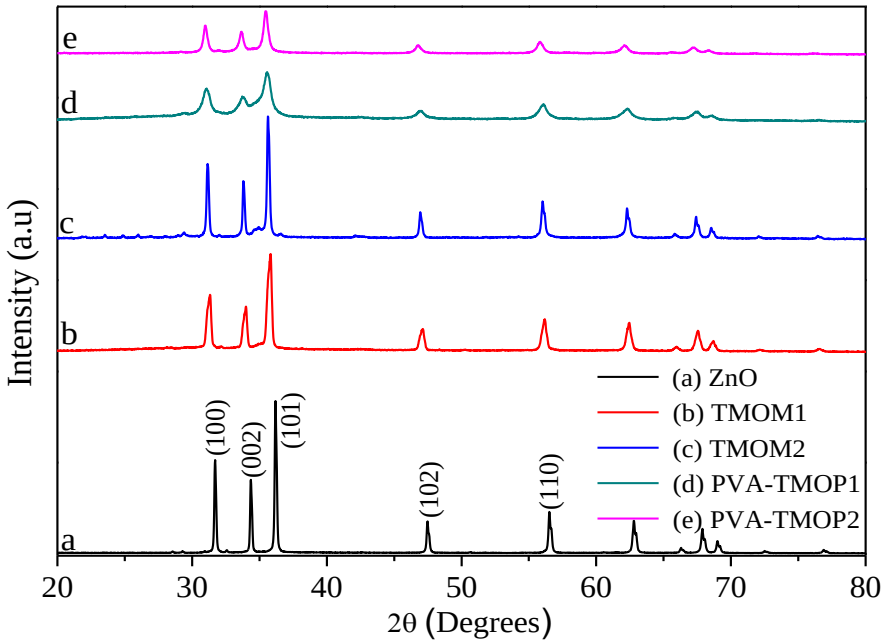

Figure 25. XRD patterns of ZnO NPs and ternary metal oxide without PVA (TMOM1 and TMOM2) and with PVA (PVA-TMOP1 and PVA-TMOP2) calcined at 500 °C.

As optimized, the SAV of PVA-TMOP1 NC is higher than ZnO NPs, BMONCs, and other TMONCs. Therefore, the precursors' percentage and PVA amount optimization was considered for PVA-TMOP1 NC. The precursors' percentage amount optimization was studied by taking a constant PVA amount of 0.7 g. From the data of the precursor's percentage optimization (Figure 26 and Table 12), it was observed that as the percentage of zinc oxide decreases from 90 – 30%, the crystallite size also decreases from 29 to 9 nm. It indicates that an increase in the amount of Fe_2O_3 and Mn_2O_3 caused improvement in the SAV of the NCs. Besides, as the percentage of Fe_2O_3 and Mn_2O_3 increases, the peak shift and appearance of Fe_2O_3 and Mn_2O_3 peaks on the XRD pattern was detected [see Figure 26 inset labels (c) - (g)]. The shift is due to the ZnO crystal distortion that affects the applications of the NCs, although, this is reported to be due to the development of Fe_2O_3 and Mn_2O_3 NPs that have not had boundary contact with ZnO (Hamrouni, Moussa, Di Paola, et al., 2014; Hamrouni, Moussa, Parrino, et al., 2014; Lachheb et al., 2017; Xu et al., 2014). Herein, the precursors' percentage optimization was conducted to prevent the secondary phase formation by controlling the percentage of Fe_2O_3 or/and Mn_2O_3. The XRD peaks of both ZnO NPs and NCs are consistent with the hexagonal ZnO phase. It is due to the smaller percentages of iron and manganese oxides. The absence of NCs peaks shift relative to ZnO (for only 10% of Fe_2O_3 and Mn_2O_3) shows the nonappearance of

structural distortion on the ZnO lattice attributed to Fe^{3+} or Mn^{3+} ion inclusion. It means that Fe_2O_3 or/and Mn_2O_3 NPs are present as a separate phase by forming local heterojunctions with ZnO (Lachheb et al., 2017).

Table 12. XRD data for precursor's percentage optimization.

	Precursors				XRD data			
Code	PVA (g)	ZNH (%)	INH (%)	MSH (%)	2θ (°)	FWHM (radians)	Height (a.u)	D (nm)
30(0.7)	0.7	30	35	35	40.86	0.93657	103	9
50(0)	0.0	50	25	25	34.16	0.20103	1978	43
50(0.7)	0.7	50	25	25	42.71	0.86927	171	10
50(1.5)	1.5	50	25	25	42.56	0.52567	269	17
70(0.7)	0.7	70	15	15	35.34	0.39173	284	22
90(0.7)	0.7	90	5	5	34.16	0.29477	1383	29
100(0)	0	100	0	0	34.10	0.14723	11128	59

ZNH = $Zn(NO_3)_2.6H_2O$, INH = $Fe(NO_3)_3.9H_2O$, and MSH = $MnSO_4.H_2O$

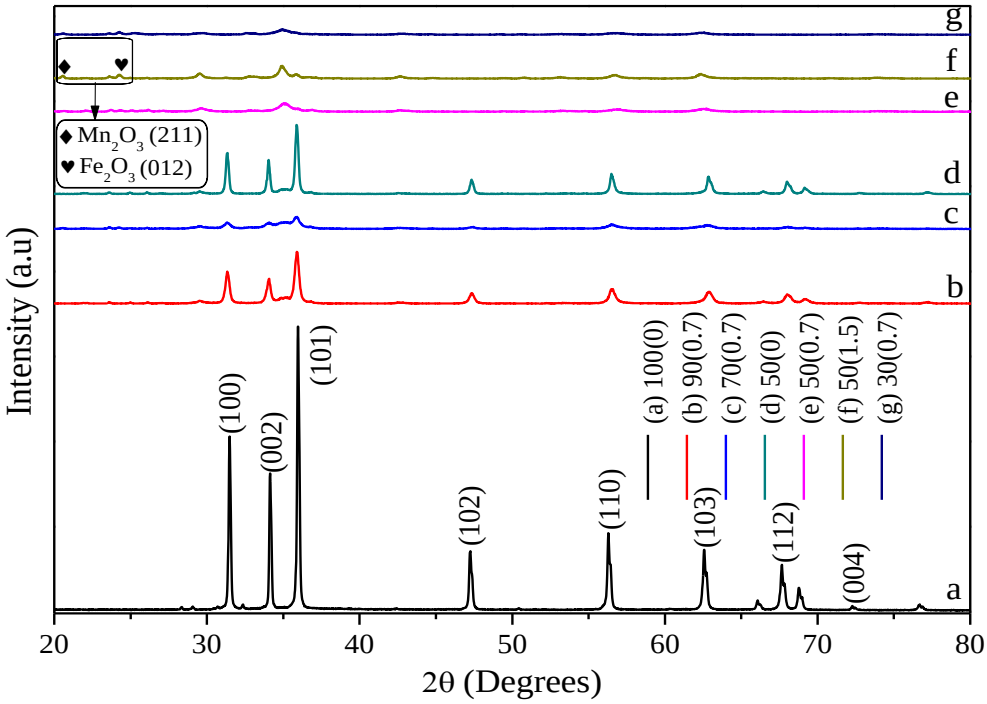

Figure 26. XRD patterns of PVA-TMOP1 NCs calcined at 500 °C: precursor's percentage optimization.

By taking the 90% zinc precursor that has no structural distortion, the PVA amount optimization was conducted by taking different PVA amounts (0 – 3 g). Increasing the PVA amount from 0 to 1.5 g caused decreasing the approximate crystallite size from 59

nm to 7 nm (Figure 27 and Table 13). Further increasing the amount of PVA to 3 g caused an increase in the crystallite size to 15 nm, consistent result was also reported earlier (Karami et al., 2010) and explained to be due to the polarity and solubility of PVA and precursors. Among these, NC synthesized using 1.5 g PVA showed the smallest approximate average crystallite size of 7 nm. The full width at half maximum (FWHM) has a substantial relationship with the size of the crystallite; the broader the FWHM, the smaller is the size of the crystallite.

Table 13. XRD data for PVA amount optimization.

Code	PVA (g)	2θ (°)	FWHM (radians)	Height (a.u)	D (nm)
100(0)	0.0	34.10	0.14723	11128	59
90(0)	0.0	33.64	0.31557	6812	28
90(0.2)	0.2	34.14	0.26493	1409	33
90(0.4)	0.4	34.14	0.28463	876	30
90(0.7)	0.7	34.16	0.29477	1383	29
90(1.5)	1.5	34.07	1.33877	370	7
90(3)	3.0	34.14	0.58477	887	15

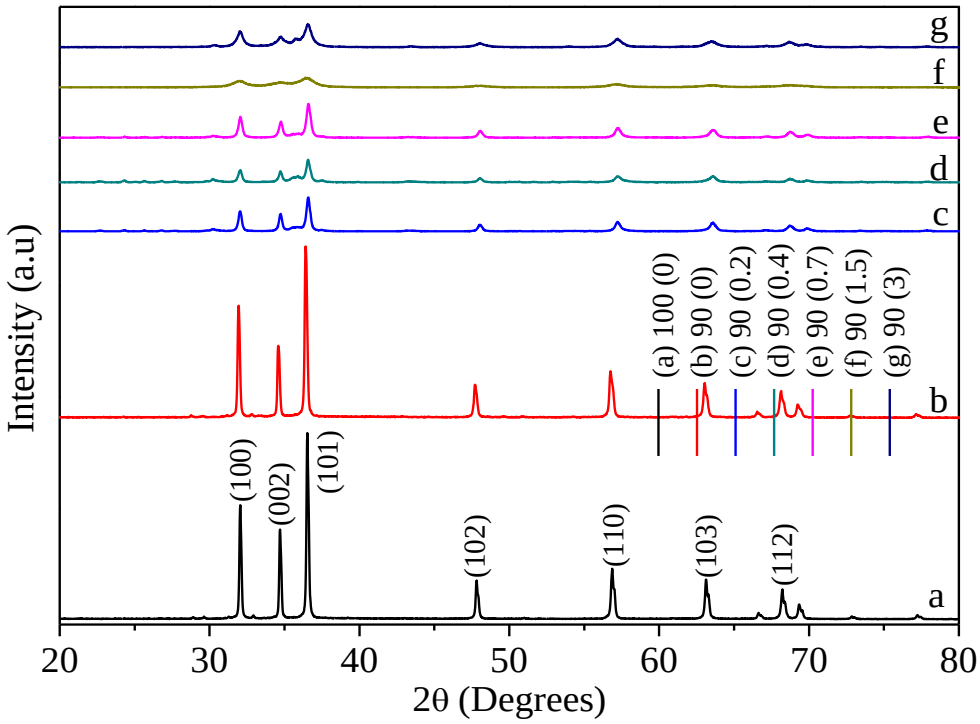

Figure 27. XRD patterns of PVA-TMOP1 NCs calcined at 500 °C: PVA optimization using constant 90, 5, and 5% of zinc, iron, and manganese salt precursors.

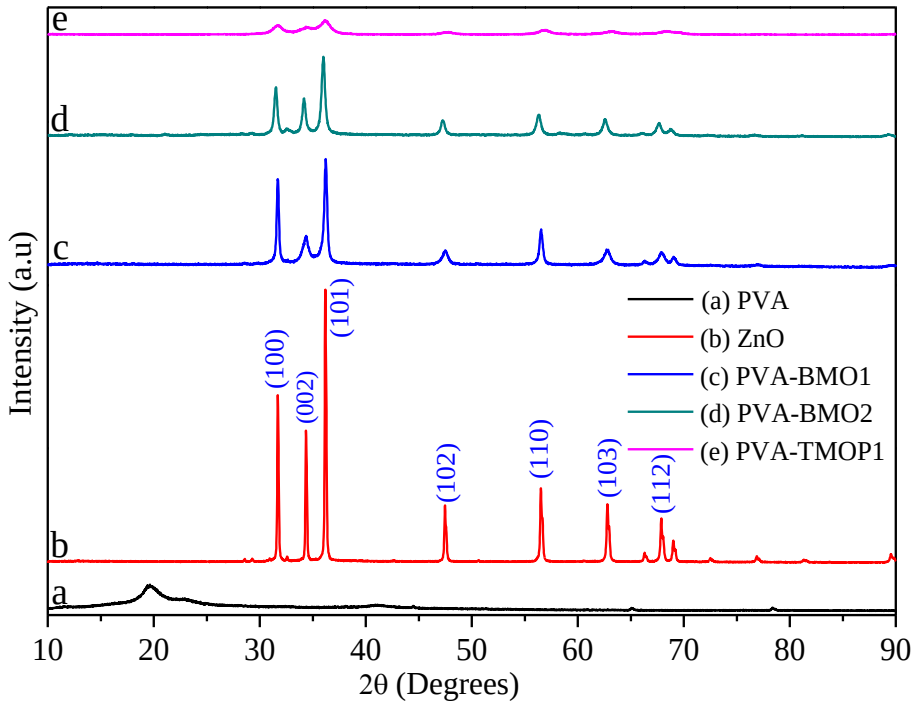

Figure 28. XRD patterns of PVA polymer, ZnO NPs and PVA-BMO1, PVA-BMO2, and PVA-TMOP1 NCs calcined at 500 °C.

The XRD patterns of PVA, ZnO NPs, and optimized binary and ternary metal oxide NCs are given in Figure 28. The XRD peaks of PVA did not appear on the XRD patterns of binary and ternary NCs; it corroborates the complete decompositions of PVA at 500 °C as confirmed from the DTG analysis. The PVA-TMOP1 NC showed enhanced SAV, compared to ZnO NPs and the two binary metal oxide NCs. In conclusion, the overall XRD results of NPs and NCs indicated an enhancement in SAV for the NCs materials due to the presence of PVA as a capping agent and metal oxides as heterojunctions.

4.1.3. BET analysis

For an efficient environmental waste management system, the surface-active sites and optimized pore volume of the NPs and NCs are significant (Rosman et al., 2019). The BET method is the most widely used procedure for measuring the SSA and pore size distribution of the porous materials (Rosman et al., 2019). Based on the Barrett–Joyner–Halenda and molecular simulation at 77 K, N_2 gas was employed as an adsorbate for the characterization of the textural properties of amorphous, semi-crystalline, and crystalline porous materials. The BET plots of ZnO, Fe_2O_3, Mn_2O_3 NPs, and NCs are depicted in

Figures 29 - 32(b). The combined BET plots of ZnO NPs, PVA-BMO1, PVA-BMO2, and PVA-TMOP1 NCs are also presented in Figure 33. The ink-bottled, cylindrical, and slit-shapes are the three basic pore shape models (ALOthman, 2012; Broekhoff, 1979; Thommes et al., 2015). As seen in Figures 29 - 32, all the NPs and NCs have a resemblance to the cylindrical shape model. The BET data is treated according to a BET adsorption isotherm linear equation (equation 49):

$$\frac{P/P_o}{n\,(1-P/P_o)} = \frac{C-1}{(n_m C)}(P/P_o) + \frac{1}{n_m C} \qquad (49)$$

Where, P_o is the saturated vapor pressure of N_2 gas in pa; P is the partial vapor pressure of N_2 gas in pa; n is the volume of N_2 gas adsorbed at standard temperature and pressure (STP) in mL; n_m is the BET monolayer capacity; C is a dimensionless constant related to the enthalpy of N_2 gas adsorption on the single, BMONCs, and TMONCs adsorbent.

The linear plots of equation 49 should yield a straight line in the approximate relative pressure range of 0.05 to 0.3 (Becker et al., 2011; Boningari et al., 2018; Raghupathi et al., 2011). To be acceptable, the linear regression value (R^2) should be greater than or close to 0.995. Except for Mn_2O_3 (0.9887), the R^2 values for the entire NPs and NCs are in agreement (Figures 30-32(a) and Tables 14 – 16). The non-fitting of R^2 for Mn_2O_3 may be due to significant bulk absorption or small mass changes (Naderi, 2015). From the linear plots, the slope $[(C-1)/n_m C]$ and the intercept $(1/n_m C)$ were obtained. n_m is defined as $1/(\text{slope} + \text{intercept})$. The SSA in $m^2 \cdot g^{-1}$ is calculated by equation 50:

$$a_s = \frac{n_m L\, \sigma_m}{m\, x\, 22400} \qquad (50)$$

Where, a_s is the BET SSA of the single, BMONCs, and TMONCs of mass m in grams, L is Avogadro constant (6.022×10^{23} mol^{-1}), σ_m is the molecular adsorptive cross-sectional area occupied by N_2 gas molecule in the complete monolayer (0.162 nm^2 for N_2 gas), 22400 is the volume occupied by 1 mole of N_2 gas at STP, in mL. The symbols used are those as per IUPAC manual (Cohen et al., 2007; Mills & Jones, 1990).

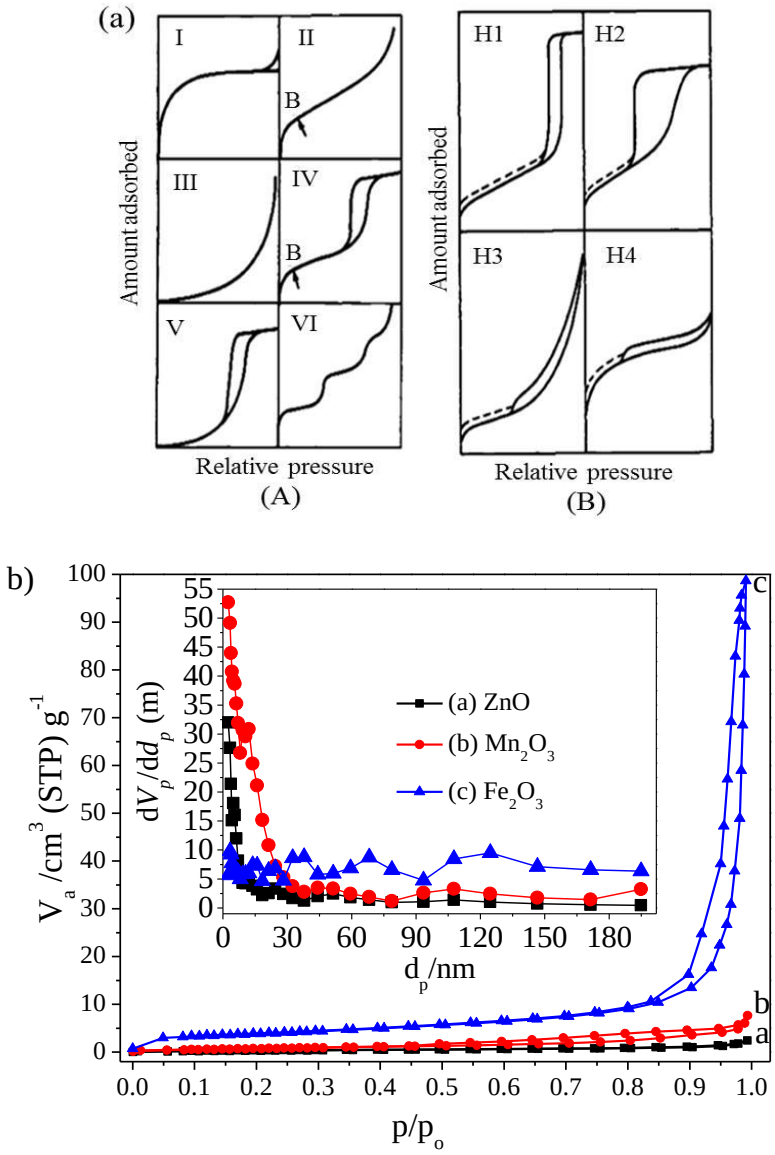

Figure 29 (a) The IUPAC classification (A) and hysteresis loops (B) (P. Kumar et al., 2016), (b) the combined BET plots of ZnO, Fe_2O_3, Mn_2O_3 NPs calcined at 500 °C (Inset: the respective pore size distributions based on the Barrett–Joyner–Halenda method).

Among six types of adsorption isotherms (Type I-VI) (Kumar et al., 2016), for mesoporous materials, it should look like a Type II or/and Type VI isotherms. The adsorption hysteresis loop shape that arises due to the none-overlying of the adsorption-desorption arc also has a close correlation with the size distribution, shape, and connectivity of the pores. The appearances of the synthesized NPs and NCs look like a typical IV isotherm with an H3 hysteresis loop. High adsorption capacities and sharp inflection at a high relative pressure (P/P0 > 0.8) indicate the coexistence of mesopores and macropores size distribution (Liu et al., 2016). The sharp capillary condensation step

between 0.40 - 0.85 for PVA-TMOP2 shows the presence of mesoporous materials with narrow pore size distribution (Lei et al., 2020).

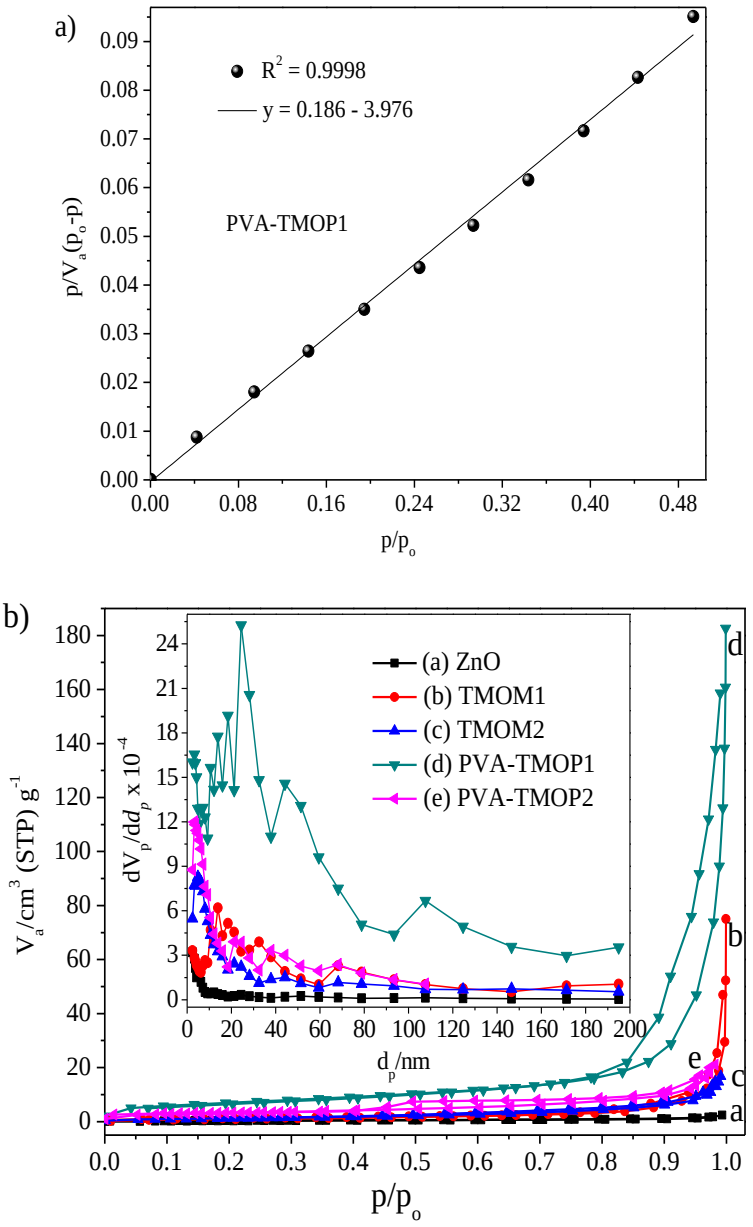

Figure 30. (a) The adsorption isotherm linear plot of PVA-TMOP1 NC, (b) the combined BET plots of ZnO NPs and TMOM1, TMOM2, PVA-TMOP1, and PVA-TMOP2 NCs calcined at 500 °C (Inset: the respective pore size distributions based on the Barrett–Joyner–Halenda method).

According to the BET theory, the value of *C* [(slope/intercept) + 1] has a close relationship with the shape of the isotherms. If its value is ≥ 80, the isotherm knee becomes sharp. < 50

indicates the presence of overlap between monolayer and multilayer adsorption, for < 2 the isotherm becomes either Type III or Type V. For defining the BET monolayer capacity of the NCs, the value recommended to be ≥ 80 (Thommes et al., 2015). As seen from Tables 14 - 16, the *C* values of ZnO, Mn_2O_3 NPs and BMO1, BMO2, and PVA-BMO1 NCs are < 80, and the *C* values for the other NPs and NCs is greater than 80. For PVA-BMO1, PVA-TMOM1, and PVA-TMOP1 NCs their slope is 0, which means not possible to define the value of *C* from the (slope/intercept) + 1 formula.

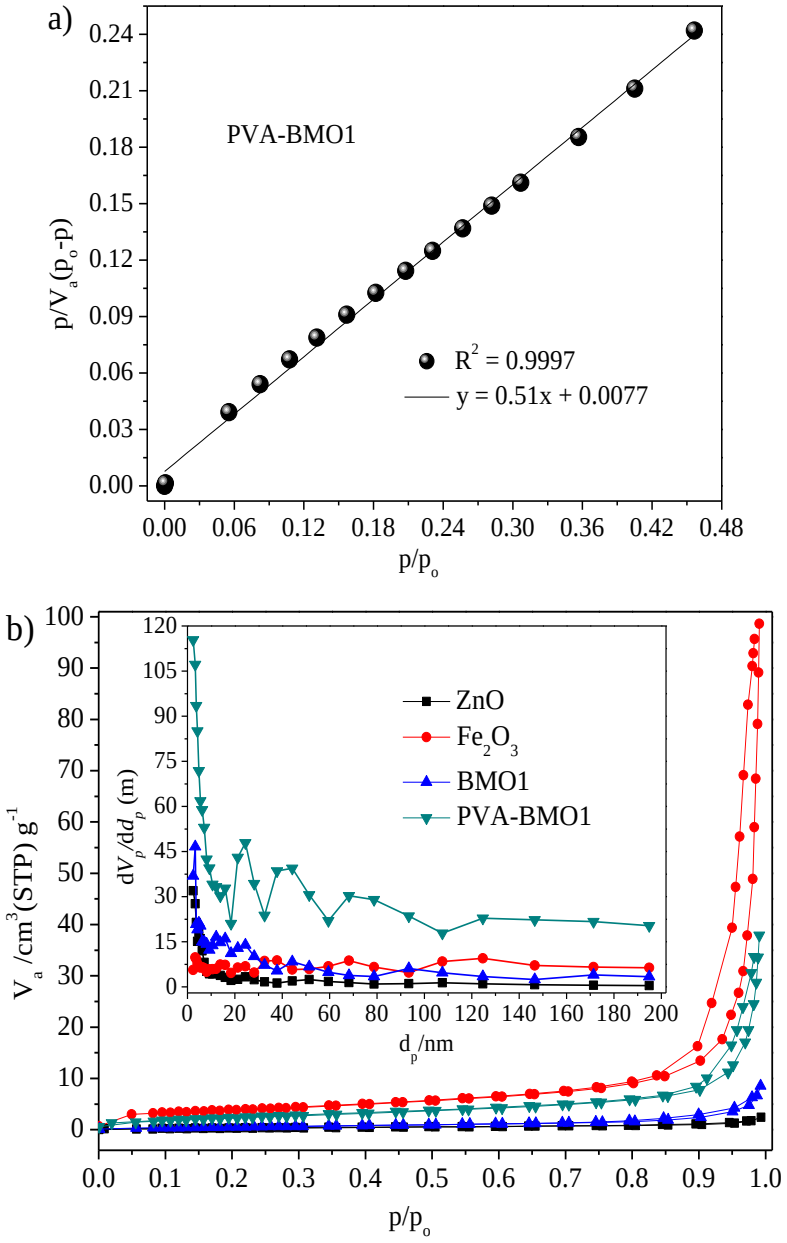

Figure 31. (a) The adsorption isotherm linear plots of PVA-BMO1 NC, (b) the combined BET plots of ZnO and Fe_2O_3 NPs and BMO1 and PVA-BMO1 NCs calcined at 500 °C (Inset: the respective pore size distributions).

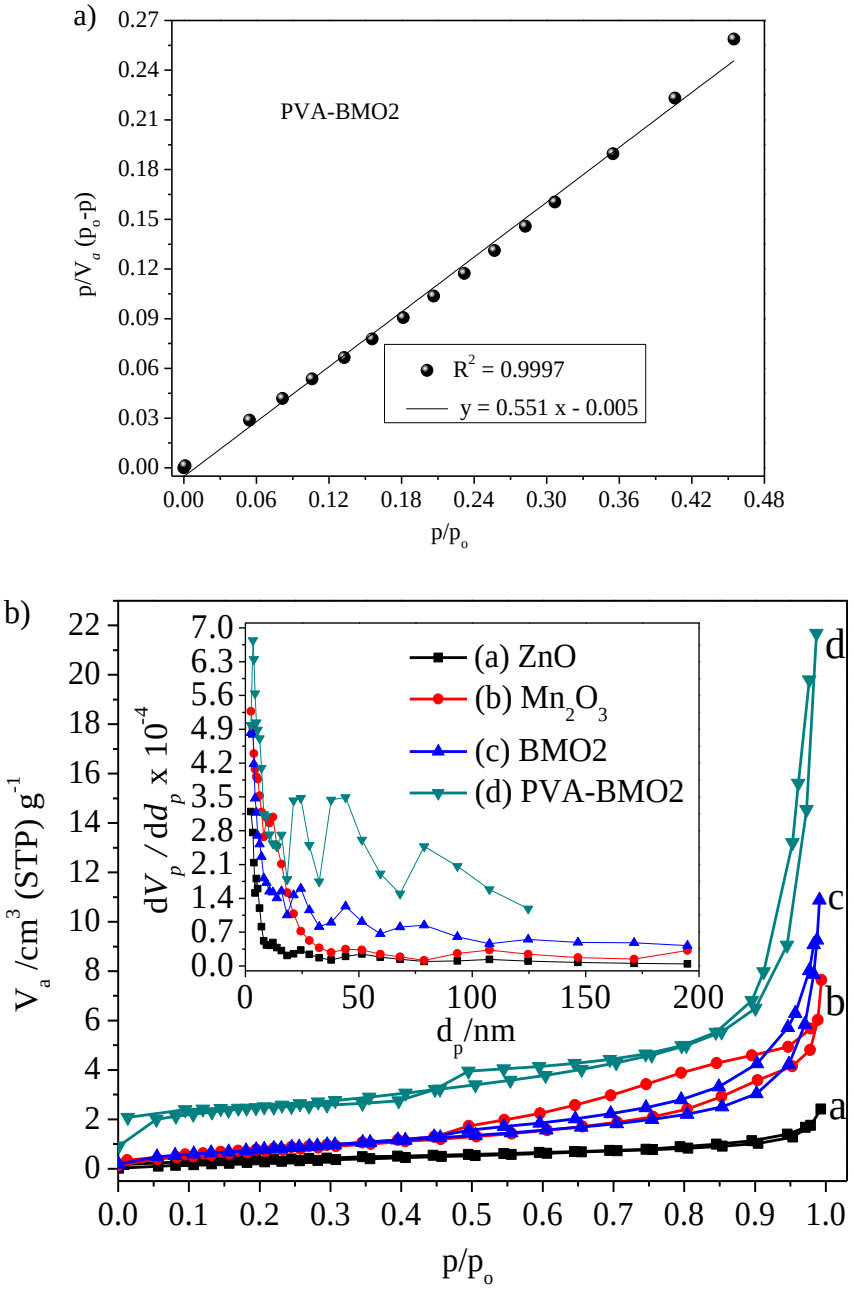

Figure 32. (a) adsorption isotherm linear plots of PVA-BMO2 NC, (b) the combined BET plots of ZnO and Mn_2O_3 NPs and BMO2 and PVA-BMO2 NCs calcined at 500 °C (Inset: the respective pore size distributions).

Table 14. The BET Textural properties result for single ZnO, Fe_2O_3 NPs, and Zn-Fe oxides NCs.

	ZnO	Fe_2O_3	BMO1	PVA-BMO1
Weight (g)	0.0791	0.0732	0.0765	0.0541
dv (cm^3)	16.219	15.711	15.800	16.296
Adsorbed	27	35	28	32
Desorbed	24	30	23	25
Slope	2.4216	0.3232	2.2125	0.4770
Intercept	0.4605	0.0015	0.0382	0.0150
R^2	0.9943	0.9997	0.9923	0.9995
Vm (cm^3g^{-1})	0.3470	3.0806	0.4443	2.0324
as(BET) ($m^2\ g^{-1}$)	1.51	13.40	1.93	8.85
C	6.26	222.25	58.96	32.82
Pv ($cm^3\ g^{-1}$)	0.0035	0.1434	0.0118	0.0556
dP (nm)	9.296	42.785	24.449	25.120

Table 15. The BET Textural properties result for ZnO, Mn_2O_3 NPs, and Zn-Mn oxides NCs.

	ZnO	Mn_2O_3	BMO2	PVA-BMO2
Weight (g)	0.0791	0.0762	0.1190	0.0624
dv (cm^3)	16.219	15.145	15.428	15.125
Adsorbed	27	28	29	27
Desorbed	24	24	21	26
Slope	2.4216	1.4223	1.4115	0.5162
Intercept	0.4605	0.0660	0.038	-
R^2	0.9943	0.9887	0.9946	0.9997
Vm (cm^3g^{-1})	0.3470	0.6719	0.6899	1.0208
as(BET) ($m^2\ g^{-1}$)	1.51	2.92	3.00	8.43
C	6.258	22.534	38.097	0.000
Pv ($cm^3\ g^{-1}$)	0.0035	0.0099	0.0159	0.0335
dP (nm)	9.296	13.513	21.205	15.909

Table 16. The BET Textural properties result for ZnO, Fe_2O_3, Mn_2O_3 NPs, and TMONCs.

	ZnO	Fe_2O_3	Mn_2O_3	TMOM1	TMOM2	PVA-TMOP1	PVA-TMOP2
Weight (g)	0.0791	0.0732	0.0762	0.1060	0.0747	0.0875	0.0724
dv (cm^3)	16.219	15.711	15.145	15.927	16.820	16.695	15.939
Adsorbed	27	35	28	30	24	27	29
Desorbed	24	30	24	22	22	23	26
Slope	2.4216	0.3232	1.4223	0.9744	0.9728	0.1819	0.3871
Intercept	0.4605	0.0015	0.0660	0.0000	0.0068	0.0000	0.0008
R^2	0.9943	0.9997	0.9887	0.9958	0.9988	0.9997	0.9998
Vm (cm^3g^{-1})	0.3470	3.0806	0.6719	1.0263	1.0208	5.4975	2.5780
as(BET) (m^2 g^{-1})	1.51	13.40	2.92	4.47	4.44	23.90	11.20
C	6.26	222.25	22.53	-	143.84	-	501.95
Pv (cm^3 g^{-1})	0.0035	0.1434	0.0099	0.0248	0.0328	0.1539	0.0326
dP (nm)	9.296	42.785	13.513	22.174	29.492	25.722	11.609

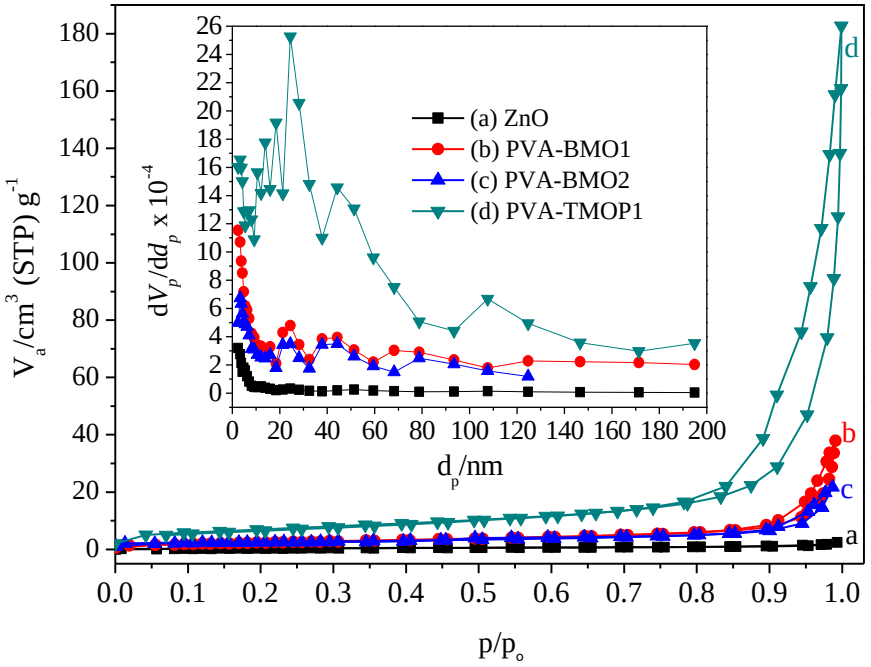

Figure 33. BET plots of ZnO NPs and PVA-BMO1, PVA-BMO2, PVA-TMOP1, and PVA-TMOP2 NCs calcined at 500 °C (Inset: the respective BJH pore size distribution plots).

The relatively large SSA and narrow mesoporous channels provide enough space and facilitate the rapid adsorption of molecules. The pore size distributions of the NPs and NCs were expressed in terms of the Barrett-Joyner-Halenda (BJH) curve. According to the IUPAC classification, NPs or NCs that have a pore size diameter of < 2.0 nm are

categorized as microporous, in the range between 2.0 to 50.0 nm as mesoporous, and > 50.0 nm as macroporous (ALOthman, 2012; Thommes et al., 2015; Zhao et al., 1996). As seen in Tables 14 - 16, for all single NPs, BMONCs, and TMONCs, the average pore size distribution is in the range of 9 – 43 nm, which indicates the domination of the mesoporous pore size distribution.

The appearance of pore size distribution peaks higher than 60 nm indicates the presence of some macroporous distribution (Figure 29 – 33 inset) (Liu et al., 2016). The narrowly and insignificant distributed pore size between 1 and 2 nm for PVA-TMOP1 NC corresponds to micropores. The pore size distribution curves show a relatively wider distribution for PVA-TMOP1 NC, which is consistent with the SEM results. Therefore, the NPs and NCs have meso-macroporous size distribution, with the mesoporous structure as dominant. Compared to single metal oxides, BMONCs, and other TMONCs, the PVA-TMOP1 showed enhanced SSA and optimized pore volume. In conclusion, the SAV and SSA of single ZnO, Fe_2O_3, and Mn_2O_3 NPs and BMONCs and TMONCs materials were successfully optimized using XRD pattern and BET analysis. Among them, the ternary PVA-TMOP1 NC was found to exhibit superior SAV and SSA values.

4.1.4. UV-vis and UV-vis-DRS analysis

The UV-vis-DRS spectroscopic analysis was applied to study the optical properties of the synthesized ZnO NPs and binary and ternary NCs powder. Besides, the UV-vis spectroscopic analysis was also applied to their suspensions. The optical properties along with Kubelka–Munk (K–M) plots of ZnO NPs and PVA-BMO1, PVA-BMO2, and PVA-TMOP1 NCs are given in Figures 34 and 35. Their percent reflectance versus wavelength plot shows a characteristic absorption edge near 380 nm (Figure 34). Compared to the other NCs (PVA-BMO1, PVA-BMO2, and PVA-TMOP1), pure ZnO NPs show high reflectance in the visible region. In fact, due to its broader bandgap energies (3.17 eV), it responds only to UV absorption. However, for the binary and ternary NCs, the reflectance in the visible region was reduced. The PVA-BMO1 and PVA-TMOP1 NCs have low reflectance (∼45%), compared to ZnO NPs. The order of reflectance was obtained to be as follows; ZnO > PVA-BMO2 > PVA-BMO1 ≅ PVA-TMOP1. This enhanced optical absorption for the NCs is due to the increased surface imperfection of the porous nature of the NCs as confirmed by the SEM and BET analysis (Nsib et al., 2015).

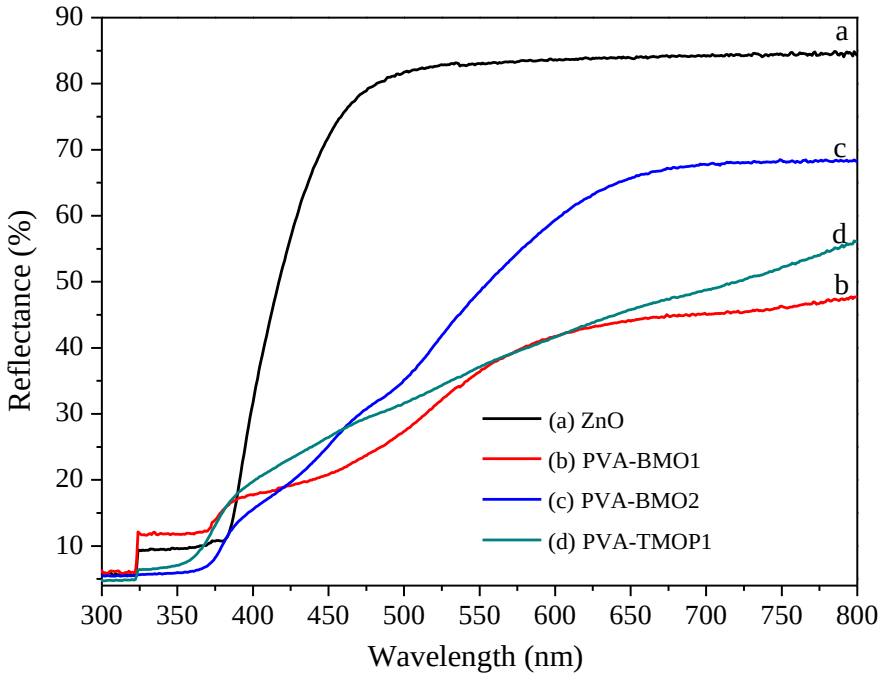

Figure 34. DRS plots of ZnO NPs and PVA-BMO1, PVA-BMO2, and PVA-TMOP1 NCs calcined at 500 °C.

In the parabolic band structure, the bandgap energy E_g and the absorption coefficient of a direct bandgap semiconductor α are related through equation 51 (Kumar Jangir et al., 2017):

$$(\alpha h\nu)^{1/n} = A(h\nu - E_g) \quad (51)$$

Where, h is Planck's constant, ν is the photon's frequency, and A is the slope in the linear region. Taking the *K–M* scattering coefficient *S* as a constant concerning the wavelength, and using the remission function in equation 51, the following expression was derived (equation 52):

$$(F(R)h\nu)^2 = A(h\nu - E_g) \quad (52)$$

Where, *F(R)* is equal to *K/S*, the molar absorption coefficient *K* is equal to $(1\text{-}R)^2$, the scattering factor *S* is equal to 2*R*, and *R* is the reflectance of the NPs and NCs and is defined as %*R*/100.

As shown in Figure 35(a) and (b), the direct and indirect bandgap energies of ZnO NPs and PVA-BMO1, PVA-BMO2, and PVA-TMOP1 NCs were measured by the extrapolation of the linear portion of the direct *K–M* function plots. Except for PVA-BMO2 NC of indirect *K–M* plots, the result showed the presence of non-noticeable bandgap change. The occurrence of pronounced redshift and obtaining the bandgap of around 2.0 eV in the presence of Mn_2O_3 is in good agreement with previously reported values work (Naeem et al., 2015, 2016; Saravanan et al., 2014). Compared to the single ZnO NPs, the observed slight bandgap tuning (blue shift) for the PVA-TMOP1 NCs attributed to the quantum confinement effects (Shah et al., 2014).

The non-obvious bandgap change was also further confirmed from the nanopowder suspension of UV-vis analysis. The analysis was performed during the PVA amount and precursors percentage crystallite size optimization of PVA-TMOP1 NCs. All samples show a characteristic absorption maximum (λ_{max}/nm) in the range of 330-350 nm [Figure 36(a) and (b)]. As seen in Figure 37(a) and (b), the direct and indirect bandgap energy of PVA and precursors percentage optimized PVA-TMOP1 NC was determined using Tauc plots (Coulter & Birnie, 2018).

Equation 51 also relates the optical absorption and difference between the energy of the photon and the bandgap (Kumar Jangir et al., 2017). The nature of the direct allowed/direct forbidden and indirect allowed/indirect forbidden electronic transition is dependent on the 1/n value. 1/2, 3/2, 2, and 3 are the values for direct allowed, direct forbidden, indirect allowed, and indirect forbidden electronic transition, respectively (Coulter & Birnie, 2018). The direct allowed transition for PVA and precursors percentage optimized PVA-TMONCs was determined to be 3.23 and 3.32 eV, and the indirect allowed transition is 3.03 and 2.99 eV, respectively. As confirmed by the XRD pattern, the non-existence of noticeable bandgap change on the UV-vis spectra confirms the non-incorporation of either Fe^0/Mn^0 metals or Fe^{3+}/Mn^{3+} ions in the ZnO crystalline lattice (Maya-Treviño et al., 2015). Furthermore, due to the presence of ionic radius differences between zinc, iron, and manganese ions, instead of doping, the formation of heterojunctions is also recommended for high-grade catalyst performance (Yu et al., 2016).

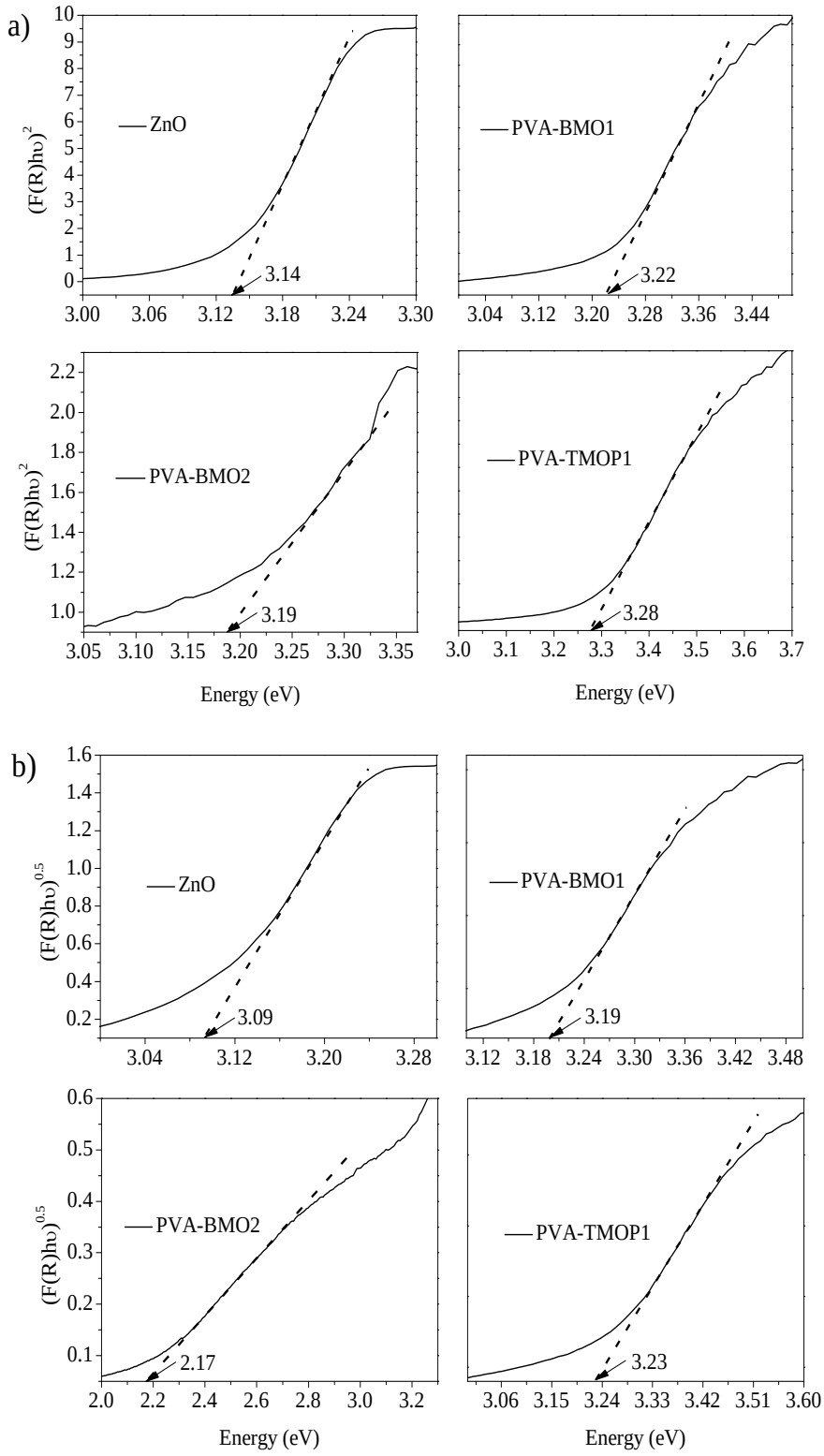

Figure 35. The direct (a) and indirect (b) K–M plots of ZnO NPs and PVA-BMO1, PVA-BMO2, and PVA-TMOP1 NCs calcined at 500 °C.

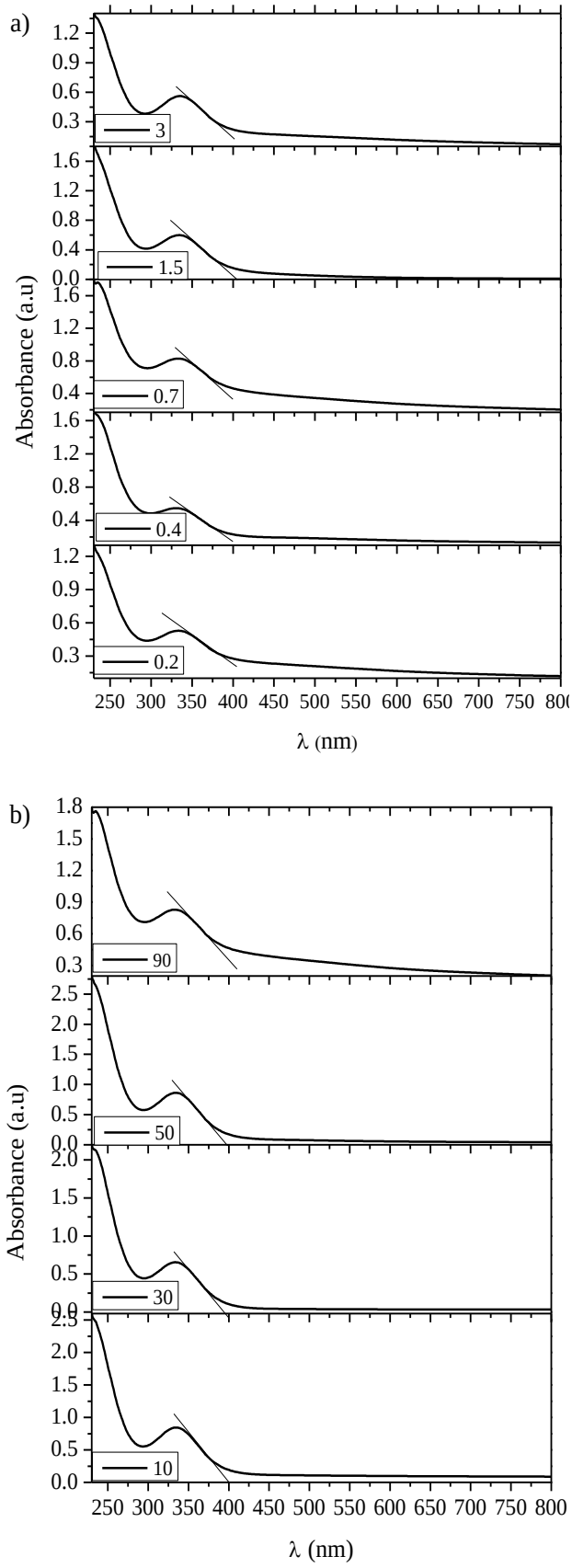

Figure 36. UV-vis spectra of (a) PVA amount optimization, (b) precursor's percentage optimization for PVA-TMOP1 NCs calcined at 500 °C.

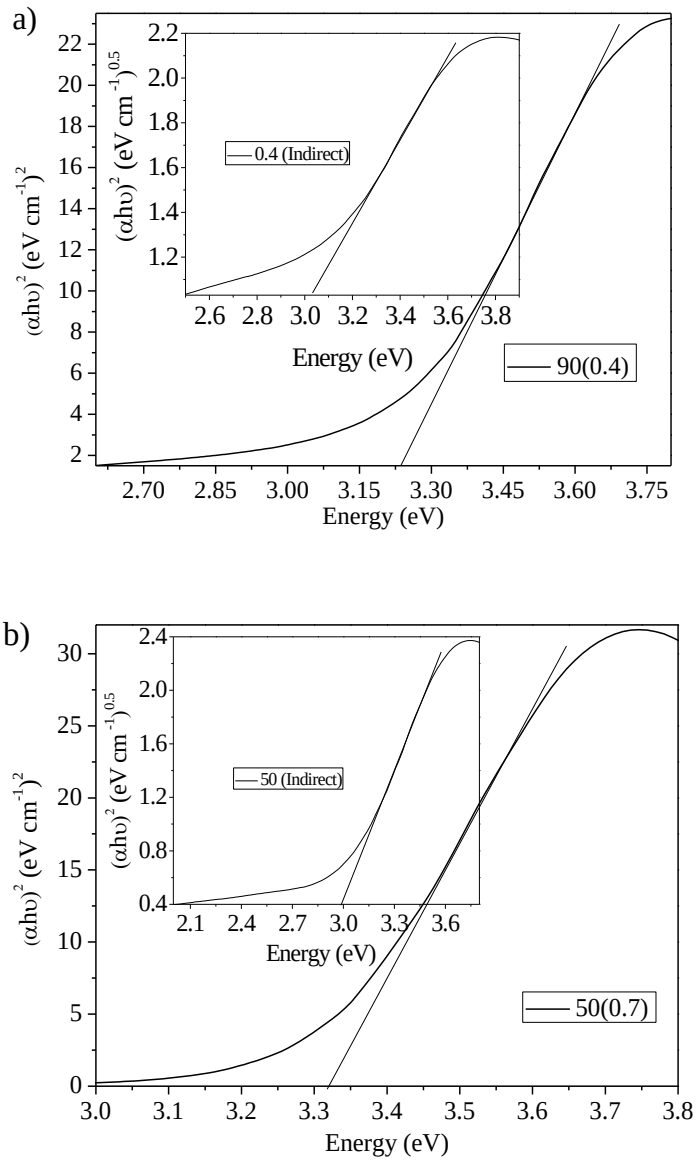

Figure 37. The direct allowed transition Tauc plots of (a) PVA and (b) precursors percentage optimized PVA-TMOP1 NCs calcined at 500 °C (Inset: the respective indirect allowed transition).

4.1.5. FT-IR analysis

The FTIR spectra that provide information about the functional group features of single ZnO NPs and BMONCs and TMONCs before calcination (U) and after calcination (C) are shown in Figures 38 - 40. The combined FTIR plots of ZnO NPs and PVA-BMO1, PVA-BMO2, and PVA-TMOP1 NCs are given in Figure 41. The broad absorptions band around ~3650 and ~1650 cm^{-1} for Figures 38 - 40 are due to the stretching vibration of chemisorbed hydroxyl groups and physisorbed water molecules. Semiconductor metal

oxide exhibits a strong absorption band below 1000 cm^{-1}; this is attributed to their transverse optical stretching modes (Anžlovar et al., 2011; Yang et al., 2010). The FTIR spectrum of ZnO NPs and NCs showed a characteristic absorption band in the range of 450 - 550 cm^{-1}. For the highly crystalline ZnO NPs, the absorption peaks were divided into two parts. While for the NCs, only one peak at about 450 cm^{-1} was observed. These absorption peaks correlate with the transverse-optical (TO)- and longitudinal-optical (LO)-phonon frequency (Yang et al., 2010).

The shape, number, and wavenumber position of the bands are dependent on the chemical composition, morphology, and crystal structure of the NPs and NCs (see Figure 42). If the morphology of the NPs and NCs changed from spherical (zero) dimension to one, two, or three-dimensional morphology, the broadness and splitting also increased (Fatehah et al., 2014; Sigoli et al., 1997). The wavenumber position shifts and peak number differences were noticed between the ZnO NPs and NCs. The wavenumber shift is dependent on the strength or weakness of the metal-oxygen bond (Parler et al., 2001; Wachs, 1996). The shift to the higher wavenumber/frequency for the calcined NCs compared to the uncalcined was due to the increased rigidity of the metal-oxygen network as condensation occurs (Lan et al., 1993). As seen in Figures 38 – 40, there are shifts towards lower wavenumber/frequency stretches for PVA-BMO2 and PVA-TMOP1 (3560 cm^{-1}), compared to the ZnO and PVA-BMO1 (3655 cm^{-1}). It was indicating that the introduction of the Mn_2O_3 phase was weakening the metal-oxygen bond (Parler et al., 2001). In fact, the less stable properties of the PVA-BMO2 were confirmed on the DTG analysis. Besides, the observed shift may also be due to the surface passivation influences of PVA during synthesis, indicating that the existence of a hydrogen bond between the PVA (O-H group) and metal oxide's surface (Hong et al., 2009).

The presence of irregular morphologies for ZnO NPs and spherical morphologies for NCs has been confirmed from SEM image analysis. Comparing the spectra of calcined NPs/NCs with uncalcined NCs (Figures 38-40), the obtained distinctive peak for uncalcined NCs at ~1450 cm^{-1} is due to the bending vibration of the PVA CH_2 group (Huang et al., 2016; Sudha et al., 2012). The absorption peaks that appeared at ~1640 and ~1400 cm^{-1} are either due to C=C and C-C stretching, respectively, or symmetric and asymmetric stretching vibration of the C=O/C-O group (Ahmed et al., 2018; Huang et al.,

2016; Tabrizi Hafez Moghaddas et al., 2019). The absorption bands that appeared at ~940 cm^{-1} is ascribed to the symmetric C-H and bending vibration of the $–CH_3$ group. The source for the other peaks is from the intermediate impurities created during synthesis (Anžlovar et al., 2011; Znaidi et al., 2003).

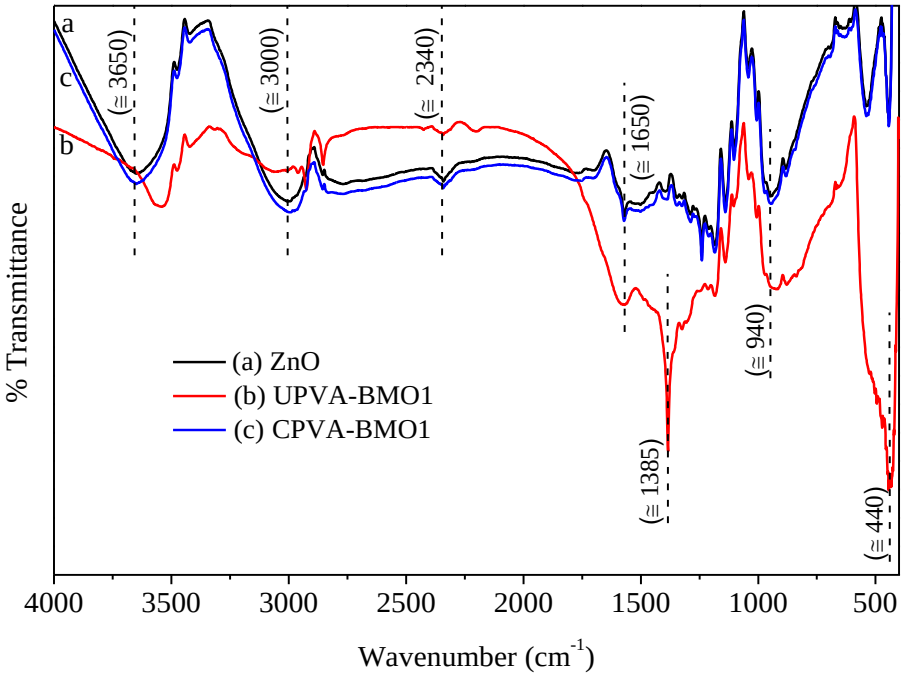

Figure 38. FT-IR spectra of calcined (C) ZnO NPs, calcined PVA-BMO1 NC, and uncalcined (U) PVA-BMO1 NC.

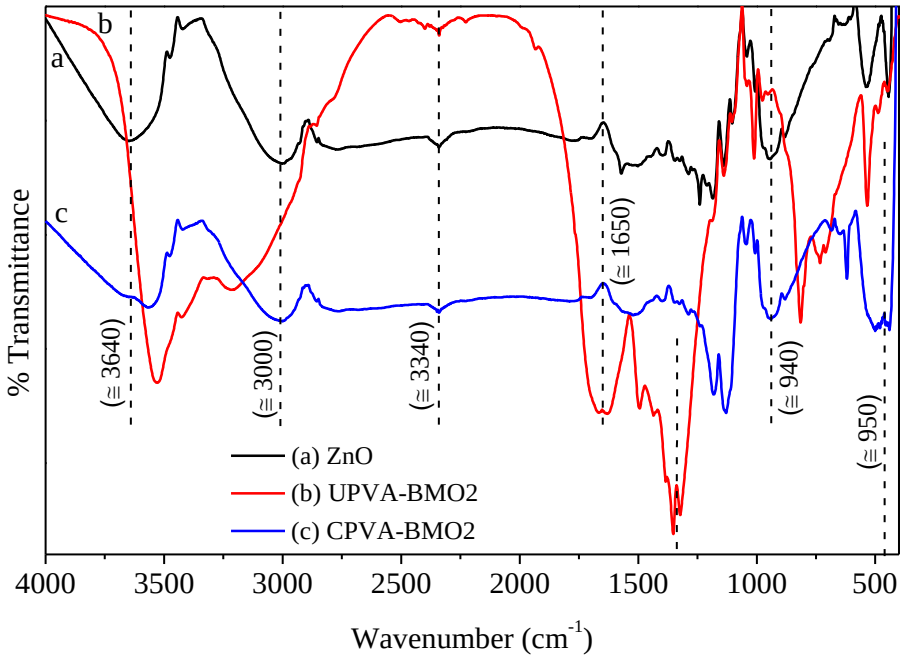

Figure 39. FT-IR spectra of calcined (C) ZnO NPs, calcined PVA-BMO2 NC and uncalcined (U) PVA-BMO2 NC.

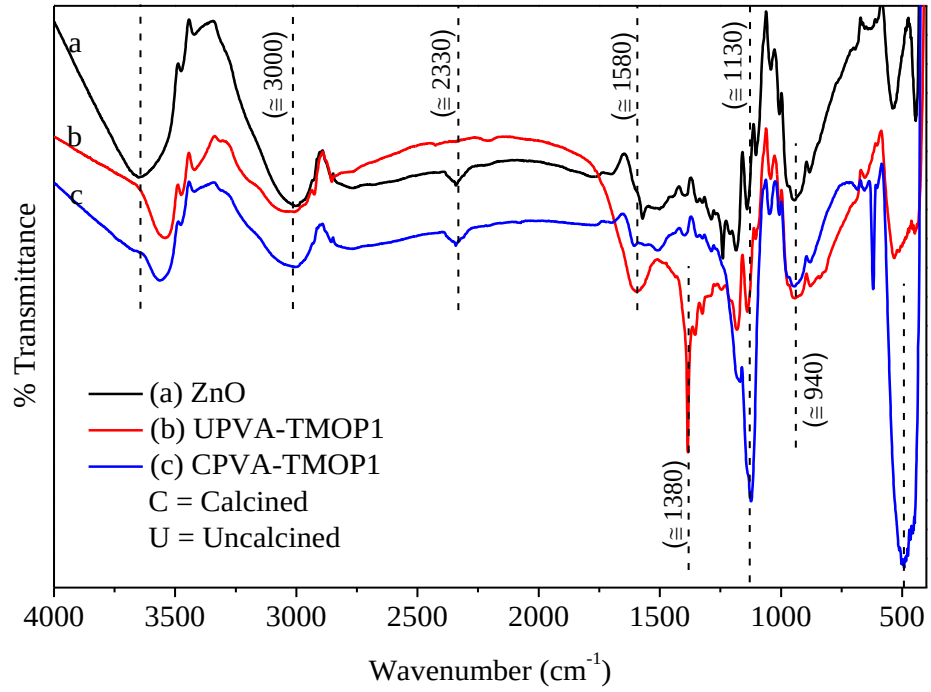

Figure 40. FT-IR spectra of calcined (C) ZnO NPs, calcined PVA-TMOP1 NC and uncalcined (U) PVA-TMOP1 NC.

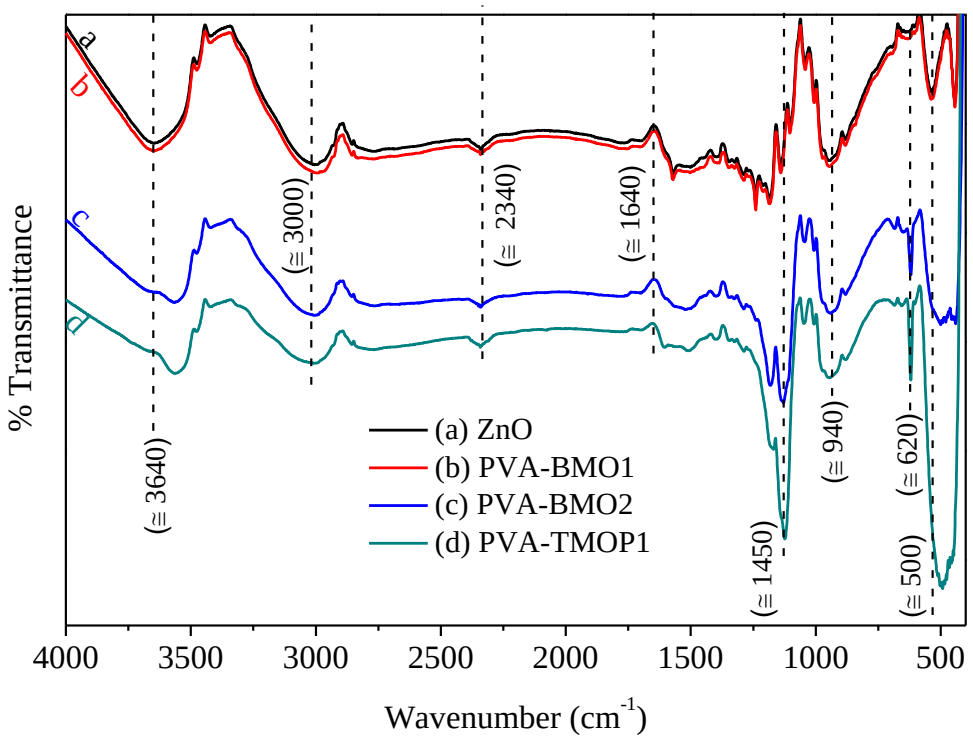

Figure 41. FT-IR spectra of ZnO NPs and PVA-BMO1, PVA-BMO2, and PVA-TMOP1 NCs calcined at 500 °C.

4.1.6. SEM-EDX analysis

The SEM-EDX is an instrument that creates magnified images that reveal microscopic-scale information on the size, shape, composition, crystallography, and other physical and chemical properties of a specimen (Goldstein et al., 2018). The SEM images of ZnO NPs and BMO1, BMO2, TMOM1, TMOM2, and PVA-TMOP2 NCs are shown in Figure 42(a)-(f), respectively. The SEM images of PVA-BMO1, PVA-BMO2, and PVA-TMOP1 NCs are also shown in Figure 43(a)-(c). As seen from the SEM images of the BMONCs and TMONCs synthesized without PVA, their aggregation/agglomeration behavior is higher compared to PVA-BMONCs and PVA-TMONCs synthesized using PVA. The morphology of BMONCs and TMONCs also has higher crystallinity compared to the PVA-BMONCs and PVA-TMONCs, which complies with the XRD results. The SEM images of BMO2 and TMOM2 NCs show greater crystallinity [Figure 42(c) and (e)]. The crystallinity of BMO1 and TMOM1 NCs is less compared to the BMO2 and TMOM2; however, they have a highly agglomerated/aggregated appearance [Figure 42(b) and (d)]. In the agglomeration of BMO1, the particles are present as adhering to each other due to high surface energy (Moeinian & Akhbari, 2015) creating bigger and heavier aggregates. The distance between the agglomerated particles is smaller and a remnant magnetization is observed, also in the off-state condition (Phulé et al., 1999). This internal magnetization of one aggregate attracts others making materials performance decay faster (Dassisti & Brunetti, 2020).

For the adsorption of pollutants and photocatalysis (Mazaheri & Kalbasi, 2015; Zhang et al., 2011), as gas sensors (Du et al., 2007), and as electrodes material (Linglu Yang et al., 2005); the high porosity and high SSA provide sufficient active sites different from solid structures. The porous nature of PVA-TMOP1 NC also assists in the creations of fast charge transport properties and good interaction with electrolyte solutions during the electrochemical process (Laurenti & Cauda, 2018) [Figure 43(a)]. The SEM images of PVA-TMOP2 NCs [Figure 42 (f)] and PVA-TMOP1, PVA-BMO1, and PVA-BMO2 (Figure 43(a) – (c), respectively) have better porosity compared to the other NPs and NCs, a consistent result was also noted from the BET analysis.

.

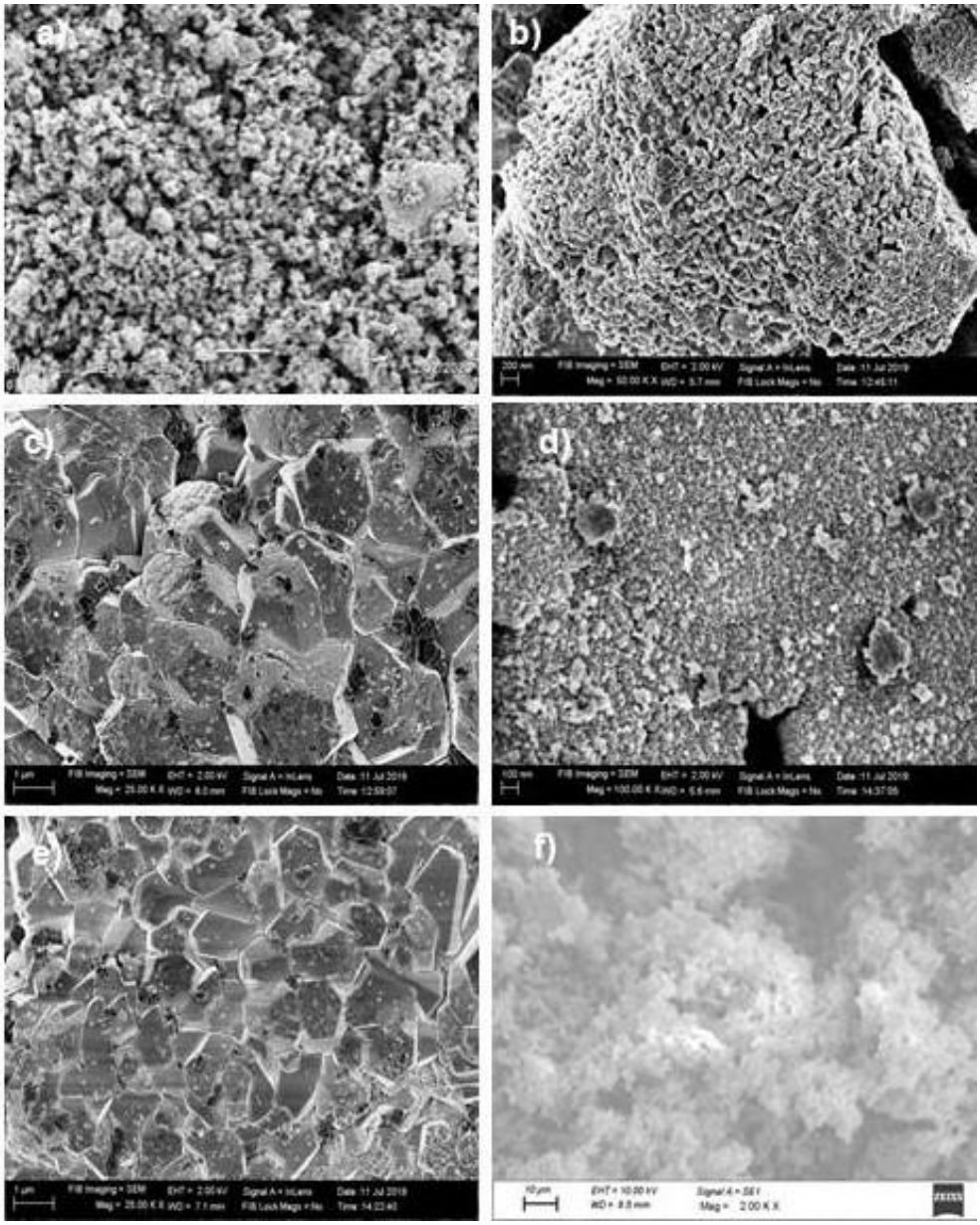

Figure 42. SEM morphology of (a) ZnO NPs and (b) BMO1, (c) BMO2, (d) TMOM1, (e) TMOM2, and (f) PVA-TMOP2 NCs calcined at 500 °C.

The SEM images obtained for samples synthesized during precursors' percentage and PVA amount optimizations for PVA-TMOP1 NC are shown in Figures 44 and 45, respectively. The images are taken with similar magnification. As seen from the percentage optimization SEM images (Figure 44), an increase in the quantity of zinc precursor percentage from 30 to 90, results in enhancing the porous nature of the NCs. It is due to an increase in the auto-combustion process as understood during the experiment. The final image in Figure 44 is the morphology of PVA-TMOP1 NC at high resolution. As seen from the image, highly dispersed particles are clearly visible. The image also showed the porous nature of the material. The inset image is the auto-combusted image

during synthesis at the final drying process at about 110 °C. As seen from Figure 45 of ZnO NPs synthesized without PVA [100(0)], it has agglomerated morphology. Loading of 0.2 g to 1.5 g of PVA, the morphology was appeared to have a less agglomerated/aggregated and porous nature. The PVA amount of 1.5 g has a flat type of morphology. The final 3 g of PVA loaded image show a highly condensed porous morphology.

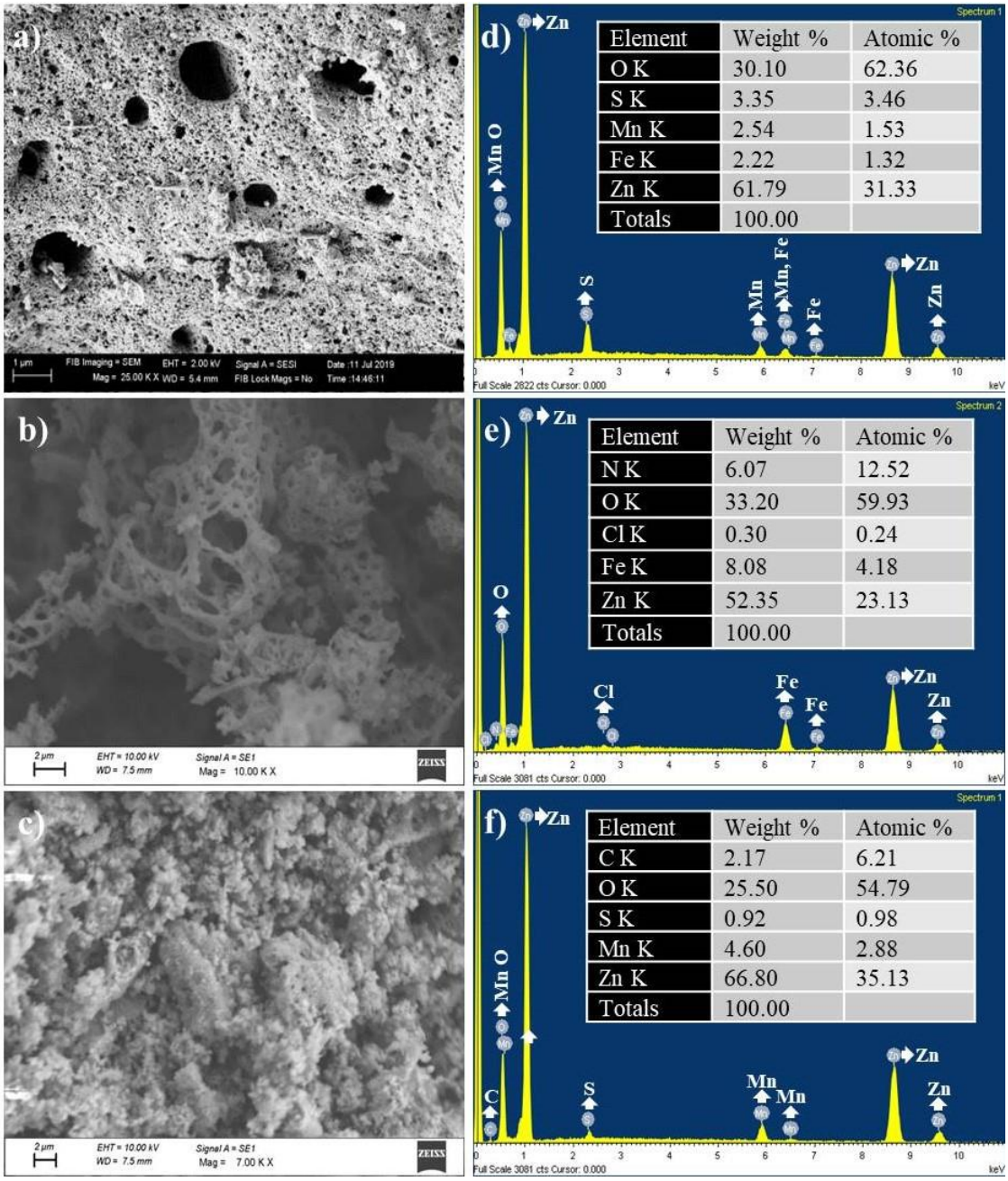

Figure 43. SEM images and the respective EDX spectra of (a and d) PVA-TMOP1, (b and f) PVA-BMO1, (c and f) PVA-BMO2 NCs, respectively calcined at 500 °C. Inset (b-f) the EDX compositional analysis.

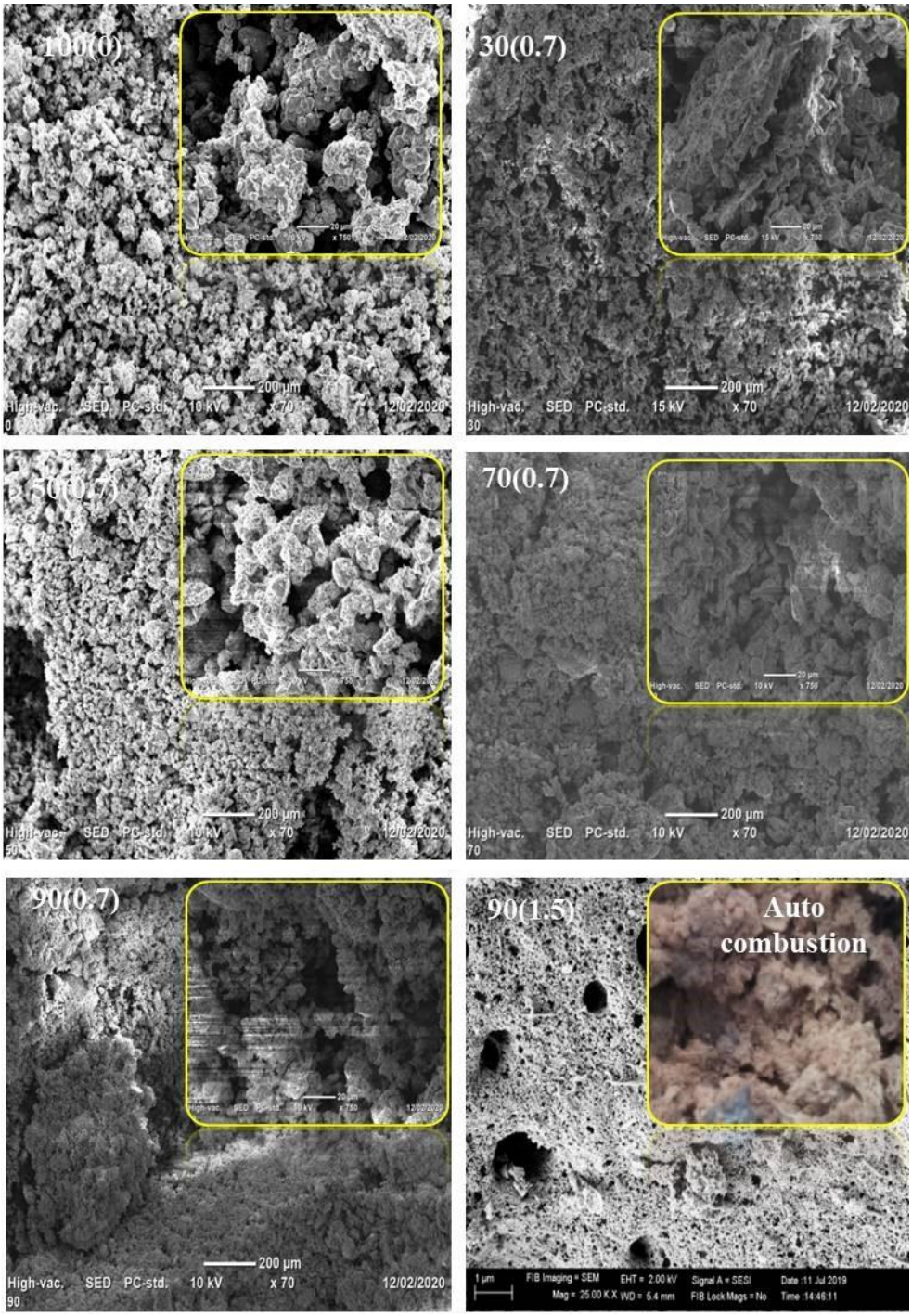

Figure 44. SEM images of PVA-TMOP1 NCs during precursors percentage optimization using constant PVA amount. These images have 200 µm scales with x70 magnification for normal and 20 µm scales with x750 magnification for the inset.

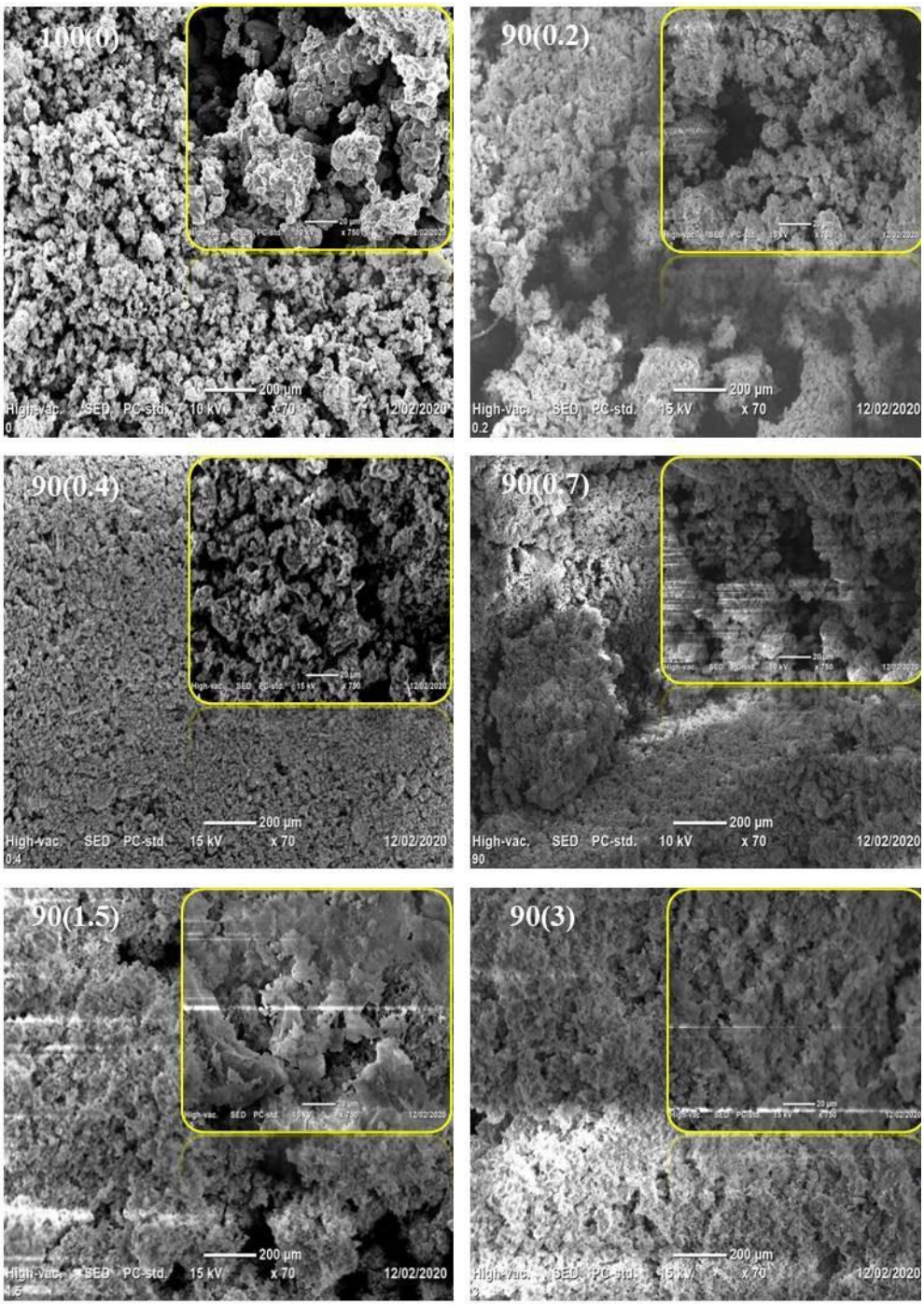

Figure 45. SEM images of PVA-TMOP1 NC during PVA optimization using constant precursors percentage, respectively. These images have 200 µm scales with x70 magnification for normal and 20 µm scales with x750 magnification for the inset.

The compositional analysis by EDX technique showed the presence of the expected Zn, Mn, Fe, S, and O elemental compositions in all BMONCs and TMONCs [Figure 43(d) - (f)]. For PVA-TMOP1, PVA-BMO1, and PVA-BMO2 the major peaks at 1, 0.5, and 6.5 keV were identified for Zn, Mn, and Fe, respectively (Adil et al., 2017; Khurram et al.,

2021). However, S on PVA-TMOP1; Cl and N on PVA-BMO1; C and S on PVA-BMO2 as impurities were observed. The source for these impurities is most probably from the $MnSO_4.H_2O$ precursor during synthesis and standards used during analysis.

4.1.7. TEM analysis

The TEM, SAED, and d-spacing analyses conducted for PVA-TMOP1, PVA-BMO1, and PVA-BMO2 NCs are given in Figure 46(a)-(c). From the TEM images, the sizes of the synthesized NCs were found to be in the nanometer range (~10 – 70 nm); this complies with the XRD analysis. From the TEM images, it is also possible to visualize the presence of twins separated by boundaries (oriented attachment) between metal oxides (Penn, 1998). During oriented attachment, due to fission as a driving force, the particles share a common crystallographic orientation (Penn, 1998; Xue et al., 2014; Jing Zhang et al., 2010). The introduction of capping ligands has been reported to play multiple roles, including i) promoting or inhibiting aggregation and thus influencing oriented attachment growth, or ii) hindering Ostwald ripening from occurring and thus facilitating oriented attachment (Xue et al., 2014). It leads to the formation of heterojunctions between the metal oxides that assists in continuous charge transfer capability (Muñoz-Rojas et al., 2008; Zeng et al., 2017). The HRTEM image analysis was performed using Gatan microscopy suit software [Figure 46(d)-(f)]. For PVA-TMOP1 NC, the obtained d-spacing value of 0.28 nm is consistent with the (002) plane of ZnO NPs and 0.34 nm is matching to (221) plane of α-Mn_2O_3 [Figure 46(d)] (Liu et al., 2016; Zhao et al., 2018). The lattice fringe with an adjacent d-spacing value of 0.368 nm corresponds to the (012) atomic plane of α-Fe_2O_3 (Yan et al., 2011). Yet, the lattice fringes of α-Fe_2O_3 were not found on the HRTEM image of PVA-BMO1 NC, which is possibly due to the highly dispersed state of it or because of a random selection of the crystallite during resolution [Figure 46(e)]. Besides, as seen in Figure 46(f), the d-spacing value of ~0.343 nm is corresponding to the (221) atomic plane of α-Mn_2O_3 (Zhao et al., 2018). Herein also, the lattice fringes of ZnO were not detected on the HRTEM image of PVA-BMO2 NC, which is because of a random selection of the crystallite during resolution.

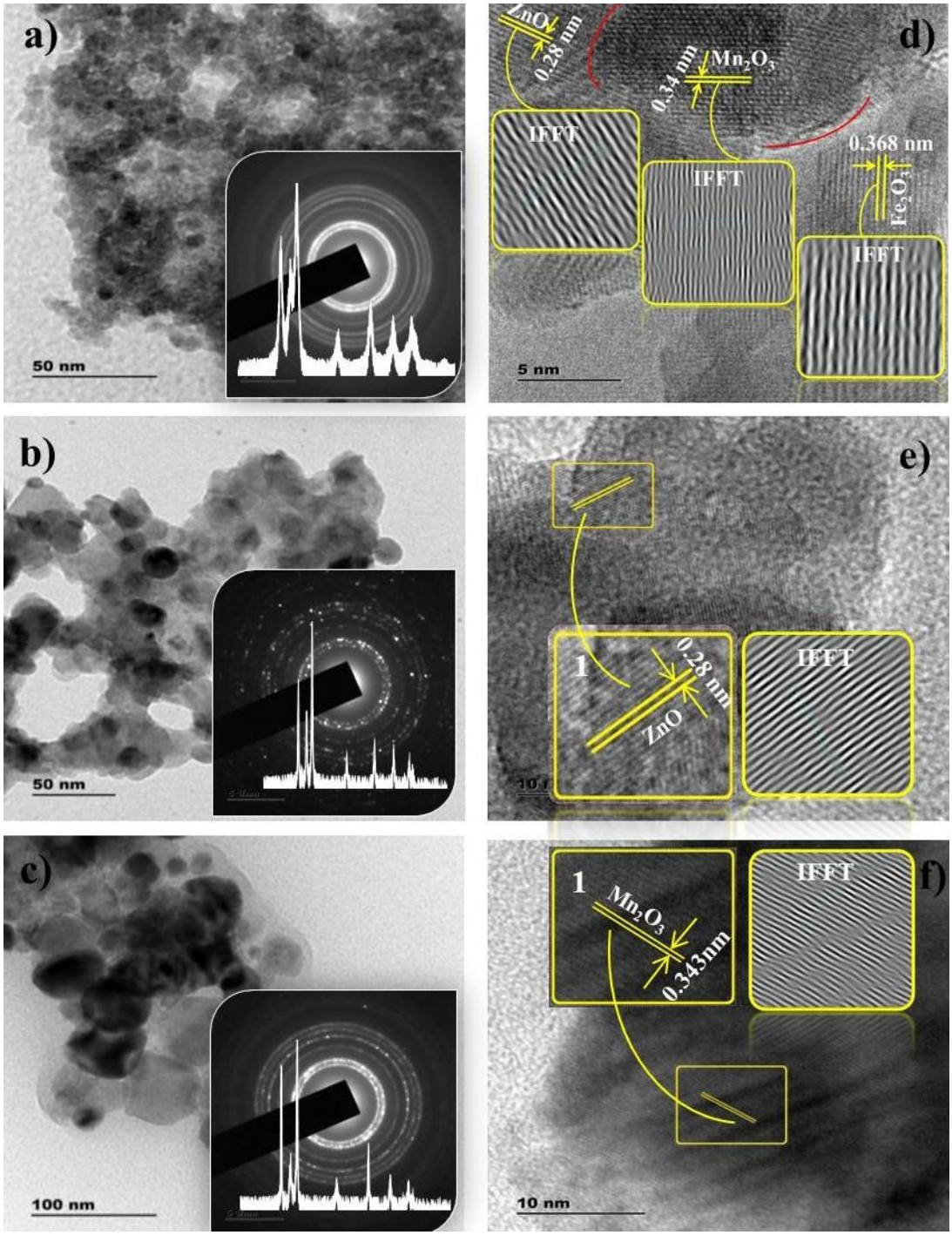

Figure 46. (a-c) TEM images of PVA-TMOP1, PVA-BMO1, and PVA-BMO2 NCs, respectively (inset: the respective SEAD rings and XRD pattern), (d-f) the respective HRTEM image [Inset: 1 (magnified)]. IFFT: Inverse fast Fourier transmission.

The stacking faults (type surface defects) on the inverse fast Fourier transmission (IFFT) analysis of the HRTEM image indicate the porous/semi-crystalline nature of the NCs (see IFFT images of Figure 46(d)-(f) inset). The measured interplanar spacing of diffraction rings on fast Fourier transform selected-area electron diffraction (SAED) patterns of

0.2864, 0.2543, 0.1969, 0.1663, 0.1520, 0.1419, 0.1278, and 0.1104 nm for PVA-TMOP1 NC matches with the hexagonal wurtzite ZnO structure as detected on the XRD pattern (Figure 46(a) inset). The SAED patterns for PVA-BMO2 NC (0.2860, 0.2707, 0.1996, 0.1717, 0.1559, 0.1445, and 0.1150 nm) (Figure 46(c) inset) also matches with the hexagonal wurtzite ZnO structure. The SAED patterns of 0.2900, 0.2540, 0.2042, 0.1671, 0.1609, 0.1652, 0.1297, 0.1500, and 1070 nm for PVA-BMO1 NC (Figure 46(b) inset) also in close relationship with ZnO structure. Yet, the additional uneven spots were observed on the PVA-TMOP1 and PVA-BMOP1 NCs, these spots are most probably for Mn_2O_3 or/and Fe_2O_3. The diffraction spots present exactly on the SAED rings indicate the crystallinity of ZnO NPs. The spots present outside of the ring are for Fe_2O_3 or/and Mn_2O_3 (Zhai et al., 2012). None of the spots were detected in PVA-TMOP1 NC, this diffuse rings pattern on the PVA-TMOP1 NC indicates the less crystalline properties of the sample. Besides, unlike that of PVA-TMOP1 and PVA-BMO1 NCs (Figure 46(a) and (b), respectively), the presence of two different crystallites for PVA-BMO2 [Figure 46(c)]; shows the presence of two distinct metal oxides.

4.1.8. XPS analysis

On the XRD and TEM analysis, there are certain doubts on distinguishing the metal oxide phases (oxidation state and chemical composition). These doubts were further clarified on the XPS analysis. Figures 47 and 48 are the XPS analysis results of ZnO NPs and PVA-BMO1, PVA-BMO2, and PVA-TMOP1 NCs. The inset plots are the high-resolution spectrum of the elements. The zinc (Zn 2p, 3s, 3p), iron (Fe 2p, 3p), manganese (Mn 2p, 3p), and oxygen (O 1s, 2s) are expected from the composition of ZnO, Fe_2O_3, and Mn_2O_3. The typical survey spectrum of the ZnO NPs was depicted in Figure 47(a), which shows the presence of Zn 2p, O 1s, and C 1s elements [Figure 47(a) inset (i - iii)]. As seen in Figure 47(a) inset (iii), the high resolution ZnO NPs peaks at ~1022.0 eV and 1045.2 eV correspond to Zn $2p_{3/2}$ and $2p_{1/2}$, respectively (Mao, 2019).

The typical wide scan survey spectrum of the PVA-BMO1 NC is depicted in Figure 47(b), which shows the presence of Zn 2p, Fe 2p, O 1s [(Figure 47(b) inset (i - iii)], and C 1s chemical states. The high-resolution spectrum of Fe is given in Figure 47(b) inset (ii), the electron binding energy of Fe ($2p_{3/2}$, ~711 eV and $2p_{1/2}$, ~725 eV) is consistent with that of Fe_2O_3 and is in good agreement with the literature (Wu et al., 2010). Besides, the $2p_{3/2}$

and $2p_{1/2}$ are accompanied by satellite structures on their high binding-energy side, indicated by arrows at the respective 720 eV and 730 eV, which are the fingerprints of the electronic structures of Fe^{3+} (Fe_2O_3) (Yu Liu et al., 2012; Wu et al., 2010). The binding energies at ~1022.2 eV and 1045.4 eV are consistent with the electronic states of Zn $2p_{3/2}$ and $2p_{1/2}$, respectively.

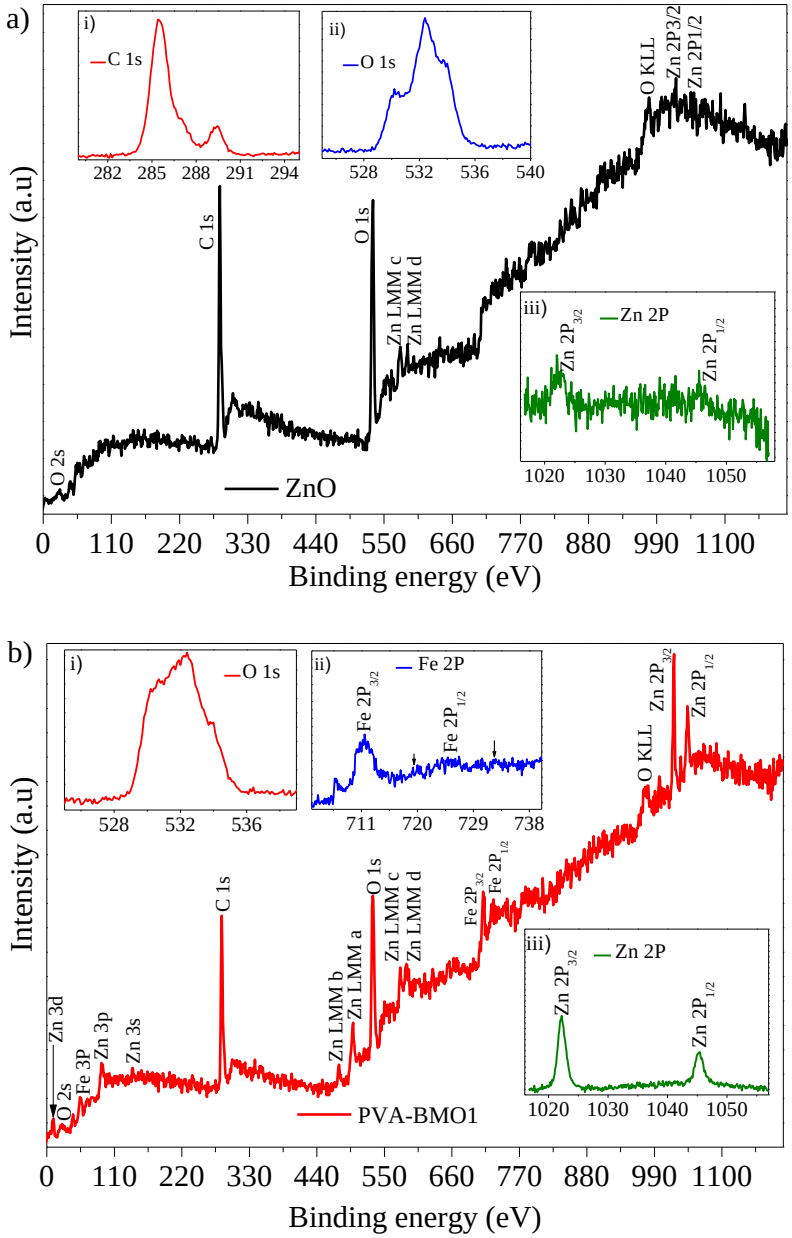

Figure 47. XPS plots of (a) ZnO, (b) PVA-BMO1 calcined at 500 °C. Insets are the high-resolution XPS spectrum.

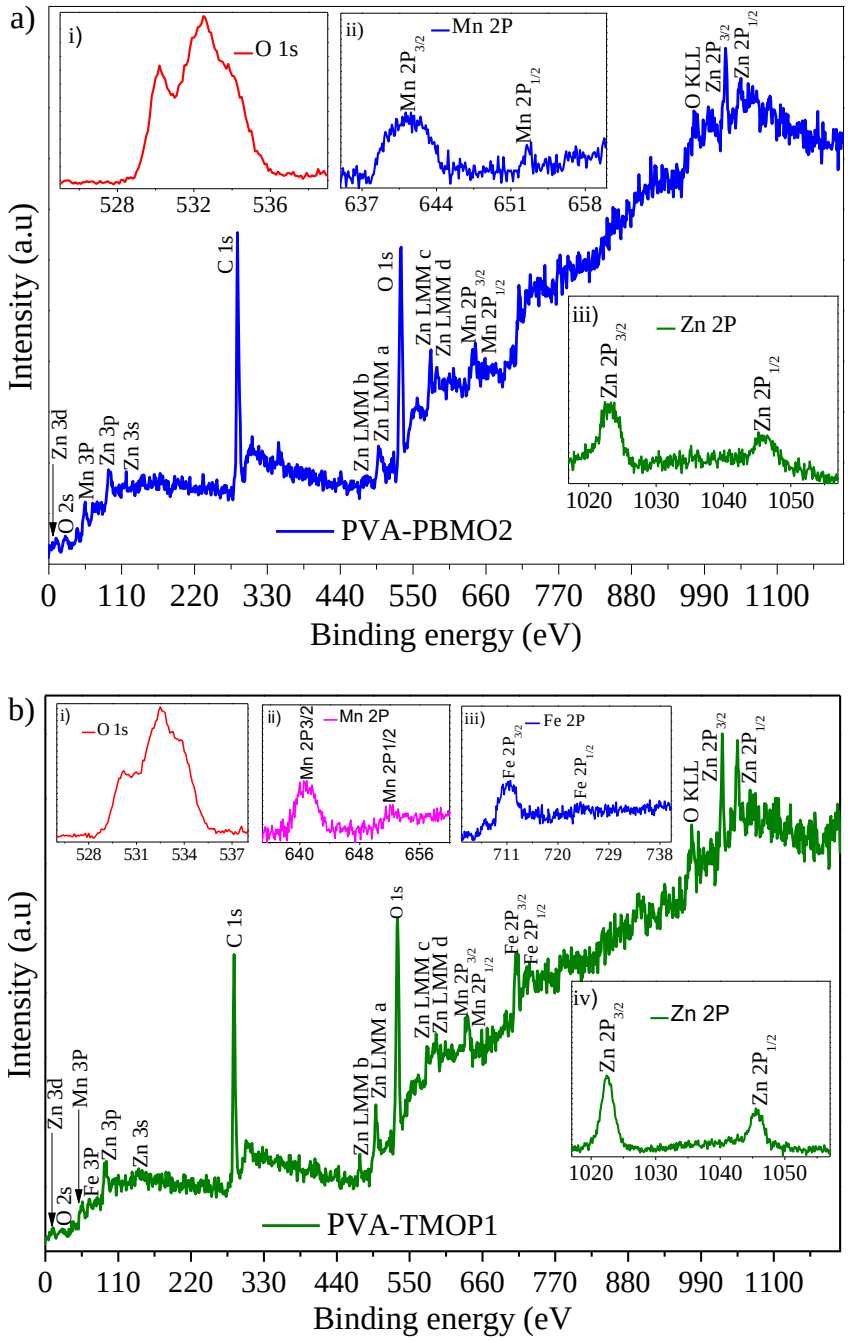

Figure 48, XPS plots of (a) PVA-BMO2, (b) PVA-TMOP1 calcined at 500 °C. Insets are the high-resolution XPS spectrum.

The wide scan survey spectrum of the PVA-BMO2 NC is depicted in Figure 48(a), which shows the presence of Zn 2p, Mn 2p, O1s [Figure 48(a) inset (i - iii)], and C 1s chemical states. The high-resolution Mn 2p orbital region shows the binding energies of Mn $2p_{3/2}$ and Mn $2p_{1/2}$ peaks exist at binding energies of 641.1 eV and 653.2 eV [Figure 48(a) inset (ii)] is also in good agreement with the literature (Saravanan et al., 2015). The approximate splitting energy of 12.1 eV between Mn $2p_{3/2}$ and Mn $2p_{1/2}$ is a typical value

for Mn^{3+} (Mn_2O_3) (Guorui Yang et al., 2014). Figure 48(a) inset (iii) displays a high-resolution spectrum of Zn, the peaks at 1022.7 eV and 1045.8 eV correspond to Zn $2p_{3/2}$ and $2p_{1/2}$, respectively. Figure 48(b) confirms the presence of Zn 2p, Mn 2p, Fe 2p, O 1s [Figure 48(b) inset (i - iv)], and C 1s chemical states in the PVA-TMOP1 NC. As seen in Figure 48(b) inset (ii), the Mn $2p_{3/2}$ and Mn $2p_{1/2}$ peaks exist at binding energies of 641.1 eV and 653.7 eV; whereas, the Fe $2p_{3/2}$ and Mn $2p_{1/2}$ peaks exist at binding energies of 711.3 eV and 722.3 eV. The binding energy of Zn 2p in the PVA-BMO1, PVA-BMO2, and PVA-TMOP1 NCs show a positive shift compared to that of pure ZnO (1022.0 eV). This shift is reported to be due to the electron transfer from the Fermi level of ZnO to the Fermi level of Fe_2O_3 or/and Mn_2O_3 (Hu et al., 2011; Yu Liu et al., 2012; Jun Zhang et al., 2011).

4.1.9. CV and EIS analysis

The electrochemical properties of ZnO NPs and PVA-BMO1, PVA-BMO2, and PVA-TMOP1 NCs were investigated by EIS and CV analytical techniques. The CV plots of these NPs and NCs at different scan rates are given in Figures 49 - 51 (a) and (b). For ZnO NPs [Figure 49(a)], an increase in the scan rates, a slight increase in the redox peak current was observed, yet, the oxidation-reduction peaks were not found. Figure 49(a) inset (i) is the magnified plot of ZnO NPs modified electrode and Figure 49(a) inset (ii) is for the un-modified electrode. For PVA-TMOP1 [Figure 49 (b)], an increase in the scan rate caused a slight increase in the redox peak current. Unlike that of ZnO NPs, a pair of fast and reversible redox reaction was noticed for PVA-TMOP1 NC [see Figure 49(c)]. This quick and reversible redox reactions is clarified to be due to the porous nature of the NCs that allows rapid proton intercalation and de-intercalation processes without affecting the performance of the electrode (Liu et al., 2019). This is also in compliance with the BET, XRD, SEM, and EIS characterizations results. The obtained peak potential difference ($\Delta E_{a,c}$) between anodic peak potential peak (E_{pa}) (+0.401V) and cathodic peak potential peak (E_{pc}) (+0.323V) is 0.078 V. This smaller $\Delta E_{a,c}$ (0.078 V) value also indicates the capability of the PVA-TMOP1 NC to be more reversible.

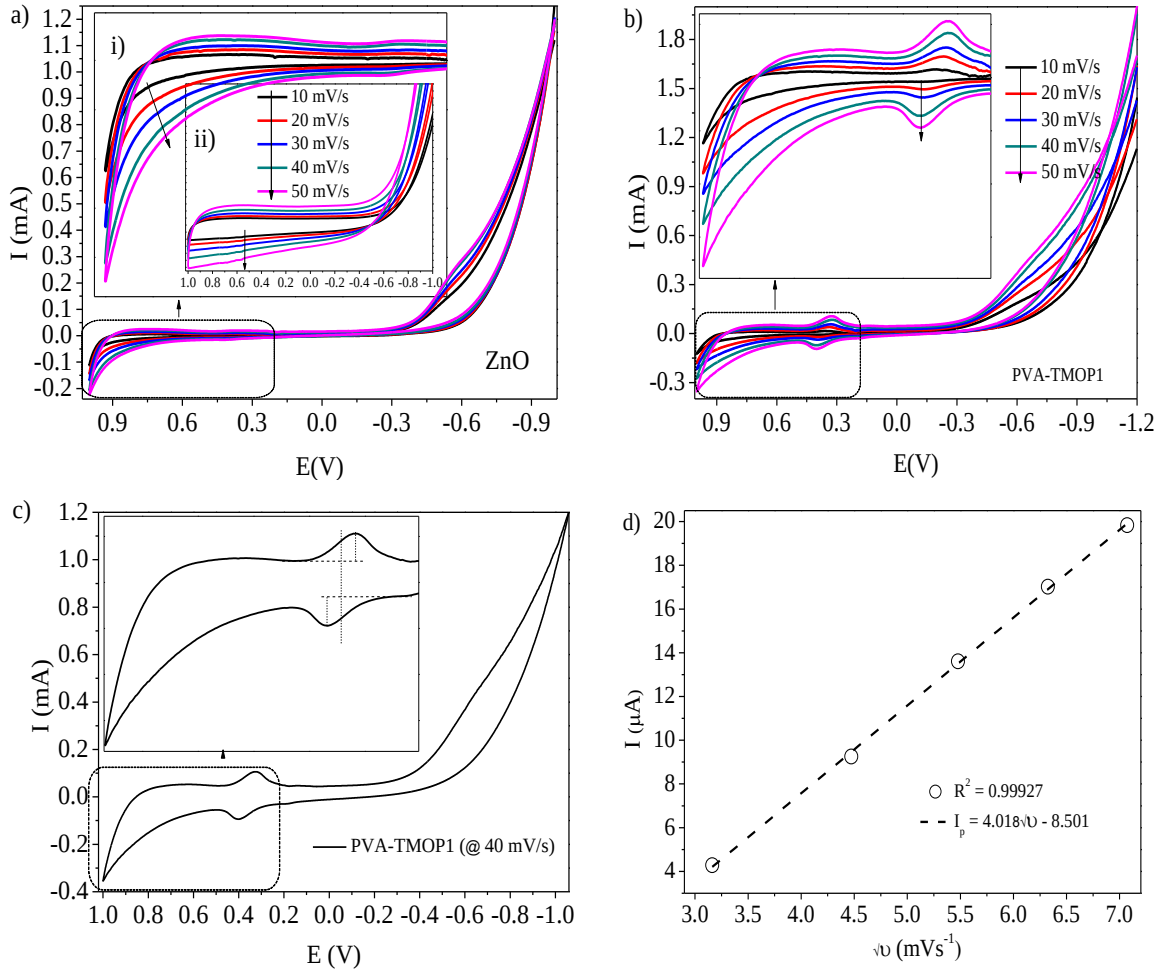

Figure 49. CV plots of (a) ZnO NPs, (b) PVA-TMOP1 NC electrode, (c) CV plot of PVA-TMOP1 NC @ 40 mV/s, and (d) PVA-TMOP1 NC linear plot.

Figure 50(a) and (b) show the CV plots of ZnO NPs and PVA-BMO1 NC at different scan rates, respectively. For PVA-BMO1 NC, an increase in the scan rate caused a slight increase in the redox peak current. Unlike that of ZnO, a pair of redox peaks was also noticed for PVA-BMO1 NC [Figure 50(c)]. The obtained peak potential difference ($\Delta E_{a,c}$) between anodic peak potential (E_{pa}) (+0.391V) and cathodic peak potential (E_{pc}) (+0.370V) is 0.021 V. This smaller $\Delta E_{a,c}$ value, also indicates the capability of the PVA-BMO1 NC to be fast and more reversible. This enhanced current reduction and oxidation responses for the PVA-TMOP1 and PVA-BMO1 NCs verifies the presence of improved electron transport between the electrolyte medium and the modified NCs electrode (Gopinathan et al., 2015). It is most probably due to the porous nature of the NCs, revealing the presence of a non-restricted pathway for electron transfer. Furthermore, this obvious electron transport potential for the NCs also shows the formation of heterojunctions between metal oxides (Jun Zhang et al., 2011). It is also consistent with

the BET, XRD, SEM, and electrochemical impedance spectroscopic (EIS) analysis results. In addition to the porosity and formations of heterojunctions between the metal oxides, these reversible redox peaks, which have not appeared on the ZnO NPs may also be resulting from the conversion of Fe^{2+} and Fe^{3+} (equation 53) (Yan Wang et al., 2018).

$$Fe(OH)_2 + OH^- \leftrightarrow FeOOH + H_2O + e^- \quad (53)$$

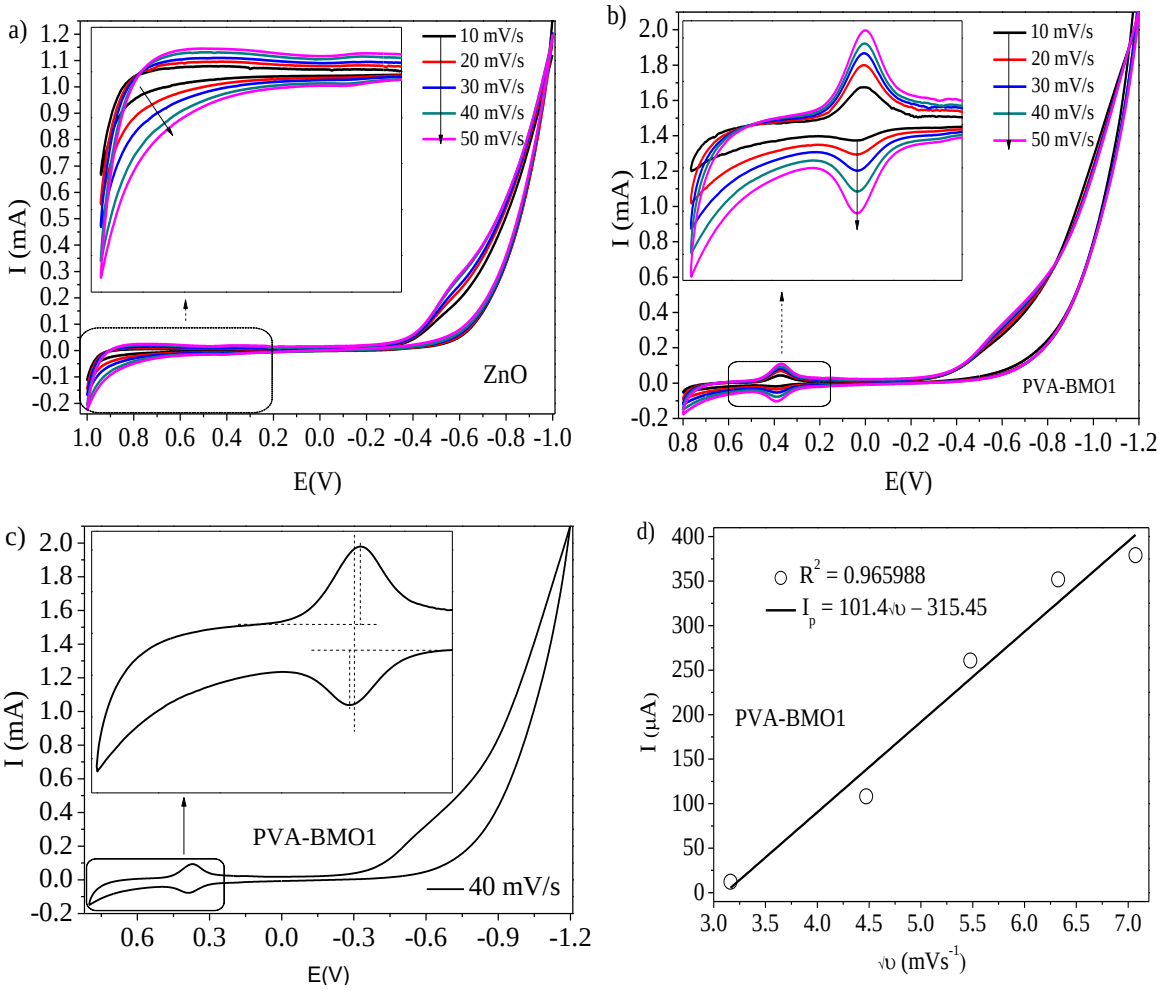

Figure 50. CV plots of (a) ZnO NPs and (b) PVA-BMO1 NC electrode at different scan rates, (c) CV plot of PVA-BMO1 @ 40 mV/s, and (d) PVA-BMO1 NC linear plot.

From the CV plots at different scan rates for PVA-BMO2, the oxidation-reduction peaks were also observed (see Figure 51(b) inset). The probable mechanism of these redox peaks is mainly attributed to the reaction of Mn^{3+}/Mn^{4+} (equation 54) involving OH^- chemisorption/intercalation into Mn_2O_3 structure (Han et al., 2020; Nathan et al., 2008; Xu et al., 2017). The effect of the scan rate on the increment of the redox peak current was

also detected. The linear relationship plotted between the oxide peak current (I_p) versus the scan rate (υ) is shown in Figures 49 and 50(d) and Figure 51(c) for PVA-TMOP1, PVA-BMO1, and PVA-BMO2 NCs, respectively. Depending on the coefficient of determination (R^2) value, for PVA-TMOP1 and PVA-BMO2, good linearity between the scan rate and i_{pa} was obtained within the range of 10 to 50 mV/s. The fitting of their linear curve confirms the presence of a surface-confined process on the modified electrode surface (Tang et al., 2008) and the domination of adsorption controlled electrocatalytic process. The non-fitting of the PVA-BMO1 linear plot justifies the diffusion-dependent electrocatalytic process (Suresh et al., 2014; Tang et al., 2008).

$$Mn\,[Mn]\,O_3 + OH^- \leftrightarrow Mn^{4-} + [Mn^{3-}]\,OH^-\,O_3 + e^- \qquad (54)$$

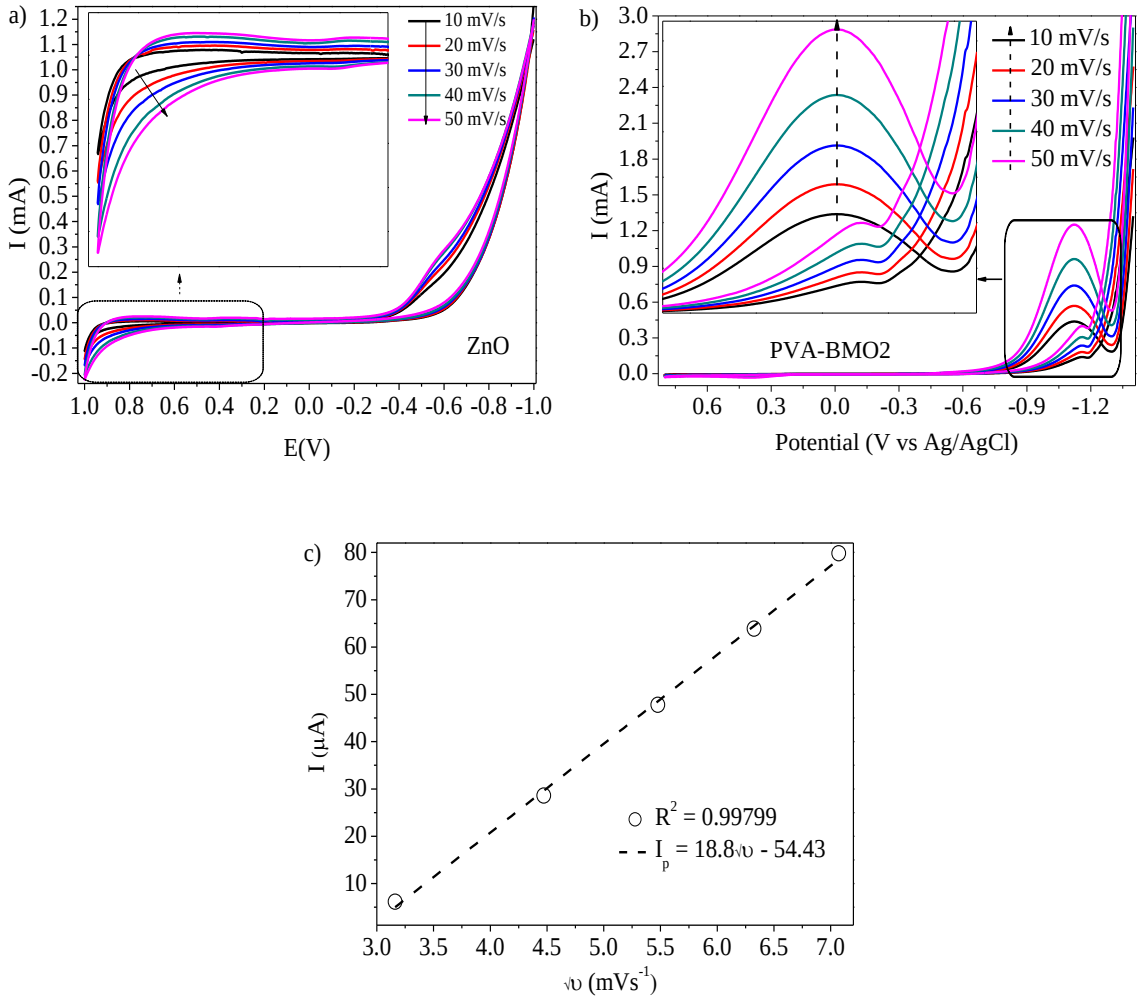

Figure 51. CV plots of (a) ZnO NPs, (b) PVA-BMO2 NCs electrode at different scan rates, and (c) PVA-BMO2 NC linear plot.

For further understanding of the electrochemical properties of the ZnO NPs and NCs, the electrochemical impedance spectroscopic (EIS) test was conducted. Figure 52(a) – (c) shows the EIS plots of PVA-TMOP1, PVA-BMO1, and PVA-BMO2 NCs, respectively in comparison to ZnO NPs. The Nyquist plot was used to understand the resistance properties of the NPs and NCs. The semicircular portion at a higher frequency is equal to the charge transfer resistance (R_{ct}) at the contact interface of the electrode and electrolyte solution (Li et al., 2011; Xie et al., 2014). As seen from the combined EIS plots in Figure 53, the semicircular diameter of PVA-TMOP1 NC is much smaller than the ZnO NPs and two binary NCs. It indicates that PVA-TMOP1 NC has much lower resistance/higher charge transfer ability and probably a higher photoelectron-hole pair's separation efficiency.

The R_{ct} values of ZnO NPs and PVA-BMO1, PVA-BMO2, and PVA-TMOP1 NCs were obtained to be 65, 25, 61, and 7Ω, respectively. These results show that the charge transfer capability is in the order of PVA-TMOP1 > PVA-BMO1 > PVA-BMO2 > ZnO. This enhanced conductivity for the NCs can be attributed to the formation of a heterojunction between metal oxides and their porous nature (Khan et al., 2015; Khan et al., 2016; Yuanying Liu et al., 2014). Besides, increasing the heterojunction to the ternary (PVA-TMOP1) shows enhanced charge transfer capability. As reported (Suryavanshi & Rajpure, 2018), this is attributed to the more negative band position values of the NCs, compared to ZnO NPs alone, indicating greater electron/hole recombination hindrance capacity. The linear portion at lower frequencies is known as the Warburg resistance, which is related to ion transport/ions diffusion from the electrolyte to the surface of the electrode (Kasap et al., 2019).

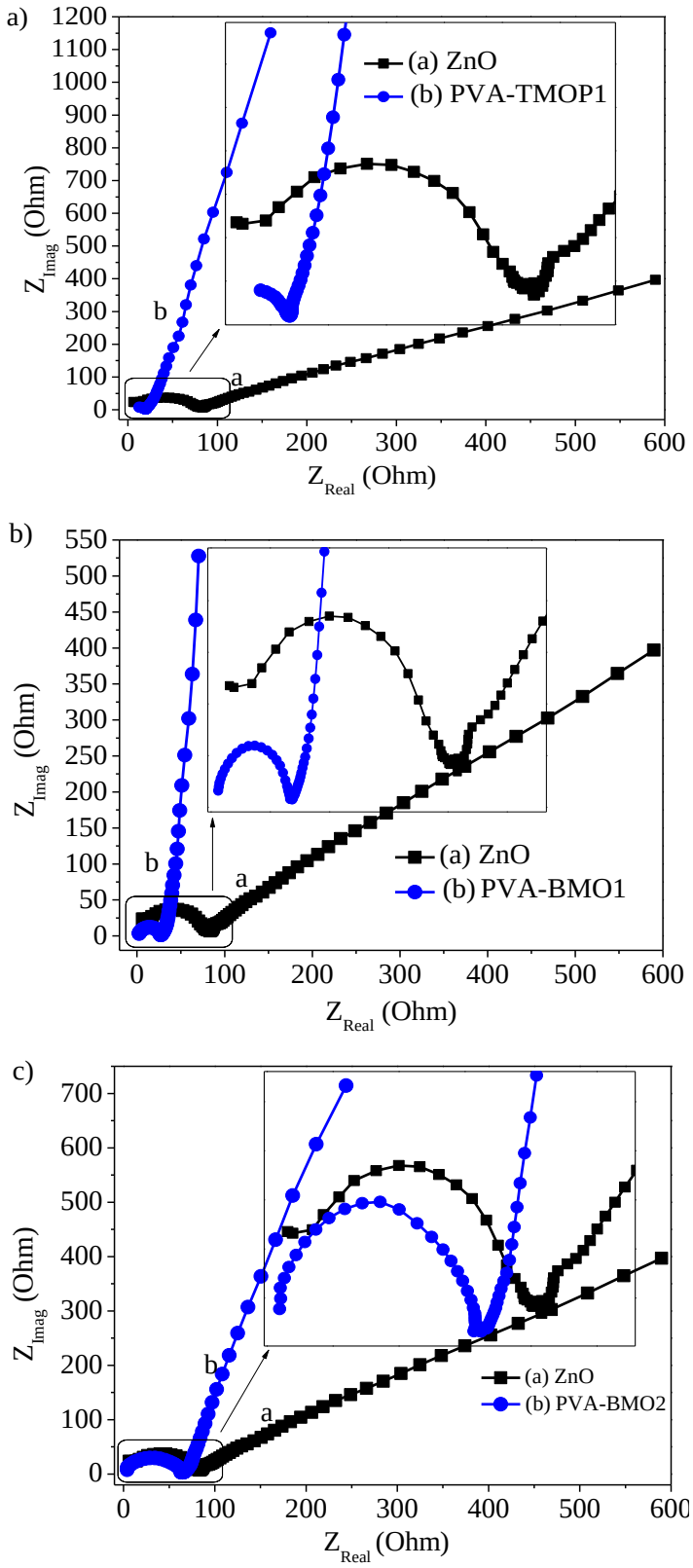

Figure 52. Electrochemical impedance spectroscopic plots of (a) PVA-TMOP1, (b) PVA-BMO1, (c) PVA-BMO2 NCs.

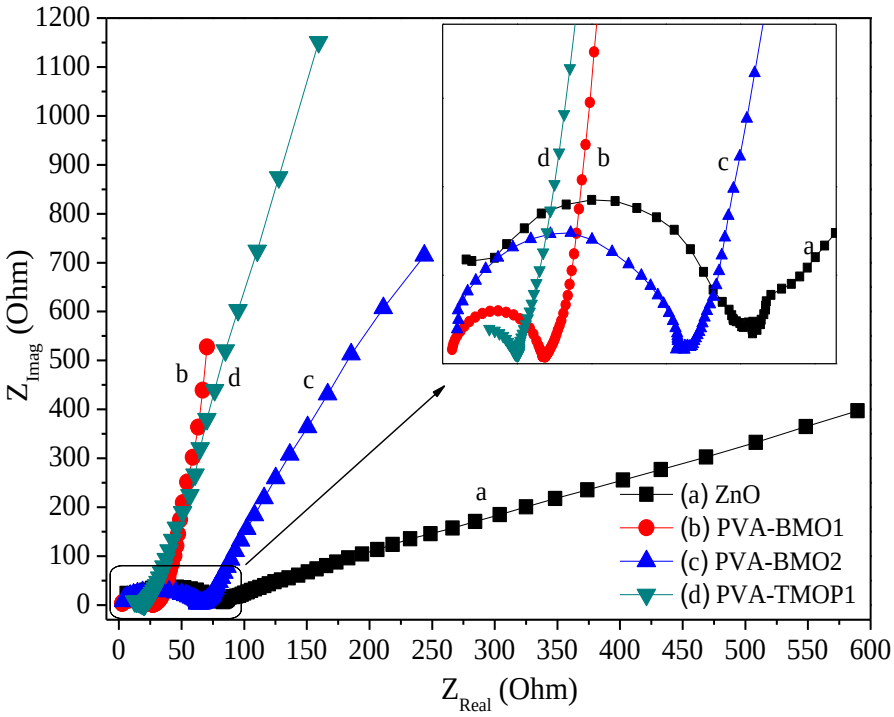

Figure 53. EIS spectra of ZnO, PVA-BMO1, PVA-BMO2, and PVA-TMOP1 NCs (Inset: their magnified EIS plots).

4.2. Adsorption Studies

Adsorption is a surface phenomenon in which adsorbate molecules bind to a solid surface. The three common adsorption steps include film diffusion, pore diffusion, and surface reaction) (Lin & Wang, 2008). Besides, 1) the diffusion of the reactants from the bulk phase (boundary layer) to the external surface of the catalyst pellet, 2) diffusion of the reactant from the pore mouth through the catalyst pores to the immediate vicinity of the internal catalytic surface; the point where the chemical transformation occurs, 3) adsorption of reactants on the inner catalytic surface, 4) reaction at specific active sites on the catalyst surface, 5) desorption of the products from the inner surface, 6) diffusion of the products from the interior of the pellet to the pore mouth at the external surface, and 7) diffusion of the products from the external pellet surface to the bulk fluid are the seven classical steps involved in the adsorption process [Figure 55(a)]. If external transport is greater than internal transport, the rate is governed by particle diffusion. If external transport is less than internal transport, the rate is governed by film diffusion and if external transport approximately equal to internal transport, the transport of adsorbate ions to the boundary may not be possible at a significant rate thus, the formation of a liquid

film surrounding the adsorbent particles takes place through the proper concentration gradient (Klaewkla et al., 2011).

During all the above-mentioned processes, two main types of interaction, namely, physical and chemical, are possible between adsorbent and adsorbate; the former is known as physisorption, and the latter is chemisorption. Physisorption is a result of attractive forces between sorbent and adsorbate molecules, whereas chemisorption provides a stronger bond as it involves the transfer or sharing of electrons between adsorbent and adsorbate species (Zhou et al., 2014). It is reported that (Lei et al., 2017), the porous materials can simultaneously possess a high SAV and high settling velocity in aqueous media, and have outstanding adsorption capacity. Herein, the optimized PVA-TMOP1 NC that has high SAV and SSA compared to all the other NPs and NCs was used to study the adsorption process of MB dye.

4.2.1. Optimization

Figure 54(a) shows the calibration curve used during the initial MB dye optimization process. As seen in Figure 54(b) of PVA-TMOP1 adsorbent dosage optimization, the adsorption of MB increases rapidly as the dosage increases from 0.005 to 0.02 g. This is due to the presence of unoccupied active sites of the adsorbent (Xia et al., 2011). However, after the saturation site of 0.02 g, a further increase in dosage does not result in increasing the removal efficiency plateaus, consistent result was also achieved (Lan Huong et al., 2018). Therefore, 0.02 g is taken as an optimum PVA-TMOP1 adsorbent amount for further MB dye adsorption experiments.

The degree of ionization of MB dye adsorbate and the surface charge of the PVA-TMOP1 NC adsorbent is dependent on the pH of the solution. In the acidic pH range, due to the presence of H^+ ions, the surface site of the PVA-TMOP1 NC functional group will be protonated. While, in alkaline pH due to the OH^- ions, the surface occupies a negative charge. Due to the presence of electrostatic repulsion between positively charged PVA-TMOP1 adsorbent and cationic MB dye, at acidic pH, the adsorption efficiency decreases [Figure 54(c)]. At the alkaline pH, the electrostatic attraction between the deprotonated negatively charged PVA-TMOP1 with cationic MB dye occurred, so did enhancement of the adsorption process. As seen in the proposed mechanism of the adsorption of MB on

PVA-TMOP1 [Figure 55(b)], at alkaline pH, the positively charged nitrogen atom from MB dye can form a hydrogen bond with the hydroxide groups from the PVA-TMOP1 adsorbent.

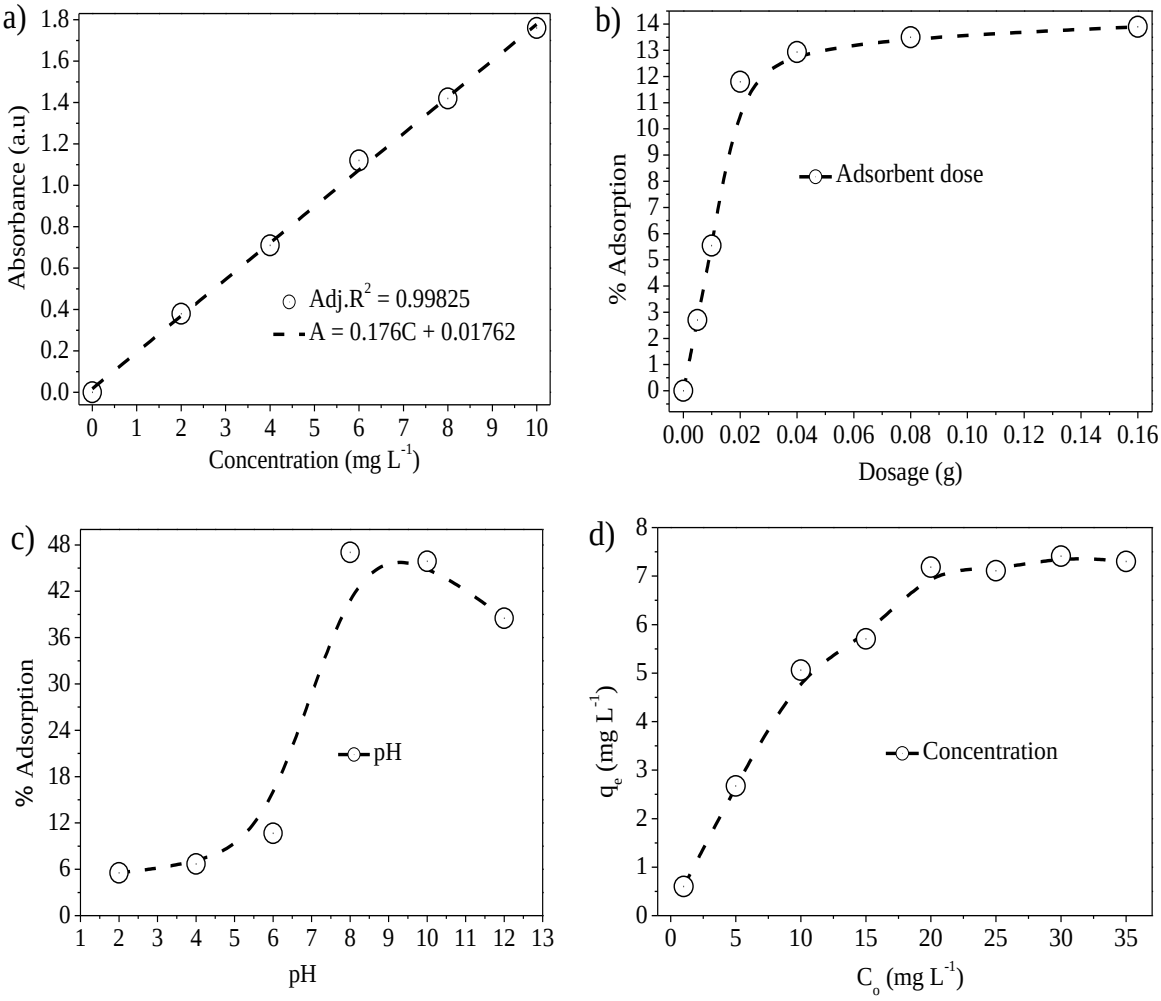

Figure 54. (a) Calibration curve obtained during concentration optimization test, (b) adsorbent dosage optimization, (c) pH of the solution optimization, (d) initial concentration optimization of MB dye adsorption on the PVA-TMOP1 NC.

Figure 54(d) shows the influence of initial MB dye concentration on the removal efficiency of the PVA-TMOP1 NC. An increase at initial MB dye concentration leads to an increase in the adsorption capacity. This is because the ratio of the initial number of moles of MB dye to the available surface sites of PVA-TMOP1 NC is large and subsequently the fractional adsorption becomes independent of MB dye initial concentration and consequently higher adsorption yields were obtained. However, at higher concentrations, most of the PVA-TMOP1 NC adsorption sites are occupied by ions,

and the available sites of adsorption would become fewer, hence the percentage removal of MB dye become constant.

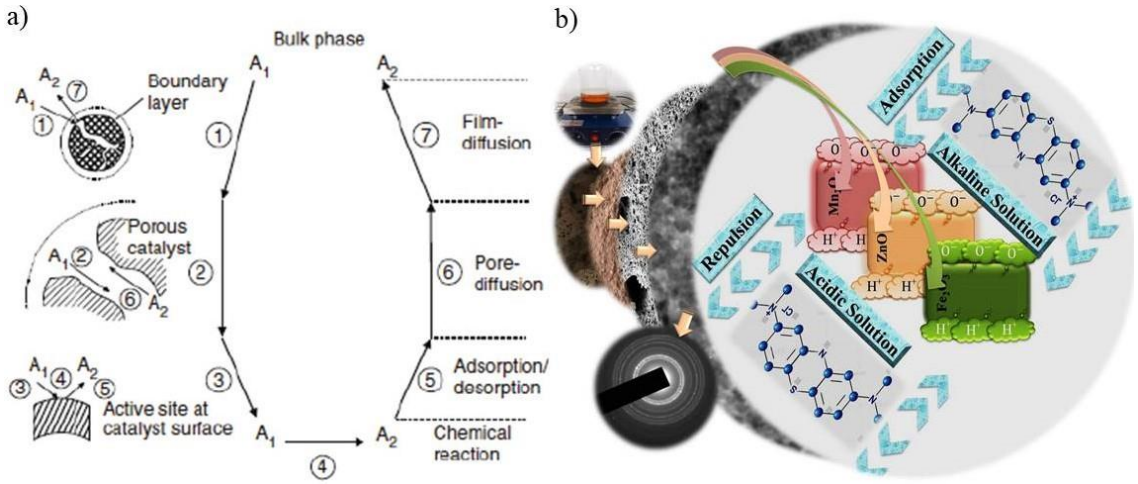

Figure 55. a) Individual steps of a simple, heterogeneous catalytic fluid–solid reaction A1 → A2 carried out on a porous catalyst (Klaewkla et al., 2011), b) proposed possible adsorption mechanisms of MB dye on PVA-TMOP1 NC.

4.2.2. Adsorption kinetics studies

Among the three adsorption process of adsorption kinetics, viz., (i) external surface adsorption, (ii) intraparticle diffusion (IPD), and (iii) equilibrium adsorption (Cui et al., 2015), the first, fast external adsorption process, occurred up to 70 minutes, the second, IPD, occurred up to 90 minutes, and the third, equilibrium adsorption process, starts at 110 minutes [Figure 56(a)] (Lan Huong et al., 2018). For further time-dependent experimental data interpretation, the PFO, PSO, Elovich, IPD, and Bangham linear equations (equations 9 - 13) have been applied, as seen in Figure 56(b)-(f). The respective adsorption coefficient and constant values are given in Table 17.

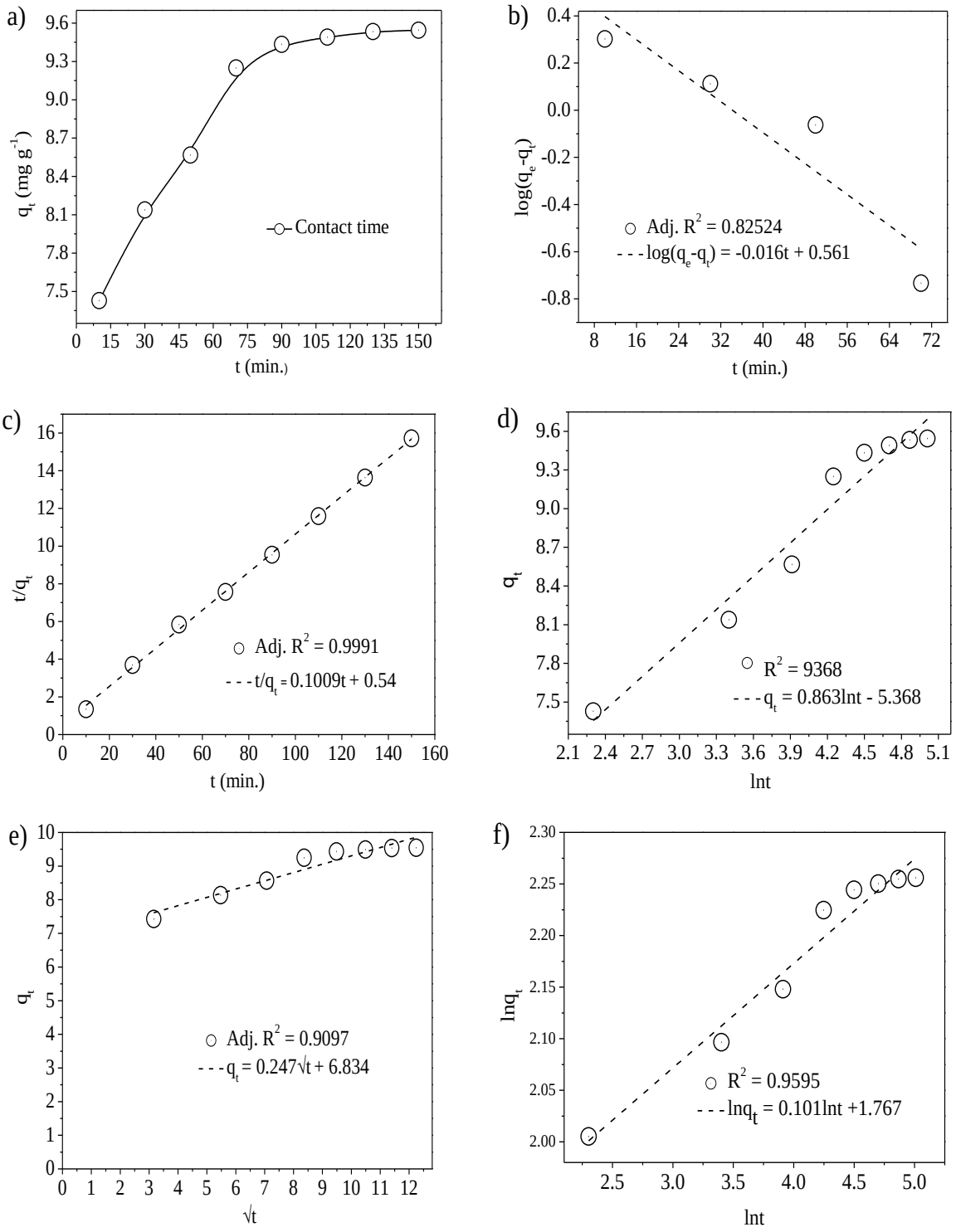

Figure 56. (a) Adsorption kinetics plot of MB dye adsorption on PVA-TMOP1 NC, (b) pseudo first order, (c) pseudo second order, (d) Elovich, (e) intra-particle diffusion (f) Bangham kinetics models. (@ dosage = 0.02 g, pH = 8.2, concentration = 20 mg L^{-1}, agitation speed = 140 rpm).

Comparing the R^2 values of the adsorption kinetics models, the PSO adsorption-reaction model [Figure 56(c)] and the Bangham model [Figure 56(f)] relatively fit well. The well-

fitting of the PSO model indicates the chemisorption type of adsorption process to be the rate-determining step. This adsorption process occurs through the transfer of electrons or a chemical reaction between MB dye adsorbate and PVA-TMOP1 NC adsorbent (Cui et al., 2015; Mohammadi et al., 2014). However, to state that the PFO [Figure 56(b)] and PSO models fit well, their theoretical and experimental values should also be close to each other. Frequently, the obtained theoretical value becomes less than yet close to the experimentally obtained value (Mohammadi et al., 2014). The theoretical (9.43 $\mathrm{mg\,g^{-1}}$) and experimentally obtained (3.64 $\mathrm{mg\,g^{-1}}$) values of PFO have not had a close relationship, while the theoretical (9.43 $\mathrm{mg\,g^{-1}}$) and experimental (9.91 $\mathrm{mg\,g^{-1}}$) values of PSO have a close relation.

As seen in Figure 56(e), the IPD model failed to show good fitting, and its linear line also does not pass through the origin. Hence, the adsorption process is not under the control of the adsorption-diffusion process. Therefore, the MB dye adsorption on the PVA-TMOP1 NC is dominantly dependent on the adsorption-reaction type. The Elovich model that is commonly applied in chemisorption systems (Bernal et al., 2020) also showed relatively better fitting [Figure 56(d)]. Actually, it also has confirmation from the CV Ip versus υ linear plot, which suggests that the electrocatalytic process is adsorption controlled for PVA-TMOP1 NC [see Figure 49(d)]. However, the well-fitting of the Bangham model indicates the presence of pore diffusion in the adsorption process [Figure 56(f)] (Edet & Ifelebuegu, 2020). The presence of this pore diffusion is also consistent with the BET and SEM interpretations of PVA-TMOP1 NC porous property.

Table 17. Kinetics coefficient and constant values of MB dye adsorption on PVA-TMOP1 NC.

	PFO			*PSO*			*Elovich*		*IPD*			*Bangham*		
q_e^* $(mg\ g^{-1}$	K_1	q_e $(mg\ g^{-1})$	R^2	K_2	q_e $(mg\ g^{-1})$	R^2	β	R^2	C	K_{id}	R^2	m	k_b	R^2
9.43	0.037	3.64	0.82524	1.85	9.91	0.9991	0.95	0.9368	0.049	2.83	0.9097	2.22	-0.42	0.9595

* is the theoretical equilibrium absorption capacity

4.2.3. Adsorption isotherms studies

The adsorption isotherm models give physicochemical information about the adsorption process, adsorbate-adsorbent interaction, adsorption characteristics, and adsorption efficiency of PVA-TMOP1 NC adsorbent (Ng et al., 2002). The concentration optimization data conducted using different initial MB dye concentrations [Figure 54(d)] were fitted with adsorption isotherm models (Figure 57). The respective absorption coefficient and constant values of the adsorption process are given in Table 18. Depending on the R^2 value of the adsorption isotherm models (equations 3 - 8), the Langmuir and FH models show better fitting. From the Langmuir plot [Figure 57(a)], the R_L value lies between 0 and 1 (0.05), indicating the favorability of the adsorption process (Su et al., 2018). The fitting of the Langmuir model shows the presence of monolayer MB dye adsorbate coverage on the surface of the PVA-TMOP1 NC adsorbent, which is consistent with the PSO model interpretation. The maximum adsorption capacity of the adsorbent determined from the Langmuir isotherm model is 7.75 $\mathrm{mg\,g^{-1}}$. Several studies showed greater adsorption capacity (Chen et al., 2011; Dutta et al., 2011), although, lesser adsorption capacity (Al-Khateeb & Mahmood, 2016; Subbareddy et al., 2020), compared to our materials. Therefore, our material has a moderate adsorption capacity towards the adsorption of methylene blue dye.

The Freundlich [Figure 57(b)], D-RK [Figure 57(c)], Temkin [Figure 57(d)], and FG [Figure 57(f)] isotherm models are responsible for the heterogeneity of the adsorbent sites, adsorption mean free energy, adsorbate/adsorbate interactions, and surface characteristics of the adsorbate, respectively (Ayawei et al., 2017). Among them, Freundlich and Temkin's models do relatively fit well. The Freundlich isotherm model is responsible for the heterogeneity of the adsorbent sites. Generally, if the value of constant n is between 1 and 10, the adsorption process becomes acceptable (Ng et al., 2002). The obtained n values from the Freundlich model is in between 1 and 10 (1.59) for this work, indicating the favorability of the adsorption process. As confirmed by the Langmuir isotherm model, the value of 1/n is closer to 1 shows the homogeneous nature of the PVA-TMOP1 NC adsorbent surface.

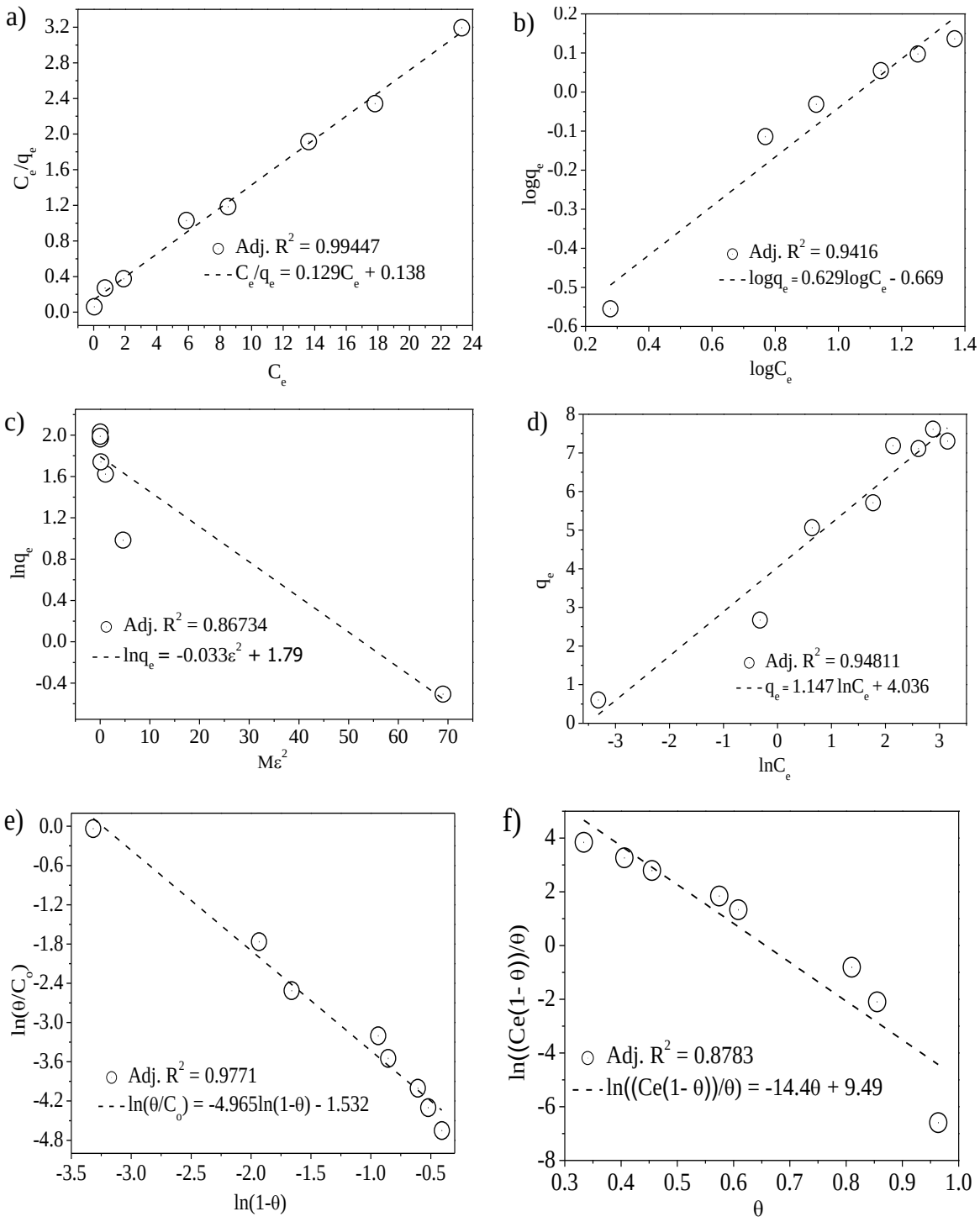

Figure 57**.** Adsorption isotherm plots of MB dye adsorption on PVA-TMOP1 NC (a) Langmuir, (b) Freundlich, (c) Dubinin-Radushkevich, (d) Temkin, (e) Flory-Huggins, (f) Fowler-Guggenheim models**.** (@ dosage = 0.02 g, pH = 8.2, agitation speed = 140 rpm, contact time = 90 min.).

The Temkin adsorption isotherm medal, which explains the adsorption system to be based on heat (Ng et al., 2002), fits well with the equilibrium binding constant k_T values of 1.002

L mg^{-1}. The Temkin isotherm constant b value of 2.16 kJ mol^{-1} shows the adsorption process seems to involve a chemisorption type of adsorption process (Hu et al., 2011). The indication of the characteristic surface coverage and spontaneity of the reaction (−3.8 $kJ\ mol^{-1}$) is obtained from the FH model equation [Figure 57(e)]. The obtained negative heat of adsorption (w) value of −17.838 $kJ\ mol^{-1}$ from the FG model confirmed the presence of repulsive interaction between adsorbed MB dye molecules (adsorbate/adsorbate interactions). It confirms the Langmuir monolayer coverage interpolation.

Table 18. Adsorption isotherm coefficient and constants for adsorption of MB dye onto PVA-TMOP1 NC.

	Langmuir		*Freundlich*		*D-RK*		*Temkin*		*FH*			*FG*	
q_m	K_L				*E*		*b*			ΔG			*W*
$(mg\ g^{-1})$	$(L\ mg^{-1})$	R_L	k_f	*1/n*	$(kJ\ mol^{-1})$	β	$(kJ\ mol^{-1})$	k_T	*n*	$(kJ\ mol^{-1})$	k_{FH}	k_{FG}	$(kJ\ mol^{-1})$
7.75	0.94	0.05	0.21	0.629	8.5	0.033	2.16	1.002	−4.96	−3.80	0.216	7.58e-5	−17.838

4.3. Photocatalytic Activities and Mechanism

The porous NCs have more surface defects that improve light absorption efficiency and increase photocatalytic degradation activity (Xin Li et al., 2016; Prabakaran & Pillay, 2019; Tian et al., 2019). It's well-known that irradiation of ZnO photocatalyst with suitable energy produces electron (e^-) and hole (h^+) pairs on the surface of the photocatalyst. On the reduction half-reaction, e^- reacts with dissolved oxygen and creates superoxide radical ($O_2^{\bullet -}$) and the hydroxide radicals ($OH^\bullet$). Whereas, on the oxidation half-reaction, the h^+ reacts with water and form additional $OH^\bullet$. The occurrence of these two reactions is dependent on the band potential of the photocatalyst. The $OH^\bullet$ oxidizing agent reacts with adsorbed toxic pollutants and produces a nontoxic byproduct. However, applying single ZnO as a photocatalyst may face an e^-/h^+ recombination problem. This recombination problem, particularly in the nanosized range, leads to the diminution of their quantum efficiency. It is also understood from the past studies that, sometimes the e^-/h^+ recombination may also initiate highly desirable reactions and consequences in the dissipation of radiant energy (Lachheb et al., 2017).

Among several strategies developed for the improvement of the charge transfer capabilities of the photocatalysts, the formation of an interface between two or more metal oxide semiconductors is one of the viable schemes (Mohd Adnan et al., 2016). The design and fabrication of an interface significantly assist the process of continuous transfer of electrons from the more negative conduction band (CB) potential to the lower CB potential and holes from less negative valence band (VB) potential to the more negative VB (Jiamprasertboon et al., 2019). Furthermore, forming a hybrid also enhances the active sites, polarity, porous nature, and broad bandgap properties of the materials.

Except for PVA-BMO2 NC on the indirect Kubelka–Munk plot, the Uv-vis-DRS (Figure 35) analysis confirms the non-existence of noticeable bandgap change between ZnO NPs and NCs. This can be explained by the fact that, the non-incorporation of either Fe^{3+} or Mn^{3+} ions in the ZnO crystalline lattice, which further indicates the presence of only local heterojunction between ZnO and Fe_2O_3 or/and Mn_2O_3 (Lachheb et al., 2017; Maya-Treviño et al., 2015). Therefore, the UV lamp was used for this study as an irradiation source. The photodegradation experiment was conducted using the CR and AO8 dyes at a maximum absorption wavelength of 494 and 484 nm, respectively.

The photodegradation activity of the ZnO, PVA-BMO1, PVA-BMO2 was shown in Figure 58(a) – (f). The proposed possible photodegradation mechanism of PVA-BMO1 and PVA-BMO2 NCs were given in Figure 59(a) and (b), respectively. The ZnO and PVA-BMO2 showed decent photocatalytic activities on AO8 dye with 9.85% and 10.6% degradation for the first 15 minutes, respectively, with a maximum degradation of 62.2% for ZnO and 74.35% for PVA-BMO2. The obtained rate constant *k* value for ZnO and PVA-BMO2 was 0.005819 $min.^{-1}$ and 0.008646 $min.^{-1}$, respectively. The ZnO NPs also showed good photocatalytic activities on the CR dye with the rate constant *k* value of 0.005622 $min.^{-1}$. The good photocatalytic activities of ZnO NPs may be due to the presence of some defects (vacancy or/and interstitial) that prevent the e^-/h^+ recombination.

The superior photocatalytic activities of PVA-BMO2 on AO8 dye, even better than PVA-TMOP1 NC, is probably due to the formation of a suitable staggered type heterojunction [Figure 59(b)]. In the staggered gap type of heterojunction, the electrons transferred from the more negative CB potential of ZnO to the lower CB potential of Mn_2O_3. The holes transferred from the more positive VB potential of Mn_2O_3 to the less positive VB potential of ZnO (Jiamprasertboon et al., 2019). Herein, the electrons and holes separation improved, and improvement in the photocatalytic efficiency arisen (Marschall, 2014). In fact, the PVA-BMO2 NC also showed redshift on the indirect Kubelka–Munk plot (Figure 35), which assists for broad-spectrum light absorption efficiency (Hu & Yang, 2017). However, the photocatalytic activity of PVA-BMO2 on the CR dye is not good. Actually, the typical anionic diazo CR dye has a highly stable structure, which makes it difficult to degrade (Lei et al., 2017).

The photocatalytic activities of PVA-BMO1 NC on both CR and AO8 dyes are poor. This reflects the enhancement in the electron-hole recombination, probably due to the formation of a straddling gap type of heterojunction [Figure 59(a)] (Hu & Yang, 2017; Xu et al., 2018). In the straddling gap type of heterojunction, the electrons transferred from the more negative CB potential of ZnO to the lower CB potential of Fe_2O_3. The holes also transferred from the less negative VB potential of ZnO to the more negative VB potential of Fe_2O_3 (Jiamprasertboon et al., 2019). Thus, the electrons and holes collected and recombine on the Fe_2O_3, and the weakening of the photocatalytic efficiency occurred (Marschall, 2014).

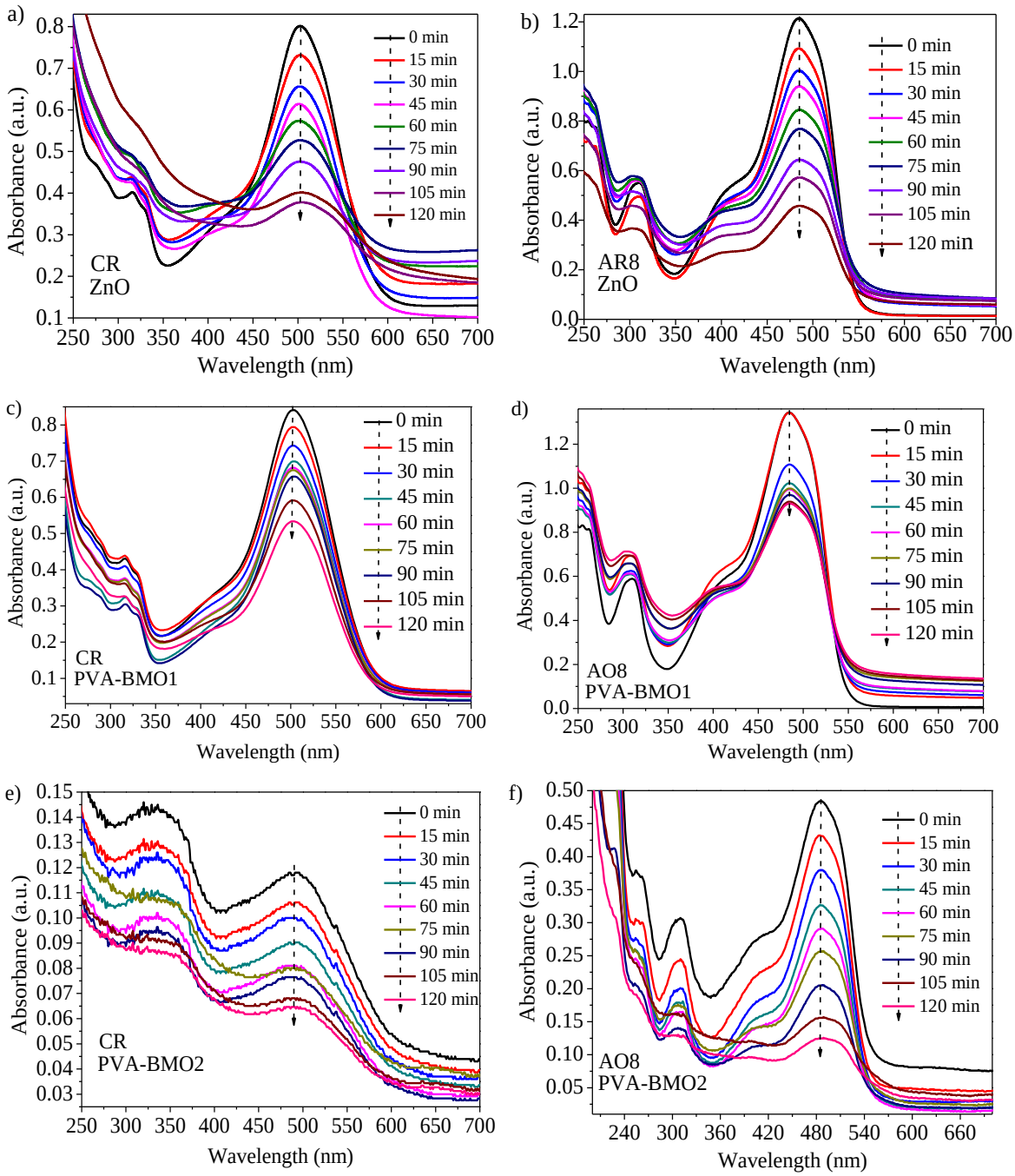

Figure 58. Absorbance vs. wavelength photocatalytic activities plots of ZnO (a and b), PVA-BMO1 (c and d), PVA-BMO2 (e and f). (a), (c), and (e) are for congo red dye and (b), (d), and (f) are for acid orange-8 dye.

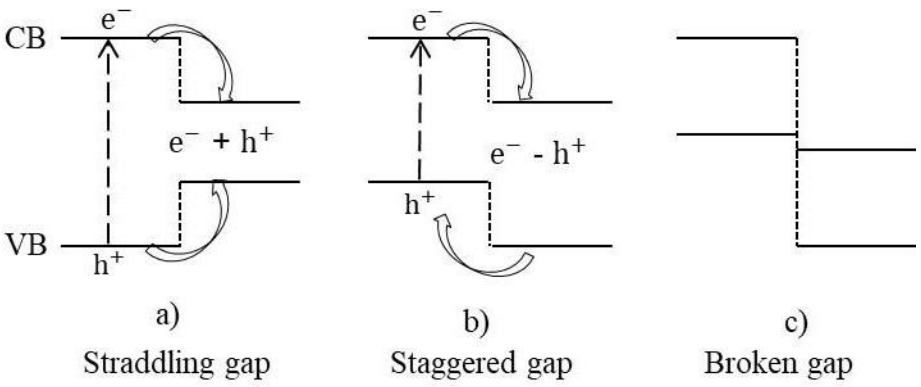

Figure 59. Three types of proposed band alignment for semiconductor heterojunction, including (a) straddling gap (type I), (b) staggered gap (type II), and (c) broken gap (type III) (Hu & Yang, 2017).

As confirmed from the characterization techniques, the PVA-TMOP1 NC exhibited enhanced SAV and better charge transfer capability compared to ZnO NPs and the two binary NCs. The PVA-TMOP1 NC has good photodegradation activity on both stable CR and AO8 dyes, unlike that of ZnO NPs and the two binary NCs. In fact, simultaneous degradation of a mixture of dyes would have been more prone to real case applications as textile dyes are mixtures. The absorbance (a.u.) versus wavelength (nm) plots of CR and AO8 dyes for PVA-TMOP1 NC was given in Figure 60(a) and (b). From the %degradation versus time (min) plot, in the first 15 minutes, approximately 17 % and 15 % of degradation took place for the CR and AO8 dyes, respectively. The maximum degradation of 68 % for CR dye and 70 % for AO8 dye was observed [Figure 60(c) and (d)]. The obtained rate constant *k* value for CR and AO8 dyes was 0.007141 $min.^{-1}$ and 0.005627 $min.^{-1}$, respectively. The half-life (time required for degradation of the AO8 and CR dyes to half of its initial amount) is the point at which the C/C_o and $1 - (C/C_o)$ curves intersect (Akhil et al., 2016). The obtained degradation half-life value was approximately 105 minutes for CR and 119 minutes for AO8 dye [Figure 60(e) and (f)].

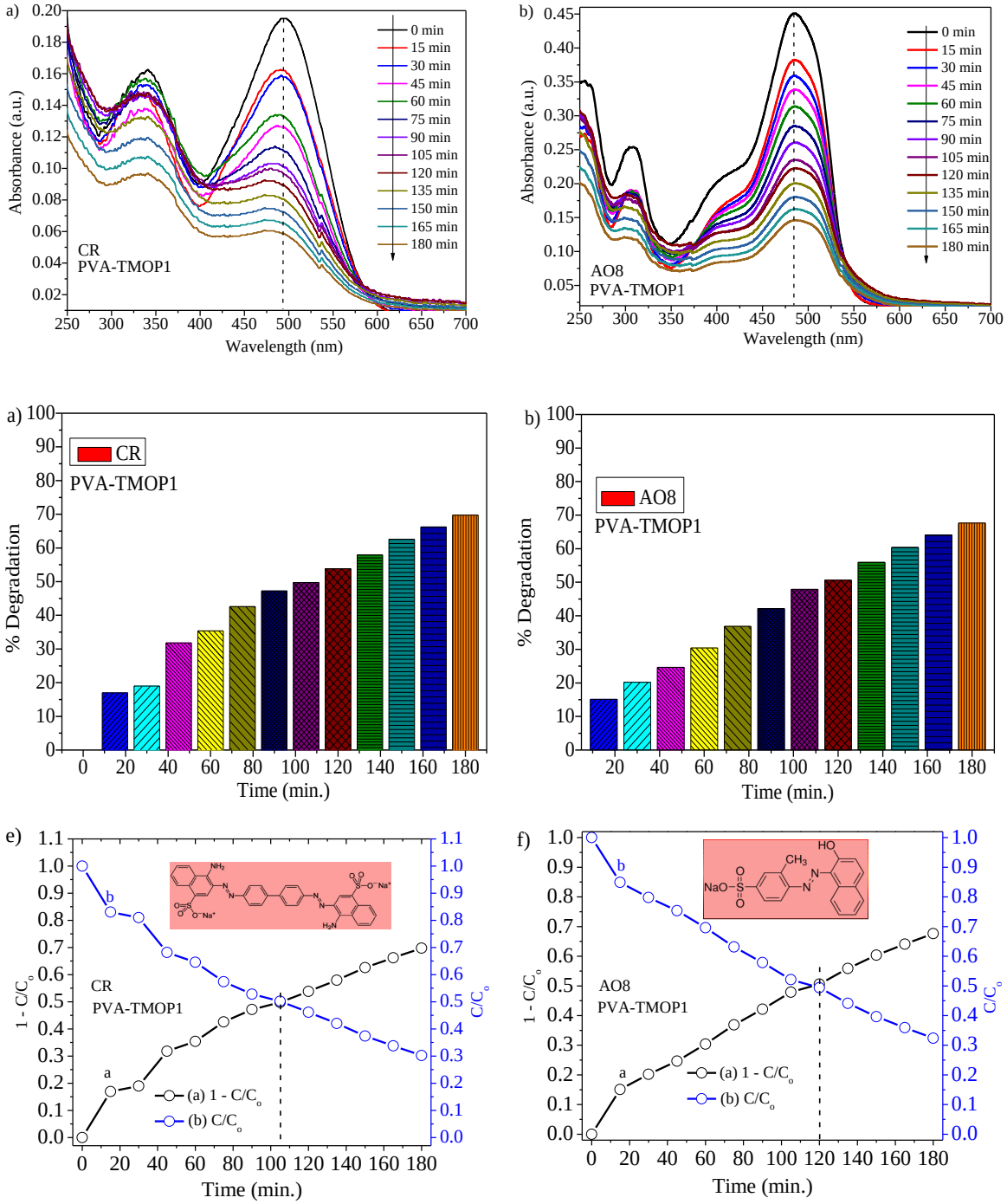

Figure 60. Photocatalytic activities of the PVA-TMOP1 NC: (a and b) absorbance Vs. wavelength, (c and d) % degradation, (e and f) 1-C/C_o Vs. t and C/C_o Vs. t plots of CR and AO8, respectively.

Metal oxides have unique electronic configuration/bandgap features resulting in the absorbance of a characteristic wavelength of light. However, the band edges position of metal oxides is dependent on the surface charge (Beranek, 2011). For an efficient photocatalytic reaction, the bottom of the CB needs to be more negative than the reduction

potential of H^+/H_2, and the top of the VB needs to be more positive than the reduction potential of O_2/H_2O (Hoffmann et al., 1995; Mills & Le Hunte, 1997). Also, it is beneficial for the oxidation potential of the hydroxyl radicals and the reduction potential of peroxide radicals to be in between the bandgap of the catalyst from the thermodynamic point of view (Vinu & Madras, 2010). Depending on the electronegativity values of metal oxides (Abdullah Mirzaie et al., 2012), the redox potential of n-type ZnO, n-type Fe_2O_3 (Ganguly et al., 2015), and p-type Mn_2O_3 (Naeem et al., 2016; Saravanan et al., 2014; Zhao et al., 2018) before heterojunction was reported being as seen in Figure 61(a).

Hence, for confirming the presence of an appropriate heterojunction and proper charge transfer synergy, analysis using electrochemical techniques such as CV and EIS is significant (Beranek, 2011). As seen in Figures 49 and 53 of the respective CV and EIS analysis, the PVA-TMOP1 NC shows a quick and reversible redox reaction that indicates the presence of relatively better charge transfer properties. The presence of good charge transfer property shows the formations of heterojunctions/local contact between metal oxides, which has a prominent effect on reducing the electron/hole recombination. Based on the analysis results and reviews (Lachheb et al., 2017; Tama et al., 2019; Jun Zhang et al., 2011), a possible proposed photocatalytic mechanism was proposed as shown in Figure 61(a) before heterojunctions and Figure 61(b) after heterojunctions.

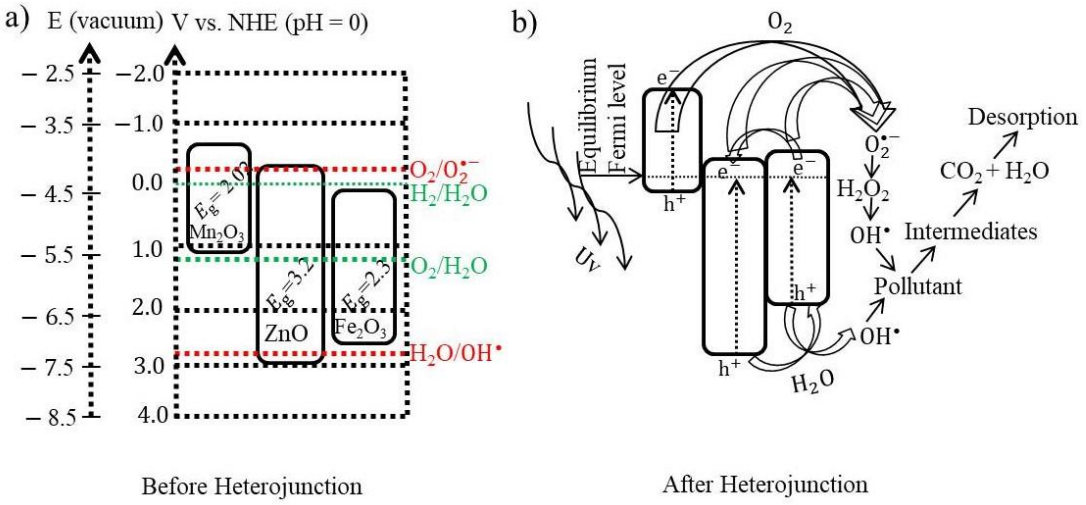

Figure 61. (a) The proposed a possible Bandgap energy and band edge positions of ZnO, Fe_2O_3 and, Mn_2O_3 NPs before heterojunction, and (b) the proposed a possible mechanism after heterojunctions.

During heterojunction, the Fermi level of metal oxides needs to become in its stable equilibrium stage. For equilibration, their energy band starts to move up and down by transferring electrons. This electron drifts, until the Fermi level equalizes, took place due to the presence of difference in the work function between the metal oxides (Lachheb et al., 2017; Tama et al., 2019). Then, a depletion layer that has a significant role in the electron transfer capability developed at the interface of the heterojunctions (Jun Zhang et al., 2011). ZnO NPs has a higher charge carrier concentration compared to the Fe_2O_3; therefore, the gap between the CB and Fermi level for Fe_2O_3 is higher compared to ZnO. This lead to reducing the CB of ZnO compared to the CB of Fe_2O_3 after heterojunctions. Also, important to note that, the Fermi level of p-type Mn_2O_3 existing near the VB. Hence, during UV irradiation, the photogenerated electrons either localize on the ZnO CB or diffuse to the VB or/and defects of the Mn_2O_3. The holes move to the VB of Fe_2O_3. Therefore, the recombination of the electrons and holes diminishes resulting in the enhancement of photocatalytic activity (Lachheb et al., 2017). The main steps involved in the reaction process of photocatalytic degradation under UV light irradiation are given in Figure 61(b).

4.4. Sensor Activities and Mechanism

Using CV and amperometric measurements, the sensing capacity of the PVA-TMOP1 NC were tested on ascorbic acid [Figure 62(a) and (b)]. As seen in Figure 62(a) CV plot and Figure 62(b) amperometry plot, the potential of the synthesized PVA-TMOP1 NC for ascorbic acid sensing has been confirmed. The PVA-TMOP1 NC exhibited superior ascorbic acid detecting capabilities with a higher peak current at a lower potential of 0.223 V. An increase in the concentration of ascorbic acid caused an increase in current. The sensing cycle on the amperometry analysis also finished within a few seconds, indicating that the synthesized NC detects the ascorbic acid in very little time [Figure 62(b)]. From the linear dependence of the anodic peak current (Ip) on the ascorbic concentration [Figure 62(c)], it can be concluded that the oxidation process is a type of adsorption-controlled one (Suresh et al., 2014).

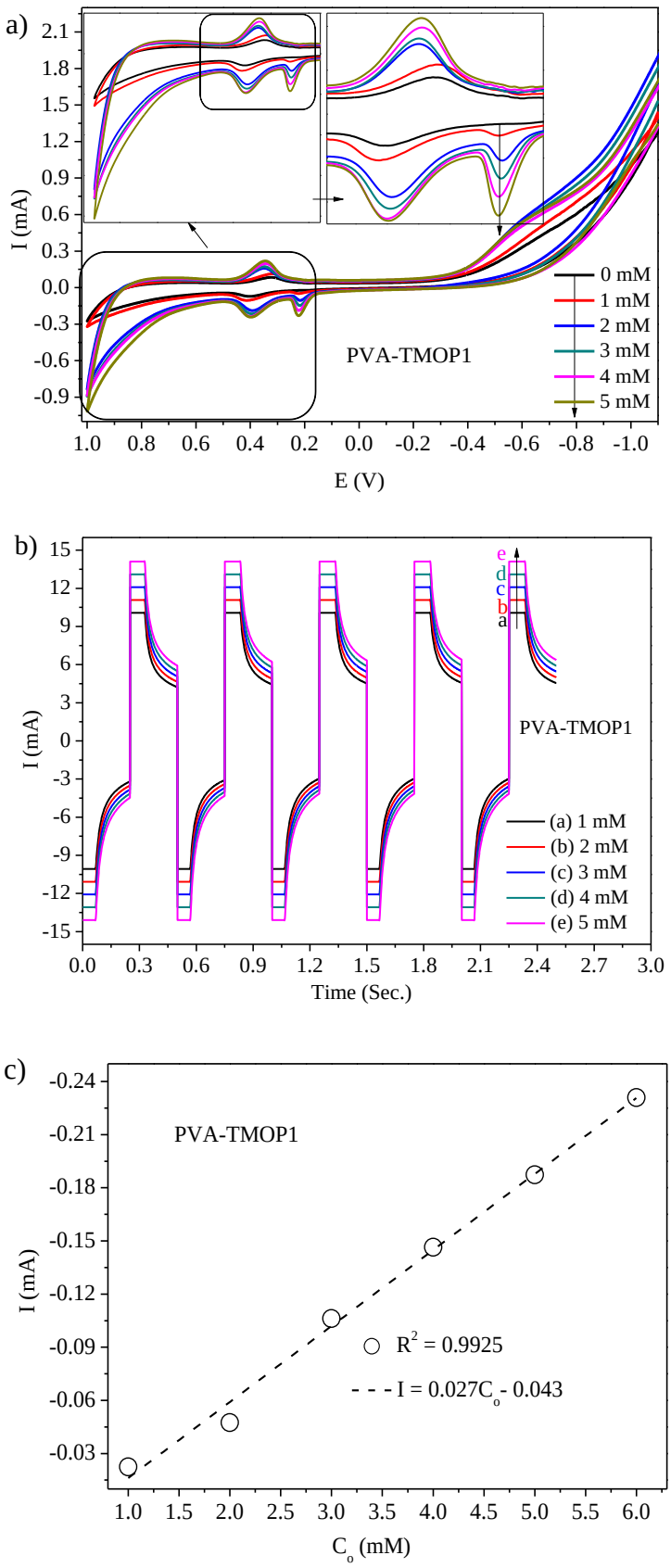

Figure 62. Ascorbic acid sensing by PVA-TMOP1 NC (a) CV plot at different concentrations, (b) amperometric plot at different concentrations, (c) variation of anodic peak current with ascorbic concentration.

The CV plots executed at different scan rates conducted for ascorbic acid detecting capabilities of ZnO NPs and PVA-BMO1 and PVA-BMO2 NCs are also given in Figures 63-65. The bare-ZnO NPs showed a naught oxidation peak because of the inert electrochemical response toward ascorbic acid [Figure 63]. The PVA-BMO1 and PVA-BMO2 NCs exhibited higher ascorbic acid detecting capabilities. The PVA-BMO1 exhibited greater ascorbic acid detecting capabilities with a higher peak current at a lower potential of 0.214 V. However, compared to the two binary NCs [Figures 64 and 65]; the PVA-TMOP1 NC exhibited relatively better ascorbic acid detecting capabilities. This relative greater sensing capability for the ternary materials is because of the combined effects of manganese oxide and iron oxides. Moreover, the good ascorbic acid detection properties of the NCs at lower potential is explained to be due to the formation of heterojunction, porosity, and high SAV of the NCs that offer more active sites (Khan et al., 2016; Murugan et al., 2019).

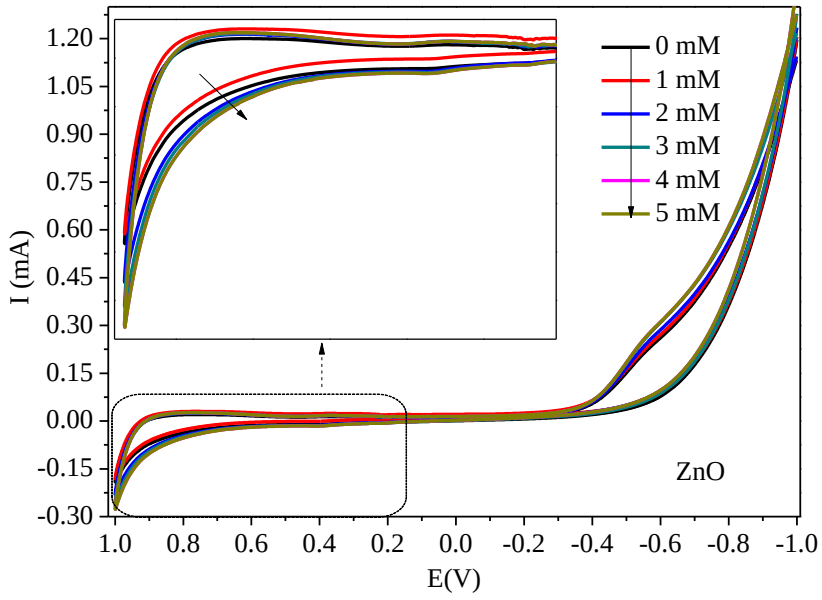

Figure 63. Electrochemical properties of ZnO NPs: CV ascorbic acid sensing curve at different concentrations.

Besides, owning to the mesoporous property of the synthesized materials, it allows a rapid charge transfer process (Khan et al., 2015; Yuanying Liu et al., 2014). It further shows the presence of novel electron transfer kinetics between the NCs and ascorbic acid molecules. In fact, this free electron transfer due to the formation of proper heterojunction (Alam et al., 2020; Ghanbari & Bonyadi, 2018; Huang et al., 2013; Khan et al., 2016; Murugan et

al., 2019) and the porous nature of the materials (Khan et al., 2015; Khan et al., 2016; Yuanying Liu et al., 2014) was explained in the previous studies. A possible two electrons transfer electrochemical oxidation mechanism of ascorbic acid to dehydroascorbic acid is given in Figure 66 (Fabregat et al., 2014; Murugan et al., 2019).

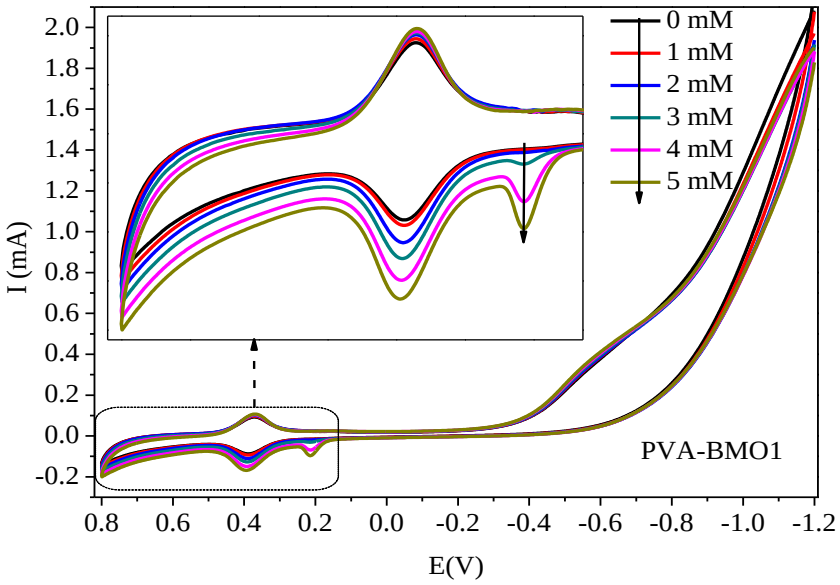

Figure 64. Electrochemical properties of PVA-BMO1 NC: CV ascorbic acid sensing curve at different concentrations.

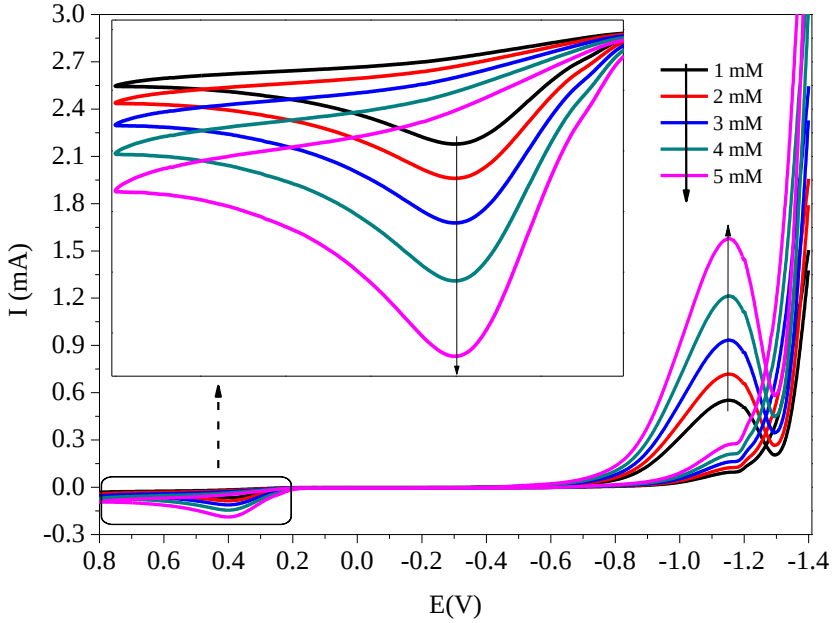

Figure 65. Electrochemical properties of PVA-BMO2 NC: CV ascorbic acid sensing curve at different concentrations.

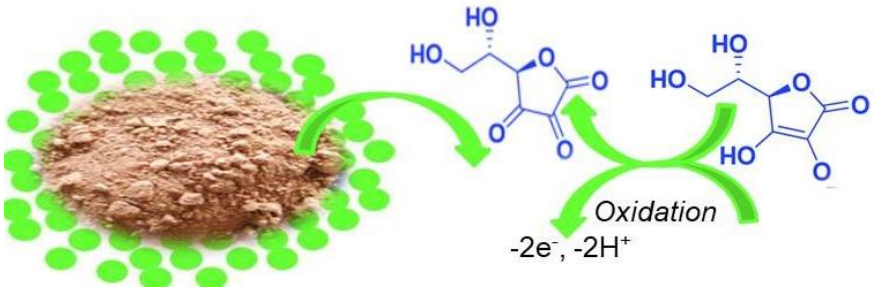

Figure 66. The proposed mechanism of electrochemical oxidation reactions for electrocatalytic oxidation of AA to dehydro-ascorbic acid at the NCs sensor (Murugan et al., 2019).

4.5. Antibacterial Activity Studies

The antibacterial activities of ZnO NPs and PVA-TMOP1 synthesized using different PVA amounts and precursor percentages are examined against *E. coli and S. aureus* bacterial strains [Figures 67(a) – (d) and 68(a) – (b)]. As seen in Figures 67 and 68 and Table 19, ZnO NPs do not show antibacterial activity for both Gram-negative and Gram-positive bacteria. It is due to its higher crystallite size/smaller SAV value, compared to the NCs. As reported, the antibacterial activity of ZnO NPs is dependent on its crystallite size; the smaller the size, the higher the antibacterial activity (Raghupathi et al., 2011). However, all the other ZnO-based binary and ternary NCs showed better antibacterial activities. As confirmed from the XRD, HRTEM, and BET analysis, this enhanced antibacterial activity for the NCs is due to their small crystallite sizes and porosity, which provide superior contact with the surface of the bacteria. The approximate average crystallite size for PVA-TMONCs was found to be in the range between 10 and 30 nm, whereas the size for ZnO remained at 60 nm. The amount of PVA and percentages of metal oxide precursor optimization and the respective zone of inhibition values are given in Table 19. The bactericidal effect of NPs was found to be the same yet slightly higher for Gram-negative bacteria compared to the Gram-positive bacteria. It is due to the difference in the structural composition of Gram-positive and Gram-negative bacteria (Santhoshkumar et al., 2017).

Compared to gram-positive bacteria, the cell wall of gram-negative bacteria is more complex, which acts as a permeability barrier for the absorption of ROS. Moreover, the membrane of gram-positive bacteria has a less negative charge compared to gram-negative

bacteria that increase the absorption of negatively charged ROS species (Gordon et al., 2011; Russell, 2003). As seen from the result (Table 19), by increasing the zinc precursor percentage from 10 to 50%, the antibacterial activity increases. However, further increasing its percentage to 90% caused decreasing the antibacterial activity. The maximum diameter of the zone of inhibition for 50% PVA-TMONC at 125 µg/mL concentration was determined to be 28 mm and 29 mm for *E. coli* and *S. aureus* bacteria, respectively. Based on these results, it is possible to conclude that, the synthesized PVA-TMONCs exhibited significant antibacterial action on both Gram-positive and Gram-negative bacteria.

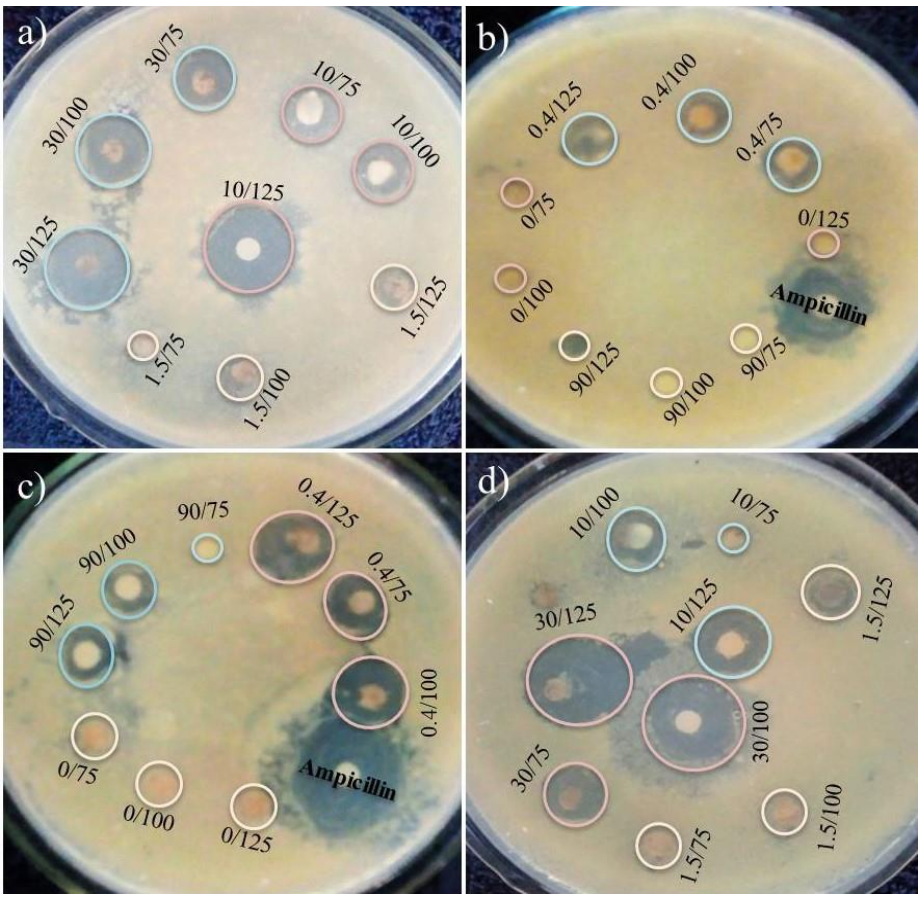

Figure 67. The antibacterial activity for PVA amount and precursors percentage optimization; (a and b) *S. aureus* and (c and d) *E. coli.*

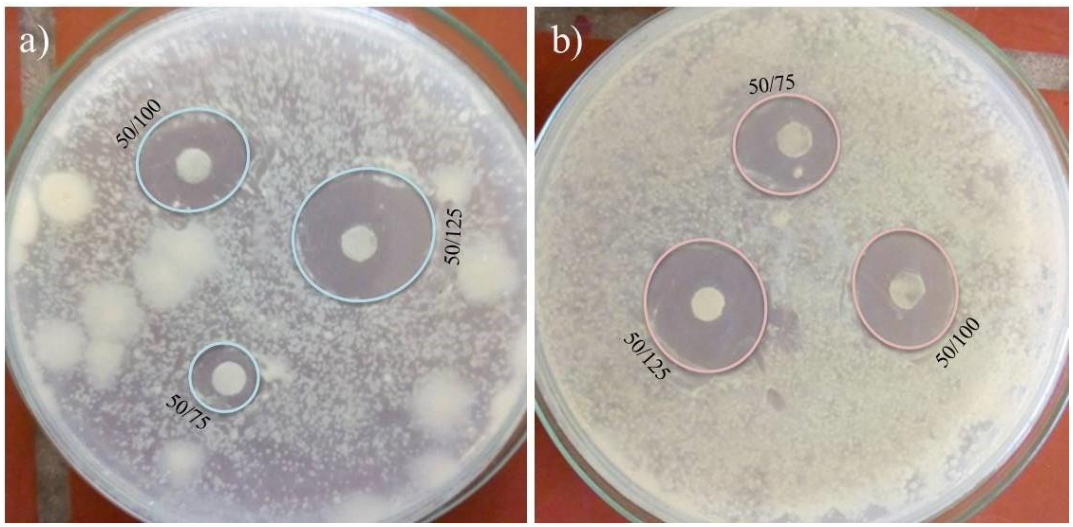

Figure 68. The antibacterial activity of optimized PVA-TMONC towards (a) *S. aureus* (b) *E. coli*.

Table 19. The zone of inhibition *(ZI/mm)* of PVA optimization against bacteria for PVA-TMOP1 NC.

Code	Concentration (µg/mL)	*E. coli* (ZI/mm)	*S. aureus* (ZI/mm)	Code	Concentration (µg/mL)	*E. coli* (ZI/mm)	*S. aureus* (ZI/mm)
	75	6	6	10	75	6	9
	100	6	6		100	11	12
0	125	6	6		125	18	20
	75	16	12	30	75	13	15
	100	20	16		100	20	21
0.4	125	21	18		125	28	23
	75	6	6	50	75	13	17
	100	6	6		100	20	22
1.5	125	8	10		125	28.25	29
Ampicillin	125	22	20				

ZI = zone of inhibition

Depending on the antibacterial activity experiment conducted for ZnO NPs and PVA-TMONCs; the 50% and 90% zinc precursor percentage amounts are selected for PVA-BMONCs antibacterial test. As seen in Figure 69(a)-(d) and Table 20, the PVA-BMONCs have shown better antibacterial activity, compared to ZnO NPs. As the percentage of ZnO in the NCs reduced from 90 to 50, an enhancement in the antibacterial activity was observed, which is similar to the work reported earlier (Gordon et al., 2011). The bactericidal activity of the NCs is similar for both Gram-negative and Gram-positive bacteria. It indicates that both the direct and indirect ROS generation is possible

mechanisms towards bacterial death (Thakur et al., 2019). Compared to the other ZnO NPs and NCs (Table 20), PVA-BMO2-50 NC has a relatively high zone of inhabitations for all bacteria. Yet, the highest zone of inhibition was detected on PVA-BMO1-50 (SS4) NC on *E. coli* bacteria (24 mm). However, compared to the binary NCs, the ternary NCs materials have showed better antibacterial activity.

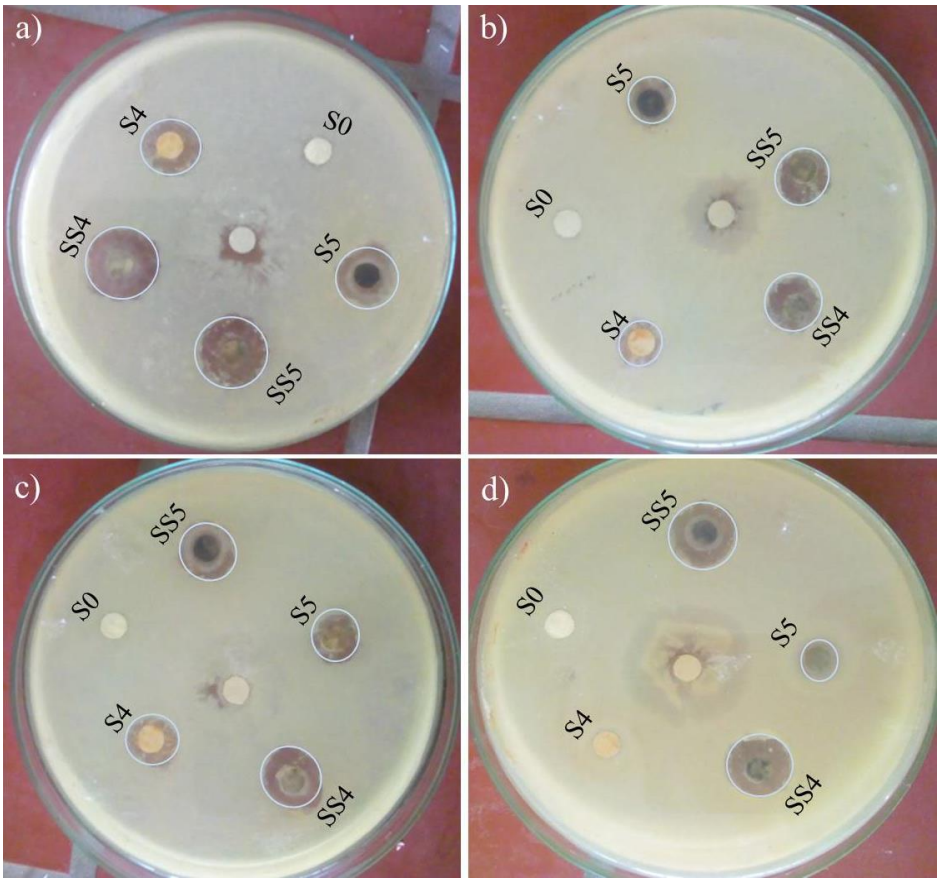

Figure 69. Antibacterial activity of Ampicillin (center (a-d)), ZnO NPs, and PVA-BMONCs towards (a) *E. coli*, (b) *S. aureus*, (c) *P. aeruginosa*, (d) *B. subtills* bacteria.

Table 20. The zone of inhibition (*ZI/mm*) for Ampicillin, ZnO, and PVA-BMONCs against *E. coli*, *S. aureus*, *P. aeruginosa*, and *B. subtills* bacteria using 125 µg mL^{-1} concentrations.

Code	*E. coli*	*S. aureus*	*P. aeruginosa*	*B. subtills*
ZnO(S0)	6	6	6	6
PVA-BMO1-90(S4)	14	13	13	12
PVA-BMO1-50(SS4)	24	18	22	20
PVA-BMO2-90(S5)	19	16	16	16
PVA-BMO2-50(SS5)	23	20	22	22
Ampicillin	10	12	6	19

Antibacterial activities of NPs act only when in contact with bacterial cell walls, various means of promoting NPs-bacterial contacts such as electrostatic attraction, Vander Waals forces, and receptor–ligand and hydrophobic interactions have been known. Once inside cells, NPs interact with the microbial cellular machinery to inhibit enzymes, deactivate proteins, induce oxidative stress and electrolyte imbalance, and modify gene expression levels. The electrostatic force of attraction depends on the surface area available for interaction, this interaction leads to membrane disruption, and this disruption, in turn, increases permeability, eventually pulling more NPs into the microbial system with simultaneous leakage of cellular contents. Once NPs enter into the cell generate ROS (Jagadeeshan & Parsanathan, 2019).

Generally, the antibacterial activity occurs due to the interaction of negatively charged bacterial cells (through dissociation of carboxylic groups) and positively charged metal oxides NPs (Stoimenov et al., 2002). The direct and indirect ways are the two mechanisms by which metal oxide NPs cause bacterial death. In the direct mechanism, the interaction of the positively charged NPs with negatively charged microorganisms leads to the disruption of the cell wall (the above path in Figure 70). It leads to the generation of intracellular ROS through the damaging of bacterial enzymes (Zholobak et al., 2016). The generated ROS further damages the DNA, RNA, and protein, which leads to bacterial cell death. The indirect mechanism that mostly occurred in gram-negative bacteria (which has an outer membrane/polysaccharide layer) is due to the interaction of the NPs with the intercellular space. Due to this interaction, the generated ROS outside the cell (the lower path in Figure 70) leads to the damaging of the bacterial cell (Kannan & Sundrarajan, 2014).

The interaction of NPs with microorganisms (Zhang et al., 2008) and the formation of ROS by the effect of light radiation and without light radiation (Jalal et al., 2010) was suggested as the main mechanisms towards bacterial death. The release of antimicrobial ions through the solubility of metal oxides and the formation of ROS is also reported to be the other mechanism of the NPs (Das et al., 2017; Espitia et al., 2012; Kasemets et al., 2009). However, the release of these ions may have toxic effects during discarding after the experiment. As confirmed from the XRD pattern and UV-vis-DRS spectra analysis, the non-appearance of any band position shift indicates the absence of any structural distortion in ZnO NPs attributed to the incorporation of Fe^{3+}/Mn^{3+}. Therefore, the release

of ions is not the probable antibacterial mechanism in this work. This may also indicate the high stability/insolubility of these metal oxides in the media used during the antibacterial activity. The proposed mechanism of degradation developed is believed to be due to the direct interaction, which means the damaging of the outer cell wall through electrostatic contact between NPs and bacteria, leading to the generation of intracellular ROS and the indirect ways of contact which means interaction of the NPs with the environment (intercellular space) around the bacteria and extracellular generation of ROS (Zholobak et al., 2016) leads to the protein oxidation, nucleic acid degradation, and disruption of biochemical processes by penetrating through the cell membranes of the bacteria (Nair et al., 2009).

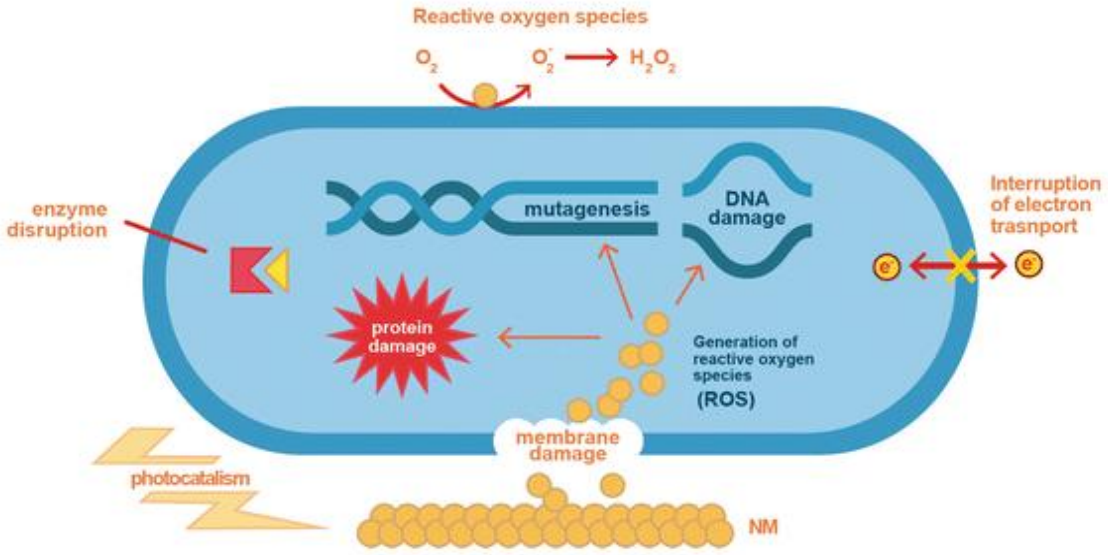

Figure 70. The direct and indirect antibacterial activity mechanism**s**, after interaction with the target cells, metal nanoparticles can induce loss of membrane integrity, oxidative stress, and injury to proteins and DNA (Rai & Shegokar, 2017).

Three features play a role in the generation of ROS: active redox cycling; pro-oxidant functional groups on the MeO-NP surface; and cell–particle interactions (Nel, 2006). The change in electronic properties and reduction in particle size produces reactive groups on the surface of the particles. These reactive sites are the center of interaction between molecular oxygen and electron donor/acceptor active sites and result in the formation of $O_2^{\bullet -}$. This $O_2^{\bullet -}$ will further produce more ROS through Fenton-type reactions (the catalytic process that converts hydrogen peroxide, a product of mitochondrial oxidative respiration,

into a highly toxic hydroxyl free radical). It is the reaction of ferrous iron (Fe^{2+}) and hydrogen peroxide (H_2O_2). In this reaction, ferric iron (Fe^{3+}) and hydroxyl radical are produced. $O_2^{\bullet -}$. The generated $O_2^{\bullet -}$ damaged iron-sulfur (Fe–S) clusters in the electron transport chain, releasing more ferrous ions thus decreasing ATP production. These ferrous ions are oxidized by the Fenton reaction, generating more OH• (Jagadeeshan & Parsanathan, 2019; Raghunath & Perumal, 2017).

5. CONCLUSIONS AND RECOMMENDATIONS

The development of advanced materials is the current necessity for environmental protection, improvised electronic devices, and nanomedicine applications. The present work reports the synthesis and characterization of single, binary, and ternary ZnO-based nanomaterials for adsorption, photocatalysis, sensor, and antibacterial activity studies. The sol-gel technique followed by the auto-combustion procedure was developed for the synthesis of porous binary and ternary NCs. Compared to the co-precipitation, the sol-gel method presented a better SAV for the synthesized NCs. The zinc nitrate precursor exhibited good auto-combustion progression than the zinc acetate salt precursor. The porous nature of the NCs is confirmed from the SEM image, SAED ring, and BET analysis. The thermal stability study conducted using DTG/DSC techniques showed the activation of PVA polymer degradation by metal oxides. The optimized calcination temperature of 500 °C was found from DTG analysis and used for consecutive characterization and application tests. Using the XRD pattern and TEM analysis, the crystallite size of the synthesized NPs and NCs was confirmed to be in the nanometer (7nm - 70 nm) range. The crystallite size of the synthesized PVA-TMOP1 NC has six times lower than that of ZnO NPs. The porosity PVA-TMOP1 NC also exhibited fifteen times greater SSA than ZnO NPs. The EDX, XPS, and HRTEM analyses were applied for the compositional investigation of the NCs, respectively. The CV and EIS techniques were applied to verify the charge transfer synergy improvements from ZnO NPs to binary and to the ternary NCs. The adsorption efficiency of PVA-TMOP1 NC that exhibited optimum SAV and SSA value was tested on the MB dye. Among the applied adsorption isotherm models, the Langmuir and FH models were found relatively well-fitting with 7.75 $\mathrm{mg\,g^{-1}}$ removal efficiency. The PSO adsorption-reaction kinetics model fits well. These adsorption investigations showed the domination of the monolayer/chemisorption type of adsorption. The efficiency of ZnO NPs and PVA-BMO1, PVA-BMO2, and PVA-TMOP1 NCs further tested on the CR and AO 8 dyes degradation, AA sensing, and antibacterial activity. The PVA-BMO2 showed relatively better activity only on AO8 dye. However, the PVA-TMOP1 NC showed good activity on both CR and AO8 dyes. Compared to ZnO NPs; the PVA-BMONCs and PVA-TMONCs have superior ascorbic acid sensing and antibacterial activities. The highest antibacterial zone of inhibition for PVA-BMONCs and PVA-TMONCs was determined to be 24 and 28 mm, respectively on *E. coli* bacteria. In

conclusion, the synthesized NCs exhibited good performance towards adsorption, photocatalysis, electrochemical, sensor, and antibacterial activity applications.

The following points are recommended for future work:

- Further characterization of the selected composites by PL and Zeta potential
- Optimization of parameters such as the pH of the solutions, calcination temperature, calcination time and aging time, precursors type, zinc precursors percentage (< 10%), solvents used during synthesis.
- Checking the effects of scavengers and EPR characterization to determine the dominant reactive species in the degradation process, simultaneous degradation of mixed dyes, and conducting the degradation process considering real dye effluents.
- Estimating the flat band potentials from banggap measurement by CV and UV-Vis.
- Further sensor investigation including for single Fe_2O_3, Mn_2O_3, and other various biomolecules.
- Applying microscopy techniques and optimizing the concentrations of the catalyst during the antibacterial activity study.

Fund number

- **ASTU/SP – R/122/21**

References

6. REFERENCES

Abd-Elrahman, M. I. (2013). Synthesis of Polyvinyl Alcohol–Zinc Oxide Composite by Mechanical Milling: Thermal and Infrared Studies. *Nanoscale and Microscale Thermophysical Engineering*, *17*(3), 194–203. https://doi.org/10.1080/15567265.2013.776152

Abdullah Mirzaie, R., Kamrani, F., Anaraki Firooz, A., & Khodadadi, A. A. (2012). Effect of α-Fe_2O_3 addition on the morphological, optical and decolorization properties of ZnO nanostructures. *Materials Chemistry and Physics*, *133*(1), 311–316. https://doi.org/10.1016/j.matchemphys.2012.01.029

Achouri, F., Corbel, S., Aboulaich, A., Balan, L., Ghrabi, A., Ben Said, M., & Schneider, R. (2014). Aqueous synthesis and enhanced photocatalytic activity of ZnO/Fe_2O_3 heterostructures. *Journal of Physics and Chemistry of Solids*, *75*(10), 1081–1087. https://doi.org/10.1016/j.jpcs.2014.05.013

Achouri, F., Merlin, C., Corbel, S., Alem, H., Mathieu, L., Balan, L., Medjahdi, G., Ben Said, M., Ghrabi, A., & Schneider, R. (2018). ZnO Nanorods with High Photocatalytic and Antibacterial Activity under Solar Light Irradiation. *Materials*, *11*(11), 2158. https://doi.org/10.3390/ma11112158

Adeleye, A. S., Conway, J. R., Garner, K., Huang, Y., Su, Y., & Keller, A. A. (2016). Engineered nanomaterials for water treatment and remediation: Costs, benefits, and applicability. *Chemical Engineering Journal*, *286*, 640–662. https://doi.org/10.1016/j.cej.2015.10.105

Adesina, A. A. (2004). Industrial exploitation of photocatalysis: progress, perspectives and prospects. *Catalysis Surveys from Asia*, *8*(4), 265–273. https://doi.org/10.1007/s10563-004-9117-0

Adil, S., Assal, M., Kuniyil, M., Khan, M., Shaik, M. R., Alwarthan, A., Labis, J., & Siddiqui, M. R. (2017). Synthesis and comparative catalytic study of zinc oxide (ZnO_x) nanoparticles promoted $MnCO_3$, MnO_2 and Mn_2O_3 for selective oxidation of benzylic alcohols using molecular oxygen. *Materials Express*, *7*(2), 79–92. https://doi.org/10.1166/mex.2017.1357

Ahmad, A., Ullah, S., Ahmad, W., Yuan, Q., Taj, R., Khan, A. U., Rahman, A. U., & Khan, U. A. (2020). Zinc oxide-selenium heterojunction composite: Synthesis, characterization and photo-induced antibacterial activity under visible light irradiation. *Journal of Photochemistry and Photobiology B: Biology*, *203*(September 2019), 111743. https://doi.org/10.1016/j.jphotobiol.2019.111743

Ahmed, M. J. (2016). Application of agricultural based activated carbons by microwave and conventional activations for basic dye adsorption: Review. *Journal of Environmental Chemical Engineering*, *4*(1), 89–99. https://doi.org/10.1016/j.jece.2015.10.027

Ahmed, R., Tariq, M., Ali, I., Asghar, R., Noorunnisa Khanam, P., Augustine, R., & Hasan, A. (2018). Novel electrospun chitosan/polyvinyl alcohol/zinc oxide nanofibrous mats with antibacterial and antioxidant properties for diabetic wound healing. *International Journal of Biological Macromolecules*, *120*, 385–393. https://doi.org/10.1016/j.ijbiomac.2018.08.057

Ahmed, S., Rasul, M. G., Brown, R., & Hashib, M. A. (2011). Influence of parameters on the heterogeneous photocatalytic degradation of pesticides and phenolic contaminants in wastewater: A short review. *Journal of Environmental Management*, *92*(3), 311–330. https://doi.org/10.1016/j.jenvman.2010.08.028

Ahmed, S., Rasul, M. G., Martens, W. N., Brown, R., & Hashib, M. A. (2011). Advances in Heterogeneous Photocatalytic Degradation of Phenols and Dyes in Wastewater: A Review. *Water, Air, & Soil Pollution*, *215*(1–4), 3–29. https://doi.org/10.1007/s11270-010-0456-3

Akhil, K., Jayakumar, J., Gayathri, G., & Khan, S. S. (2016). Effect of various capping agents on photocatalytic, antibacterial and antibiofilm activities of ZnO nanoparticles. *Journal of Photochemistry and Photobiology B: Biology*, *160*, 32–42. https://doi.org/10.1016/j.jphotobiol.2016.03.015

Akkari, M., Aranda, P., Belver, C., Bedia, J., Ben Haj Amara, A., & Ruiz-Hitzky, E. (2018). ZnO/sepiolite heterostructured materials for solar photocatalytic degradation of pharmaceuticals in wastewater. *Applied Clay Science*, *156*(January), 104–109. https://doi.org/10.1016/j.clay.2018.01.021

Al-Khateeb, I., & Mahmood, M. (2016). Adsorption, Thermodynamics and Kinetics of Methylene Blue on Nano Structured ZnO Crystals. *American Chemical Science Journal*, *13*(4), 1–9. https://doi.org/10.9734/ACSJ/2016/25000

Alam, M. M., Mukhlish, M. Z. Bin, Tazrin, A., Jui, N. A., Asiri, A. M., Rahman, M. M., Islam, M. A., & Uddin, M. T. (2020). A novel highly selective electrochemical chlorobenzene sensor based on ternary oxide RuO_2/ZnO/TiO_2 nanocomposites. *RSC Advances*, *10*(54), 32532–32547. https://doi.org/10.1039/D0RA05824F

Alder, C. M., Hayler, J. D., Henderson, R. K., Redman, A. M., Shukla, L., Shuster, L. E., & Sneddon, H. F. (2016). Updating and further expanding GSK's solvent sustainability guide. *Green Chemistry*, *18*(13), 3879–3890. https://doi.org/10.1039/C6GC00611F

Ali, D. A., El-Katori, E. E., & Kasim, E. A. (2019). Sol-Gel Sonochemical Triton X-100 Templated Synthesis of Fe_2O_3/ZnO Nanocomposites Toward Developing Photocatalytic Degradation of Organic Pollutants. *Zeitschrift Für Physikalische Chemie*. https://doi.org/10.1515/zpch-2019-1518

ALOthman, Z. (2012). A Review: Fundamental Aspects of Silicate Mesoporous Materials. *Materials*, *5*(12), 2874–2902. https://doi.org/10.3390/ma5122874

Amin, M. O., Madkour, M., & Al-Hetlani, E. (2018). Metal oxide nanoparticles for latent fingerprint visualization and analysis of small drug molecules using surface-assisted laser desorption/ionization mass spectrometry. *Analytical and Bioanalytical Chemistry*, *410*(20), 4815–4827. https://doi.org/10.1007/s00216-018-1119-2

Amsaveni, P., Nivetha, A., Sakthivel, C., Suresh Philip, C., & Prabha, I. (2020). Effectiveness of surfactants for unique hierarchical Mn_2O_3 nanomaterials as enhanced oxidative catalysts, antibacterial agents, and photocatalysts. *Journal of Physics and Chemistry of Solids*, *144*(September 2019), 109429. https://doi.org/10.1016/j.jpcs.2020.109429

An, H., Zhou, J., Li, J., Zhu, B., Wang, S., Zhang, S., Wu, S., & Huang, W. (2009). Deposition of Pt on the stable nanotubular TiO_2 and its photocatalytic performance. *Catalysis Communications*, *11*(3), 175–179. https://doi.org/10.1016/j.catcom.2009.09.020

Anandan, S., Ohashi, N., & Miyauchi, M. (2010). ZnO-based visible-light photocatalyst: Band-gap engineering and multi-electron reduction by co-catalyst. *Applied Catalysis B: Environmental*, *100*(3–4), 502–509. https://doi.org/10.1016/j.apcatb.2010.08.029

Anaya-Esparza, L., Montalvo-González, E., González-Silva, N., Méndez-Robles, M., Romero-Toledo, R., Yahia, E., & Pérez-Larios, A. (2019). Synthesis and Characterization of TiO_2-ZnO-MgO Mixed Oxide and Their Antibacterial Activity. *Materials*, *12*(5), 698. https://doi.org/10.3390/ma12050698

Anžlovar, A., Kogej, K., Crnjak Orel, Z., & Žigon, M. (2011). Polyol mediated nano size zinc oxide and nanocomposites with poly(methyl methacrylate). *Express Polymer Letters*, *5*(7), 604–619. https://doi.org/10.3144/expresspolymlett.2011.59

Applerot, G., Lipovsky, A., Dror, R., Perkas, N., Nitzan, Y., Lubart, R., & Gedanken, A. (2009). Enhanced Antibacterial Activity of Nanocrystalline ZnO Due to Increased ROS-Mediated Cell Injury. *Advanced Functional Materials*, *19*(6), 842–852. https://doi.org/10.1002/adfm.200801081

Arakha, M., Saleem, M., Mallick, B. C., & Jha, S. (2015). The effects of interfacial potential on antimicrobial propensity of ZnO nanoparticle. *Scientific Reports*, *5*(1), 9578. https://doi.org/10.1038/srep09578

Areerob, Y., Cho, J. Y., Jang, W. K., & Oh, W. (2018). Enhanced sonocatalytic degradation of organic dyes from aqueous solutions by novel synthesis of mesoporous Fe_3O_4-graphene/ZnO@SiO_2 nanocomposites. *Ultrasonics Sonochemistry*, *41*(August 2017), 267–278. https://doi.org/10.1016/j.ultsonch.2017.09.034

Atla, S. B., Lin, W.-R., Chien, T.-C., Tseng, M.-J., Shu, J.-C., Chen, C.-C., & Chen, C.-Y. (2018). Fabrication of Fe_3O_4/ZnO magnetite core shell and its application in photocatalysis using sunlight. *Materials Chemistry and Physics*, *216*(June), 380–386. https://doi.org/10.1016/j.matchemphys.2018.06.020

Ayawei, N., Ebelegi, A. N., & Wankasi, D. (2017). Modelling and Interpretation of Adsorption Isotherms. *Journal of Chemistry*, *2017*, 1–11. https://doi.org/10.1155/2017/3039817

Bai, S., Tian, K., Han, N., Guo, J., Luo, R., Li, D., & Chen, A. (2020). A novel rGO-decorated ZnO/$BiVO_4$ heterojunction for the enhancement of NO_2 sensing properties. *Inorganic Chemistry Frontiers*, *7*(4), 1026–1033. https://doi.org/10.1039/C9QI01608B

Bai, X., Wang, L., Zong, R., Lv, Y., Sun, Y., & Zhu, Y. (2013). Performance Enhancement of ZnO Photocatalyst via Synergic Effect of Surface Oxygen Defect and Graphene Hybridization. *Langmuir*, *29*(9), 3097–3105. https://doi.org/10.1021/la4001768

Bala, N., Saha, S., Chakraborty, M., Maiti, M., Das, S., Basu, R., & Nandy, P. (2015). Green synthesis of zinc oxide nanoparticles using Hibiscus subdariffa leaf extract: effect of temperature on synthesis, anti-bacterial activity and anti-diabetic activity. *RSC Advances*, *5*(7), 4993–5003. https://doi.org/10.1039/C4RA12784F

Basnet, Parita, Samanta, D., Inakhunbi Chanu, T., Mukherjee, J., & Chatterjee, S. (2019). Assessment of synthesis approaches for tuning the photocatalytic property of ZnO nanoparticles. *SN Applied Sciences*, *1*(6), 633. https://doi.org/10.1007/s42452-019-0642-x

Basnet, Pradip, Larsen, G. K., Jadeja, R. P., Hung, Y., & Zhao, Y. (2013). α-Fe_2O_3 Nanocolumns and Nanorods Fabricated by Electron Beam Evaporation for Visible Light Photocatalytic and Antimicrobial Applications. *Applied Materials & Interfaces*, *5*(6), 2085–2095. https://doi.org/10.1021/am303017c

Bazazi, S., Arsalani, N., Khataee, A., & Tabrizi, A. G. (2018). Comparison of ball milling-hydrothermal and hydrothermal methods for synthesis of ZnO nanostructures and evaluation of their photocatalytic performance. *Journal of Industrial and Engineering Chemistry*, *62*, 265–272. https://doi.org/10.1016/j.jiec.2018.01.004

Becker, J., Raghupathi, K. R., St. Pierre, J., Zhao, D., & Koodali, R. T. (2011). Tuning of the Crystallite and Particle Sizes of ZnO Nanocrystalline Materials in Solvothermal Synthesis and Their Photocatalytic Activity for Dye Degradation. *The Journal of Physical Chemistry C*, *115*(28), 13844–13850. https://doi.org/10.1021/jp2038653

Behtaj Lejbini, M., & Sangpour, P. (2019). Hydrothermal synthesis of α-Fe_2O_3-decorated MoS2 nanosheets with enhanced photocatalytic activity. *Optik*, *177*(July 2018), 112–117. https://doi.org/10.1016/j.ijleo.2018.09.019

Bendjabeur, S., Zouaghi, R., Kaabeche, O. N. ., & Sehili, T. (2017). Parameters Affecting Adsorption and Photocatalytic Degradation Behavior of Gentian Violet under UV Irradiation with Several Kinds of TiO_2 as a Photocatalyst. *International Journal of Chemical Reactor Engineering*, *15*(4). https://doi.org/10.1515/ijcre-2016-0206

Beranek, R. (2011). (Photo)electrochemical Methods for the Determination of the Band Edge Positions of TiO_2-Based Nanomaterials. *Advances in Physical Chemistry*, *2011*(Iv), 1–20. https://doi.org/10.1155/2011/786759

Bernal, V., Giraldo, L., & Moreno-Piraján, J. C. (2020). A new methodology to determine the effect of the adsorbate-adsorbent interactions on the analgesic adsorption onto activated carbon using kinetic and calorimetry data. *Environmental Science and Pollution Research*, *27*(29), 36639–36650. https://doi.org/10.1007/s11356-020-09725-w

Bhatia, S., & Verma, N. (2017). Photocatalytic activity of ZnO nanoparticles with optimization of defects. *Materials Research Bulletin*, *95*, 468–476. https://doi.org/10.1016/j.materresbull.2017.08.019

Bian, X., Hong, K., Ge, X., Song, R., Liu, L., & Xu, M. (2015). Functional Hierarchical Nanocomposites Based on ZnO Nanowire and Magnetic Nanoparticle as Highly Active Recyclable Photocatalysts. *The Journal of Physical Chemistry C*, *119*(4), 1700–1705. https://doi.org/10.1021/jp5108312

Bigiani, L., Maccato, C., Gasparotto, A., Sada, C., & Barreca, D. (2019). Structure and properties of Mn_3O_4 thin films grown on single crystal substrates by chemical vapor deposition. *Materials Chemistry and Physics*, *223*(July 2018), 591–596. https://doi.org/10.1016/j.matchemphys.2018.11.047

Boehm, H. P. (1966). Chemical Identification of Surface Groups. In *The Physics Teacher* (Vol. 14, Issue 1, pp. 179–274). https://doi.org/10.1016/S0360-0564(08)60354-5

Boningari, T., Inturi, S. N. R., Suidan, M., & Smirniotis, P. G. (2018). Novel one-step synthesis of nitrogen-doped TiO_2 by flame aerosol technique for visible-light photocatalysis: Effect of synthesis parameters and secondary nitrogen (N) source. *Chemical Engineering Journal*, *350*(February), 324–334. https://doi.org/10.1016/j.cej.2018.05.122

Bora, T., Sathe, P., Laxman, K., Dobretsov, S., & Dutta, J. (2017). Defect engineered visible light active ZnO nanorods for photocatalytic treatment of water. *Catalysis Today*, *284*, 11–18. https://doi.org/10.1016/j.cattod.2016.09.014

Bozkurt Çırak, B., Caglar, B., Kılınç, T., Morkoç Karadeniz, S., Erdoğan, Y., Kılıç, S., Kahveci, E., Ercan Ekinci, A., & Çırak, Ç. (2019). Synthesis and characterization of ZnO nanorice decorated TiO2 nanotubes for enhanced photocatalytic activity. *Materials Research Bulletin*, *109*(April 2018), 160–167. https://doi.org/10.1016/j.materresbull.2018.09.039

Broekhoff, J. C. P. (1979). Mesopore Determination from Nitrogen Sorption Isotherms: Fundamentals, Scope, Limitations. In *Studies in Surface Science and Catalysis* (Vol. 3, Issue C, pp. 663–684). Elsevier Scientific Publishing Company. https://doi.org/10.1016/S0167-2991(09)60243-3

Bumajdad, A., Nazeer, A. A., Al Sagheer, F., Nahar, S., & Zaki, M. I. (2018). Controlled Synthesis of ZrO_2 Nanoparticles with Tailored Size, Morphology and Crystal Phases via Organic/Inorganic Hybrid Films. *Scientific Reports*, *8*(1), 3695. https://doi.org/10.1038/s41598-018-22088-0

Byzynski, G., Pereira, A. P., Volanti, D. P., Ribeiro, C., & Longo, E. (2018). High-performance ultraviolet-visible driven ZnO morphologies photocatalyst obtained by microwave-assisted hydrothermal method. *Journal of Photochemistry and Photobiology A: Chemistry*, *353*, 358–367. https://doi.org/10.1016/j.jphotochem.2017.11.032

Cai, A., Sun, Y., Du, L., & Wang, X. (2015). Hierarchical Ag_2O–ZnO–Fe_3O_4 composites with enhanced visible-light photocatalytic activity. *Journal of Alloys and Compounds*, *644*, 334–340. https://doi.org/10.1016/j.jallcom.2015.03.236

Cao, X., & Wang, N. (2011). A novel non-enzymatic glucose sensor modified with Fe_2O_3 nanowire arrays. *The Analyst*, *136*(20), 4241. https://doi.org/10.1039/c1an15367f

Charles, J., Bradu, C., Morin-Crini, N., Sancey, B., Winterton, P., Torri, G., Badot, P.-M., & Crini, G. (2016). Pollutant removal from industrial discharge water using individual and combined effects of adsorption and ion-exchange processes: Chemical abatement. *Journal of Saudi Chemical Society*, *20*(2), 185–194. https://doi.org/10.1016/j.jscs.2013.03.007

Chen, C., Li, Z., Lin, H., Wang, G., Liao, J., Li, M., Lv, S., & Li, W. (2016). Enhanced visible light photocatalytic performance of ZnO nanowires integrated with CdS and Ag2S. *Dalton Transactions*, *45*(9), 3750–3758. https://doi.org/10.1039/C5DT04533A

Chen, D., Wang, Z., Ren, T., Ding, H., Yao, W., Zong, R., & Zhu, Y. (2014). Influence of Defects on the Photocatalytic Activity of ZnO. *The Journal of Physical Chemistry C*, *118*(28), 15300–15307. https://doi.org/10.1021/jp5033349

Chen, F., Ho, P., Ran, R., Chen, W., Si, Z., Wu, X., Weng, D., Huang, Z., & Lee, C. (2017). Synergistic effect of CeO_2 modified TiO_2 photocatalyst on the enhancement of visible light photocatalytic performance. *Journal of Alloys and Compounds*, *714*, 560–566. https://doi.org/10.1016/j.jallcom.2017.04.138

Chen, H., Zhao, J., & Dai, G. (2011). Silkworm exuviae—A new non-conventional and low-cost adsorbent for removal of methylene blue from aqueous solutions. *Journal of Hazardous Materials*, *186*(2–3), 1320–1327. https://doi.org/10.1016/j.jhazmat.2010.12.006

Chen, M., Zhao, E., Yan, Q., Hu, Z., Xiao, X., & Chen, D. (2016). The Effect of Crystal Face of Fe_2O_3 on the Electrochemical Performance for Lithium-ion Batteries. *Scientific Reports*, *6*(1), 29381. https://doi.org/10.1038/srep29381

Chen, X., Wu, Z., Liu, D., & Gao, Z. (2017). Preparation of ZnO Photocatalyst for the Efficient and Rapid Photocatalytic Degradation of Azo Dyes. *Nanoscale Research Letters*, *12*(1), 143. https://doi.org/10.1186/s11671-017-1904-4

Chiang, Y., & Lin, C. (2013). Photocatalytic decolorization of methylene blue in aqueous solutions using coupled ZnO/SnO_2 photocatalysts. *Powder Technology*, *246*, 137–143. https://doi.org/10.1016/j.powtec.2013.04.033

Ciciliati, M. A., Silva, M. F., Fernandes, D. M., de Melo, M. A. C., Hechenleitner, A. A. W., & Pineda, E. A. G. (2015). Fe-doped ZnO nanoparticles: Synthesis by a modified sol–gel method and characterization. *Materials Letters*, *159*, 84–86. https://doi.org/10.1016/j.matlet.2015.06.023

Cohen, E. R., Mills, I., Strauss, H. L., Frey, J. G., Mills, I., Homann, K., & Kuchitsu, K. (2007). Quantities , Units and Symbols in Physical Chemistry. *International Union of Pure and Applied Chemistry*, *233*(3), 11–13.

Coulter, J. B., & Birnie, D. P. (2018). Assessing Tauc Plot Slope Quantification: ZnO Thin Films as a Model System. *Physica Status Solidi (B)*, *255*(3), 1700393. https://doi.org/10.1002/pssb.201700393

Cui, L., Wang, Y., Hu, L., Gao, L., Du, B., & Wei, Q. (2015). Mechanism of Pb(II) and methylene blue adsorption onto magnetic carbonate hydroxyapatite/graphene oxide. *RSC Advances*, *5*(13), 9759–9770. https://doi.org/10.1039/C4RA13009J

Dadi, R., Azouani, R., Traore, M., Mielcarek, C., & Kanaev, A. (2019). Antibacterial activity of ZnO and CuO nanoparticles against gram positive and gram negative strains. *Materials Science and Engineering: C*, *104*(July), 109968. https://doi.org/10.1016/j.msec.2019.109968

Dai, Y., Tang, Q., Zhang, Z., Yu, C., Li, H., Xu, L., Zhang, S., & Zou, Z. (2018). Enhanced mechanical, thermal, and UV-shielding properties of poly(vinyl alcohol)/metal–organic framework nanocomposites. *RSC Advances*, *8*(67), 38681–38688. https://doi.org/10.1039/C8RA07143H

Daneshvar, N., Salari, D., & Khataee, A. . (2004). Photocatalytic degradation of azo dye acid red 14 in water on ZnO as an alternative catalyst to TiO_2. *Journal of Photochemistry and Photobiology A: Chemistry*, *162*(2–3), 317–322. https://doi.org/10.1016/S1010-6030(03)00378-2

Das, B., Dash, S. K., Mandal, D., Ghosh, T., Chattopadhyay, S., Tripathy, S., Das, S., Dey, S. K., Das, D., & Roy, S. (2017). Green synthesized silver nanoparticles destroy multidrug resistant bacteria via reactive oxygen species mediated membrane damage. *Arabian Journal of Chemistry*, *10*(6), 862–876. https://doi.org/10.1016/j.arabjc.2015.08.008

Dassisti, M., & Brunetti, G. (2020). Introduction to Magnetorheological Fluids. In *Reference Module in Materials Science and Materials Engineering* (pp. 1–16). Elsevier. https://doi.org/10.1016/B978-0-12-803581-8.11744-8

Davari, N., Farhadian, M., Nazar, A. R. S., & Homayoonfal, M. (2017). Degradation of diphenhydramine by the photocatalysts of ZnO/Fe_2O_3 and TiO_2/Fe_2O_3 based on clinoptilolite: Structural and operational comparison. *Journal of Environmental Chemical Engineering*, *5*(6), 5707–5720. https://doi.org/10.1016/j.jece.2017.10.052

Dehghani-Dashtabi, M., Hekmatara, H., & Seyed-Yazdi, J. (2019). Synthesis and improved photoactivity of magnetic quaternary nanocomposites consisting of Fe_3O_4@ZnO core@shell nanoparticles decorated on graphene-oxide grafted poly-

citric acid. *Physica B: Condensed Matter*, *553*(August 2018), 11–17. https://doi.org/10.1016/j.physb.2018.10.020

Dey, A., & Sarkar, S. K. (2020). Room Temperature ZnO and Au-ZnO Quantum Dots Thin Film Gas Sensor Fabrication for Detecting of Volatile Organic Compound Gases. *IEEE Sensors Journal*, *20*(21), 12602–12609. https://doi.org/10.1109/JSEN.2020.3002967

Di Mauro, A., Fragalà, M. E., Privitera, V., & Impellizzeri, G. (2017). ZnO for application in photocatalysis: From thin films to nanostructures. *Materials Science in Semiconductor Processing*, *69*(March), 44–51. https://doi.org/10.1016/j.mssp.2017.03.029

Dickhout, J. M., Moreno, J., Biesheuvel, P. M., Boels, L., Lammertink, R. G. H., & de Vos, W. M. (2017). Produced water treatment by membranes: A review from a colloidal perspective. *Journal of Colloid and Interface Science*, *487*, 523–534. https://doi.org/10.1016/j.jcis.2016.10.013

Díez-Pascual, A. M., & Díez-Vicente, A. L. (2014). Development of Nanocomposites Reinforced with Carboxylated Poly(ether ether ketone) Grafted to Zinc Oxide with Superior Antibacterial Properties. *ACS Applied Materials & Interfaces*, *6*(5), 3729–3741. https://doi.org/10.1021/am500171x

Doan Thi, T. U., Nguyen, T. T., Thi, Y. D., Ta Thi, K. H., Phan, B. T., & Pham, K. N. (2020). Green synthesis of ZnO nanoparticles using orange fruit peel extract for antibacterial activities. *RSC Advances*, *10*(40), 23899–23907. https://doi.org/10.1039/D0RA04926C

Du, N., Zhang, H., Chen, B. D., Ma, X. Y., Liu, Z., Wu, J. B., & Yang, D. R. (2007). Porous Indium Oxide Nanotubes: Layer-by-Layer Assembly on Carbon-Nanotube Templates and Application for Room-Temperature NH_3 Gas Sensors. *Advanced Materials*, *19*(12), 1641–1645. https://doi.org/10.1002/adma.200602128

Dutta, S., Bhattacharyya, A., Ganguly, A., Gupta, S., & Basu, S. (2011). Application of Response Surface Methodology for preparation of low-cost adsorbent from citrus fruit peel and for removal of Methylene Blue. *Desalination*, *275*(1–3), 26–36. https://doi.org/10.1016/j.desal.2011.02.057

Edet, U. A., & Ifelebuegu, A. O. (2020). Kinetics, Isotherms, and Thermodynamic Modeling of the Adsorption of Phosphates from Model Wastewater Using Recycled Brick Waste. *Processes*, *8*(6), 665. https://doi.org/10.3390/pr8060665

Eliana, & Bojorge, N. (2011). Graphite-Composites Alternatives for Electrochemical Biosensor. In *Metal, Ceramic and Polymeric Composites for Various Uses* (Issue July 2011). InTech. https://doi.org/10.5772/17957

Elizalde-González, M. P., & García-Díaz, L. E. (2010). Application of a Taguchi L16 orthogonal array for optimizing the removal of Acid Orange 8 using carbon with a low specific surface area. *Chemical Engineering Journal*, *163*(1–2), 55–61. https://doi.org/10.1016/j.cej.2010.07.040

Espitia, P. J. P., Soares, N. de F. F., Coimbra, J. S. dos R., de Andrade, N. J., Cruz, R. S., & Medeiros, E. A. A. (2012). Zinc Oxide Nanoparticles: Synthesis, Antimicrobial Activity and Food Packaging Applications. *Food and Bioprocess Technology*, *5*(5), 1447–1464. https://doi.org/10.1007/s11947-012-0797-6

Fabregat, G., Casanovas, J., Redondo, E., Armelin, E., & Alemán, C. (2014). A rational design for the selective detection of dopamine using conducting polymers. *Phys. Chem. Chem. Phys.*, *16*(17), 7850–7861. https://doi.org/10.1039/C4CP00234B

Fang, J., Fan, H., Ma, Y., Wang, Z., & Chang, Q. (2015). Surface defects control for ZnO nanorods synthesized by quenching and their anti-recombination in photocatalysis. *Applied Surface Science*, *332*, 47–54. https://doi.org/10.1016/j.apsusc.2015.01.139

Farooq, M. H., Aslam, I., Anam, H. S., Tanveer, M., Ali, Z., Ghani, U., & Boddula, R. (2019). Improved photocatalytic performance of reduced zinc oxide (ZnO) novel morphology of astray like microstructure under solar light irradiation. *Materials Science for Energy Technologies*, *2*(2), 181–186. https://doi.org/10.1016/j.mset.2019.01.005

Fatehah, M. O., Aziz, H. A., & Stoll, S. (2014). Stability of ZnO Nanoparticles in Solution. Influence of pH, Dissolution, Aggregation and Disaggregation Effects. *Journal of Colloid Science and Biotechnology*, *3*(1), 75–84. https://doi.org/10.1166/jcsb.2014.1072

Feng, X., & Lou, X. (2015). The effect of surfactants-bound magnetite (Fe_3O_4) on the photocatalytic properties of the heterogeneous magnetic zinc oxides nanoparticles. *Separation and Purification Technology*, *147*, 266–275. https://doi.org/10.1016/j.seppur.2015.04.036

Fernández, L., Gamallo, M., González-Gómez, M. A., Vázquez-Vázquez, C., Rivas, J., Pintado, M., & Moreira, M. T. (2019). Insight into antibiotics removal: Exploring the photocatalytic performance of a Fe_3O_4/ZnO nanocomposite in a novel magnetic sequential batch reactor. *Journal of Environmental Management*, *237*(December 2018), 595–608. https://doi.org/10.1016/j.jenvman.2019.02.089

Franco, Sacco, De Marco, & Vaiano. (2019). Zinc Oxide Nanoparticles Obtained by Supercritical Antisolvent Precipitation for the Photocatalytic Degradation of Crystal Violet Dye. *Catalysts*, *9*(4), 346. https://doi.org/10.3390/catal9040346

Ganguly, A., Anjaneyulu, O., Ojha, K., & Ganguli, A. K. (2015). Oxide-based nanostructures for photocatalytic and electrocatalytic applications. *CrystEngComm*, *17*(47), 8978–9001. https://doi.org/10.1039/C5CE01343G

Gao, Y., Yan, M., & Korshin, G. V. (2015). Effects of Ionic Strength on the Chromophores of Dissolved Organic Matter. *Environmental Science & Technology*, *49*(10), 5905–5912. https://doi.org/10.1021/acs.est.5b00601

Gebreyohannes, G., Moges, F., Sahile, S., & Raja, N. (2013). Isolation and characterization of potential antibiotic producing actinomycetes from water and sediments of Lake Tana, Ethiopia. *Asian Pacific Journal of Tropical Biomedicine*, *3*(6), 426–435. https://doi.org/10.1016/S2221-1691(13)60092-1

Ghafari, E., Feng, Y., Liu, Y., Ferguson, I., & Lu, N. (2017). Investigating process-structure relations of ZnO nanofiber via electrospinning method. *Composites Part B: Engineering*, *116*(December), 40–45. https://doi.org/10.1016/j.compositesb.2017.02.026

Ghanbari, K., & Bonyadi, S. (2018). An electrochemical sensor based on reduced graphene oxide decorated with polypyrrole nanofibers and zinc oxide–copper oxide p–n junction heterostructures for the simultaneous voltammetric determination of ascorbic acid, dopamine, paracetamol, and tryptoph. *New Journal of Chemistry*, *42*(11), 8512–8523. https://doi.org/10.1039/C8NJ00857D

Ghosh, S. S., Choubey, C., & Sil, A. (2019). Photocatalytic response of Fe, Co, Ni doped ZnO based diluted magnetic semiconductors for spintronics applications. *Superlattices and Microstructures*, *125*(July 2018), 271–280. https://doi.org/10.1016/j.spmi.2018.10.028

Goldstein, J. I., Newbury, D. E., Michael, J. R., Ritchie, N. W. M., Scott, J. H. J., Joy, D. C., Goldstein, J. I., Newbury, D. E., Michael, J. R., Ritchie, N. W. M., Scott, J. H. J., & Joy, D. C. (2018). SEM Image Interpretation. In *Scanning Electron Microscopy and X-Ray Microanalysis* (pp. 111–121). Springer New York. https://doi.org/10.1007/978-1-4939-6676-9_7

Gómez-Pastora, J., Dominguez, S., Bringas, E., Rivero, M. J., Ortiz, I., & Dionysiou, D. D. (2017). Review and perspectives on the use of magnetic nanophotocatalysts (MNPCs) in water treatment. *Chemical Engineering Journal*, *310*, 407–427. https://doi.org/10.1016/j.cej.2016.04.140

Gopinathan, E., Viruthagiri, G., Shanmugam, N., & Sathiya priya, S. (2015). Optical, surface analysis and antibacterial activity of ZnO–CuO doped cerium oxide nanoparticles. *Optik*, *126*(24), 5830–5835. https://doi.org/10.1016/j.ijleo.2015.09.014

Gordon, T., Perlstein, B., Houbara, O., Felner, I., Banin, E., & Margel, S. (2011). Synthesis and characterization of zinc/iron oxide composite nanoparticles and their antibacterial properties. *Colloids and Surfaces A: Physicochemical and Engineering Aspects*, *374*(1–3), 1–8. https://doi.org/10.1016/j.colsurfa.2010.10.015

Goyal, P., Chakraborty, S., & Misra, S. K. (2018). Multifunctional Fe_3O_4-ZnO nanocomposites for environmental remediation applications. *Environmental Nanotechnology, Monitoring & Management*, *10*(November 2017), 28–35. https://doi.org/10.1016/j.enmm.2018.03.003

Grilli, M. L. (2020). Metal Oxides. *Metals*, *10*(6), 820. https://doi.org/10.3390/met10060820

Guaratini, C. C. I., & Zanoni, M. V. B. (2000). Corantes têxteis. *Química Nova*, *23*(1), 71–78. https://doi.org/10.1590/S0100-40422000000100013

Guo, H.-L., Zhu, Q., Wu, X.-L., Jiang, Y.-F., Xie, X., & Xu, A.-W. (2015). Oxygen deficient ZnO 1−x nanosheets with high visible light photocatalytic activity. *Nanoscale*, *7*(16), 7216–7223. https://doi.org/10.1039/C5NR00271K

Gupta, S., Sindhu, S., Varman, K. A., Ramamurthy, P. C., & Madras, G. (2012). Hybrid nanocomposite films of polyvinyl alcohol and ZnO as interactive gas barrier layers for electronics device passivation. *RSC Advances*, *2*(30), 11536. https://doi.org/10.1039/c2ra21714g

Gutha, Y., Pathak, J. L., Zhang, W., Zhang, Y., & Jiao, X. (2017). Antibacterial and wound healing properties of chitosan/poly(vinyl alcohol)/zinc oxide beads (CS/PVA/ZnO). *International Journal of Biological Macromolecules*, *103*, 234–241. https://doi.org/10.1016/j.ijbiomac.2017.05.020

Habibi-Yangjeh, A., & Shekofteh-Gohari, M. (2017). Novel magnetic Fe_3O_4/ZnO/$NiWO_4$ nanocomposites: Enhanced visible-light photocatalytic performance through p-n heterojunctions. *Separation and Purification Technology*, *184*, 334–346. https://doi.org/10.1016/j.seppur.2017.05.007

Hameed, B., Din, A., & Ahmad, A. (2007). Adsorption of methylene blue onto bamboo-based activated carbon: Kinetics and equilibrium studies. *Journal of Hazardous Materials*, *141*(3), 819–825. https://doi.org/10.1016/j.jhazmat.2006.07.049

Hamrouni, A., Moussa, N., Di Paola, A., Parrino, F., Houas, A., & Palmisano, L. (2014). Characterization and photoactivity of coupled ZnO–$ZnWO_4$ catalysts prepared by a sol–gel method. *Applied Catalysis B: Environmental*, *154–155*, 379–385. https://doi.org/10.1016/j.apcatb.2014.02.042

Hamrouni, A., Moussa, N., Parrino, F., Di Paola, A., Houas, A., & Palmisano, L. (2014). Sol–gel synthesis and photocatalytic activity of ZnO–SnO_2 nanocomposites. *Journal of Molecular Catalysis A: Chemical*, *390*, 133–141. https://doi.org/10.1016/j.molcata.2014.03.018

Han, D. (2020). Sol-gel autocombustion synthesis of zinc oxide foam decorated with holes and its use as acetic acid gas sensor at sub-ppm level. *Ceramics International*, *46*(3), 3304–3310. https://doi.org/10.1016/j.ceramint.2019.10.036

Han, G., Liu, Y., Yang, W., Geng, S., Cui, W., & Yu, Y. (2019). Fabrication, characterization, and magnetic properties of exchange-coupled porous $BaFe_8Al_4O_{19}/Co_{0.6}Zn_{0.4}Fe_2O_4$ nanocomposite magnets. *Nanoscale*, *11*(22), 10629–10635. https://doi.org/10.1039/C9NR01544B

Han, H., Sial, Q. A., Kalanur, S. S., & Seo, H. (2020). Binder assisted self-assembly of graphene oxide/Mn_2O_3 nanocomposite electrode on Ni foam for efficient supercapacitor application. *Ceramics International*, *46*(10), 15631–15637. https://doi.org/10.1016/j.ceramint.2020.03.111

Han, J., Li, Y., Wang, Y., Li, R., Zhang, H., Yan, Y., Ye, K., Cheng, K., Cao, D., & Wang, G. (2017). Economical, facile synthesis of network-like carbon nanosheets and their use as an enhanced electrode material for sensitive detection of ascorbic acid. *RSC Advances*, *7*(51), 32020–32026. https://doi.org/10.1039/C6RA28805G

Haque, M. M., Muneer, M., & Bahnemann, D. W. (2006). Semiconductor-mediated photocatalyzed degradation of a herbicide derivative, chlorotoluron, in aqueous suspensions. *Environmental Science and Technology*, *40*(15), 4765–4770. https://doi.org/10.1021/es060051h

Haseena, S., Shanavas, S., Duraimurugan, J., Ahamad, T., Alshehri, S. M., Acevedo, R., & Jayamani, N. (2020). Study on photocatalytic and antibacterial properties of phase pure Fe_2O_3 nanostructures synthesized using Caralluma Fimbriata and Achyranthes Aspera leaves. *Optik*, *203*(October 2019), 164047. https://doi.org/10.1016/j.ijleo.2019.164047

Hashim, F. S., Alkaim, A. F., Mahdi, S. M., & Omran Alkhayatt, A. H. (2019). Photocatalytic degradation of GRL dye from aqueous solutions in the presence of ZnO/Fe_2O_3 nanocomposites. *Composites Communications*, *16*(July), 111–116. https://doi.org/10.1016/j.coco.2019.09.008

Hassan Basri, H., Talib, R. A., Sukor, R., Othman, S. H., & Ariffin, H. (2020). Effect of Synthesis Temperature on the Size of ZnO Nanoparticles Derived from Pineapple Peel Extract and Antibacterial Activity of ZnO–Starch Nanocomposite Films. *Nanomaterials*, *10*(6), 1061. https://doi.org/10.3390/nano10061061

Hazarika, K. K., Goswami, C., Saikia, H., Borah, B. J., & Bharali, P. (2018). Cubic Mn_2O_3 nanoparticles on carbon as bifunctional electrocatalyst for oxygen reduction and oxygen evolution reactions. *Molecular Catalysis*, *451*(December), 153–160. https://doi.org/10.1016/j.mcat.2017.12.012

He, L., Tong, Z., Wang, Z., Chen, M., Huang, N., & Zhang, W. (2018). Effects of calcination temperature and heating rate on the photocatalytic properties of ZnO prepared by pyrolysis. *Journal of Colloid and Interface Science*, *509*, 448–456.

https://doi.org/10.1016/j.jcis.2017.09.021

Herrmann, J.-M. (2010). Fundamentals and misconceptions in photocatalysis. *Journal of Photochemistry and Photobiology A: Chemistry*, *216*(2–3), 85–93. https://doi.org/10.1016/j.jphotochem.2010.05.015

Herrmann, J. (1999). Heterogeneous photocatalysis: fundamentals and applications to the removal of various types of aqueous pollutants. *Catalysis Today*, *53*(1), 115–129. https://doi.org/10.1016/S0920-5861(99)00107-8

Hoffmann, M. R., Martin, S. T., Choi, W., & Bahnemann, D. W. (1995). Environmental Applications of Semiconductor Photocatalysis. *Chemical Reviews*, *95*(1), 69–96. https://doi.org/10.1021/cr00033a004

Hofmann, U., Kottenhahn, H., & Morcos, S. (1966). Adsorption of Methylene Blue on Clays. *Angewandte Chemie International Edition in English*, *5*(2), 247–248. https://doi.org/10.1002/anie.196602473

Hong, R. Y., Li, J. H., Chen, L. L., Liu, D. Q., Li, H. Z., Zheng, Y., & Ding, J. (2009). Synthesis, surface modification and photocatalytic property of ZnO nanoparticles. *Powder Technology*, *189*(3), 426–432. https://doi.org/10.1016/j.powtec.2008.07.004

Hood, M. I., & Skaar, E. P. (2012). Nutritional immunity: transition metals at the pathogen–host interface. *Nature Reviews Microbiology*, *10*(8), 525–537. https://doi.org/10.1038/nrmicro2836

Hoseinpour, V., & Ghaemi, N. (2018). Novel ZnO–MnO_2–Cu_2O triple nanocomposite: Facial synthesis, characterization, antibacterial activity and visible light photocatalytic performance for dyes degradation-A comparative study. *Materials Research Express*, *5*(8), 085012. https://doi.org/10.1088/2053-1591/aad2c6

Houas, A. (2001). Photocatalytic degradation pathway of methylene blue in water. *Applied Catalysis B: Environmental*, *31*(2), 145–157. https://doi.org/10.1016/S0926-3373(00)00276-9

Hu, C., Lu, L., Zhu, Y., Li, R., & Xing, Y. (2018). Morphological controlled preparation and photocatalytic activity of zinc oxide. *Materials Chemistry and Physics*, *217*(January), 182–191. https://doi.org/10.1016/j.matchemphys.2018.06.068

Hu, W., & Yang, J. (2017). Two-dimensional van der Waals heterojunctions for functional materials and devices. *Journal of Materials Chemistry C*, *5*(47), 12289–12297. https://doi.org/10.1039/c7tc04697a

Hu, X., Wang, J., Liu, Y., Li, X., Zeng, G., Bao, Z., Zeng, X., Chen, A., & Long, F. (2011). Adsorption of chromium (VI) by ethylenediamine-modified cross-linked magnetic chitosan resin: Isotherms, kinetics and thermodynamics. *Journal of Hazardous Materials*, *185*(1), 306–314. https://doi.org/10.1016/j.jhazmat.2010.09.034

Hu, Y., Qian, H., Liu, Y., Du, G., Zhang, F., Wang, L., & Hu, X. (2011). A microwave-assisted rapid route to synthesize ZnO/ZnS core–shell nanostructures via controllable surface sulfidation of ZnO nanorods. *CrystEngComm*, *13*(10), 3438. https://doi.org/10.1039/c1ce05111c

Huang, C.-Y., Hu, K.-H., & Wei, Z.-H. (2016). Comparison of cell behavior on pva/pva-gelatin electrospun nanofibers with random and aligned configuration. *Scientific Reports*, *6*(1), 37960. https://doi.org/10.1038/srep37960

Huang, J., Dai, Y., Gu, C., Sun, Y., & Liu, J. (2013). Preparation of porous flower-like CuO/ZnO nanostructures and analysis of their gas-sensing property. *Journal of Alloys and Compounds*, *575*, 115–122. https://doi.org/10.1016/j.jallcom.2013.04.094

Ibupoto, Z. H., Shah, S. M. U. A., Khun, K., & Willander, M. (2012). Electrochemical L-lactic acid sensor based on immobilized ZnO nanorods with lactate oxidase. *Sensors*, *12*(3), 2456–2466. https://doi.org/10.3390/s120302456

Irie, H., Miura, S., Kamiya, K., & Hashimoto, K. (2008). Efficient visible light-sensitive photocatalysts: Grafting Cu(II) ions onto TiO_2 and WO_3 photocatalysts. *Chemical Physics Letters*, *457*(1–3), 202–205. https://doi.org/10.1016/j.cplett.2008.04.006

Jagadeeshan, S., & Parsanathan, R. (2019). *Nano-metal Oxides for Antibacterial Activity* (pp. 59–90). https://doi.org/10.1007/978-3-030-04477-0_3

Jalal, R., Goharshadi, E. K., Abareshi, M., Moosavi, M., Yousefi, A., & Nancarrow, P. (2010). ZnO nanofluids: Green synthesis, characterization, and antibacterial activity. *Materials Chemistry and Physics*, *121*(1–2), 198–201. https://doi.org/10.1016/j.matchemphys.2010.01.020

Janotti, A., & Van de Walle, C. G. (2009). Fundamentals of zinc oxide as a semiconductor. *Reports on Progress in Physics*, *72*(12), 126501. https://doi.org/10.1088/0034-4885/72/12/126501

Jaramillo-Páez, C., Sánchez-Cid, P., Navío, J. A., & Hidalgo, M. C. (2018). A comparative assessment of the UV-photocatalytic activities of ZnO synthesized by different routes. *Journal of Environmental Chemical Engineering*, *6*(6), 7161–7171. https://doi.org/10.1016/j.jece.2018.11.004

Jassby, D., Farner Budarz, J., & Wiesner, M. (2012). Impact of Aggregate Size and Structure on the Photocatalytic Properties of TiO_2 and ZnO Nanoparticles. *Environmental Science & Technology*, *46*(13), 6934–6941. https://doi.org/10.1021/es202009h

Jiamprasertboon, A., Kafizas, A., Sachs, M., Ling, M., Alotaibi, A. M., Lu, Y., Siritanon, T., Parkin, I. P., & Carmalt, C. J. (2019). Heterojunction α-Fe_2O_3/ZnO Films with Enhanced Photocatalytic Properties Grown by Aerosol-Assisted Chemical Vapour Deposition. *Chemistry–A European Journal*, chem.201902175. https://doi.org/10.1002/chem.201902175

Jiang, J., & Du, X. (2014). Sensitive electrochemical sensors for simultaneous determination of ascorbic acid, dopamine, and uric acid based on Au@Pd-reduced graphene oxide nanocomposites. *Nanoscale*, *6*(19), 11303–11309. https://doi.org/10.1039/C4NR01774A

Jin, S.-E., Jin, J. E., Hwang, W., & Hong, S. W. (2019). Photocatalytic antibacterial application of zinc oxide nanoparticles and self-assembled networks under dual UV irradiation for enhanced disinfection. *International Journal of Nanomedicine*, *Volume 14*, 1737–1751. https://doi.org/10.2147/IJN.S192277

Jin, X., Xu, H., Qiu, S., Jia, M., Wang, F., Zhang, A., & Jiang, X. (2017). Direct photolysis of oxytetracycline: Influence of initial concentration, pH and temperature. *Journal of Photochemistry and Photobiology A: Chemistry*, *332*, 224–231. https://doi.org/10.1016/j.jphotochem.2016.08.032

Joe, A., Park, S., Shim, K., Kim, D., Jhee, K., Lee, H., Heo, C., Kim, H., & Jang, E. (2017). Antibacterial mechanism of ZnO nanoparticles under dark conditions. *Journal of Industrial and Engineering Chemistry*, *45*, 430–439.

https://doi.org/10.1016/j.jiec.2016.10.013

Jones, N., Ray, B., Ranjit, K. T., & Manna, A. C. (2008). Antibacterial activity of ZnO nanoparticle suspensions on a broad spectrum of microorganisms. *FEMS Microbiology Letters*, *279*(1), 71–76. https://doi.org/10.1111/j.1574-6968.2007.01012.x

Kannan, S. K., & Sundrarajan, M. (2014). A Green Approach for the Synthesis of a Cerium Oxide Nanoparticle: Characterization and Antibacterial Activity. *International Journal of Nanoscience*, *13*(03), 1450018. https://doi.org/10.1142/S0219581X14500185

Karami, H., Aminifar, A., Tavallali, H., & Namdar, Z.-A. (2010). PVA-Based Sol–Gel Synthesis and Characterization of CdO–ZnO Nanocomposite. *Journal of Cluster Science*, *21*(1), 1–9. https://doi.org/10.1007/s10876-009-0277-y

Karunakaran, C., & Vinayagamoorthy, P. (2017). Superparamagnetic core/shell Fe2O3/ZnO nanosheets as photocatalyst cum bactericide. *Catalysis Today*, *284*, 114–120. https://doi.org/10.1016/j.cattod.2016.11.022

Karunakaran, C., Vinayagamoorthy, P., & Jayabharathi, J. (2014). Nonquenching of Charge Carriers by Fe_3O_4 Core in Fe_3O_4/ZnO Nanosheet Photocatalyst. *Langmuir*, *30*(49), 15031–15039. https://doi.org/10.1021/la5039409

Kasap, S., Kaya, I. I., Repp, S., & Erdem, E. (2019). Superbat: battery-like supercapacitor utilized by graphene foam and zinc oxide (ZnO) electrodes induced by structural defects. *Nanoscale Advances*, *1*(7), 2586–2597. https://doi.org/10.1039/C9NA00199A

Kasemets, K., Ivask, A., Dubourguier, H.-C., & Kahru, A. (2009). Toxicity of nanoparticles of ZnO, CuO and TiO2 to yeast Saccharomyces cerevisiae. *Toxicology in Vitro*, *23*(6), 1116–1122. https://doi.org/10.1016/j.tiv.2009.05.015

Kaur, A., Anderson, W. A., Tanvir, S., & Kansal, S. K. (2019). Solar light active silver/iron oxide/zinc oxide heterostructure for photodegradation of ciprofloxacin, transformation products and antibacterial activity. *Journal of Colloid and Interface Science*, *557*, 236–253. https://doi.org/10.1016/j.jcis.2019.09.017

Kaviya, S., Kabila, S., & Jayasree, K. V. (2017). Hexagonal bottom-neck ZnO nano pencils: A study of structural, optical and antibacterial activity. *Materials Letters*, *204*, 57–60. https://doi.org/10.1016/j.matlet.2017.06.018

Kaviyarasu, K., Maria Magdalane, C., Kanimozhi, K., Kennedy, J., Siddhardha, B., Subba Reddy, E., Rotte, N. K., Sharma, C. S., Thema, F. T., Letsholathebe, D., Mola, G. T., & Maaza, M. (2017). Elucidation of photocatalysis, photoluminescence and antibacterial studies of ZnO thin films by spin coating method. *Journal of Photochemistry and Photobiology B: Biology*, *173*(June), 466–475. https://doi.org/10.1016/j.jphotobiol.2017.06.026

Ketteler, G., Weiss, W., Ranke, W., & Schlögl, R. (2001). Bulk and surface phases of iron oxides in an oxygen and water atmosphere at low pressure. *Physical Chemistry Chemical Physics*, *3*(6), 1114–1122. https://doi.org/10.1039/b009288f

Khalafi, T., Buazar, F., & Ghanemi, K. (2019). Phycosynthesis and Enhanced Photocatalytic Activity of Zinc Oxide Nanoparticles Toward Organosulfur Pollutants. *Scientific Reports*, *9*(1), 6866. https://doi.org/10.1038/s41598-019-43368-3

Khan, M. A. M., Kumar, S., Alhazaa, A. N., & Al-Gawati, M. A. (2018). Modifications in structural, morphological, optical and photocatalytic properties of ZnO:Mn nanoparticles by sol-gel protocol. *Materials Science in Semiconductor Processing*, *87*(July), 134–141. https://doi.org/10.1016/j.mssp.2018.07.016

Khan, M. M., Harunsani, M. H., Tan, A. L., Hojamberdiev, M., Azamay, S., & Ahmad, N. (2020). Antibacterial activities of zinc oxide and Mn-doped zinc oxide synthesized using Melastoma malabathricum (L.) leaf extract. *Bioprocess and Biosystems Engineering*, *43*(8), 1499–1508. https://doi.org/10.1007/s00449-020-02343-3

Khan, S. A., Khan, S. B., & Asiri, A. M. (2015). Core–shell cobalt oxide mesoporous silica based efficient electro-catalyst for oxygen evolution. *New Journal of Chemistry*, *39*(7), 5561–5569. https://doi.org/10.1039/C5NJ00521C

Khan, S. B., Ahmed, M. S., & Asiri, A. M. (2016). Amperometric sensor for ascorbic acid using a gold electrode modified with $ZnO@SiO_2$ nanospheres. *New Journal of Chemistry*, *40*(10), 8438–8443. https://doi.org/10.1039/C6NJ00115G

Khurram, R., Wang, Z., & Ehsan, M. F. (2021). α-Fe_2O_3-based nanocomposites: synthesis, characterization, and photocatalytic response towards wastewater treatment. *Environmental Science and Pollution Research*, *28*(14), 17697–17711. https://doi.org/10.1007/s11356-020-11778-w

Klaewkla, R., Arend, M., & F., W. (2011). A Review of Mass Transfer Controlling the Reaction Rate in Heterogeneous Catalytic Systems. In *Mass Transfer - Advanced Aspects* (Issue April). InTech. https://doi.org/10.5772/22962

Kolm, S.-C. (2009). General properties of processes. In *Reciprocity* (pp. 290–297). Cambridge University Press. https://doi.org/10.1017/CBO9780511492334.023

Köse, H., Karaal, Ş., Aydın, A. O., & Akbulut, H. (2015). A facile synthesis of zinc oxide/multiwalled carbon nanotube nanocomposite lithium ion battery anodes by sol–gel method. *Journal of Power Sources*, *295*, 235–245. https://doi.org/10.1016/j.jpowsour.2015.06.135

Kumar Jangir, L., Kumari, Y., Kumar, A., Kumar, M., & Awasthi, K. (2017). Investigation of luminescence and structural properties of ZnO nanoparticles, synthesized with different precursors. *Materials Chemistry Frontiers*, *1*(7), 1413–1421. https://doi.org/10.1039/C7QM00058H

Kumar, M. R. A., Abebe, B., Nagaswarupa, H. P., Murthy, H. C. A., Ravikumar, C. R., & Sabir, F. K. (2020). Enhanced photocatalytic and electrochemical performance of TiO2-Fe2O3 nanocomposite: Its applications in dye decolorization and as supercapacitors. *Scientific Reports*, *10*(1), 1249. https://doi.org/10.1038/s41598-020-58110-7

Kumar, P., Kim, K.-H., Kwon, E. E., & Szulejko, J. E. (2016). Metal–organic frameworks for the control and management of air quality: advances and future direction. *Journal of Materials Chemistry A*, *4*(2), 345–361. https://doi.org/10.1039/C5TA07068F

Kumar, S. G., & Rao, K. S. R. K. (2017). Comparison of modification strategies towards enhanced charge carrier separation and photocatalytic degradation activity of metal oxide semiconductors (TiO_2, WO_3 and ZnO). *Applied Surface Science*, *391*, 124–148. https://doi.org/10.1016/j.apsusc.2016.07.081

Kumar, S., Krishnakumar, B., Sobral, A. J. F. N., & Koh, J. (2019). Bio-based (chitosan/PVA/ZnO) nanocomposites fi lm : Thermally stable and photoluminescence material for removal of organic dye. *Carbohydrate Polymers*, *205*(October 2018),

559–564. https://doi.org/10.1016/j.carbpol.2018.10.108

Lachheb, H., Ajala, F., Hamrouni, A., Houas, A., Parrino, F., & Palmisano, L. (2017). Electron transfer in ZnO–Fe_2O_3 aqueous slurry systems and its effects on visible light photocatalytic activity. *Catalysis Science & Technology*, *7*(18), 4041–4047. https://doi.org/10.1039/C7CY01085K

Lan Huong, P. T., Tu, N., Lan, H., Thang, L. H., Van Quy, N., Tuan, P. A., Dinh, N. X., Phan, V. N., & Le, A.-T. (2018). Functional manganese ferrite/graphene oxide nanocomposites: effects of graphene oxide on the adsorption mechanisms of organic MB dye and inorganic As(VI) ions from aqueous solution. *RSC Advances*, *8*(22), 12376–12389. https://doi.org/10.1039/C8RA00270C

Lan, L., Gnappi, G., & Montenero, A. (1993). Infrared study of EPOXS-TEOS-TPOT gels. *Journal of Materials Science*, *28*(8), 2119–2123. https://doi.org/10.1007/BF00367571

Larina, O. V., Kyriienko, P. I., Balakin, D. Y., Vorokhta, M., Khalakhan, I., Nychiporuk, Y. M., Matolín, V., Soloviev, S. O., & Orlyk, S. M. (2019). Effect of ZnO on acid–base properties and catalytic performances of ZnO/ZrO_2–SiO_2 catalysts in 1,3-butadiene production from ethanol–water mixture. *Catalysis Science & Technology*, *9*(15), 3964–3978. https://doi.org/10.1039/C9CY00991D

Laurenti, M., & Cauda, V. (2018). Porous Zinc Oxide Thin Films: Synthesis Approaches and Applications. *Coatings*, *8*(2), 67. https://doi.org/10.3390/coatings8020067

Lawrence, M. C., Pilling, P. A., Epa, V. C., Berry, A. M., Ogunniyi, A. D., & Paton, J. C. (1998). The crystal structure of pneumococcal surface antigen PsaA reveals a metal-binding site and a novel structure for a putative ABC-type binding protein. *Structure*, *6*(12), 1553–1561. https://doi.org/10.1016/S0969-2126(98)00153-1

Lee, S., & Xu, H. (2016). Size-Dependent Phase Map and Phase Transformation Kinetics for Nanometric Iron(III) Oxides ($\gamma \rightarrow \varepsilon \rightarrow \alpha$ Pathway). *The Journal of Physical Chemistry C*, *120*(24), 13316–13322. https://doi.org/10.1021/acs.jpcc.6b05287

Lefatshe, K., Muiva, C. M., & Kebaabetswe, L. P. (2017). Extraction of nanocellulose and in-situ casting of ZnO/cellulose nanocomposite with enhanced photocatalytic and antibacterial activity. *Carbohydrate Polymers*, *164*, 301–308. https://doi.org/10.1016/j.carbpol.2017.02.020

Lei, C., Pi, M., Jiang, C., Cheng, B., & Yu, J. (2017). Synthesis of hierarchical porous zinc oxide (ZnO) microspheres with highly efficient adsorption of Congo red. *Journal of Colloid and Interface Science*, *490*, 242–251. https://doi.org/10.1016/j.jcis.2016.11.049

Lei, M., Zhou, X., Zou, Y., Ma, J., Alharthi, F. A., Alghamdi, A., Yang, X., & Deng, Y. (2020). A facile construction of heterostructured ZnO/Co_3O_4 mesoporous spheres and superior acetone sensing performance. *Chinese Chemical Letters*. https://doi.org/10.1016/j.cclet.2020.10.041

Lei, Y., Huo, J., & Liao, H. (2018). Fabrication and catalytic mechanism study of CeO_2-Fe_2O_3-ZnO mixed oxides on double surfaces of polyimide substrate using ion-exchange technique. *Materials Science in Semiconductor Processing*, *74*(August 2017), 154–164. https://doi.org/10.1016/j.mssp.2017.10.032

León-Silva, S., Fernández-Luqueño, F., & López-Valdez, F. (2016). Silver Nanoparticles (AgNP) in the Environment: a Review of Potential Risks on Human and Environmental Health. *Water, Air, & Soil Pollution*, *227*(9), 306.

https://doi.org/10.1007/s11270-016-3022-9

Li, J., Liu, Z., & Zhu, Z. (2015). Enhanced photocatalytic activity in $ZnFe_2O_4$–ZnO–Ag_3PO_4 hollow nanospheres through the cascadal electron transfer with magnetical separation. *Journal of Alloys and Compounds*, *636*, 229–233. https://doi.org/10.1016/j.jallcom.2015.02.176

Li, N., Tian, Y., Zhao, J., Zhang, J., Zhang, J., Zuo, W., & Ding, Y. (2017). Efficient removal of chromium from water by Mn_3O_4@ZnO/Mn_3O_4 composite under simulated sunlight irradiation: Synergy of photocatalytic reduction and adsorption. *Applied Catalysis B: Environmental*, *214*, 126–136. https://doi.org/10.1016/j.apcatb.2017.05.041

Li, N., Zhang, J. J., Tian, Y., Zhao, J., Zhang, J. J., & Zuo, W. (2017). Precisely controlled fabrication of magnetic 3D γ-Fe_2O_3@ZnO core-shell photocatalyst with enhanced activity: Ciprofloxacin degradation and mechanism insight. *Chemical Engineering Journal*, *308*(73), 377–385. https://doi.org/10.1016/j.cej.2016.09.093

Li, Xiaojuan, Jin, B., Huang, J., Zhang, Q., Peng, R., & Chu, S. (2018). Fe_2O_3/ZnO/$ZnFe_2O_4$ composites for the efficient photocatalytic degradation of organic dyes under visible light. *Solid State Sciences*, *80*, 6–14. https://doi.org/10.1016/j.solidstatesciences.2018.03.016

Li, Xin, Yu, J., & Jaroniec, M. (2016). Hierarchical photocatalysts. *Chemical Society Reviews*, *45*(9), 2603–2636. https://doi.org/10.1039/C5CS00838G

Li, Z., Mi, Y., Liu, X., Liu, S., Yang, S., & Wang, J. (2011). Flexible graphene/MnO_2 composite papers for supercapacitor electrodes. *Journal of Materials Chemistry*, *21*(38), 14706. https://doi.org/10.1039/c1jm11941a

Liao, W., Zheng, T., Wang, P., Tu, S., & Pan, W. (2010). Efficient microwave-assisted photocatalytic degradation of endocrine disruptor dimethyl phthalate over composite catalyst ZrO_x/ZnO. *Journal of Environmental Sciences*, *22*(11), 1800–1806. https://doi.org/10.1016/S1001-0742(09)60322-3

Lin, C.-I., & Wang, L.-H. (2008). Rate equations and isotherms for two adsorption models. *Journal of the Chinese Institute of Chemical Engineers*, *39*(6), 579–585. https://doi.org/10.1016/j.jcice.2008.04.003

Lin, Z., Liu, P., Yan, J., & Yang, G. (2015). Matching energy levels between TiO_2 and α-Fe_2O_3 in a core–shell nanoparticle for visible-light photocatalysis. *Journal of Materials Chemistry A*, *3*(28), 14853–14863. https://doi.org/10.1039/C5TA02958A

Liu, B., You, Y., Zhang, H., Wu, H., Jin, J., & Liu, H. (2016). Synthesis of ZnO nano-powders via a novel PVA-assisted freeze-drying process. *RSC Advances*, *6*(111), 110349–110355. https://doi.org/10.1039/C6RA24154A

Liu, D., Lv, Y., Zhang, M., Liu, Y., Zhu, Y., Zong, R., & Zhu, Y. (2014). Defect-related photoluminescence and photocatalytic properties of porous ZnO nanosheets. *Journal of Materials Chemistry A*, *2*(37), 15377. https://doi.org/10.1039/C4TA02678K

Liu, J., He, J., Wang, L., Li, R., Chen, P., Rao, X., Deng, L., Rong, L., & Lei, J. (2016). NiO-PTA supported on ZIF-8 as a highly effective catalyst for hydrocracking of Jatropha oil. *Scientific Reports*, *6*(1), 23667. https://doi.org/10.1038/srep23667

Liu, J., Xu, T., Sun, X., Bai, J., & Li, C. (2019). Preparation of stable composite porous nanofibers carried SnO_x-ZnO as a flexible supercapacitor material with excellent electrochemical and cycling performance. *Journal of Alloys and Compounds*, *807*,

151652. https://doi.org/10.1016/j.jallcom.2019.151652

Liu, K., Qin, Y., Muhammad, Y., Zhu, Y., Tang, R., Chen, N., Shi, H., Zhang, H., Tong, Z., & Yu, B. (2019). Effect of Fe_3O_4 content and microwave reaction time on the properties of Fe_3O_4/ZnO magnetic nanoparticles. *Journal of Alloys and Compounds*, *781*, 790–799. https://doi.org/10.1016/j.jallcom.2018.12.085

Liu, T., Li, Y., Du, Q., Sun, J., Jiao, Y., Yang, G., Wang, Z., Xia, Y., Zhang, W., Wang, K., Zhu, H., & Wu, D. (2012). Adsorption of methylene blue from aqueous solution by graphene. *Colloids and Surfaces B: Biointerfaces*, *90*(1), 197–203. https://doi.org/10.1016/j.colsurfb.2011.10.019

Liu, X., Ye, L., Liu, S., Li, Y., & Ji, X. (2016). Photocatalytic Reduction of CO_2 by ZnO Micro/nanomaterials with Different Morphologies and Ratios of {0001} Facets. *Scientific Reports*, *6*(1), 38474. https://doi.org/10.1038/srep38474

Liu, Yanjun, Sun, L., Wu, J., Fang, T., Cai, R., & Wei, A. (2015). Preparation and photocatalytic activity of ZnO/Fe_2O_3 nanotube composites. *Materials Science and Engineering: B*, *194*(12), 9–13. https://doi.org/10.1016/j.mseb.2014.12.021

Liu, Yu, Yu, L., Hu, Y., Guo, C., Zhang, F., & Wen (David) Lou, X. (2012). A magnetically separable photocatalyst based on nest-like γ-Fe_2O_3/ZnO double-shelled hollow structures with enhanced photocatalytic activity. *Nanoscale*, *4*(1), 183–187. https://doi.org/10.1039/C1NR11114K

Liu, Yuanying, Pang, H., Wei, C., Hao, M., Zheng, S., & Zheng, M. (2014). Mesoporous ZnO-NiO architectures for use in a high-performance nonenzymatic glucose sensor. *Microchimica Acta*, *181*(13–14), 1581–1589. https://doi.org/10.1007/s00604-014-1275-9

Loos, R., Hanke, G., & Eisenreich, S. J. (2003). Multi-component analysis of polar water pollutants using sequential solid-phase extraction followed by LC-ESI-MS. *Journal of Environmental Monitoring*, *5*(3), 384. https://doi.org/10.1039/b300440f

Lu, H., Wang, S., Zhao, L., Li, J., Dong, B., & Xu, Z. (2011). Hierarchical ZnO microarchitectures assembled by ultrathin nanosheets: hydrothermal synthesis and enhanced photocatalytic activity. *Journal of Materials Chemistry*, *21*(12), 4228. https://doi.org/10.1039/c0jm03390a

Lutukurthi, D. N. V. V. K., Dutta, S., & Behara, D. K. (2020). Effect of ignition temperature and fuel amount on photocatalytic activity of solution combustion synthesized ZnO. *Ceramics International*, *46*(14), 22419–22428. https://doi.org/10.1016/j.ceramint.2020.05.324

Macák, J. M., Tsuchiya, H., Ghicov, A., & Schmuki, P. (2005). Dye-sensitized anodic TiO2 nanotubes. *Electrochemistry Communications*, *7*(11), 1133–1137. https://doi.org/10.1016/j.elecom.2005.08.013

Machala, L., Tuček, J., & Zbořil, R. (2011). Polymorphous Transformations of Nanometric Iron(III) Oxide: A Review. *Chemistry of Materials*, *23*(14), 3255–3272. https://doi.org/10.1021/cm200397g

Madan, S., Shaw, R., Tiwari, S. S. K., & Tiwari, S. S. K. (2019). Adsorption dynamics of Congo red dye removal using ZnO functionalized high silica zeolitic particles. *Applied Surface Science*, *487*(April), 907–917. https://doi.org/10.1016/j.apsusc.2019.04.273

Madkour, M., Bumajdad, A., & Al-sagheer, F. (2019). To what extent do polymeric stabilizers affect nanoparticles characteristics? *Advances in Colloid and Interface Science*, *270*, 38–53. https://doi.org/10.1016/j.cis.2019.05.004

Mahamuni-Badiger, P. P., Patil, P. M., Patel, P. R., Dhanavade, M. J., Badiger, M. V., Marathe, Y. N., & Bohara, R. A. (2020). Electrospun poly(3-hydroxybutyrate- co-3-hydroxyvalerate)/polyethylene oxide (PEO) microfibers reinforced with ZnO nanocrystals for antibacterial and antibiofilm wound dressing applications. *New Journal of Chemistry*, *44*(23), 9754–9766. https://doi.org/10.1039/D0NJ01384F

Mahamuni, P. P., Patil, P. M., Dhanavade, M. J., Badiger, M. V., Shadija, P. G., Lokhande, A. C., & Bohara, R. A. (2019). Synthesis and characterization of zinc oxide nanoparticles by using polyol chemistry for their antimicrobial and antibiofilm activity. *Biochemistry and Biophysics Reports*, *17*(September 2018), 71–80. https://doi.org/10.1016/j.bbrep.2018.11.007

Mallakpour, S., Abdolmaleki, A., & Moosavi, S. E. (2015). Green Route for the Synthesis of Alanine-based Poly(amide-imide) Nanocomposites Reinforced with the Modified ZnO by Poly(vinyl alcohol) as a Biocompatible Coupling Agent. *Polymer-Plastics Technology and Engineering*, *54*(14), 1448–1456. https://doi.org/10.1080/03602559.2014.996907

Mallakpour, S., & Adnany Sadaty, M. (2016). Preparation and characterization of nanocomposites based on poly(vinyl alcohol) and vitamin B1-modified TiO_2 and evaluation of the optical, mechanical, and thermal properties. *Colloid and Polymer Science*, *294*(12), 2099–2107. https://doi.org/10.1007/s00396-016-3974-8

Mao, N. (2019). Investigating the Heteronjunction between ZnO/Fe_2O_3 and g-C_3N_4 for an Enhanced Photocatalytic H_2 production under visible-light irradiation. *Scientific Reports*, *9*(1), 12383. https://doi.org/10.1038/s41598-019-48730-z

Marschall, R. (2014). Semiconductor Composites : Strategies for Enhancing Charge Carrier Separation to Improve Photocatalytic Activity. *MaterialsViews*, 2421–2440. https://doi.org/10.1002/adfm.201303214

Maya-Treviño, M. L., Villanueva-Rodríguez, M., Guzmán-Mar, J. L., Hinojosa-Reyes, L., & Hernández-Ramírez, A. (2015). Comparison of the solar photocatalytic activity of $ZnO–Fe_2O_3$ and $ZnO–Fe^0$ on 2,4-D degradation in a CPC reactor. *Photochemical & Photobiological Sciences*, *14*(3), 543–549. https://doi.org/10.1039/C4PP00274A

Mayank, Kumar, Y., Periyasamy, L., & Viswanath, A. K. (2019). Fabrication and a detailed study of antibacterial properties of α-Fe_2O_3/NiO nanocomposites along with their structural, optical, thermal, magnetic and cytotoxic features. *Nanotechnology*, *30*(18), 185101. https://doi.org/10.1088/1361-6528/ab0124

Mazaheri, O., & Kalbasi, R. J. (2015). Preparation and characterization of Ni/mZSM-5 zeolite with a hierarchical pore structure by using KIT-6 as silica template: an efficient bi-functional catalyst for the reduction of nitro aromatic compounds. *RSC Advances*, *5*(43), 34398–34414. https://doi.org/10.1039/C5RA02349A

Miao, Y., Zhang, H., Yuan, S., Jiao, Z., & Zhu, X. (2016). Preparation of flower-like ZnO architectures assembled with nanosheets for enhanced photocatalytic activity. *Journal of Colloid and Interface Science*, *462*, 9–18. https://doi.org/10.1016/j.jcis.2015.09.064

Mills, A., & Le Hunte, S. (1997). An overview of semiconductor photocatalysis. *Journal of Photochemistry and Photobiology A: Chemistry*, *108*(1), 1–35. https://doi.org/10.1016/S1010-6030(97)00118-4

Mills, I., & Jones, R. N. (1990). Quantities, Units and Symbols in Physical Chemistry. *Vibrational Spectroscopy*, *1*(1), 105–106. https://doi.org/10.1016/0924-2031(90)80016-w

Miranda, A. C., Lepretti, M., Rizzo, L., Caputo, I., Vaiano, V., Sacco, O., Lopes, W. S., & Sannino, D. (2016). Surface water disinfection by chlorination and advanced oxidation processes: Inactivation of an antibiotic resistant E. coli strain and cytotoxicity evaluation. *Science of The Total Environment*, *554–555*, 1–6. https://doi.org/10.1016/j.scitotenv.2016.02.189

Mishra, M., & Chun, D.-M. (2015). α-Fe_2O_3 as a photocatalytic material: A review. *Applied Catalysis A: General*, *498*, 126–141. https://doi.org/10.1016/j.apcata.2015.03.023

Mittal, A., Mittal, J., Malviya, A., & Gupta, V. K. (2009). Adsorptive removal of hazardous anionic dye "Congo red" from wastewater using waste materials and recovery by desorption. *Journal of Colloid and Interface Science*, *340*(1), 16–26. https://doi.org/10.1016/j.jcis.2009.08.019

Modirshahla, N., Behnajady, M. A., & Ghanbary, F. (2007). Decolorization and mineralization of C.I. Acid Yellow 23 by Fenton and photo-Fenton processes. *Dyes and Pigments*, *73*(3), 305–310. https://doi.org/10.1016/j.dyepig.2006.01.002

Moeinian, M., & Akhbari, K. (2015). How the guest molecules in nanoporous Zn(II) metal-organic framework can prevent agglomeration of ZnO nanoparticles. *Journal of Solid State Chemistry*, *225*, 459–463. https://doi.org/10.1016/j.jssc.2015.02.017

Mohammadi, A., Daemi, H., & Barikani, M. (2014). Fast removal of malachite green dye using novel superparamagnetic sodium alginate-coated Fe_3O_4 nanoparticles. *International Journal of Biological Macromolecules*, *69*, 447–455. https://doi.org/10.1016/j.ijbiomac.2014.05.042

Mohammadi Arvanag, F., Bayrami, A., Habibi-Yangjeh, A., & Rahim Pouran, S. (2019). A comprehensive study on antidiabetic and antibacterial activities of ZnO nanoparticles biosynthesized using Silybum marianum L seed extract. *Materials Science and Engineering: C*, *97*(November 2018), 397–405. https://doi.org/10.1016/j.msec.2018.12.058

Moharreri, E., Hines, W. A., Biswas, S., Perry, D. M., He, J., Murray-Simmons, D., & Suib, S. L. (2018). Comprehensive Magnetic Study of Nanostructured Mesoporous Manganese Oxide Materials and Implications for Catalytic Behavior. *Chemistry of Materials*, *30*(3), 1164–1177. https://doi.org/10.1021/acs.chemmater.7b05280

Mohd Adnan, M. A., Julkapli, N. M., & Abd Hamid, S. B. (2016). Review on ZnO hybrid photocatalyst: impact on photocatalytic activities of water pollutant degradation. *Reviews in Inorganic Chemistry*, *36*(2), 77–104. https://doi.org/10.1515/revic-2015-0015

Moradi, S., Aberoomand-Azar, P., Raeis-Farshid, S., Abedini-Khorrami, S., & Givianrad, M. H. (2016). The effect of different molar ratios of ZnO on characterization and photocatalytic activity of TiO_2/ZnO nanocomposite. *Journal of Saudi Chemical Society*, *20*(4), 373–378. https://doi.org/10.1016/j.jscs.2012.08.002

Munawar, T., Yasmeen, S., Hasan, M., Mahmood, K., Hussain, A., Ali, A., Arshad, M. I., & Iqbal, F. (2020). Novel tri-phase heterostructured ZnO–Yb_2O_3–Pr_2O_3 nanocomposite; structural, optical, photocatalytic and antibacterial studies. *Ceramics International*, *46*(8), 11101–11114. https://doi.org/10.1016/j.ceramint.2020.01.130

Munawar, T., Yasmeen, S., Hussain, A., Akram, M., & Iqbal, F. (2020). Novel direct dual-Z-scheme ZnO-Er_2O_3-Yb_2O_3 heterostructured nanocomposite with superior photocatalytic and antibacterial activity. *Materials Letters*, *264*, 127357. https://doi.org/10.1016/j.matlet.2020.127357

Muñoz-Rojas, D., Oró-Solé, J., & Gómez-Romero, P. (2008). From Nanosnakes to Nanosheets: A Matrix-Mediated Shape Evolution. *The Journal of Physical Chemistry C*, *112*(51), 20312–20318. https://doi.org/10.1021/jp808187w

Murugan, N., Kumar, T. H. V., Devi, N. R., & Sundramoorthy, A. K. (2019). A flower-structured MoS_2-decorated f-MWCNTs/ZnO hybrid nanocomposite-modified sensor for the selective electrochemical detection of vitamin C. *New Journal of Chemistry*, *43*(38), 15105–15114. https://doi.org/10.1039/C9NJ02993A

Nadargi, D. Y., Tamboli, M. S., Patil, S. S., Dateer, R. B., Mulla, I. S., Choi, H., & Suryavanshi, S. S. (2020). Microwave-Epoxide-Assisted Hydrothermal Synthesis of the CuO/ZnO Heterojunction: a Highly Versatile Route to Develop H_2S Gas Sensors. *ACS Omega*, *5*(15), 8587–8595. https://doi.org/10.1021/acsomega.9b04475

Naderi, M. (2015). Surface Area. In *Progress in Filtration and Separation* (pp. 585–608). Elsevier. https://doi.org/10.1016/B978-0-12-384746-1.00014-8

Naeem, R., Ali Ehsan, M., Yahya, R., Sohail, M., Khaledi, H., & Mazhar, M. (2016). Fabrication of pristine Mn_2O_3 and Ag–Mn_2O_3 composite thin films by AACVD for photoelectrochemical water splitting. *Dalton Transactions*, *45*(38), 14928–14939. https://doi.org/10.1039/C6DT02656G

Naeem, R., Yahya, R., Pandikumar, A., Huang, N. M., Misran, M., Arifin, Z., & Mazhar, M. (2015). Photoelectrochemical properties of morphology controlled manganese, iron, nickel and copper oxides nanoball thin films deposited by electric field directed aerosol assisted chemical vapour deposition. *Materials Today Communications*, *4*, 141–148. https://doi.org/10.1016/j.mtcomm.2015.06.004

Nagvenkar, A. P., Deokar, A., Perelshtein, I., & Gedanken, A. (2016). A one-step sonochemical synthesis of stable ZnO–PVA nanocolloid as a potential biocidal agent. *Journal of Materials Chemistry B*, *4*(12), 2124–2132. https://doi.org/10.1039/C6TB00033A

Nagvenkar, A. P., Perelshtein, I., Piunno, Y., Mantecca, P., & Gedanken, A. (2019). Sonochemical One-Step Synthesis of Polymer-Capped Metal Oxide Nanocolloids: Antibacterial Activity and Cytotoxicity. *ACS Omega*, *4*(9), 13631–13639. https://doi.org/10.1021/acsomega.9b00181

Nair, S., Sasidharan, A., Divya Rani, V. V., Menon, D., Nair, S., Manzoor, K., & Raina, S. (2009). Role of size scale of ZnO nanoparticles and microparticles on toxicity toward bacteria and osteoblast cancer cells. *Journal of Materials Science: Materials in Medicine*, *20*(S1), 235–241. https://doi.org/10.1007/s10856-008-3548-5

Najafi, M., Di Giacomo, F., Zhang, D., Shanmugam, S., Senes, A., Verhees, W., Hadipour, A., Galagan, Y., Aernouts, T., Veenstra, S., & Andriessen, R. (2018). Highly Efficient and Stable Flexible Perovskite Solar Cells with Metal Oxides Nanoparticle Charge Extraction Layers. *Small*, *14*(12), 1702775. https://doi.org/10.1002/smll.201702775

Naskar, A., Lee, S., & Kim, K. (2020). Antibacterial potential of Ni-doped zinc oxide nanostructure: comparatively more effective against Gram-negative bacteria including multi-drug resistant strains. *RSC Advances*, *10*(3), 1232–1242. https://doi.org/10.1039/C9RA09512H

Nathan, T., Cloke, M., & Prabaharan, S. R. S. (2008). Electrode Properties of Mn_2O_3 Nanospheres Synthesized by Combined Sonochemical/Solvothermal Method for Use in Electrochemical Capaci. *Journal of Nanomaterials*, *2008*(1), 1–8. https://doi.org/10.1155/2008/948183

Nayak, A., Sahoo, J. K., Sahoo, S. K., & Sahu, D. (2020). Removal of congo red dye from aqueous solution using zinc oxide nanoparticles synthesised from Ocimum sanctum (Tulsi leaf): a green approach. *International Journal of Environmental Analytical Chemistry*, *00*(00), 1–22. https://doi.org/10.1080/03067319.2020.1842386

Naz, S., Islam, M., Tabassum, S., Fernandes, N. F., Carcache de Blanco, E. J., & Zia, M. (2019). Green synthesis of hematite (α-Fe_2O_3) nanoparticles using Rhus punjabensis extract and their biomedical prospect in pathogenic diseases and cancer. *Journal of Molecular Structure*, *1185*, 1–7. https://doi.org/10.1016/j.molstruc.2019.02.088

Nel, A. (2006). Toxic Potential of Materials at the Nanolevel. *Science*, *311*(5761), 622–627. https://doi.org/10.1126/science.1114397

Ng, C., Losso, J. N., Marshall, W. E., & Rao, R. M. (2002). Freundlich adsorption isotherms of agricultural by-product-based powdered activated carbons in a geosmin–water system. *Bioresource Technology*, *85*(2), 131–135. https://doi.org/10.1016/S0960-8524(02)00093-7

Nguyen, T. T., Nam, S.-N., Kim, J., & Oh, J. (2020). Photocatalytic degradation of dissolved organic matter under ZnO-catalyzed artificial sunlight irradiation system. *Scientific Reports*, *10*(1), 13090. https://doi.org/10.1038/s41598-020-69115-7

Nikazar, M., Alizadeh, M., Lalavi, R., & Rostami, M. (2014). The optimum conditions for synthesis of Fe_3O_4/ZnO core/shell magnetic nanoparticles for photodegradation of phenol. *Journal of Environmental Health Science and Engineering*, *12*(1), 21. https://doi.org/10.1186/2052-336X-12-21

Nsib, M. F., Naffati, N., Rayes, A., Moussa, N., & Houas, A. (2015). Effect of some operational parameters on the hydrogen generation efficiency of Ni-ZnO/PANI composite under visible-light irradiation. *Materials Research Bulletin*, *70*, 530–538. https://doi.org/10.1016/j.materresbull.2015.04.067

Ohtani, B. (2010). Photocatalysis A to Z—What we know and what we do not know in a scientific sense. *Journal of Photochemistry and Photobiology C: Photochemistry Reviews*, *11*(4), 157–178. https://doi.org/10.1016/j.jphotochemrev.2011.02.001

Ong, C. B., Ng, L. Y., & Mohammad, A. W. (2018). A review of ZnO nanoparticles as solar photocatalysts: Synthesis, mechanisms and applications. *Renewable and Sustainable Energy Reviews*, *81*(August 2017), 536–551. https://doi.org/10.1016/j.rser.2017.08.020

Owonubi, S. J., Ateba, C. N., & Revaprasadu, N. (2020). Co-assembled ZnO-Fe_2O_{3x}-CuO_x nano-oxide materials for antibacterial protection. *Phosphorus, Sulfur, and Silicon and the Related Elements*, *0*(0), 1–7. https://doi.org/10.1080/10426507.2020.1764955

Ozkan, E., Ozkan, F. T., Allan, E., & Parkin, I. P. (2015). The use of zinc oxide nanoparticles to enhance the antibacterial properties of light-activated polydimethylsiloxane containing crystal violet. *RSC Advances*, *5*(12), 8806–8813. https://doi.org/10.1039/c4ra13649g

Padalia, H., Baluja, S., & Chanda, S. (2017). Effect of pH on Size and Antibacterial Activity of Salvadora oleoides Leaf Extract-Mediated Synthesis of Zinc Oxide Nanoparticles. *BioNanoScience*, *7*(1), 40–49. https://doi.org/10.1007/s12668-016-

0387-6

Pallela, P. N. V. K., Ummey, S., Ruddaraju, L. K., Gadi, S., Cherukuri, C. S., Barla, S., & Pammi, S. V. N. (2019). Antibacterial efficacy of green synthesized α-Fe_2O_3 nanoparticles using Sida cordifolia plant extract. *Heliyon*, *5*(11), e02765. https://doi.org/10.1016/j.heliyon.2019.e02765

Panchal, P., Paul, D. R., Sharma, A., Hooda, D., Yadav, R., Meena, P., & Nehra, S. P. (2019). Phytoextract mediated ZnO/MgO nanocomposites for photocatalytic and antibacterial activities. *Journal of Photochemistry and Photobiology A: Chemistry*, *385*(August), 112049. https://doi.org/10.1016/j.jphotochem.2019.112049

Pang, S., He, Y., Zhong, R., Guo, Z., He, P., Zhou, C., Xue, B., Wen, X., & Li, H. (2019). Multifunctional ZnO/TiO_2 nanoarray composite coating with antibacterial activity, cytocompatibility and piezoelectricity. *Ceramics International*, *45*(10), 12663–12671. https://doi.org/10.1016/j.ceramint.2019.03.076

Parler, C. M., Ritter, J. A., & Amiridis, M. D. (2001). Infrared spectroscopic study of sol–gel derived mixed-metal oxides. *Journal of Non-Crystalline Solids*, *279*(2–3), 119–125. https://doi.org/10.1016/S0022-3093(00)00401-4

Patel, K., Raj, B. S., Chen, Y., & Lou, X. (2017). Novel folic acid conjugated Fe_3O_4-ZnO hybrid nanoparticles for targeted photodynamic therapy. *Colloids and Surfaces B: Biointerfaces*, *150*((Patel K.; Lou X., x.lou@curtin.edu.au) Department of Chemical Engineering, Curtin University, Bentley, Australia), 317–325. https://doi.org/10.1016/j.colsurfb.2016.10.045

Paul, D., Mangla, S., & Neogi, S. (2020). Antibacterial study of CuO-NiO-ZnO trimetallic oxide nanoparticle. *Materials Letters*, *271*, 127740. https://doi.org/10.1016/j.matlet.2020.127740

Pavithra, K. S., Yashoda, M. P., Prasannakumar, S., & Mutalik, S. (2020). Viscosity and thermal conductivity of ZnO–water-based nanofluids stabilized by grafted SMA-g-MPEG comb-shaped copolymer for heat transfer applications. *Iranian Polymer Journal*, *29*(2), 185–196. https://doi.org/10.1007/s13726-020-00784-x

Peik-See, T., Pandikumar, A., Nay-Ming, H., Hong-Ngee, L., & Sulaiman, Y. (2014). Simultaneous Electrochemical Detection of Dopamine and Ascorbic Acid Using an Iron Oxide/Reduced Graphene Oxide Modified Glassy Carbon Electrode. *Sensors*, *14*(8), 15227–15243. https://doi.org/10.3390/s140815227

Penn, R. L. (1998). Imperfect Oriented Attachment: Dislocation Generation in Defect-Free Nanocrystals. *Science*, *281*(5379), 969–971. https://doi.org/10.1126/science.281.5379.969

Phulé, P. P., Mihalcin, M. P., & Genc, S. (1999). The role of the dispersed-phase remnant magnetization on the redispersibility of magnetorheological fluids. *Journal of Materials Research*, *14*(7), 3037–3041. https://doi.org/10.1557/JMR.1999.0407

Pirhashemi, M., Habibi-Yangjeh, A., & Rahim Pouran, S. (2018). Review on the criteria anticipated for the fabrication of highly efficient ZnO-based visible-light-driven photocatalysts. *Journal of Industrial and Engineering Chemistry*, *62*, 1–25. https://doi.org/10.1016/j.jiec.2018.01.012

Prabakaran, E., & Pillay, K. (2019). Synthesis of N-doped ZnO nanoparticles with cabbage morphology as a catalyst for the efficient photocatalytic degradation of methylene blue under UV and visible light. *RSC Advances*, *9*(13), 7509–7535. https://doi.org/10.1039/C8RA09962F

Prasad, A. R., Basheer, S. M., Gupta, I. R., Elyas, K. K., & Joseph, A. (2020). Investigation on Bovine Serum Albumin (BSA) binding efficiency and antibacterial activity of ZnO nanoparticles. *Materials Chemistry and Physics*, *240*(September 2019), 122115. https://doi.org/10.1016/j.matchemphys.2019.122115

Precious Ayanwale, A., & Reyes-López, S. Y. (2019). ZrO_2–ZnO Nanoparticles as Antibacterial Agents. *ACS Omega*, *4*(21), 19216–19224. https://doi.org/10.1021/acsomega.9b02527

Premanathan, M., Karthikeyan, K., Jeyasubramanian, K., & Manivannan, G. (2011). Selective toxicity of ZnO nanoparticles toward Gram-positive bacteria and cancer cells by apoptosis through lipid peroxidation. *Nanomedicine: Nanotechnology, Biology and Medicine*, *7*(2), 184–192. https://doi.org/10.1016/j.nano.2010.10.001

Pype, M., Lawrence, M. G., Keller, J., & Gernjak, W. (2016). Reverse osmosis integrity monitoring in water reuse: The challenge to verify virus removal – A review. *Water Research*, *98*, 384–395. https://doi.org/10.1016/j.watres.2016.04.040

Qamar, M. T., Aslam, M., Ismail, I. M. I., Salah, N., & Hameed, A. (2016). The assessment of the photocatalytic activity of magnetically retrievable ZnO coated c-Fe_2O_3 in sunlight exposure. *Chemical Engineering Journal*, *283*, 656–667. https://doi.org/10.1016/j.cej.2015.08.002

Qamar, M. T., Aslam, M., Rehan, Z. A., Soomro, M. T., Basahi, J. M., Ismail, I. M. I., Almeelbi, T., & Hameed, A. (2017). The influence of p-type Mn_3O_4 nanostructures on the photocatalytic activity of ZnO for the removal of bromo and chlorophenol in natural sunlight exposure. *Applied Catalysis B: Environmental*, *201*, 105–118. https://doi.org/10.1016/j.apcatb.2016.08.004

Radhamani, A. V., Shareef, K. M., & Rao, M. S. R. (2016). ZnO@MnO_2 Core–Shell Nanofiber Cathodes for High Performance Asymmetric Supercapacitors. *ACS Applied Materials & Interfaces*, *8*(44), 30531–30542. https://doi.org/10.1021/acsami.6b08082

Raghunath, A., & Perumal, E. (2017). Metal oxide nanoparticles as antimicrobial agents: a promise for the future. *International Journal of Antimicrobial Agents*, *49*(2), 137–152. https://doi.org/10.1016/j.ijantimicag.2016.11.011

Raghupathi, K. R., Koodali, R. T., & Manna, A. C. (2011). Size-Dependent Bacterial Growth Inhibition and Mechanism of Antibacterial Activity of Zinc Oxide Nanoparticles. *Langmuir*, *27*(7), 4020–4028. https://doi.org/10.1021/la104825u

Rahman, Q. I., Ahmad, M., Misra, S. K., & Lohani, M. (2013). Effective photocatalytic degradation of rhodamine B dye by ZnO nanoparticles. *Materials Letters*, *91*, 170–174. https://doi.org/10.1016/j.matlet.2012.09.044

Rahmanian, R., Mozaffari, S. A., & Abedi, M. (2015). Disposable urea biosensor based on nanoporous ZnO film fabricated from omissible polymeric substrate. *Materials Science and Engineering: C*, *57*, 387–396. https://doi.org/10.1016/j.msec.2015.08.004

Rai, M., & Shegokar, R. (2017). Metal Nanoparticles in Pharma. In M. Rai, Ph.D & R. Shegokar, Ph.D (Eds.), *Metal Nanoparticles in Pharma*. Springer International Publishing. https://doi.org/10.1007/978-3-319-63790-7

Rajeshwar, K., Osugi, M. E., Chanmanee, W., Chenthamarakshan, C. R., Zanoni, M. V. B., Kajitvichyanukul, P., & Krishnan-Ayer, R. (2008). Heterogeneous photocatalytic treatment of organic dyes in air and aqueous media. *Journal of Photochemistry and*

Photobiology C: Photochemistry Reviews, *9*(4), 171–192. https://doi.org/10.1016/j.jphotochemrev.2008.09.001

Rajith Kumar, C. R., Betageri, V. S., Nagaraju, G., Pujar, G. H., H S, O., & M S, L. (2020). One-pot green synthesis of ZnO–CuO nanocomposite and their enhanced photocatalytic and antibacterial activity. *Advances in Natural Sciences: Nanoscience and Nanotechnology*, *11*(1), 015009. https://doi.org/10.1088/2043-6254/ab6c60

Ramos-Delgado, N. A., Gracia-Pinilla, M. Á., Mangalaraja, R. V., O'Shea, K., & Dionysiou, D. D. (2016). Industrial synthesis and characterization of nanophotocatalysts materials: titania. *Nanotechnology Reviews*, *5*(5). https://doi.org/10.1515/ntrev-2016-0007

Rashmi, B. N., Harlapur, S. F., Avinash, B., Ravikumar, C. R., Nagaswarupa, H. P., Anil Kumar, M. R., Gurushantha, K., & Santosh, M. S. (2020). Facile green synthesis of silver oxide nanoparticles and their electrochemical, photocatalytic and biological studies. *Inorganic Chemistry Communications*, *111*(August 2019), 107580. https://doi.org/10.1016/j.inoche.2019.107580

Ray, P. G., Biswas, S., Roy, T., Ghosh, S., Majumder, D., Basak, P., Roy, S., & Dhara, S. (2019). Sonication Assisted Hierarchical Decoration of Ag-NP on Zinc Oxide Nanoflower Impregnated Eggshell Membrane: Evaluation of Antibacterial Activity and in Vitro Cytocompatibility [Research-article]. *ACS Sustainable Chemistry & Engineering*, *7*(16), 13717–13733. https://doi.org/10.1021/acssuschemeng.9b01185

Ren, M., Frimmel, F. H., & Abbt-Braun, G. (2015). Multi-cycle photocatalytic degradation of bezafibrate by a cast polyvinyl alcohol/titanium dioxide (PVA/TiO_2) hybrid film. *Journal of Molecular Catalysis A: Chemical*, *400*(February), 42–48. https://doi.org/10.1016/j.molcata.2015.02.004

Rice, M. E. (2000). Ascorbate regulation and its neuroprotective role in the brain. *Trends in Neurosciences*, *23*(5), 209–216. https://doi.org/10.1016/S0166-2236(99)01543-X

Rizzo, L., Selcuk, H., Nikolaou, A. D., Meriç Pagano, S., & Belgiorno, V. (2014). A comparative evaluation of ozonation and heterogeneous photocatalytic oxidation processes for reuse of secondary treated urban wastewater. *Desalination and Water Treatment*, *52*(7–9), 1414–1421. https://doi.org/10.1080/19443994.2013.787953

Robati, D., Mirza, B., Ghazisaeidi, R., Rajabi, M., Moradi, O., Tyagi, I., Agarwal, S., & Gupta, V. K. (2016). Adsorption behavior of methylene blue dye on nanocomposite multi-walled carbon nanotube functionalized thiol (MWCNT-SH) as new adsorbent. *Journal of Molecular Liquids*, *216*, 830–835. https://doi.org/10.1016/j.molliq.2016.02.004

Rosa, A. L., Tacca, L. L., Frauenheim, T., & Lima, E. N. (2019). Electronic and optical properties of Mn impurities in ultra-thin ZnO nanowires: Insights from density-functional theory. *Physica E: Low-Dimensional Systems and Nanostructures*, *109*(December 2018), 6–10. https://doi.org/10.1016/j.physe.2018.12.030

Rosman, N., Wan Salleh, W. N., Aziz, F., Ismail, A. F., Harun, Z., Bahri, S. S., & Nagai, K. (2019). Electrospun Nanofibers Embedding $ZnO/Ag_2CO_3/Ag_2O$ Heterojunction Photocatalyst with Enhanced Photocatalytic Activity. *Catalysts*, *9*(7), 565. https://doi.org/10.3390/catal9070565

Roy, A. (1995). Determination of the flatband potential of semiconductor particles in suspension by photovoltage measurement. *International Journal of Hydrogen Energy*, *20*(8), 627–630. https://doi.org/10.1016/0360-3199(94)00105-9

Rufus, A., Sreeju, N., Vilas, V., & Philip, D. (2017). Biosynthesis of hematite (α-Fe_2O_3) nanostructures: Size effects on applications in thermal conductivity, catalysis, and antibacterial activity. *Journal of Molecular Liquids*, *242*, 537–549. https://doi.org/10.1016/j.molliq.2017.07.057

Russell, A. D. (2003). Similarities and differences in the responses of microorganisms to biocides. *Journal of Antimicrobial Chemotherapy*, *52*(5), 750–763. https://doi.org/10.1093/jac/dkg422

Safari, M., Rostami, M., Alizadeh, M., Alizadehbirjandi, A., Nakhli, S. A., & Aminzadeh, R. (2014). Response surface analysis of photocatalytic degradation of methyl tert-butyl ether by core/shell Fe_3O_4/ZnO nanoparticles. *Journal of Environmental Health Science and Engineering*, *12*(1), 1. https://doi.org/10.1186/2052-336X-12-1

Sahoo, R., Mundamajhi, A., & Das, S. K. (2019). Growth of ZnO nanoparticles prepared from cost effective laboratory grade ZnO powder and their application in UV photocatalytic dye decomposition. *Journal of Materials Science: Materials in Electronics*, *30*(5), 4541–4547. https://doi.org/10.1007/s10854-019-00743-0

Saif, S., Tahir, A., Asim, T., Chen, Y., Khan, M., & Adil, S. F. (2019). Green synthesis of ZnO hierarchical microstructures by Cordia myxa and their antibacterial activity. *Saudi Journal of Biological Sciences*, *26*(7), 1364–1371. https://doi.org/10.1016/j.sjbs.2019.01.004

Saikia, L., Bhuyan, D., Saikia, M., Malakar, B., Dutta, D. K., & Sengupta, P. (2015). Photocatalytic performance of ZnO nanomaterials for self sensitized degradation of malachite green dye under solar light. *Applied Catalysis A: General*, *490*(15), 42–49. https://doi.org/10.1016/j.apcata.2014.10.053

Sakthivel, S., Neppolian, B., Shankar, M. V., Arabindoo, B., Palanichamy, M., & Murugesan, V. (2003). Solar photocatalytic degradation of azo dye: comparison of photocatalytic efficiency of ZnO and TiO_2. *Solar Energy Materials and Solar Cells*, *77*(1), 65–82. https://doi.org/10.1016/S0927-0248(02)00255-6

Santhoshkumar, J., Kumar, S. V., & Rajeshkumar, S. (2017). Synthesis of zinc oxide nanoparticles using plant leaf extract against urinary tract infection pathogen. *Resource-Efficient Technologies*, *3*(4), 459–465. https://doi.org/10.1016/j.reffit.2017.05.001

Saravanan, R., Gupta, V. K. K., Narayanan, V., & Stephen, A. (2014). Visible light degradation of textile effluent using novel catalyst ZnO/γ-Mn_2O_3. *Journal of the Taiwan Institute of Chemical Engineers*, *45*(4), 1910–1917. https://doi.org/10.1016/j.jtice.2013.12.021

Saravanan, R., Khan, M. M., Gupta, V. K., Mosquera, E., Gracia, F., Narayanan, V., & Stephen, A. (2015). ZnO/Ag/Mn_2O_3 nanocomposite for visible light-induced industrial textile effluent degradation, uric acid and ascorbic acid sensing and antimicrobial activity. *RSC Advances*, *5*(44), 34645–34651. https://doi.org/10.1039/C5RA02557E

Saravanan, R., Thirumal, E., Gupta, V. K., Narayanan, V., & Stephen, A. (2013). The photocatalytic activity of ZnO prepared by simple thermal decomposition method at various temperatures. *Journal of Molecular Liquids*, *177*, 394–401. https://doi.org/10.1016/j.molliq.2012.10.018

Sekar, A. D., Kumar, V., Muthukumar, H., Gopinath, P., & Matheswaran, M. (2019). Electrospinning of Fe-doped ZnO nanoparticles incorporated polyvinyl alcohol nanofibers for its antibacterial treatment and cytotoxic studies. *European Polymer*

Journal, *118*(January), 27–35. https://doi.org/10.1016/j.eurpolymj.2019.05.038

Selim, M. S., Hamouda, H., Hao, Z., Shabana, S., & Chen, X. (2020). Design of γ-AlOOH, γ-MnOOH, and α-Mn_2O_3 nanorods as advanced antibacterial active agents. *Dalton Transactions*, *49*(25), 8601–8613. https://doi.org/10.1039/D0DT01689F

Shah, A. H., Manikandan, E., Basheer Ahamed, M., Ahmad Mir, D., & Ahmad Mir, S. (2014). Antibacterial and Blue shift investigations in sol–gel synthesized $Cr_xZn_{1-x}O$ Nanostructures. *Journal of Luminescence*, *145*, 944–950. https://doi.org/10.1016/j.jlumin.2013.09.023

Shawaphun, S., Manangan, T., & Wacharawichanant, S. (2010). Thermo- and Photo-Degradation of LDPE and PP Films Using Metal Oxides as Catalysts. *Advanced Materials Research*, *93–94*, 505–508. https://doi.org/10.4028/www.scientific.net/AMR.93-94.505

Shekofteh-Gohari, M., & Habibi-Yangjeh, A. (2017). Fe_3O_4/ZnO/$CoWO_4$ nanocomposites: Novel magnetically separable visible-light-driven photocatalysts with enhanced activity in degradation of different dye pollutants. *Ceramics International*, *43*(3), 3063–3071. https://doi.org/10.1016/j.ceramint.2016.11.115

Sheng, J., Xie, Y., & Zhou, Y. (2009). Adsorption of methylene blue from aqueous solution on pyrophyllite. *Applied Clay Science*, *46*(4), 422–424. https://doi.org/10.1016/j.clay.2009.10.006

Shimada, T., Yasui, T., Yonese, A., Yanagida, T., Kaji, N., Kanai, M., Nagashima, K., Kawai, T., & Baba, Y. (2020). Mechanical Rupture-Based Antibacterial and Cell-Compatible ZnO/SiO2 Nanowire Structures Formed by Bottom-Up Approaches. *Micromachines*, *11*(6), 610. https://doi.org/10.3390/mi11060610

Shooshtari, N. M., & Ghazi, M. M. (2017). An investigation of the photocatalytic activity of nano α-Fe_2O_3/ZnO on the photodegradation of cefixime trihydrate. *Chemical Engineering Journal*, *315*, 527–536. https://doi.org/10.1016/j.cej.2017.01.058

Sigoli, F. A., Davolos, M. R., & Jafelicci, M. (1997). Morphological evolution of zinc oxide originating from zinc hydroxide carbonate. *Journal of Alloys and Compounds*, *262–263*, 292–295. https://doi.org/10.1016/S0925-8388(97)00404-0

Sin, J., Tan, S., Quek, J., Lam, S., & Mohamed, A. R. (2018). Facile fabrication of hierarchical porous ZnO/Fe_3O_4 composites with enhanced magnetic, photocatalytic and antibacterial properties. *Materials Letters*, *228*, 207–211. https://doi.org/10.1016/j.matlet.2018.06.027

Singh, R., & Dutta, S. (2019). The role of pH and nitrate concentration in the wet chemical growth of nano-rods shaped ZnO photocatalyst. *Nano-Structures & Nano-Objects*, *18*, 100250. https://doi.org/10.1016/j.nanoso.2019.01.009

Singh, S., Barick, K. C., & Bahadur, D. (2013). Fe_3O_4 embedded ZnO nanocomposites for the removal of toxic metal ions, organic dyes and bacterial pathogens. *Journal of Materials Chemistry A*, *1*(10), 3325. https://doi.org/10.1039/c2ta01045c

Sivula, K., Le Formal, F., & Grätzel, M. (2011). Solar Water Splitting: Progress Using Hematite (α-Fe_2O_3) Photoelectrodes. *ChemSusChem*, *4*(4), 432–449. https://doi.org/10.1002/cssc.201000416

Stoimenov, P. K., Klinger, R. L., Marchin, G. L., & Klabunde, K. J. (2002). Metal Oxide Nanoparticles as Bactericidal Agents. *Langmuir*, *18*(17), 6679–6686. https://doi.org/10.1021/la0202374

Su, H., Li, W., Han, Y., & Liu, N. (2018). Magnetic carboxyl functional nanoporous polymer: synthesis, characterization and its application for methylene blue adsorption. *Scientific Reports*, *8*(1), 6506. https://doi.org/10.1038/s41598-018-24873-3

Subbareddy, Y., Kumar, R. N., Sudhakar, B. K., Reddy, K. R., Martha, S. K., & Kaviyarasu, K. (2020). A facile approach of adsorption of acid blue 9 on aluminium silicate-coated Fuller's Earth—Equilibrium and kinetics studies. *Surfaces and Interfaces*, *19*(January), 100503. https://doi.org/10.1016/j.surfin.2020.100503

Subramani, A., & Jacangelo, J. G. (2015). Emerging desalination technologies for water treatment: A critical review. *Water Research*, *75*, 164–187. https://doi.org/10.1016/j.watres.2015.02.032

Sudha, M., Senthilkumar, S., Hariharan, R., Suganthi, A., & Rajarajan, M. (2012). Controlled reduction of the deleterious effects of photocatalytic activity of ZnO nanoparticles by PVA capping. *Journal of Sol-Gel Science and Technology*, *61*(1), 14–22. https://doi.org/10.1007/s10971-011-2584-7

Sui, X. M., Shao, C. L., & Liu, Y. C. (2005). White-light emission of polyvinyl alcoho*l*/ZnO hybrid nanofibers prepared by electrospinning. *Applied Physics Letters*, *87*(11), 113115. https://doi.org/10.1063/1.2048808

Sun, J., Cai, S., Li, Q., Li, Z., & Xu, G. (2020). UV-irradiation induced biological activity and antibacterial activity of ZnO coated magnesium alloy. *Materials Science and Engineering C*, *114*(April), 110997. https://doi.org/10.1016/j.msec.2020.110997

Surendra, B. S., Nagaswarupa, H. P., Anantharaju, K. S., Anil Kumar, M. R., Nagabhushana, H., & Shetty, K. (2018). Acid Activation of Bentonite Clay under Microwave Irradiation: Characterization, Cyclic Voltammetry and Photocatalytic activity. *Materials Today: Proceedings*, *5*(10), 22643–22651. https://doi.org/10.1016/j.matpr.2018.06.639

Suresh, R., Giribabu, K., Manigandan, R., Stephen, A., & Narayanan, V. (2014). Fabrication of Ni–Fe_2O_3 magnetic nanorods and application to the detection of uric acid. *RSC Advances*, *4*(33), 17146. https://doi.org/10.1039/c4ra00725e

Suryavanshi, R. D., & Rajpure, K. Y. (2018). Spray deposited Fe_2O_3 and stratified Fe_2O_3/ZnO novel photoelectrode for photoelectrocatalytic degradation of benzoic acid under solar light illumination. *Journal of Photochemistry and Photobiology A: Chemistry*, *357*, 72–80. https://doi.org/10.1016/j.jphotochem.2018.02.008

Tabrizi Hafez Moghaddas, S. M., Elahi, B., Darroudi, M., & Javanbakht, V. (2019). Green synthesis of hexagonal-shaped zinc oxide nanosheets using mucilage from flaxseed for removal of methylene blue from aqueous solution. *Journal of Molecular Liquids*, *296*, 111834. https://doi.org/10.1016/j.molliq.2019.111834

Tama, A. M., Das, S., Dutta, S., Bhuyan, M. D. I., Islam, M. N., & Basith, M. A. (2019). MoS_2 nanosheet incorporated α-Fe_2O_3/ZnO nanocomposite with enhanced photocatalytic dye degradation and hydrogen production ability. *RSC Advances*, *9*(69), 40357–40367. https://doi.org/10.1039/C9RA07526G

Tan, I. A. W., Ahmad, A. L., & Hameed, B. H. (2008). Adsorption of basic dye on high-surface-area activated carbon prepared from coconut husk: Equilibrium, kinetic and thermodynamic studies. *Journal of Hazardous Materials*, *154*(1–3), 337–346. https://doi.org/10.1016/j.jhazmat.2007.10.031

Tang, C.-F., Kumar, S. A., & Chen, S.-M. (2008). Zinc oxide/redox mediator composite films-based sensor for electrochemical detection of important biomolecules. *Analytical Biochemistry*, *380*(2), 174–183. https://doi.org/10.1016/j.ab.2008.06.004

Taufik, A., Kalim, I., & Saleh, R. (2015). Preparation, Characterization and Photocatalytic Activity of Multifunctional Fe_3O_4/ZnO/CuO Hybrid Nanoparticles. *Materials Science Forum*, *827*, 37–42. https://doi.org/10.4028/www.scientific.net/msf.827.37

Tedla, H., Díaz, I., Kebede, T., & Taddesse, A. M. (2015). Synthesis, characterization and photocatalytic activity of zeolite supported ZnO/Fe_2O_3/MnO_2 nanocomposites. *Journal of Environmental Chemical Engineering*, *3*(3), 1586–1591. https://doi.org/10.1016/j.jece.2015.05.012

Thakur, N., Manna, P., & Das, J. (2019). Synthesis and biomedical applications of nanoceria, a redox active nanoparticle. *Journal of Nanobiotechnology*, *17*(1), 84. https://doi.org/10.1186/s12951-019-0516-9

Thambidurai, S., Gowthaman, P., Venkatachalam, M., & Suresh, S. (2020). Enhanced bactericidal performance of nickel oxide-zinc oxide nanocomposites synthesized by facile chemical co-precipitation method. *Journal of Alloys and Compounds*, *830*, 154642. https://doi.org/10.1016/j.jallcom.2020.154642

Thommes, M., Kaneko, K., Neimark, A. V., Olivier, J. P., Rodriguez-Reinoso, F., Rouquerol, J., & Sing, K. S. W. (2015). Physisorption of gases, with special reference to the evaluation of surface area and pore size distribution (IUPAC Technical Report). *Pure and Applied Chemistry*, *87*(9–10), 1051–1069. https://doi.org/10.1515/pac-2014-1117

Tian, C., Zhang, Q., Wu, A., Jiang, M., Liang, Z., Jiang, B., & Fu, H. (2012). Cost-effective large-scale synthesis of ZnO photocatalyst with excellent performance for dye photodegradation. *Chemical Communications*, *48*(23), 2858. https://doi.org/10.1039/c2cc16434e

Tian, S., Liu, Q., Sun, J., Zhu, M., Wu, S., & Zhao, X. (2019). Mesoporous ZnO nanorods array with a controllable area density for enhanced photocatalytic properties. *Journal of Colloid and Interface Science*, *534*, 389–398. https://doi.org/10.1016/j.jcis.2018.09.049

Tikare, R. R., Powar, R. R., Parale, V. G., Park, H.-H., Shinde, T. J., & Kanase, D. G. (2020). Influence of Zn-substitution on structural, morphological, electrical, and gas sensing properties of $ZnAl_2O_4$ (x = 0.1 to 0.5) synthesized by a sol-gel auto-combustion method. *Ceramics International*, *October*. https://doi.org/10.1016/j.ceramint.2020.11.021

Tong, X., Zhang, H., & Li, D. Y. (2015). Effect of Annealing Treatment on Mechanical Properties of Nanocrystalline α-iron: an Atomistic Study. *Scientific Reports*, *5*(1), 8459. https://doi.org/10.1038/srep08459

Vahdat Vasei, H., Masoudpanah, S. M., Adeli, M., Aboutalebi, M. R., & Habibollahzadeh, M. (2019). Mesoporous honeycomb-like ZnO as ultraviolet photocatalyst synthesized via solution combustion method. *Materials Research Bulletin*, *117*(January), 72–77. https://doi.org/10.1016/j.materresbull.2019.04.024

Vinu, R., & Madras, G. (2010). Environmental remediation by photocatalysis. *Journal of the Indian Institute of Science*, *90*(2), 189–230.

Viswanathan, K., Kim, I., Kasi, G., Sadeghi, K., Thanakkasaranee, S., & Seo, J. (2020). Facile approach to enhance the antibacterial activity of ZnO nanoparticles. *Advances*

in Applied Ceramics, *0*(0), 1–9. https://doi.org/10.1080/17436753.2020.1777507

Wachs, I. E. (1996). Raman and IR studies of surface metal oxide species on oxide supports: Supported metal oxide catalysts. *Catalysis Today*, *27*(3–4), 437–455. https://doi.org/10.1016/0920-5861(95)00203-0

Wahab, R., Khan, F., & Al-Khedhairy, A. A. (2020). Peanut-shaped ZnO nanostructures: A driving force for enriched antibacterial activity and their statistical analysis. *Ceramics International*, *46*(1), 307–316. https://doi.org/10.1016/j.ceramint.2019.08.264

Wang, Da, Hosteen, O., & Fierke, C. A. (2012). ZntR-mediated transcription of zntA responds to nanomolar intracellular free zinc. *Journal of Inorganic Biochemistry*, *111*, 173–181. https://doi.org/10.1016/j.jinorgbio.2012.02.008

Wang, Desong, Wang, Y., Li, X., Luo, Q., An, J., & Yue, J. (2008). Sunlight photocatalytic activity of polypyrrole–TiO_2 nanocomposites prepared by 'in situ' method. *Catalysis Communications*, *9*(6), 1162–1166. https://doi.org/10.1016/j.catcom.2007.10.027

Wang, H., Zhou, P., Guo, R., Wang, Y., Zhan, H., & Yuan, Y. (2018). Synthesis of Rectorite/Fe_3O_4/ZnO Composites and Their Application for the Removal of Methylene Blue Dye. *Catalysts*, *8*(3), 107. https://doi.org/10.3390/catal8030107

Wang, Jing, Xia, Y., Dong, Y., Chen, R., Xiang, L., & Komarneni, S. (2016). Defect-rich ZnO nanosheets of high surface area as an efficient visible-light photocatalyst. *Applied Catalysis B: Environmental*, *192*, 8–16. https://doi.org/10.1016/j.apcatb.2016.03.040

Wang, Junpeng, Wang, Z., Huang, B., Ma, Y., Liu, Y., Qin, X., Zhang, X., & Dai, Y. (2012). Oxygen Vacancy Induced Band-Gap Narrowing and Enhanced Visible Light Photocatalytic Activity of ZnO. *ACS Applied Materials & Interfaces*, *4*(8), 4024–4030. https://doi.org/10.1021/am300835p

Wang, R., Hao, Q., Feng, J., Wang, G. C., Ding, H., Chen, D., & Ni, B. (2019). Enhanced separation of photogenerated charge carriers and catalytic properties of ZnO-MnO_2 composites by microwave and photothermal effect. *Journal of Alloys and Compounds*, *786*, 418–427. https://doi.org/10.1016/j.jallcom.2019.02.009

Wang, S., Kuang, P., Cheng, B., Yu, J., & Jiang, C. (2018). ZnO hierarchical microsphere for enhanced photocatalytic activity. *Journal of Alloys and Compounds*, *741*, 622–632. https://doi.org/10.1016/j.jallcom.2018.01.141

Wang, W., Yu, L., Yang, H., Hong, K., Qiao, Z., & Wang, H. (2015). Growth mechanism of ZnO nanorod/Fe_3O_4 nanoparticle composites and their photocatalytic properties. *Physica E: Low-Dimensional Systems and Nanostructures*, *74*, 71–73. https://doi.org/10.1016/j.physe.2015.06.024

Wang, X., Li, Q., Zhou, C., Cao, Z., & Zhang, R. (2019). ZnO rod/reduced graphene oxide sensitized by α-Fe_2O_3 nanoparticles for effective visible-light photoreduction of CO2. *Journal of Colloid and Interface Science*, *554*, 335–343. https://doi.org/10.1016/j.jcis.2019.07.014

Wang, Yan, Chen, Z., Lei, T., Ai, Y., Peng, Z., Yan, X., Li, H., Zhang, J., Wang, Z. M., & Chueh, Y.-L. (2018). Hollow $NiCo_2S_4$ Nanospheres Hybridized with 3D Hierarchical Porous rGO/Fe_2O_3 Composites toward High-Performance Energy Storage Device. *Advanced Energy Materials*, *8*(16), 1703453. https://doi.org/10.1002/aenm.201703453

Wang, Yingming, Ge, S., Cheng, W., Hu, Z., Shao, Q., Wang, X., Lin, J., Dong, M., Wang, J., & Guo, Z. (2020). Microwave Hydrothermally Synthesized Metal–Organic Framework-5 Derived C-doped ZnO with Enhanced Photocatalytic Degradation of Rhodamine B. *Langmuir*, *36*(33), 9658–9667. https://doi.org/10.1021/acs.langmuir.0c00395

Wang, Yuxian, Sun, H., Ang, H. M., Tadé, M. O., & Wang, S. (2014). Facile Synthesis of Hierarchically Structured Magnetic MnO_2/$ZnFe_2O_4$ Hybrid Materials and Their Performance in Heterogeneous Activation of Peroxymonosulfate. *ACS Applied Materials & Interfaces*, *6*(22), 19914–19923. https://doi.org/10.1021/am505309b

Wu, J., Shi, S., Wang, X., Li, J., Zong, R., & Chen, W. (2014). Controlled synthesis and optimum luminescence of Sm^{3+}-activated nano/submicroscale ceria particles by a facile approach. *J. Mater. Chem. C*, *2*(15), 2786–2792. https://doi.org/10.1039/C3TC32424A

Wu, P., Du, N., Zhang, H., Jin, L., & Yang, D. (2010). Functionalization of ZnO nanorods with γ-Fe_2O_3 nanoparticles: Layer-by-layer synthesis, optical and magnetic properties. *Materials Chemistry and Physics*, *124*(2–3), 908–911. https://doi.org/10.1016/j.matchemphys.2010.08.009

Wu, Z., & Wu, W. (2015). Shape control of inorganic nanoparticles from solution. *Nanoscale*, *8*, 1237–1259. https://doi.org/10.1039/c5nr07681a

Xia, J., Wang, A., Liu, X., & Su, Z. (2011). Preparation and characterization of bifunctional, Fe_3O_4/ZnO nanocomposites and their use as photocatalysts. *Applied Surface Science*, *257*(23), 9724–9732. https://doi.org/10.1016/j.apsusc.2011.05.114

Xia, S., Meng, Y., Zhou, X., Xue, J., Pan, G., & Ni, Z. (2016). Ti/ZnO–Fe_2O_3 composite: Synthesis, characterization and application as a highly efficient photoelectrocatalyst for methanol from CO_2 reduction. *Applied Catalysis B: Environmental*, *187*, 122–133. https://doi.org/10.1016/j.apcatb.2016.01.027

Xie, J., Hao, Y. J., Zhou, Z., Meng, X. C., Yao, L., Bian, L., & Wei, Y. (2014). Fabrication and characterization of ZnO particles with different morphologies for photocatalytic degradation of pentachlorophenol. *Research on Chemical Intermediates*, *40*(5), 1937–1946. https://doi.org/10.1007/s11164-013-1091-6

Xie, J., Li, Y., Zhao, W., Bian, L., & Wei, Y. (2011). Simple fabrication and photocatalytic activity of ZnO particles with different morphologies. *Powder Technology*, *207*(1–3), 140–144. https://doi.org/10.1016/j.powtec.2010.10.019

Xie, J., Zhang, L., Li, M., Hao, Y., Lian, Y., Li, Z., & Wei, Y. (2015). α-Fe_2O_3 modified ZnO flower-like microstructures with enhanced photocatalytic performance for pentachlorophenol degradation. *Ceramics International*, *41*(8), 9420–9425. https://doi.org/10.1016/j.ceramint.2015.03.320

Xu, J., Sun, Y., Lu, M., Wang, L., Zhang, J., Qian, J., & Kim, E. J. (2017). Fabrication of porous Mn_2O_3 microsheet arrays on nickel foam as high–rate electrodes for supercapacitors. *Journal of Alloys and Compounds*, *717*, 108–115. https://doi.org/10.1016/j.jallcom.2017.04.239

Xu, K., Xu, Y., Zhang, H., Peng, B., Shao, H., Ni, G., Li, J., Yao, M., Lu, H., Zhu, H., & Soukoulis, C. M. (2018). The role of Anderson's rule in determining electronic, optical and transport properties of transition metal dichalcogenide heterostructures. *Physical Chemistry Chemical Physics*, *20*(48), 30351–30364. https://doi.org/10.1039/C8CP05522J

Xu, M., Li, Q., & Fan, H. (2014). Monodisperse nanostructured Fe_3O_4/ZnO microrods using for waste water treatment. *Advanced Powder Technology*, *25*(6), 1715–1720. https://doi.org/10.1016/j.apt.2014.06.019

Xue, X., Penn, R. L., Leite, E. R., Huang, F., & Lin, Z. (2014). Crystal growth by oriented attachment: kinetic models and control factors. *CrystEngComm*, *16*(8), 1419. https://doi.org/10.1039/c3ce42129e

Yagub, M. T., Sen, T. K., Afroze, S., & Ang, H. M. (2014). Dye and its removal from aqueous solution by adsorption: A review. *Advances in Colloid and Interface Science*, *209*, 172–184. https://doi.org/10.1016/j.cis.2014.04.002

Yamamoto, O. (2001). Influence of particle size on the antibacterial activity of zinc oxide. *International Journal of Inorganic Materials*, *3*(7), 643–646. https://doi.org/10.1016/S1466-6049(01)00197-0

Yan, H., Zhang, J., You, C., Song, Z., Yu, B., & Shen, Y. (2009). Influences of different synthesis conditions on properties of Fe_3O_4 nanoparticles. *Materials Chemistry and Physics*, *113*(1), 46–52. https://doi.org/10.1016/j.matchemphys.2008.06.036

Yan, W., Fan, H., & Yang, C. (2011). Ultra-fast synthesis and enhanced photocatalytic properties of alpha-Fe_2O_3/ZnO core-shell structure. *Materials Letters*, *65*(11), 1595–1597. https://doi.org/10.1016/j.matlet.2011.03.026

Yang, Guidong, Yan, Z., & Xiao, T. (2012). Preparation and characterization of SnO_2/ZnO/TiO_2 composite semiconductor with enhanced photocatalytic activity. *Applied Surface Science*, *258*(22), 8704–8712. https://doi.org/10.1016/j.apsusc.2012.05.078

Yang, Guorui, Yan, W., Wang, J., & Yang, H. (2014). Fabrication and formation mechanism of Mn_2O_3 hollow nanofibers by single-spinneret electrospinning. *CrystEngComm*, *16*(30), 6907–6913. https://doi.org/10.1039/C4CE00521J

Yang, H., Zhang, Q., Chen, Y., Huang, Y., Yang, F., & Lu, Z. (2018). Ultrasonic-microwave synthesis of ZnO/BiOBr functionalized cotton fabrics with antibacterial and photocatalytic properties. *Carbohydrate Polymers*, *201*(July), 162–171. https://doi.org/10.1016/j.carbpol.2018.08.068

Yang, Linglu, Yang, Z., Cao, W., Chen, L., Xu, J., & Zhang, H. (2005). Luminescence 3D-Ordered Porous Materials Composed of CdSe and CdTe Nanocrystals. *The Journal of Physical Chemistry B*, *109*(23), 11501–11504. https://doi.org/10.1021/jp050242r

Yang, Lu, Liu, D., Huang, J., & You, T. (2014). Simultaneous determination of dopamine, ascorbic acid and uric acid at electrochemically reduced graphene oxide modified electrode. *Sensors and Actuators B: Chemical*, *193*, 166–172. https://doi.org/10.1016/j.snb.2013.11.104

Yang, S., Nie, Y., Zhang, B., Tang, X., & Mao, H. (2020). Construction of Er-doped ZnO/SiO2 composites with enhanced antimicrobial properties and analysis of antibacterial mechanism. *Ceramics International*, *46*(13), 20932–20942. https://doi.org/10.1016/j.ceramint.2020.05.149

Yang, X., Wu, Y., & Zhang, L. (2015). Synthesis of Fe_3O_4@SiO_2@MnO_2 composite magnetic submicrospheres as adsorbent for methyl orange decolouration. *Micro & Nano Letters*, *10*(1), 12–15. https://doi.org/10.1049/mnl.2014.0555

Yang, Y., Li, X., Zhao, R., Yang, J., Sun, Q., Chen, X., & Wu, X. (2018). The Study on Degradation and Separation of RhB Under UV Light by Magnetically ZnO/Fe_2O_3 Nanoparticles. *Physica Status Solidi (A)*, *215*(23), 1800416. https://doi.org/10.1002/pssa.201800416

Yang, Z., Zong, X. L., Ye, Z., Zhao, B., Wang, Q. L., & Wang, P. (2010). The application of complex multiple forklike ZnO nanostructures to rapid and ultrahigh sensitive hydrogen peroxide biosensors. *Biomaterials*, *31*(29), 7534–7541. https://doi.org/10.1016/j.biomaterials.2010.06.019

Yao, S., Feng, X., Lu, J., Zheng, Y., Wang, X., Volinsky, A. A., & Wang, L.-N. (2018). Antibacterial activity and inflammation inhibition of ZnO nanoparticles embedded TiO_2 nanotubes. *Nanotechnology*, *29*(24), 244003. https://doi.org/10.1088/1361-6528/aabac1

Yemmireddy, V. K., & Hung, Y.-C. (2017). Using Photocatalyst Metal Oxides as Antimicrobial Surface Coatings to Ensure Food Safety-Opportunities and Challenges. *Comprehensive Reviews in Food Science and Food Safety*, *16*(4), 617–631. https://doi.org/10.1111/1541-4337.12267

Yin, A., Wei, X., Cao, Y., & Li, H. (2016). High-quality molybdenum disulfide nanosheets with 3D structure for electrochemical sensing. *Applied Surface Science*, *385*, 63–71. https://doi.org/10.1016/j.apsusc.2016.05.066

Yin, Q., Qiao, R., Zhu, L., Li, Z., Li, M., & Wu, W. (2014). α-Fe_2O_3 decorated ZnO nanorod-assembled hollow microspheres: Synthesis and enhanced visible-light photocatalysis. *Materials Letters*, *135*, 135–138. https://doi.org/10.1016/j.matlet.2014.07.149

Yu, C., Chen, F., Zeng, D., Xie, Y., Zhou, W., Liu, Z., Wei, L., Yang, K., & Li, D. (2019). A facile phase transformation strategy for fabrication of novel Z-scheme ternary heterojunctions with efficient photocatalytic properties. *Nanoscale*, *11*(16), 7720–7733. https://doi.org/10.1039/C9NR00709A

Yu, W., Liu, T., Cao, S., Wang, C., & Chen, C. (2016). Constructing MnO_2/single crystalline ZnO nanorod hybrids with enhanced photocatalytic and antibacterial activity. *Journal of Solid State Chemistry*, *239*, 131–138. https://doi.org/10.1016/j.jssc.2016.04.027

Zeng, Z., Zhang, W., Arvapalli, D. M., Bloom, B., Sheardy, A., Mabe, T., Liu, Y., Ji, Z., Chevva, H., Waldeck, D. H., & Wei, J. (2017). A fluorescence-electrochemical study of carbon nanodots (CNDs) in bio- and photoelectronic applications and energy gap investigation. *Physical Chemistry Chemical Physics*, *19*(30), 20101–20109. https://doi.org/10.1039/C7CP02875J

Zhai, T., Xie, S., Zhao, Y., Sun, X., Lu, X., Yu, M., Xu, M., Xiao, F., & Tong, Y. (2012). Controllable synthesis of hierarchical ZnO nanodisks for highly photocatalytic activity. *CrystEngComm*, *14*(5), 1850. https://doi.org/10.1039/c1ce06013a

Zhang, G., Shen, X., & Yang, Y. (2011). Facile Synthesis of Monodisperse Porous ZnO Spheres by a Soluble Starch-Assisted Method and Their Photocatalytic Activity. *The Journal of Physical Chemistry C*, *115*(15), 7145–7152. https://doi.org/10.1021/jp110256s

Zhang, Jing, Huang, F., & Lin, Z. (2010). Progress of nanocrystalline growth kinetics based on oriented attachment. *Nanoscale*, *2*(1), 18–34. https://doi.org/10.1039/B9NR00047J

Zhang, Jun, Liu, X., Wang, L., Yang, T., Guo, X., Wu, S., Wang, S., & Zhang, S. (2011). Synthesis and gas sensing properties of α-Fe_2O_3@ZnO core–shell nanospindles. *Nanotechnology*, *22*(18), 185501. https://doi.org/10.1088/0957-4484/22/18/185501

Zhang, L., Ding, Y., Povey, M., & York, D. (2008). ZnO nanofluids – A potential antibacterial agent. *Progress in Natural Science*, *18*(8), 939–944. https://doi.org/10.1016/j.pnsc.2008.01.026

Zhang, L., Jiang, Y., Ding, Y., Povey, M., & York, D. (2007). Investigation into the antibacterial behaviour of suspensions of ZnO nanoparticles (ZnO nanofluids). *Journal of Nanoparticle Research*, *9*(3), 479–489. https://doi.org/10.1007/s11051-006-9150-1

Zhang, Q., Xu, M., You, B., Zhang, Q., Yuan, H., & Ostrikov, K. (2018). Oxygen Vacancy-Mediated ZnO Nanoparticle Photocatalyst for Degradation of Methylene Blue. *Applied Sciences*, *8*(3), 353. https://doi.org/10.3390/app8030353

Zhang, W., Zhang, S., Wang, J., Wang, M., He, Q., Song, J., Wang, H., & Zhou, J. (2018). Hybrid functionalized chitosan-Al_2O_3@SiO_2 composite for enhanced Cr(VI) adsorption. *Chemosphere*, *203*, 188–198. https://doi.org/10.1016/j.chemosphere.2018.03.188

Zhang, Xiaofei, Wang, Y., Liu, B., Sang, Y., & Liu, H. (2017). Heterostructures construction on TiO_2 nanobelts: A powerful tool for building high-performance photocatalysts. *Applied Catalysis B: Environmental*, *202*, 620–641. https://doi.org/10.1016/j.apcatb.2016.09.068

Zhang, Xinyu, Qin, J., Xue, Y., Yu, P., Zhang, B., Wang, L., & Liu, R. (2015). Effect of aspect ratio and surface defects on the photocatalytic activity of ZnO nanorods. *Scientific Reports*, *4*(1), 4596. https://doi.org/10.1038/srep04596

Zhang, Z., Wu, Y., Wang, Z., Zhang, X., Zhao, Y., & Sun, L. (2017). Electrospinning of Ag Nanowires/polyvinyl alcohol hybrid nanofibers for their antibacterial properties. *Materials Science and Engineering: C*, *78*, 706–714. https://doi.org/10.1016/j.msec.2017.04.138

Zhang, Z., Wu, Y., Wang, Z., Zou, X., Zhao, Y., & Sun, L. (2016). Fabrication of silver nanoparticles embedded into polyvinyl alcohol (Ag/PVA) composite nanofibrous films through electrospinning for antibacterial and surface-enhanced Raman scattering (SERS) activities. *Materials Science and Engineering: C*, *69*, 462–469. https://doi.org/10.1016/j.msec.2016.07.015

Zhao, J., Nan, J., Zhao, Z., & Li, N. (2017). Facile fabrication of novel Mn_2O_3 nanocubes with superior light-harvesting for ciprofloxacin degradation. *Catalysis Communications*, *102*, 5–8. https://doi.org/10.1016/j.catcom.2017.08.018

Zhao, J., Zhao, Z., Li, N., Nan, J., Yu, R., & Du, J. (2018). Visible-light-driven photocatalytic degradation of ciprofloxacin by a ternary Mn_2O_3/Mn_3O_4/MnO_2 valence state heterojunction. *Chemical Engineering Journal*, *353*(73), 805–813. https://doi.org/10.1016/j.cej.2018.07.163

Zhao, X. S., Lu, G. Q. (Max), & Millar, G. J. (1996). Advances in Mesoporous Molecular Sieve MCM-41. *Industrial & Engineering Chemistry Research*, *35*(7), 2075–2090. https://doi.org/10.1021/ie950702a

Zhiwen, C., Shuyuan, Z., Shun, T., Fanqing, L., Jian, W., Sizhao, J., & Yuheng, Z. (1997). Preparation and electron spin resonance effect of nanometer-sized Mn_2O_3. *Journal of Crystal Growth*, *180*(2), 280–283. https://doi.org/10.1016/S0022-0248(97)00215-7

Zholobak, N. M., Ivanov, V. K., & Shcherbakov, A. B. (2016). Interaction of nanoceria with microorganisms. In *Nanobiomaterials in Antimicrobial Therapy* (pp. 419–450). Elsevier. https://doi.org/10.1016/B978-0-323-42864-4.00012-9

Zhou, L., Pan, S., Chen, X., Zhao, Y., Zou, B., & Jin, M. (2014). Kinetics and thermodynamics studies of pentachlorophenol adsorption on covalently functionalized Fe_3O_4@SiO_2–MWCNTs core–shell magnetic microspheres. *Chemical Engineering Journal*, *257*, 10–19. https://doi.org/10.1016/j.cej.2014.07.060

Zhou, S., Shi, H., Feng, X., Xue, K., & Song, W. (2013). Design of templated nanoporous carbon electrode materials with substantial high specific surface area for simultaneous determination ofbiomolecules. *Biosensors and Bioelectronics*, *42*(1), 163–169. https://doi.org/10.1016/j.bios.2012.10.043

Znaidi, L., Soler Illia, G. J. A. A., Benyahia, S., Sanchez, C., & Kanaev, A. V. (2003). Oriented ZnO thin films synthesis by sol–gel process for laser application. *Thin Solid Films*, *428*(1–2), 257–262. https://doi.org/10.1016/S0040-6090(02)01219-1

Zou, X., Yan, X., Li, G., Tian, Y., Zhang, M., & Liang, L. (2017). Solution combustion synthesis and enhanced gas sensing properties of porous In_2O_3/ZnO heterostructures. *RSC Advances*, *7*(55), 34482–34487. https://doi.org/10.1039/c7ra04852a

Publications

7. PUBLICATIONS

1. Abebe, B.; Murthy, H. A.; Amare, E. Enhancing the Photocatalytic Efficiency of ZnO: Defects, Heterojunction, and Optimization. Environ. Nanotechnology, Monit. Manag., 2020, 14, 100336. https://doi.org/10.1016/j.enmm.2020.100336.

2. Abebe, B.; Zereffa, E. A.; Murthy, H. C. A. Synthesis of Poly(Vinyl Alcohol)-Aided ZnO/Mn 2 O 3 Nanocomposites for Acid Orange-8 Dye Degradation: Mechanism and Antibacterial Activity. ACS Omega, 2021, 6 (1), 954–964. https://doi.org/10.1021/acsomega.0c05597.

3. Abebe, B.; Murthy, H. C. A.; Zereffa, E. A. Multifunctional Application of PVA-Aided Zn–Fe–Mn Coupled Oxide Nanocomposite. Nanoscale Res. Lett., 2021, 16 (1), 1. https://doi.org/10.1186/s11671-020-03464-0.

4. Abebe, B.; Zereffa, E. A.; Tadesse, A.; Murthy, H. C. A. A Review on Enhancing the Antibacterial Activity of ZnO: Mechanisms and Microscopic Investigation. Nanoscale Res. Lett., 2020, 15 (1), 190. https://doi.org/10.1186/s11671-020-03418-6.

5. Abebe, B.; Murthy, H. C. A.; Zereffa, E. A.; Adimasu, Y. Synthesis and Characterization of ZnO/PVA Nanocomposites for Antibacterial and Electrochemical Applications. Inorg. Nano-Metal Chem., 2020, 0 (0), 1–12. https://doi.org/10.1080/24701556.2020.1814338.

6. Abebe, B.; Murthy, H. C. A.; Zereffa, E. A.; Qiang, Y. Synthesis and Characterization of PVA-Assisted Metal Oxide Nanomaterials: Surface Area, Porosity, and Electrochemical Property Improvement. J. Nanomater., 2020, 2020, 1–14. https://doi.org/10.1155/2020/6532835.

7. Abebe, B.; Murthy, H. C. A.; Zerefa, E.; Adimasu, Y. PVA Assisted ZnO Based Mesoporous Ternary Metal Oxides Nanomaterials: Synthesis, Optimization, and Evaluation of Antibacterial Activity. Mater. Res. Express, 2020, 7 (4), 045011. https://doi.org/10.1088/2053-1591/ab87d5.

8. Abebe, B.; H C, A. M.; Zerefa, E.; Abdisa, E. Porous PVA/Zn–Fe–Mn Oxide Nanocomposites: Methylene Blue Dye Adsorption Studies. Mater. Res. Express, 2020, 7 (6), 065002. https://doi.org/10.1088/2053-1591/ab94fc.

9. Abebe, B.; Ravikumar, C. R.; Zereffa, E. A.; Naveen Kumar, A.; Murthy, H. C. A. Photocatalytic and Superior Ascorbic Acid Sensor Activities of PVA/Zn-Fe-Mn Ternary Oxide Nanocomposite. Inorg. Chem. Commun., 2021, 123 (September 2020), 108343. https://doi.org/10.1016/j.inoche.2020.108343.

10. Abebe, B.; Zereffa, E. A.; Murthy, H. C. A.; Ravikumar, C. R. A Novel Poly (Vinyl Alcohol)-Aided ZnO/Fe2O3 Nanocomposite as an Ascorbic Acid Sensor. J. Mater. Sci. Mater., Electron, 2021. https://doi.org/10.1007/s10854-021-05497-2.